Optical techniques for non-destructive detection of flaws in ceramic components

Mateusz Matysiak

A dissertation submitted for the degree of Doctor of Philosophy

Heriot-Watt University

School of Engineering and Physical Sciences

May 2012

ABSTRACT

This thesis primarily concerns development of a non-destructive inspection method for 3mol% Yttria-Stabilised Zirconia Polycrystal (3Y-TZP) ceramics used for dental applications and a scoping study on applying the technique to other ceramic materials applied in thermal barrier coatings and other fields.

Zirconia ceramics are materials of great interest for various engineering applications, primarily due to their stiffness, hardness and wear resistance. These factors in combination with the complex manufacturing processes may reduce the material strength and durability due to induced cracking. Knowledge of the extent of this cracking must be obtained and often, if each part is unique as in biomedicine, the assessment must be carried out for every part non-destructively so the part can be subsequently used.

Only a few techniques are known for inspection of Zirconia ceramics, however these techniques are not able to detect flaws in thick (above 500 μm) parts. The main limitation for optical inspection of 3Y-TZP is the highly scattering nature of the material due to its multicrystalline grain structure (grains size of 500 nm) which, particularly in the visible region, reduces imaging capabilities. However, a transmission window in the mid-infrared (between 3 and 8 μm) exists opening up the potential for inspection at these wavelengths.

Mid-Infrared Transmission Imaging (MIR-TI) and Confocal Mid-Infrared Transmission Imaging (CMIR-TI) techniques were developed for inspection of 3Y-TZP parts which allow for detecting sub mm scale cracks. The measured imaging resolution for the MIR-TI is 42 ± 5 μm, whereas for the CMIR-TI it is below 38.5 ± 5 μm. The maximum sample thickness inspected with the MIR-TI and CMIR-TI is 6 mm and 3.5 mm respectively, considerably more than currently available inspection methods. The MIR-TI technique provides fast inspection of the part due to the large field of view (11 by 7 mm), however the high cost and limited imaging resolution make this technique less attractive. The CMIR-TI technique on the other hand is more cost effective due to reduced cost of the infrared sensor and it provides an enhanced imaging capabilities.

The promising results achieved with the MIR-TI and CMIR-TI techniques led to the development of reflection equivalents (Camera-MIRI and Confocal-MIRI) for ceramic coating measurements, however further in-depth experiments to determine and quantify the capabilities of both techniques are required.

DEDICATION

This thesis is dedicated to

my wife Marta, our son Adam

and my parents Maria and Jerzy

ACKNOWLEDGEMENTS

I would like to thank my supervisors Dr Jonathan Shephard and Professor Duncan Hand for all the support and guidance I received from them throughout the course of the project. Thank you for numerous meetings, which helped me to find the way through all the challenges which appeared during the project. Special gratitude to Dr Shephard for correcting my writing – I have learnt a lot, however using "a" and "the" is sometimes a mystery.

I am also grateful for Dr Nick Weston's and Renishaw plc's technical and financial support which was very valuable and enabled me to implement an industrial direction to my project. I would like to thank Dr Yvonne Huddart and Dr Nick Weston for their time spent proof reading my thesis.

Thank you to all the Applied Optics and Photonics group members for the time spent working together, for all the chats in the lab and their support during my work. I would like to highlight the always helpful hand of Dr Jonathan Parry and Frank Albri. My words of gratitude are also addressed to Professor Graham Crowder and Marian Millar for the time spent together during the FTIR and SEM measurements.

I would like to thank my wife for her patience and for continuously motivating me to finish writing up this thesis. Thank you to my son Adam for giving me an opportunity to become a child again and time off thinking about my thesis. Thank to both of you for the smile whenever I come back home from work.

My gratitude is also addressed to my parents for bringing me up to be a person as I am now. Thank you for teaching me how to achieve goals which seem to be not viable. Thank you to my grandfather Piotr for a continuous interest and supporting me in becoming a scientist/engineer.

ACADEMIC REGISTRY
Research Thesis Submission

Name*:*	MATEUSZ MATYSIAK		
School/PGI:	School of Engineering and Physical Sciences		
Version: *(i.e. First, Resubmission, Final)*	FINAL	Degree Sought (Award **and** Subject area)	Doctor of Philosophy in Physics

Declaration

In accordance with the appropriate regulations I hereby submit my thesis and I declare that:

1) the thesis embodies the results of my own work and has been composed by myself
2) where appropriate, I have made acknowledgement of the work of others and have made reference to work carried out in collaboration with other persons
3) the thesis is the correct version of the thesis for submission and is the same version as any electronic versions submitted*.
4) my thesis for the award referred to, deposited in the Heriot-Watt University Library, should be made available for loan or photocopying and be available via the Institutional Repository, subject to such conditions as the Librarian may require
5) I understand that as a student of the University I am required to abide by the Regulations of the University and to conform to its discipline.

* *Please note that it is the responsibility of the candidate to ensure that the correct version of the thesis is submitted.*

Signature of Candidate*:*		Date:	

Submission

Submitted By *(name in capitals):*	
Signature of Individual Submitting:	
Date Submitted:	

For Completion in the Student Service Centre (SSC)

Received in the SSC by *(name in capitals):*			
Method of Submission *(Handed in to SSC; posted through internal/external mail):*			
*E-thesis Submitted (**mandatory for final theses)***			
Signature:		Date:	

TABLE OF CONTENTS

ABBREVIATIONS

Δf – effective noise bandwidth,

3Y-TZP – 3mol% Yttria-Stabilised Zirconia Polycrystal,

a – spherical particle radius,

A_d – detector active region diameter,

AE – Acoustic Emission,

APS – Air Plasma Spraying,

b – Wien's displacement constant ($2.8977685 \cdot 10^{-3}$ m·K),

BST – Barium Strontium Titanate,

c – speed of light in vacuum ($3 \cdot 10^8$ m/s),

Camera-MIRI – Camera Mid-Infrared Reflection Imaging,

CC – cubic convolution interpolation,

CIP – Cold Isostatic Pressing,

CLAHE - Contrast Limited Adaptive Histogram Equalization,

CM – Confocal Microscopy,

Confocal-MIRI – Confocal Mid-Infrared Reflection Imaging,

D – detectivity,

d – step size,

D* – normalised detectivity,

dia – lens diameter,

DOF – depth of field,

DPI – Dye-Penetration Inspection,

DSLR - digital single-lens reflex camera

EB-PVD – Electron Beam Physical Vapour Deposition,

E_g – energy difference between transition states,

EM – electromagnetic wave,

ESEM – Environmental Scanning Electron Microscopy,

f - frequency,

FPA – Focal Plane Array detector,

FTIR - Fourier Transform Infrared Spectroscopy,

f_x – lens focal length,

g – lock-in gain,

h – Planck's constant (6.626·10-34 J·s),

HAZ – Heat Affected Zone,

HIP – Hot Isostatic Pressing,

HR – high resolution,

I – Irradiance,

k – light absorption of the electromagnetic wave,

LAM – Laser Assisted Machining,

LR – low resolution,

LU – Laser Ultrasonics,

M – image magnification,

m_0 – refractive index of the surrounding medium,

Mean – average value of the acquired signal,

MIR – Mid-Infrared Reflectance Imaging,

M_{pixel} – standard deviation of the quantity of pixels for all the pixel intensities (from 0 to 255 range),

N – number of lock-in input signal periods acquired in fixed amount of time per single output data point,

n – refractive index,

NA – numerical aperture,

NDT – Non-Destructive Testing,

NEP – Noise Equivalent Power,

NIR – near-infrared,

n_y - number of iterations/steps in y axis for the scanned areas,

OCT – Optical Coherence Tomography,

P – power of electromagnetic radiation,

P_0 – optical power incident on the measured sample,

P_1 – optical power transmitted through the sample

P_{noise} – noise power,

P_{signal} – power of the meaningful signal,

PSZ – Partially Stabilised Zirconia ceramics,

R – Imaging resolution,

RMS – Root Mean Square,

RSD – relative standard deviation,

S – lock-in sensitivity,

SEM – Scanning Electron Microscopy,

SFR – Spatial Frequency Response,

SLAM – Scanning Laser Acoustic Microscopy,

SNOM - Scanning Near-Field Optical Microscopy,

SNR – Signal-to-Noise ratio,

SR – Super-Resolution,

t – CMIR-TI system scanning time of the defined area,

T – optical transmittance,

TBC – Thermal Barrier Coating,

TGO – Thermally Grown Oxide,

$T_{lock\text{-}in}$ – lock-in integration time,

TT – Transformation Toughening,

TWI – Thermal Wave Imaging,

t_x – scanning time of a single line in x axis,

t_y – CMIR-TI technique time required to change the motorised stages position in y axis by one step,

TZP – Tetragonal Zirconia Polycrystal,

UT – Ultrasonic Testing,

UV – ultraviolet wavelength range,

v – motorised stages velocity/speed of movement,

V_0 – lock-in input voltage,

V_1 – lock-in output voltage,

VIS – visible light/wavelength region,

ZrO_2 – Zirconium Oxide (Zirconia),

λ – wavelength of light,

λ_0 – incident wavelength,

λ_s – relative scattering wavelength,

λ_x – wavelength in wavenumbers,

σ – standard deviation,

LIST OF PUBLICATIONS

Journal publications:

M. Matysiak, D. P. Hand, and J. D. Shephard: 'Development of optical techniques for non-contact inspection of ceramic parts', Photon08, Edinburgh, UK, 2008.

M. Matysiak, J. P. Parry, J. G. Crowder, N. Jones, K. Jonas, N. Weston, D. P. Hand, and J. D. Shephard: 'Development of an optical, non-destructive technique for inspection of Zirconia ceramic parts', Lasers and Electro-Optics 2009 and the European Quantum Electronics Conference. CLEO Europe - EQEC 2009. European Conference on, 14-19 June 2009, 2009, 1-1.

Patents filed:

N. H. H. Jones, N. J. Weston, K. B. Jonas, J. D. Shephard, D. P. Hand, and M. Matysiak: 'Optical measuring method and system', Patent PCT/GB2010/000088, United Kindgdom, 20.01.2010, 2010.

Conference papers/presentations:

M. Matysiak, J. P. Parry, J. G. Crowder, N. Jones, K. Jonas, N. Weston, D. P. Hand, and J. D. Shephard: 'Novel non-destructive techniques for inspection of Zirconia ceramic parts ', Photon10, Southampton, UK, 2010.

M. Matysiak, J. P. Parry, J. G. Crowder, D. P. Hand, J. D. Shephard, N. Jones, K. Jonas, and N. Weston: 'Development of Optical Techniques for Noncontact Inspection of Y–TZP Parts', *International Journal of Applied Ceramic Technology*, 2011, 8(1), 140-151.

M. Matysiak, J. P. Parry, F. Albri, J. G. Crowder, N. Jones, K. Jonas, N. Weston, D. P. Hand, and J. D. Shephard: 'Infrared confocal imaging for inspection of flaws in yttria-stabilized tetragonal Zirconia polycrystal (Y-TZP)', *Measurement Science and Technology*, 2011, 22(12), 125502-125511.

1. Introduction

1.1. Rationale

The increasing demand for reliable and durable materials for novel technologies, where the in-service demands go beyond that capable of being satisfied with traditional materials, has expanded the use of advanced engineering ceramics in various applications [1, 2]. The drive for performance and reliability demands that the quality control of engineering materials is critical and hence it is widely studied in research laboratories and in industry. Surpassing the current limits not only requires the development of novel materials but in parallel it also requires constant improvement and innovation of measuring and testing techniques.

Zirconia ceramics has become a material of choice in many demanding applications. 3mol% Yttria Stabilised Zirconia Polycrystal (3Y-TZP) due to its superior fracture strength, biocompatibility and toughness [3, 4] is a ubiquitous material in restorative dentistry and Yttria Stabilised Zirconia (YSZ) is commonly applied in thermal barrier coatings [5]. Apart from the aforementioned applications there are a number of other fields found in literature which are discussed in detail in section 2.1.1.

Continuous developments in Zirconia ceramics manufacturing and machining has improved the machining speed and finish [6], however the risk of damaging the part during the fabrication process still exists. Manufacturing companies such as the collaborators in this work, Renishaw plc, have a great interest in finding new cost and time effective methods for 3Y-TZP manufacturing for dental applications to enhance the yield and reduce the manufacturing cost. This is particularly difficult in the dental field where each part is unique, hence the inspection has to be carried out on every part to provide the best service for the customer. A rapid, non-destructive inspection technique for the quality control of such ceramics therefore must be developed and hence this is the prime driver for the work contained in this thesis. Additionally there are many other areas in which advanced engineering ceramics are being applied that require a robust, non-destructive inspection method, e.g. thermal barrier coatings. Therefore a reliable inspection technique would have far reaching applications and benefits for the advancement of high performance materials.

1.2. Summary of chapters

Chapter 2 provides background information on the materials and the equipment used within this work with addition of a comprehensive review of currently available inspection methods for Zirconia ceramics. The in-depth presentation of Zirconia's material properties, including the optical characteristics lay the groundings for the conclusions in the experimental section of this thesis. Theory from the imaging, image reconstruction and enhancement build an understanding of the limitations of the presently available imaging systems and the potential methods of surpassing these limitations.

Chapter 3 presents a sample catalogue which was introduced due to an extensive number of samples used in multiple chapters. These samples are used on a number of occasions to compare and to establish the imaging capabilities of the developed inspection techniques.

Chapter 4 describes the visible light measurements, hence the simplest method of inspection of 3Y-TZP ceramics. The measured optical characteristics of 3Y-TZP confirm poor optical transmittance in the visible wavelength region due to light scattering. However the opportunity to inspect deep into the bulk of the 3Y-TZP arises due to an optical transmittance window in the mid-infrared which is the motivation for the subsequent development of the mid-infrared imaging techniques.

Chapter 5 contains the development and the experimental results for the Mid-Infrared Transmission Imaging (MIR-TI) technique for inspection of thick (above 500 μm) 3Y-TZP parts. The MIR-TI technique presents a considerable improvement in detection of macro (above 1 mm in size) and micro (below 1 mm in size) scale flaws buried in the bulk of the material. The experiments carried out in this chapter lead to the assessment of the imaging capabilities of the MIR-TI system. The work in this chapter is covered in the journal publication in International Journal of Applied Ceramic Technology[7].

Chapter 6 presents a novel Confocal Mid-Infrared Transmission Imaging (CMIR-TI) technique which is the next step in the development of a suitable inspection technique for 3Y-TZP parts in an industrial process. The main motivation for CMIR-TI technique development is reduction of the cost with potential improvement of the imaging capabilities particularly for micro scale crack detection. In the experimental part the same samples which are used for assessing the MIR-TI technique are employed to compare any potential improvements in the CMIR-TI imaging resolution. The work in

this chapter is covered in the journal publication in Measurement Science and Technology [8].

Chapter 7 describes two mid-infrared reflectance techniques based on camera (Camera Mid-Infrared Reflection Imaging (Camera-MIRI)) and confocal (Confocal Mid-Infrared Reflection Imaging (Confocal-MIRI) [9]) approaches which can be employed for detecting flaws in ceramic coatings. Various ceramic coatings are investigated to establish the feasibility and the limitations of both these mid-infrared reflection techniques. The work in this chapter is contained within the Patent titled Optical measuring method and system which was filed in 2010 [9].

Chapter 8 concludes the thesis and presents a potential scope for further improvements. Future work for mid-infrared imaging techniques to enhance their imaging capabilities and imaging speed are also discussed.

References:

[1] S. R. T. V. Thamaraiselvi: 'Biological Evaluation of Bioceramic Materials - A Review', *Trends Biomater. Artif. Organs*, 2004, 18(1), 9-17.

[2] S. T. Buljan and S. F. Wayne: 'Wear and design of ceramic cutting tool materials', *Wear*, 1989, 133(2), 309-321.

[3] I. Denry and J. R. Kelly: 'State of the art of zirconia for dental applications', *Dental Materials*, 2008, 24(3), 299-307.

[4] A. R. Curtis, A. J. Wright and G. J. P. Fleming: 'The influence of surface modification techniques on the performance of a Y-TZP dental ceramic', *Journal of Dentistry*, 2006, 34(3), 195-206.

[5] R. Vassen, X. Cao, F. Tietz, D. Basu and D. Stöver: 'Zirconates as New Materials for Thermal Barrier Coatings', *J. Am. Ceram. Soc.*, 2000, 83(8), 2023-2028.

[6] F. C. Dear: 'Laser Machining Of Medical Grade Zirconia Ceramic For Dental Reconstruction Applications', PhD thesis, Heriot Watt University, Edinburgh, 2008.

[7] M. Matysiak, J. P. Parry, J. G. Crowder, D. P. Hand, J. D. Shephard, N. Jones, K. Jonas and N. Weston: 'Development of Optical Techniques for Noncontact Inspection of Y–TZP Parts', *International Journal of Applied Ceramic Technology*, 2011, 8(1), 140-151.

[8] M. Matysiak, J. P. Parry, F. Albri, J. G. Crowder, N. Jones, K. Jonas, N. Weston, D. P. Hand and J. D. Shephard: 'Infrared confocal imaging for inspection of flaws in yttria-stabilized tetragonal zirconia polycrystal (Y-TZP)', *Measurement Science and Technology*, 2011, 22(12), 125502-125511.

[9] N. H. H. Jones, N. J. Weston, K. B. Jonas, J. D. Shephard, D. P. Hand and M. Matysiak: 'Optical measuring method and system', Patent PCT/GB2010/000088, United Kindgdom, 20.01.2010, 2010.

2. Literature review and background

This chapter presents the basic underpinning theory to which the author refers in the experimental part. The currently available inspection techniques set the benchmark to which the developed inspection techniques in this work can be compared. It is also highlighted why there is a room for significant improvement for the inspection of highly scattering ceramics. In addition to the presentation of competing or existing inspection techniques some basic theory and parameters are brought to the attention of the reader to support the statements derived during the analysis of experimental results.

2.1. Overview of ceramics

The techniques presented in this work were mainly developed for the inspection of Zirconia-based ceramics, including 3mol% Yttria-Stabilised Zirconia Polycrystal (3Y-TZP) and Yttria-Stabilised Zirconia (YSZ). Dependent on availability, measurements on some other ceramic types were also carried out.

2.1.1. Zirconia ceramics

3Y-TZP belongs to a family of Zirconia-based ceramics which are known for their high toughness (fracture toughness of 13 $MPa \cdot m^{1/2}$ for 3Y-TZP), low thermal conductivity (2.2 $W \cdot (m \cdot K)^{-1}$ for 3Y-TZP) and bio-compatibility [1-3]. These unique properties make this material of great interest for many applications from medical [2, 3] to high temperature [4, 5] and high mechanical wear environments [6, 7]. In the medical field 3Y–TZP is particularly of interest for dental restorations [8] and orthopaedic implants [9, 10] due to its strength and biocompatibility.

Ceramic materials are inorganic compounds consisting of metallic and non-metallic elements which are held together with ionic and/or covalent bonds [11]. Current ceramics for engineering applications are considerably more sophisticated materials than traditional ceramics, e.g. ceramic porcelains, produced in the past. The drive to deliver materials that could meet the demands of modern applications has led to the development of this new group of advanced ceramics. These new or advanced ceramics, have many advantages in comparison to metal-based systems placing them in a very attractive position, not only in the area of performance but also cost

effectiveness. These properties include high resistance to abrasion, high heat strength, chemical inertness and high machining speeds (as tools).

Zirconia was first discovered as Baddeleyite, a mineral consisting of Zirconium Oxide (ZrO_2) in 1892 in Brazil by Hussak and in Sri Lanka and was described by tea tycoon Joseph Baddeley [12]who gave it its name. In 1929, Ruff and Ebert attempted to use the material mechanically. They used X-Ray diffraction to establish the crystal symmetry [13] and investigated possible techniques to stabilise the material [14]. The stabilisation is required to retain the desired phase of the crystalline structure. In 1951 Duwez and Brown presented the first Zirconia-Yttria compound [15].

Zirconia is a polymorphic material that can transform into three forms: cubic, monoclinic and tetragonal [16]. Pure Zirconia (ZrO_2) has a monoclinic crystal structure at room temperature [17]. With increasing temperature, above 1170°C Zirconia transforms into a tetragonal phase [18]. This transformation involves a volume change and may introduce cracks within the material structure. Above 2370°C Zirconia transforms into the cubic phase. During cooling (below 1070°C) a material transformation appears. The phase transformation which takes place during cooling results in a material volume expansion of approximately 3 to 4%. Stresses generated by the expansion can cause material cracking during sintering [18].

Pure Zirconia can be doped with other materials to enhance phase stability, (particularly in the tetragonal phase) and its strength. The main dopant used is Yttria (Y_2O_3). Apart from Yttria there are Magnesium Oxide (MgO), Calcium Oxide (CaO), and Cerium Oxide (Ce_2O_3) which are added to Zirconia to stabilise the tetragonal and/or cubic phases [19, 20].

2.1.2. Partially stabilised 3Y-TZP ceramics

Partially Stabilised Zirconia (PSZ) ceramics which 3Y-TZP belongs to, are a mixture of Zirconia polymorphs. Due to an insufficient addition of cubic phase-forming oxide (stabiliser), a cubic and tetragonal mixture is obtained. Smaller additions of the stabiliser to the pure Zirconia brings its structure into a tetragonal phase at a temperature higher than 1000°C, and a mixture of cubic and monoclinic (or tetragonal) phases at a lower temperatures. Therefore, the partially stabilised Zirconia is also called Tetragonal Zirconia Polycrystal (TZP). Usually such PSZ consists of larger than 8 mol% (2.77 wt%) of MgO, 8 mol% (3.81 wt%) of CaO, or 3 to 4 mol% (5.4-7.1 wt%) of Y_2O_3 [21].

If a sufficient quantity of the tetragonal phase is present, the combination of applied stress, magnified by the stress concentration at a crack tip, can lead to phase transformation from tetragonal to the monoclinic with accompanied volume expansion. The pure Zirconia particles in PSZ can retain the tetragonal phase at high-temperature because the cubic matrix provides a compressive force which stops the material from expansion and transformation into monoclinic phase. With addition of the stress energies from cracks propagating in bulk material, the transition from the tetragonal to the monoclinic Zirconia arises due to higher forces acting on the material lattice. The energy used by this transformation is sufficient to slow or even stop propagation of the crack. This mechanism is known as Transformation Toughening (TT), and significantly extends the reliability and lifetime of Zirconia components [19, 20, 22-24].

The dental material used in this study was supplied by C5 Medical Werks. It is stabilised with 3% of Yttria (see Appendix A). Apart from material stabilisation the material has also undergone the TT. There are two toughening mechanisms within the ceramic structure [23]. One method creates a stress zone around the crack tip during the crack propagation, and the other one involves the introduction of fibres and other particulates to bridge cracks to create reinforcements. The stresses generated during these occurrences are high enough to initiate TT. For 3Y-TZP used in this work the first mechanism was applied to toughen the material. This TT method was reported in Nature by Garvie et. al. as the new Ceramic Steel [25]. The mechanical strength of the material results from TT which actively inhibits crack propagation [23, 26]. This mechanism is possible due to the tetragonal to monoclinic phase change which occurs at a crack tip actively forcing the crack to close using the increased volume (between 3 and 5% volume increase) of the monoclinic phase [19, 22-24].

This unique property, particularly in medical applications including dental ceramics [27], increases its suitability because an additional mechanism enhancing the strength and part lifetime is present. Therefore, 3Y-TZP is often the material of choice for all-ceramic dental reconstructions [28] and hence forms the basis of investigation for this thesis.

2.1.3. Sintering of 3Y-TZP ceramics

Present advanced ceramics manufacturing processes are now more complex, providing the ability to enhance the ceramic's mechanical properties. The production of high performance oxide ceramics starts from the preparation of powders to remove unwanted

impurities and also to add other compounds which contribute in the final and desired composition. As modern engineering ceramics are generally high purity systems, minor impurities can have a dramatic effect resulting in the reduced lifetime and uncontrolled failure of the part [29, 30], hence the powder mixing is a strictly controlled process.

During the powder preparation the Y_2O_3 stabiliser is added to the powder. This keeps the material in tetragonal structure during the cooling process after sintering. Plasticisers and binders are blended with the powder to prepare it for an appropriate method of forming (pressing, extrusion, slip casting, etc.) to produce the "raw" material billets [31, 32]. With all the binders and plasticisers the powder is ready to be formed into the required shape. It is in a so called "green" state where it keeps its form but it is still soft and lacks strength. The powder is either die pressed [33, 34], hot/cold isostatic pressed [35] or it is extruded [36-38]. Another method of forming is either slip casting [39, 40], tape casting [41, 42] or injection moulding [43, 44].

During the die pressing the powder is pressed between a die and the uniaxial compression brings the powder together to form the material which can also be further processed to achieve higher density. Hot Isostatic Pressing (HIP) uses an elevated temperature and a high pressure during sintering [45, 46]. The material is encapsulated in a gas impermeable container during the process. Cold Isostatic Pressing (CIP) on the other hand uses only increased pressure to form the part [47, 48]. This extrusion process involves pushing or drawing a material through a constricting die to produce elongated shapes that have a constant cross-section. Slip casting on the other hand refers to the process where a mould is filled with a material suspension which solidifies and then the mould is opened up to extract the formed part. Tape casting uses a flat moving carrier onto which a slurry is placed. While the carrier is moving the slurry is cut to the desired shape. The last citied technique is injection moulding which is similar to the extrusion process. A heated plastic mix is pressed through a cavity in which the mould is created. The moulded part is then removed from the die and the organic binder is slowly burnt out.

Depending on the composition of the material used for the aforementioned processes the material can either solidify after the solvents have evaporated or the material can be sintered after it was shaped into the desired form. The formed "green" state parts are then pre-fired to burn out the binder. A small degree of sintering takes place, causing the Zirconia powder particles to fuse. The material transforms into "brown" state which is still porous. The porosity allows for soaking up agents which are used for changing

the colour of the material if necessary. Iron Oxide (Fe_2O_3) is used in dental ceramics to change the colouring of 3Y-TZP to more yellowish appearance [49]. The final stage of sintering shrinks the material further to achieve the desired density [50-52].

2.1.4. Fully stabilised YSZ ceramics

The cubic phase of Zirconia has also been studied intensively due to its promising thermal parameters. The very low thermal conductivity starting from 2 $W \cdot m^{-1} \cdot K^{-1}$[53] in comparison to high thermal conductivity of copper (400 $W \cdot m^{-1} \cdot K^{-1}$[54]) for example, is a result of a fully stabilised structure. By addition of more than 16 mol% of CaO (7.9 wt%), 16 mol% MgO (5.86 wt%), or 8 mol% of Y_2O_3 (13.75 wt%) [18, 55] the fully stabilised Zirconia is achieved. The cubic Zirconia has no phase transformation from room temperature up to 2,500°C. Due to the addition of Yttria the material is known as Yttria-Stabilised Zirconia (YSZ).

The excellent thermal insulation properties of YSZ have resulted in this material being commonly used as a thermal barrier coating in turbine engines [5, 56, 57]. Thermal Barrier Coating (TBC) is a layered system deposited on a substrate which provides[58]:

a) limited heat transfer through the coating to the bulk material,
b) protection of components from oxidation and hot corrosion,
c) improved strength and toughness of bulk material.

All these properties significantly increase the lifetime of the component and its resistance to harsh environments. Consequently the potential applications of TBCs are far reaching. Apart from TBCs, YSZ is often used in fuel cells due to its high corrosion resistance and high oxygen ion conductivity which allows for current generation [59]. YSZ is also used as a membrane material in gas sensors [60, 61] where high resistance to harsh environments is required.

There are two processing routes of synthesizing TBCs: EB-PVD (Electron Beam Physical Vapour Deposition) and APS (Air Plasma Spraying) [57, 62, 63] – see Figure 2.1.1. Each process results in different thermal, mechanical and morphological properties of the coating. In APS layers, pores are aligned parallel to the substrate surface and are accompanied by micro-cracks and fine grain boundaries. This structure reduces thermal conductivity of YSZ coatings as the pore volume fraction increases [63]. However, the lifetime of these coatings is lower than ones produced using EB-PVD, due to lower spallation resistance. Spallation is a process where TBC peels off

the underlying substrate [64]. Lower spallation resistance is caused by a high thermal expansion coefficient mismatch between the TBC and the substrate and also by cracking occurring during thermal cycling. In contrast, layers produced by EB-PVD have a columnar microstructure with pores perpendicular to the plane of the coating. Due to elongated intercolumnar pores the coating is better matched to the plane of the substrate and this leads to an improved spallation lifetime of TBC. The intercolumnar pores have considerably lower thermal resistance because they are generally inclined to the heat flow [63].

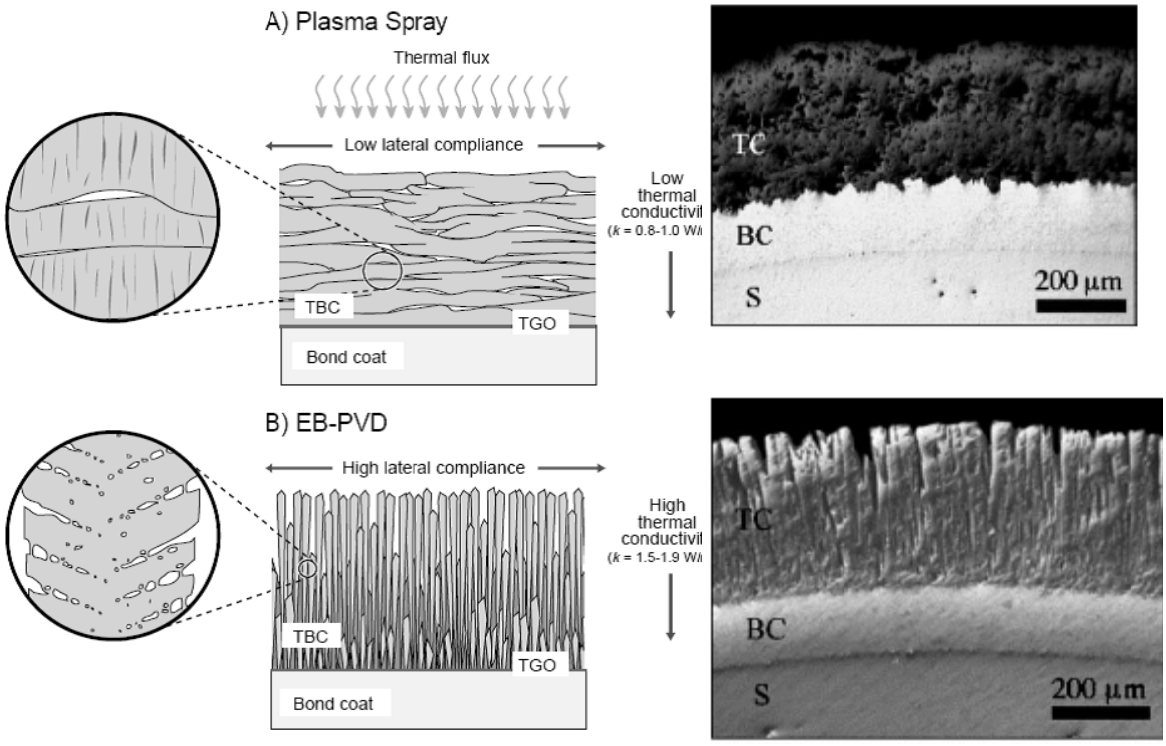

Figure 2.1.1. Morphology of thermal barrier coatings [63, 65]: Bond Coat – aluminum rich layer to form a fully protective alumina scale onto which the thermally grown (TGO) oxide may form

Three main mechanisms of spallation are buckling, wedging and wrinkling. Buckling effects may be caused by planar compressive stress within the ceramic layer and it occurs only in thin materials when generated cracks are at least sixteen times the TBC thickness. Thicker systems may be influenced by wedging which tends to happen when a through-thickness shear crack develops due to high compression. The last effect is called "wrinkling" or "rumpling" which relies on a void formation under the TBC with folding effects, causing cracking. Other phenomena that may be associated with the spallation of TBC includes sintering of YSZ and bond coat creep [66]. More information about degradation effects in TBC can be found in [67].

2.1.5. Alumina ceramics

Apart from Zirconia ceramics another material inspected in the experimental part is Alumina (Al_2O_3). Alumina, similarly to 3Y-TZP is material used in the medical field as a bone [68, 69] and tooth restoration and replacement [70, 71]. The material inspected in this work was used as a wear resistant and insulation coating for electronic applications. These involve various insulation layers for electronic components [72, 73]. The material inspected in chapter 7 was manufactured using the APS technique. Alumina is generally produced by the Bayer process invented in 1887 by the Austrian chemist K. Bayer [74]. It is generally manufactured from either aluminium ores, bauxite, alumina or aluminium oxide.

Alumina suffers from similar difficulties in terms of crack generation during sintering [75] as Zirconia, although it can also use its healing mechanisms to enhance the overall strength [76, 77]. Crack generated during machining in all ceramics is caused by thermal gradients produced by the tools which, in combination with the low thermal conduction of the ceramic material, introduce thermal shock and cracking [78, 79].

2.1.6. Titania ceramics

Titanium dioxide (TiO_2), also known as Titania is the naturally occurring oxide of titanium. Titania exists in a number of crystalline forms [80]. The most common are rutile, anatase and brookite [80-82]. Similar to Alumina, the Titania investigated in this work was sprayed onto a metal substrate, however various other manufacturing techniques are present [83, 84].

There are various applications of Titania from additives to paint and food, to photocatalytic layers [85, 86]. Photocatalytic activity (PCA) is the ability of a material to create an electron hole pair as a result of exposure to ultraviolet radiation [87]. The resulting charges are the efficient oxidizers of organic matter. TiO_2 is a good material for photocatalysis and has been extensively studied because of its potential use in sterilization, sanitation, and remediation applications [86].

2.2. Machining of 3Y-TZP ceramics

The mechanical strength of 3Y-TZP ceramics is the highest ever reported for any dental ceramic [8]. This however presents new challenges for manufacturing of Zirconia parts.

Several techniques which are applied in Zirconia ceramics machining are presented below:

a) grinding,
b) sandblasting,
c) laser processing,
d) forming.

2.2.1. Grinding and sandblasting

Grinding and sandblasting are the most common techniques used to shape the parts into its final state. Grinding is usually a finishing operation during manufacturing process which removes small amounts of material in order to achieve high accuracy and surface finish. However, with 3Y-TZP ceramics it is also used as a bulk material removal process because of the high hardness of 3Y-TZP [88, 89]. Rough phase grinding process used to remove 3Y-TZP can achieve high material removal rates (~50 mm^3/s) [90-94]. Unfortunately it is at a cost of material strength and integrity due to the metastability of tetragonal 3Y-TZP. The stresses generated during grinding are liable to trigger the tetragonal to monoclinic phase transformation with the associated volume increase leading to the formation of surface compressive stresses [78, 88, 89, 95]. This increases the flexural strength but also alters the phase integrity of the material and increases the susceptibility to premature failure.

The optimisation of the grinding process to reduce the material damage is possible but it requires a careful and often customised adjustments for custom made dental parts [88, 89, 96]. Sandblasting on the other hand can reduce the strength of the material due to chipping but when carried out carefully it can provide an enhanced strength of 3Y-TZP [88, 89]. There has been some work published on fine Y-TZP (not necessarily just 3Y-TZP) grinding for femoral heads applications [95, 97] based on brittle fracture and plastic deformation which particularly for plastic deformation resulted in little or no surface damage.

2.2.2. Laser machining

Laser processing is another solution for 3Y-TZP machining. The laser material processing "boom" started in 1983 where W. M. Steen and S. Copley started using CO_2 laser processing for machining of commercial parts [98, 99]. In 1987 the first publications discussing Zirconia ceramic laser processing were presented [100, 101].

More detailed analysis of laser machining of Zirconia and its parameters were published in 1988 [102].

The main reason leading towards Zirconia laser machining, particularly for dental applications is the fact that each part is unique, hence laser machining of the hard state 3Y-TZP was suggested [103-105]. The process using a laser is potentially much faster and more efficient but due to the thermal properties of Zirconia, i.e. low thermal conductivity and high thermal expansion, Zirconia often cracks (Figure 2.2.1). This from the material strength point of view is a crucial factor reducing its lifetime.

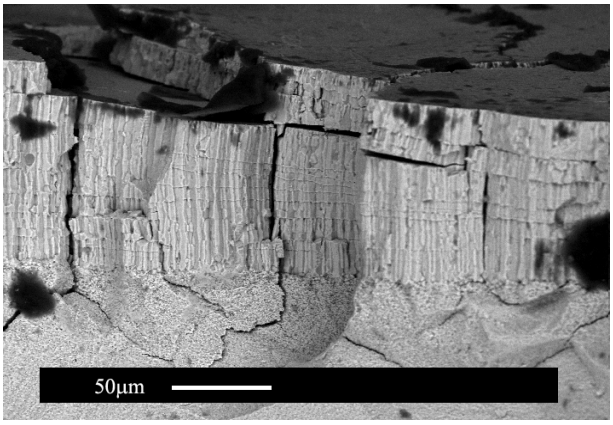

Figure 2.2.1. Scanning electron micrograph of cleaved section through a laser-drilled hole showing both re-cast material and substrate. The cracks in the re-cast material penetrate into the bulk [104].

To overcome the issue of cracking Firestone [102] suggested using a furnace to heat up the machined part ("Hot-Tooling"), thus reduce thermal gradients during laser processing. Similar approach was presented earlier as Laser Assisted Machining (LAM) which heats up a material to assist material removal. The advantages of this technique includes decreased cutting forces, increased material removal rate and increased tool life. There is however a considerable drawback of an extensive heat affected zone (HAZ) which can result in cracking if the process is not optimised carefully. In 2002 the first attempts to use LAM in Magnesia Partially Stabilised Zirconia were reported [106, 107]. The results demonstrated material deformation and the formation of a re-crystallised layer in the machined region.

Another approach of reducing HAZ during laser material processing of Zirconia is using shorter laser pulses but at a cost of machining speed. For that reason a combination of millisecond and nanosecond laser processing was developed by Dear [104]. The process allows for fast machining of bulk material and fine laser processing

which reduces the effect of HAZ after millisecond machining. Apart from the aforementioned approach a cold ablation process for ceramics machining was investigated in which, by using short femtosecond (fs) laser pulses, a reduced HAZ is achieved [108-110]. Although an excellent finish is feasible, the machining rates are low and, due to the cost of the fs laser system, economically not viable [103, 111]. Another presented alternative was employing fibre laser which provided new opportunities for medical ceramics machining [112-114]. Due to an increased output power machining of medical grade ceramics became feasible. A fibre laser was employed to cut through 13 mm thick 3Y-TZP blocks using a controlled crack propagation approach where cracks propagate between the machined holes in the material [115] – see Figure 2.2.2. This technique demonstrated high cutting rates of 1.8 mm/s.

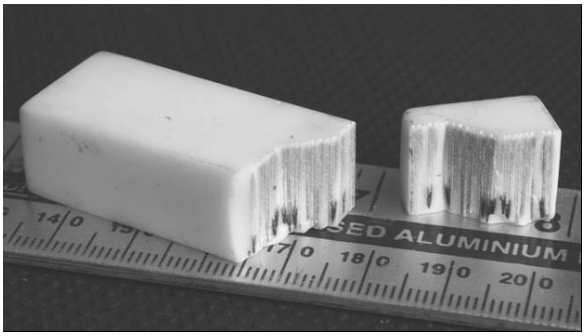

Figure 2.2.2. Laser cutting using a technique of controlled crack propagation [115]. 13 mm sample cut with fibre laser.

One of the negative effects of laser machining is blackening of the 3Y-TZP [103, 116]. The shorter the laser pulse the more heat is introduced into the material and the higher the blackening of 3Y-TZP. When the laser beam interacts with the material, temperatures reaching 1500ºC are observed around the laser path. At this temperature in 3Y-TZP a sub-stoichiometric dioxide is formed where ZrO_2 becomes ZrO_{2-X} and the oxygen atoms are released from the lattice to create vacancies [116]. The oxygen atoms are ejected into the atmosphere and they create the vacancies at the wall directly beside the incident beam. The increased temperature of the laser process and an increased number of pulses draws the oxygen from deeper layers of the material resulting in a blackened region in proximity of the laser machined area [103].

Finding the balance of laser parameters to achieve a practically viable machining rate (much faster than grinding techniques) yet avoid significant cracking is a particular problem and is difficult without an accurate material characterisation technique. These

issues highlight the need for an optical, non-contact and non-destructive testing method of Zirconia-based ceramics. By optimising and controlling the HAZ during the laser processing of Zirconia, cracking can be reduced and the laser machining process can be improved. However, there is still a likelihood of crack generation which may increase the material aging and increase the possibility of premature failure. Consequently, a truly non-contact and non-destructive technique for detecting cracks is required.

2.2.3. Forming

Apart from machining Zirconia can also be formed using; extrusion [36-38], slip casting [39, 40], tape casting [41, 42] and injection moulding [43, 44]. These techniques are common for manufacturing a series of identical parts. Unfortunately they are not suitable for bone and dental restorations because every part is unique.

There also has been some interest in machining "green" state ceramics due to lower tool wear and machining cost. "Green" state Zirconia is brittle and soft, hence lends itself to machining but it is accompanied by an approximate 22% shrinkage when transforming from "green" state to final, hard state [117]. The shrinkage can be unpredictable particularly for unique parts which makes this process more difficult as it is hard to predict the final shape.

2.3. 3Y-TZP critical crack length

One of the main objectives of this study was identifying any potential cracks which could have a detrimental effect on the part integrity and reduced in service life. The major issue concerning Zirconia-based ceramics is their sensitivity to low temperature degradation [118]. Although 3Y-TZP exhibits high toughness it is susceptible to fatigue mechanisms that can considerably reduce the lifetime of the part [119, 120]. The reduction of mechanical strength due to fatigue is caused by the propagation of natural cracks initially present in the material's microstructure [119, 120]. It has been reported [119-121] that with addition of water 3Y-TZP is more prone to failure when operating in aqueous environment due to stress-assisted reaction of water molecules with the metal-oxide bonds at the crack tip [122]. Further reduction of the material strength can be promoted by cyclic stresses [123, 124]. Since dental restorations are obviously exposed to an aqueous environment and to cyclic loading, the evaluation of the part before it goes into service is essential.

Studart [119] in his work calculated the critical crack length to be 74 μm with the cycled stress level of 500 MPa for the 3Y-TZP long prismatic beams submerged in water. This stress was 50% lower than an inert strength of the specimen so that the samples failed only due to their natural (subcritical) cracks growing to the critical size given by the maximum stress applied to the samples. The subcritical cracks size range from 12 to 30 μm. The subcritical crack growth in ceramics is produced by stress enhanced chemical reactions which occur at the crack tip [120]. It should be noted that even the naturally appearing cracks can propagate and produce critical cracks at loads as low as approximately half of the initial mechanical strength of the component [119, 120].

2.4. 3Y-TZP optical characteristics

Scattering of electromagnetic (EM) waves appears due to heterogeneities inside the material. Matter is composed of electrons and protons which when illuminated with an EM field oscillate according to the incident wave. This energy is then released and if it appears in all directions, the scattering phenomenon is present [125]. The released energy may have the frequency of the illumination wave or the frequency may change due to a Raman scattering [126, 127]. Apart from releasing the energy some of it may be transferred into phonon energy which results in crystalline structure vibrations and heat generation in the material [125] – the energy is lost due to absorption.

Both scattering and absorption reduce the flux carried out by the illuminating radiation. The attenuation of the radiation is called extinction[128, 129],therefore it can be defined as:

$$\text{Extinction} = \text{scattering} + \text{absorption}$$

Scattering is a ubiquitous phenomenon because everything around except vacuum is heterogeneous. Even in a perfect crystal at 0 K the molecules arranged regularly scatter the waves but due to their structure the interference of the scattered waves occurs, hence no scattering is visible. However, the wave velocity of propagation changes [129]. All the matter consists of particles, grains, molecules which are never distributed perfectly, uniformly and have an identical shape. This gives a rise to inhomogeneities which are the scattering centres.

Light scattering depends on:

a) light wavelength,

b) refractive index of the material,

c) particle size and density.

There are two main groups of scatterers: particles and material structure fluctuations [125, 130]. The main scatterers are usually particles. The thermodynamic fluctuations have much lower influence on overall scattering of the material [125]. The scattering which attenuates the light traversing through the material is sourced by the irregular particle structure which results in scattered waves being out of phase in illumination direction, hence the destructive interference attenuates the light intensity. The constructive interference however, appears in directions away from the illumination axis because the energy carried out by the illuminating photons has to be released somewhere if the material is non-absorbing at the particular wavelength.

Apart from the photons directly illuminating the particles in the bulk of the material, the same particles also receive the illumination scattered by the other particles. This complicates the analysis because establishing the position of each particle and quantity of particles can only be statistical. To add more the aforementioned observation presents the possible solution for particles which are separated, for example for water droplets in fog or for clouds. The scattering analysis becomes extremely complex for solids, for example for 3Y-TZP which has a density of 6.02 g/cc [103]. In Figure 2.4.1 it is noticeable that the material grains are placed irregularly and they are in contact with the nearest neighbours. This adds more complexity in the optical properties analysis because some of the light in addition to being multiply scattered may also be travelling without being scattered, by travelling through the connected grains. The in-depth analysis of light scattering in 3Y-TZP ceramics is not a part of this study, however the author covers some ground which explains and justify the results achieved in the experimental part.

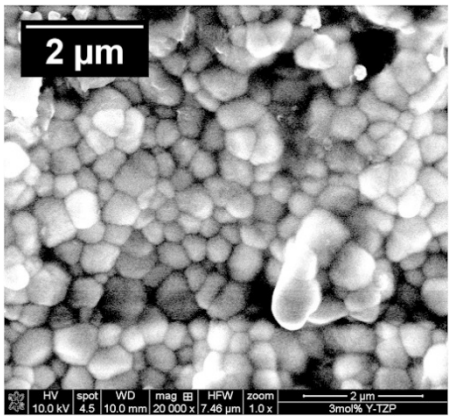

Figure 2.4.1. Densely packed 3Y-TZP grains.

Although there are very few previous studies of the optical properties of 3Y-TZP ceramics the author attempts to present the general characteristics for zirconium oxide (ZrO_2) based ceramics which gives an indication and a basis for the discussion in the experimental parts of all the chapters. ZrO_2 ceramics including 3Y-TZP are the materials with a wide band gap (5 - 7eV) which depends on the phase of the material, the preparation and the manufacturing process [131, 132].

The wide band gap results in low light absorption at room temperature in the visible (VIS) and near-infrared (NIR) region [133-137]. The absorption edge in UV gives a rise to the transition of valence electrons into orbitals with an increased state of energy [138]. This transition appears if the UV wavelength matches the energy difference between the available energy states according to equation (2.1) [126]:

$$E_g = \frac{h \cdot c}{\lambda} \qquad (2.1)$$

where, E_g is the energy difference between transition states, h is Planck's constant ($6.626 \cdot 10^{-34}$ J·s), c is the speed of light ($3 \cdot 10^8$ m/s) and λ is the light wavelength. In the infrared wavelength region the increasing absorption is associated with a lattice vibrational and rotational changes of the molecules [139].

3Y-TZP and other Zirconia-based ceramics appear white in visible light with additions of different colouring depending on manufacturing process and introduced dopants [132]. The white appearance indicates that some of the visible light incident on the material is reflected and scattered back towards the observer [125, 129]. The main cause of opacity (thin samples) and white appearance of the 3Y-TZP and other densified ceramics, particularly in the visible region, is the light scattering [138, 140]. Light scattering in Zirconia ceramics is caused by: the grain size and the pores between the grains [138, 140] which are also the scattering sources for other polycrystalline ceramics [125, 141-144]. The grain boundaries are not major scatterers [140], however they do scatter light.

One possible solution to reduce light scattering is to increase the wavelength so that it is considerably larger than the grain size [143]. For wavelengths comparable in scale to the material energy band gap photons are scattered and absorbed because their energy matches the energy band gap of the material. The longer the wavelength i.e. the larger the difference in size between the grains and the wavelength, the less the scattering

effect [144, 145]. This is typical behaviour for scattering by grains smaller than the wavelength.

The main scatterers for most polycrystalline ceramics are the pores which strongly determine the light scattering depending on their size [143, 144]. The pores (air, material impurity) appearing between the grains introduce a refractive index change which results in refraction and reflection of photons which results in light scattering [143]. Even a porosity of 0.1% can decrease the material optical transmittance by tens of percent, therefore reducing the porosity and the pore size is an important consideration particularly when developing optically transparent ceramics [138, 143].

Pores inside the bulk 3Y-TZP ceramics are often the result of processing defects which produce agglomerates and voids during the ceramic sintering stages [146]. This is a potential hazard to the material integrity. If the grain matrix densifies more rapidly than the agglomerate, tensile stress is generated which may be released in a crack formation. Conversely, if the matrix densifies less rapidly than the agglomerate circumferential crack-like voids may appear [146, 147]. The 3Y-TZP ceramics investigated in this work are described by the manufacturer as non-porous, therefore this source of light scattering can be ruled out. Apart from the material porosity in non-cubic ceramics including Zirconia another source of scattering may be material birefringence [138, 148] due to the multicrystalline structure. However this effect is not expected to play a major role in the light scattering.

The 3Y-TZP grain size is in a region of 500 nm (see Figure 2.4.1) which coincides with the visible wavelengths. This is the main source of light scattering because the material is non-porous [103, 125, 129, 146, 149, 150]. The crystalline structure of other Zirconia-based ceramics apart from 3Y-TZP also have a similar appearance in visible light and comparable results for light scattering were observed [132, 135-137].

The polycrystalline structure of 3Y-TZP ceramics influences the optical properties, including the refractive index, n. Any light travelling through the 3Y-TZP interacts with its multicrystalline structure resulting in reduced velocity of photons and their refraction. Refractive index is defined as a ratio of a speed of an electromagnetic wave in vacuum to that in matter [126]. Various studies have confirmed that for Zirconia materials the refractive index is above 2 [133, 134, 145, 146, 151-153]. The changes between various Zirconia ceramics are caused by different stabilisers and its content and by variations in the manufacturing process. For example increasing the Y_2O_3 stabiliser content lowers the refractive index of the Zirconia structure [153]. This is caused by

variation in packing density. There are less Zirconia atoms in the crystalline structure with an increased Y_2O_3 content because the increase in energetic vacancies appears due to different valence states of Zr^{4+} and Y^{3+} [133, 134, 145, 151].

Light scattering is one of the most complex phenomena in physics because it describes light propagating through statistically distributed material grains. These grains are often suspended in the medium (pores, inclusions) which often have a considerably different refractive index, thus this introduces additional complications in light scattering analysis. Light scattering analysis can be divided into two groups depending on the size relation between the wavelength illuminating a particle and the particle size. If $\alpha_s << 1$ and $|m| \cdot \alpha_s << 1$ where α_s is a dimensionless parameter defined in equation (2.2) and m represents the refractive index of the scattering particle, then Rayleigh scattering theory can be applied during the scattering analysis [125, 129, 130].

$$\alpha_s = \frac{2 \cdot \pi \cdot a}{\lambda_s} \tag{2.2}$$

where a is the spherical particle radius and λ_s is a relative scattering wavelength defined as:

$$\lambda_s = \frac{\lambda_0}{m_0} \tag{2.3}$$

where λ_0 is the incident wavelength and m_0 is the refractive index of the surrounding medium. M is commonly defined as:

$$m = n - i \cdot k \tag{2.4}$$

where n is the refraction of light (equation (2.4)) and k is the light absorption of the EM wave traversing through the material.

$$n = \frac{c}{n_m} \tag{2.5}$$

$$k = \frac{2 \cdot \pi \cdot n}{\lambda_0} \tag{2.6}$$

where c is the speed of light in vacuum and n_m is the speed of light in the material. The complex term in equation (2.4) defines light absorption of the scattering particle.

The Rayleigh criteria discussed above corresponds physically to the assumption that the particle is much smaller than the wavelength. Rayleigh scattering is often used for various atmospheric [154] and gas analysis [155]. It is for example used to explain why the blue sky is observed during the day [156].

The second group named after Gustav Mie is used for describing most spherical particle systems, including Rayleigh scattering. Mie scattering theory can be applied to the scattering which appears between the particles having the size comparable with the wavelength. This analysis is more complex and often requires significant mathematical and computational investigation. Gustav Mie first presented the theory in 1908, when he approached the problem by analysing light scattering by a homogeneous sphere [142]. Currently, the theories used for analysing multiple scattering are often based on Mie approach [125, 129].

An example of light scattering analysis of Zirconia-based ceramics using Mie theory was presented by Krell [138] and by Lin [153]. There is more Mie scattering analysis discussed with other polycrystalline ceramics [141, 143, 144]. Apart from Mie theory which can be considerably complex, there are other scattering solutions presented by Dombrovsky [157, 158], Hendricks [159] and Wood [133, 134].

2.5. Optical imaging

The main focus of this study was using a light to inspect highly scattering ceramics. To quantify and to establish the parameters of the developed techniques some theory from the optical imaging field is presented below.

2.5.1. Image interpolation techniques

The imaging system can produce images in two forms depending on the imaging technique used. The system which uses a camera as a detector generates direct images of a scene, whereas the imaging system which scans the area using for example a confocal approach generates a matrix of points which later is used to reconstruct the image. The image generation in the latter technique often requires an image interpolation technique due to non-uniformly scattered data points so that the generated image appears smooth. This was the case for the acquired data in chapter 6 due to the

equipment capabilities constraints, thus interpolation was necessary. Data interpolation is a recovery of a continuous data from a discrete data samples [160, 161]. It is a ubiquitous method of defining a continuous process, particularly in the modern era of computers.

There are various methods of interpolation ranging from linear [162], polynomial (bilinear, bicubic) [163] to spline [164] interpolation techniques. Linear interpolation uses linear equations, whereas polynomial interpolations use polynomial or higher order equations to estimate the data points between the discrete available data points. The linear interpolation, due to its low complexity, is not very precise, whereas the polynomial approach is more accurate (error is proportional to the distance between the data points to the power quantity of data points). Unfortunately it comes at a price of much higher computation requirements and more efficient image smoothing where some of the low contrast features may be lost. Spline interpolation is an alternative to the polynomial approach. It uses the advantages of the linear and polynomial methods, where the data is sectioned into smaller equal size parts and low degree polynomials are utilised to match each of the parts. The spline interpolation, similarly to polynomial interpolation, has low data reconstruction error and it requires less computation power because the data is cut and computed in small parts.

2.5.2. Image resolution

A technique used to establish the imaging resolution of the developed systems in this work was based on a USAF 1951 T-20 target (Figure 2.5.1(a)) (according to MIL-STD-150A standard).

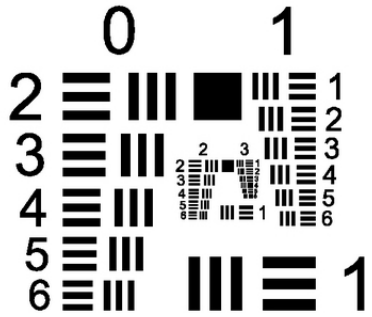

Figure 2.5.1. An Image of USAF 1951 T-20 testing target.

The USAF target consists of a series of patterns decreasing in size. Two patterns (two sets of lines) at right angles to each other are present. Each set of patterns is classified

as an element. Six elements establish one group of target patterns. The resolution of the imaging system based on the USAF standard is calculated from the Group and the Element in the Group that can be resolved by an observer by discerning the presence of three bars of the pattern in the horizontal and vertical axis. Equation (2.7) shows the formula for the resolution R measured with the USAF target [165].

$$R_{lp} = 2^{Group + (Element-1)/6} \tag{2.7}$$

R_{lp} is represented in Cycles per mm (Cy/mm) or in line pairs per mm (lp/mm) which represent a size of a single target bar and a gap between the bars, hence the name line pairs. Both these features have the same width, therefore to estimate what is the smallest feature which can be detected the resolution (R) is estimated as:

$$R = \frac{1}{2 \cdot R_{lp}} \ [\mu m] \tag{2.8}$$

The resolution results R calculated for the imaging systems in this work were presented in micrometres.

2.5.3. Image enhancement techniques

In many imaging systems, the light incident on the optical detector is ultimately converted into a digital image. Unfortunately in many cases, particularly in the mid-infrared region the detector size and the resolution produced is not sufficient to accurately sample the scene. Furthermore, the noise introduced during the optical signal conversion reduces the resolution even further. To enhance the resolution reducing the pixel size is one possible solution, however this leads to a reduced amount of light which is detected. The alternative approach is to use a larger area detector with higher number of pixels. Unfortunately this approach is a source of many challenges from both the electronics and controlling the noise. Furthermore the increasing cost for the optical components (to guide the light to the larger area detector) and the detector itself becomes unfeasible [166].

The alternative approach is to use the digital image resolution enhancement techniques called Super-Resolution (SR) image reconstruction which combine multiple low resolution (LR) image frames to create a single high resolution (HR) image. The major

advantage of the signal processing approach is that it reduces the cost and the existing LR imaging systems can still be utilised [166, 167]. The LR images are usually sampled (aliased) as well as shifted with a sub-pixel precision. The aliased image acquires the scene with a reduced/finite number of pixels. When each pixel in the new LR image has a different sub-pixel shift and aliasing is present each LR image cannot be obtained from the others. This allows for HR image generation because each LR image has unique information about the scene. To obtain these unique LR images a motion is introduced either by moving the object or the camera or by the changing position of the features in the image. Multiple scenes can be obtained from one camera when taking multiple pictures while changing sample position or from multiple cameras located in different positions. After the images are acquired the HR image is generated from LR images.

The SR image reconstruction composes of three steps: registration, interpolation, and restoration. These steps can be implemented separately or simultaneously depending on the reconstruction methods adopted. During the registration the LR images and their shifts between the reference and the remaining images are acquired [168]. The reference image most often is the first LR image acquired. The shifts in the LR images are estimated with fractional pixel accuracy and they are arbitrary, thus often LR image pixels positions are shifted in reference to the HR image grid points. For that reason the interpolation of the pixels in the HR image is required to match uniformly spaced HR grid points. The final stage is the image restoration which is applied to remove blurring and noise which occurs in the process of recording a digital image[166, 167]. There is a natural loss of spatial resolution caused by the optical distortions (out of focus, diffraction limit, etc.), motion blur due to limited shutter speed, noise that occurs within the sensor or during transmission, and insufficient sensor size or amount of pixels.

The SR methods can be categorised into two main groups: a frequency domain and a spatial domain [167, 169]. The frequency domain approach provides the advantages of low computational complexity, theoretical simplicity due to the relationship between LR images and the HR image being clearly demonstrated in the frequency domain. The frequency method is also convenient for parallel implementation, thus it is capable of reducing hardware complexity. Moreover if a new LR image arrives delayed, it can still be added (in the frequency domain) to the HR image. A disadvantage of frequency domain SR is that the analysis assumes prior knowledge of the model operators (blur, geometric transformation of LR images, noise and the measurements resolution).

Furthermore in the frequency domain SR the observation model is restricted to a global translation motion [167].

The spatial domain SR presents a more flexible approach where global and non-global motion can be accommodated. In addition spatial domain SR is less susceptible to motion and optical blur, non-ideal sampling and image compression artefacts. For that reason there is a great flexibility in choosing a motion model, the motion, the optical blur and the sampling process.

Spatial techniques use interpolation of LR images to create HR images [169] where non-uniformly spaced samples from LR images are interpolated and projected onto an HR grid [170]. To attain a sub-pixel resolution various techniques are applied including pixel shifting or varying pixels size. Another approach uses stochastic methods which treat the SR reconstruction as a statistical estimation to determine all the required parameters [171, 172]. Another two groups are the theoretic [173] and iterative [174] reconstructions. The two classes of spatial domain SR methods are Bayesian (MAP) [172] and Projection Onto Convex Sets (POCS) [171]. Unfortunately the spatial domain SR techniques require more computations, thus they are more expensive and complex compared to the frequency domain counterparts which are also advantageous in terms of flexibility.

Often the acquired images lack contrast particularly in the infrared wavelength region because there is still limited availability of high resolution infrared sensors, thus the image reconstructed by the sensor is noisy and has low contrast [175]. Contrast determines a difference in image appearance due to varying image illumination/brightness and colours which make the features in the image distinguishable from the background. Apart from the above SR techniques for resolution enhancement there are fully software based techniques which aim to enhance images by: amplitude scaling, histogram modification, noise removal, and edge enhancement [176]. During amplitude scaling each pixel intensity is adjusted either individually or using a common factor for all the pixels to increase the image contrast. During histogram modification the original image histogram is rescaled so that the histogram of the enhanced image follows a desired form. Noise removal is usually carried out using statistical filtering where the noise from the detector electronics and the sensor are compensated. Noise added to an image generally has a higher spatial frequency spectrum than the normal image components, thus applying low-pass filtering can effectively clean the image from noise. Edge enhancement techniques use various

techniques to sharpen the appearance of the edges which contribute to the overall appearance of the features in the image [177].

Amongst the aforementioned image enhancement techniques there is a group of Adaptive Histogram Equalization (AHE) methods such as Contrast Limited Adaptive Histogram Equalization (CLAHE) [178]. The main principle for CLAHE is enhancing the image contrast by dividing the image into smaller regions (even single pixels) and applying a histogram equalisation to these regions based on the intensity values from the four regions surrounding the processed region [179]. The more regions into which the image is divided the more time consuming the image enhancement process is. The CLAHE method evens out the distribution of used grey values and thus makes hidden features of the image more visible. The full grey spectrum is used to express the image.

2.5.4. Optical aberrations

Every optical imaging system suffers from aberrations which appear due to inaccurate positioning of the components, the optical components themselves and the unwanted external signal [126, 180]. Aberrations appear when the light travelling from one point in the object plane through the imaging system does not converge into a single point.

Aberrations can be divided into two groups: monochromatic and chromatic. Monochromatic aberrations are caused by the imperfections of the optical component geometry which cause: spherical aberration, coma, astigmatism, field curvature and image distortion. Spherical aberration for the lens, for example, corresponds to a dependence of a focal length on lens aperture for the rays traversing off the optical axis. For the converging lens the further the ray is from the optical axis of the lens the closer the ray intersects with the optical axis (closer to lens) after it was refracted. For the converging lens on the other hand the marginal rays are refracted more, hence cross the optical axis further away from the surface of the lens. The spherical aberration appears as a bright spot in the middle surrounded by the circular Airy discs [126]. Spherical aberration has no angle dependence, therefore it is entirely uniform.

Coma appears when rays passing through the aperture near its edge intersect the image surface at different heights from those passing through aperture centre. This smears a point out into a long narrow line that looks like a comet tail. Astigmatism results in a different focal point for the tangential (vertical plane through the object point and the lens axis) and sagittal (normal to the tangential, also through lens axis) rays. Field of

curvature is an aberration where the focal plane is not a plane surface but it is curved. This leads to the curved image appearance, thus image blurring of either the centre or the outer regions of the image. Distortion on the other hand affects only the image scale, not the image sharpness because the image scale is a function of position on the focal surface. Distortion appears because different areas of the lens have different focal lengths and magnifications. If no other aberrations are present distortion misshapes the whole image even though each point in the image is in focus. For example with a distorted image square vertices may become curved lines, thus the image appears as barrel.

The chromatic aberrations which appear for polychromatic optical systems result from the dependence of the refractive index of the optical components on the wavelength of light. Different wavelengths travel through an optical system using different paths, thus when a collimated beam of white light is focused at different points of optical axis axial chromatic aberration is introduced. If the object is off optical axis each wavelength traversing from the object region arrives at different height above the optical axis which results in lateral chromatic aberration.

2.6. Infrared radiation and imaging

Infrared radiation has found many applications from night vision [181], thermal imaging [182, 183], communications [184], metrology [185] to laser machining in medical [186] and in industrial environments [187]. The infrared light can be divided into three regions: near-infrared (from 0.75 to 3μm), mid-infrared (from 3 to 10 μm) and far-infrared (10 to 1000 μm). In this study two regions near- and mid-infrared were of interested. The infrared radiation above 5 μm is a direct measure of temperature. All objects that are not at absolute zero (0 K or -273°C) emit infrared radiation. Absolute zero defines the temperature where all molecular motion ceases, and is the coldest possible temperature [188].

Wien's displacement law [189, 190] can be used to convert between the body temperature and the emitted infrared wavelength. The definition of the Wien's displacement law states that for a blackbody, the wavelength of maximum emission of any body is inversely proportional to its absolute temperature (measured in Kelvin). As a result, as the temperature rises, the maximum (peak) of the radiant energy shifts toward the shorter wavelength (higher frequency and energy) end of the spectrum.

$$\lambda_{MAX} = \frac{b}{T} \tag{2.9}$$

where λ_{MAX} is the peak wavelength, T is the absolute temperature of the blackbody in Kelvins, and b is a Wien's displacement constant ($2.8977685 \cdot 10^{-3}$ m·K). A blackbody is an idealised physical body that absorbs all incident electromagnetic radiation, regardless of frequency or angle of incidence [191]. In thermal equilibrium blackbody emits an electromagnetic radiation called blackbody radiation which is defined according to Planck's law, meaning that it has a spectrum that depends only on the temperature of the body, not the body shape or composition. A blackbody is a perfect emitter: it emits more energy at every frequency than any other body at the same temperature [191]. The blackbody is also a perfect absorber so it absorbs all the radiation from all the directions and it also is a perfect diffuser so the energy emitted by the body propagates in all directions equally, thus the emitted energy is a function of the body temperature and wavelength.

The main advantage of using the infrared radiation is the fact that mid-infrared wavelengths carry information about the temperature distribution of the objects studied. This can provide information about potential failure in a component (before it fails) due to an excessive heat generated in the component. Moving to the very far end of the infrared spectrum radiation can penetrate materials which are not transparent at the shorter wavelengths regions and this can used for imaging as in the case of terahertz imaging [192, 193]. Also, infrared wavelengths can be used to detect harmful gases such as the development of mid-infrared quantum cascade lasers which emit at wavelengths where the gas molecules have a strong absorption [194].

Unfortunately the equipment, particularly for mid-infrared imaging, is expensive due to the limited availability of the materials and difficult manufacturing process [195]. There are also multiple absorption lines of the particles in air (which reduce the signal) including water vapour, CO_2, CO and others [196]. The most common materials for mid-infrared wavelengths are Germanium (Ge), Zinc Selenide (ZnSe) and Calcium Fluoride (CaF_2).

2.7. Mid-infrared detectors

There are two common types of infrared detectors: thermal detectors and photon detectors [197, 198]. Thermal detectors sense the heat generated in the blackbody

absorber, thus the detection process consists of two steps: the incident infrared radiation energy is converted into heat which then is converted into an electrical signal. The signal detected does not depend on the spectra of the incident beam but on the incident power, thus the effect is wavelength independent. Three types of thermal infrared detectors can be found [198-201]:

a) bolometers [202, 203] – they detect a change in electrical resistance in the blackbody absorber,
b) pyroelectric detectors [204, 205] – they detect a change in electrical polarisation of the absorber in certain classes of crystalline materials as their temperatures change,
c) thermoelectric detectors [206] – they detect a change in temperature between two opposite plates having different temperatures.

Thermal detectors are not wavelength specific, thus they can operate over a very wide range of wavelengths [198, 200]. Another advantage is the fact that thermal detectors can handle high average power without the need for attenuators. Although they can be sensitive, they suffer from a slow response time due to an elongated cooling process of the active element.

Photon detectors are quantum type detectors, meaning that they are theoretically able to detect single photons. The radiation is absorbed within the material by photon-electron interactions. A single photon can create an electron-hole pair in a semiconductor p-n junction, which contributes to the photocurrent flow. The generated electron-hole pair is a result of absorption of the photon having a discrete energy which matches the energy difference between the material valence and conduction band. For that reason these detectors are wavelength specific. They provide a high efficiency and high signal-to noise (SNR) characteristics. In addition the response time is considerably shorter compared to the thermal detectors. Unfortunately to achieve the short response time the detector area has to be cooled, often cryogenically. Photon detectors can be further subdivided into:

d) intrinsic detectors [201] which use band-to-band electron transitions caused by the photons absorption in a narrow band gap semiconductor,
e) extrinsic detectors [207] which use the material structure defects and impurities, which create additional energy levels close to the conduction band. These bands give rise to the low energy transitions (long wavelength) due to an absorption,

f) photoemissive (Schottky-barrier) detectors [198, 208] which due to an additional metallic layer next to the p-n junction are known for their typical forward semiconductor diode characteristics but with much lower turn on voltage. Schottky-barrier detectors do not rely on holes or electrons recombining when they enter the opposite type of semiconductor region as in the case of a conventional diode, thus their response is much faster. The photoemissive effect involves the emission of electrons from a surface irradiated by quanta of light energy. The electrons emitted from the surface are accelerated by a voltage to an anode, where they produce a current in an external circuit,

g) quantum well detectors [209, 210] which band gap and its structure is designed such that the energy separation between two of the states in the structure match the energy of the infrared photons to be detected.

There were two types of detectors used in this study. The first one was a Barium Strontium Titanate (BST) hybrid ferroelectric Focal Plane Array (FPA) detector which was installed in the Electrophysics PV320-L2E infrared camera. The Electrophysics camera was used in a Mid-Infrared Transmission imaging (MIR-TI) system presented in chapter 4. The camera sensor uses a pyroelectric effect which responds to changes in temperature by changing the material polarisation, thus is useful as a detector for pulsed or chopped radiation. The response time of pyroelectric detectors is faster than the response time of other thermal detectors.

The second infrared detector was a Vigo $Hg_{1-x}Cd_xTe$ photodiode [211, 212] used in a Confocal Mid-Infrared Imaging (CMIR-TI) system in chapter 5. During the past four decades Mercury Cadmium Telluride (HgCdTe) has become the most important semiconductor for the middle and long wavelength (between 3 and 30 μm) infrared photodetectors. The HgCdTe is a challenging material from the technological point of view because Hg–Te bond is weak and this results in the material structure instabilities. Uniformity and yield are still problematic. Nevertheless, the HgCdTe structure remains the leading semiconductor for infrared detectors [200]. The main advantage of the HgCdTe detectors is their flexibility in tailoring for a specific wavelength or wavelength range. Present infrared detectors are dominated by the complex band gap heterostructures, however the HgCdTe structure is the only one in which the infrared spectrum (between 2 and 26 μm) have nearly the same lattice parameter [200]. The independence of the lattice parameter on composition is a major advantage of HgCdTe over any other material.

2.8. Noise in infrared detectors

Noise defines an unwanted signal which contributes to the measured signal [213, 214], hence it reduces the detection capabilities of the detector because noise masks the desired signal. Signal-to-Noise Ratio (SNR) is a parameter which defines the relation between the power ratio of a signal P_{signal} (meaningful information) and the background noise P_{noise} (equation (2.10)) which in this study are represented in volts.

$$SNR = \frac{P_{signal}}{P_{noise}} \tag{2.10}$$

Noise in optical detectors is a complex subject due to multiple factors causing it, however it can be divided into two main categories: external and internal. The external noise appears in the detection system because of the factors which are outside of the system and often it can be compensated. The internal noise on the other hand is generated within the detector and it determines the detection limits of the device. There are four main types of noise [213, 214]:

h) Johnson noise which is generated by the thermal fluctuations which are the result of electron motion in the conducting material. Each electron motion produces a current which fluctuates in short period of time,
i) shot noise which in semiconductor it is a fluctuation of the charge carrier generation and recombination which often is called as a generation-recombination noise,
j) 1/*f* noise which power spectral density (energy or power per Hz) is inversely proportional to the detector modulation frequency, hence to minimise this noise the device should operate at as high frequency as possible,
k) photon noise – is a results of a random arrival rate of photons in the light being measured and from the background. Another source of photon noise is the thermal self-radiation of the detector itself at a finite temperature. Photon noise determines the fundamental limit to the detectivity of a photodetector.

In semiconductor infrared detectors the main sources of noise are thermal generation-recombination in the absorber and the photon noise from the background. The thermal generation-recombination noise appears due to the material having a temperature above 0 K, whereas the photon noise appears due to illumination conditions during the measurement. For photoconductive detectors the main sources are 1/f, thermal

generation-recombination and Johnson noise and are the main challenges in enhancing the SNR [215].

2.9. Material characterisation techniques

Techniques discussed in this section were employed during the Zirconia ceramics inspection. These techniques were essential to determine all the necessary structural and optical properties used for the images and data analysis.

2.9.1. Fourier Transform Infrared Spectroscopy

Fourier Transform Infrared Spectroscopy (FTIR) is a very common technique used to measure an optical absorption, reflectance and transmittance of the tested specimen [216]. The main advantage of FTIR is a rapid multi-wavelength measurement of the optical properties of the inspected part. A light beam containing many different frequencies of light is incident on the specimen at once and FTIR measures how much of that beam is absorbed by the sample. The light passing through the interferometer sweeps through the wavelengths to determine the absorption of the specimen at each inspected wavelength based on the interference between the acquired and reference (reflected from the reference mirror) signals. Depending on the sample properties some of the light frequencies are absorbed, backscattered and some are transmitted through the material. The final stage of the measurement is the conversion of the acquired data into the desired result (absorption, reflectance and transmittance spectrum) of the tested material using Fourier Transform.

2.9.2. Raman spectroscopy

Raman spectroscopy is a light scattering technique, where photons interact with a sample to produce scattered radiation of different wavelengths which then is examined with a spectrometer [217]. This scattered Raman radiation is very low (approximately 1 to 10^7 photons) [30] and it appears when the electron decays to a different energy level than that where it started. The photons emitted by Stokes-Raman scattering usually have a lower energy and frequency than that of the photons absorbed and these photons are inelastically scattered, transferring some of their energy to the molecule. The Anti-Stokes-Raman scattering on the other hand takes place when the photons emitted have a

higher energy and frequency than the photons absorbed. It is not likely at room temperature as electrons prefer to be in the ground state.

Raman spectroscopy is often used to characterise crystal structures. Various techniques such as X-Ray diffraction, Infrared spectroscopy and Raman spectroscopy can be used to carry out such measurement. Unfortunately X-Ray diffraction [218] and Infrared spectroscopy [219] require a single crystal, thin sample or a powdered form of material in order to conduct the analysis. These requirements make the sample preparation difficult and time consuming, whereas for Raman spectroscopy no sample preparation is required. For that reason Raman spectroscopy was used to investigate some structural properties of 3Y-TZP.

2.9.3. Scanning Electron Microscopy

Scanning Electron Microscopy (SEM) uses a high energy electron beam to raster scan the inspected part [220, 221]. The electrons interact with the material atoms and this provides information about surface roughness, material composition and electrical characteristics of the inspected part. The spatial resolution of the SEM depends on the size of the electron beam spot, which depends on both the wavelength of the electrons and the electron-optical system that produces the scanning beam. The resolution depends also on the extent to which the material interacts with the electron beam, however sub-nanometre scale is achievable. The great advantage of the SEM scanning is the ability to image not just the surface but also the bulk of the material in search for material composition deviation using various image magnifications. The narrow electron beam allows for a large depth of field hence 3D surface topology can be measured rapidly. Unfortunately, due to large region of interaction of the electron beam with the material surface SEM cannot be used to image single atoms.

SEM can operate in the following modes where the signals detected are produced by: secondary electrons, back-scattered electrons, X-rays, light (cathodoluminescence), specimen current and transmitted electrons. The most common approach is using secondary electrons where the electrons interact with the surface atoms of the material. When the electron beam interacts with the sample, the electrons lose energy by random scattering and absorption within a volume of interaction. The volume of interaction depends on the electron's energy, the atomic number and the density of the specimen. The energy exchanged between the electron beam and the sample results in the reflection of high-energy electrons by elastic scattering, emission of secondary electrons

by inelastic scattering and the emission of electromagnetic radiation which depending on the detector is acquired.

The specimens tested with SEM should preferably be electrically conductive, at least at the surface, and electrically grounded to prevent the accumulation of electrostatic charge at the surface (charging). Nonconductive materials tend to charge when scanned by the electron beam, and especially in secondary electron imaging mode, this causes image artefacts. One of the possible solutions is coating the tested specimen with gold or carbon.

Apart from possible charging artefacts another disadvantage of SEM is a requirement to carry out the measurement in vacuum because the electron beam is rapidly attenuated and divergent in the air. This limits the applicability of SEM for the samples having a significant amount of water vapour such as biological samples. The samples have to be dried and this changes the material characteristics. For that reason the Environmental Scanning Electron Microscope (ESEM) was developed [222]. ESEM allows the samples to be measured at low-pressure (from 1 to 50 Torr) and high humidity (up to 100%) which is advantageous for non-metallic materials because no material coating is required. Unfortunately sometimes the imaging resolution may be compromised.

2.10. Destructive inspection techniques

Continuous development of the inspection technique is ubiquitous due to an increasing demand to increase the reliability of components and parts and the yield. The two main groups of the inspection techniques can be divided into destructive and non-destructive. In this final review section the currently available technology is presented in order to highlight how challenging the inspection of highly scattering ceramics can be, thus demonstrating the limited number of techniques available and hence justify the driver to develop novel techniques as investigated in this thesis.

As the name suggests a destructive measurement results in the tested part being destroyed, hence, particularly for medical applications where each part is unique as it is tailored to an individual, this method of inspection is not feasible. However, discussion of these techniques is still relevant as they are used for the inspection of ceramic components, where identical parts are manufactured. Furthermore, the samples inspected with the developed techniques were sectioned to confirm the presence of the detected flaws.

2.10.1. Sectioning

The main destructive approach is simply to section the sample in order to reach the desired place in the bulk. The advantage of this approach is that it provides direct access to inspect the buried feature. The disadvantage on the other hand apart from the fact that the specimen is destroyed is a risk of introducing unwanted damage or additional flaws into the component before the area of interest is inspected. In addition, there is a risk of not accurately sectioning the sample which may result in the feature being damaged during the sectioning. Furthermore, if the exact position of the feature is unknown the sectioning cannot be carried out without the risk of damaging the desired feature. Sectioning of ceramics such as 3Y-TZP is particularly time consuming due to the inherent high hardness and toughness. This is acerbated if multiple sections are required to fully characterise the sample.

2.10.2. Dye-Penetration Inspection

A less invasive approach is using a Dye-Penetration Inspection (DPI) technique where dye is injected or sprayed onto the inspected part [223]. The dye penetrates the holes or crack air gaps and reveals the information about the material defects. It should be noted that if the sample is thick and highly scattering and the dye is not able to penetrate into the bulk of the material the detection of the bulk flaws is not feasible. Furthermore for the highly scattering ceramics the sample has to be thin, otherwise the crack highlighted by the dye will not be detected due to the light scattering[223]. Another disadvantage of DPI is removal of the dye if it has penetrated deeper into the material because it may not be removed completely. For that reason the DPI was classified as a destructive method.

Another disadvantage of DPI is the time of the measurement. At first the sample has to be cleaned throughout to remove any potential contaminants which could influence the measurement. Then the dye is placed on the sample surface and left for some time to penetrate the cracks. The remaining penetrant is then cleaned off and the sample is inspected. After the inspection the penetrant is removed using various chemicals.

2.11. Non-destructive inspection techniques

Non-destructive testing is a more desired approach, particularly when inspecting unique parts. It not only provides details about the measured part but it also allows the

inspected part to be further used if no defects were detected. The non-destructive techniques predominantly use light however there are also sound wave methods used for non-destructive inspection.

2.11.1. Ultrasonic testing

The first two groups of non-destructive techniques presented in the next two sections are based on acoustic wave spectroscopy. Unlike electromagnetic waves, a sound wave is a mechanical vibration which requires a medium in which to propagate. The flaws in the material can be assessed due to wave distortions on discontinuities in the material. The principle for detection of flaws is discussed using two main groups of acoustic wave spectroscopy techniques: ultrasonics and the acoustic emission approach. Although these techniques could potentially be applied for inspection of Zirconia ceramics their requirement for a contact measurement due to the high ultrasonic wave attenuation in air, ultrasonic signal attenuation and variation due to Zirconia multicrystalline nature limit their applicability [224]. In addition a high temperature dependence of the ultrasonic wave velocity makes the analysis more complex and expensive [225].

Ultrasonic Testing (UT) uses high frequency low energy waves to non-destructively inspect the material [226]. The frequencies of up to tens of MHz depending on the application can be applied. As the wave travels through the material, it partially reflects, diffracts and attenuates at defects and voids in the material structure. Depending on the setup used the signal is either transmitted through the material or reflected from the discontinuities and then detected. The first technique is called through-transmission measurement [227] and the second approach is used in pulse-echo techniques [228] (see Figure 2.11.1).

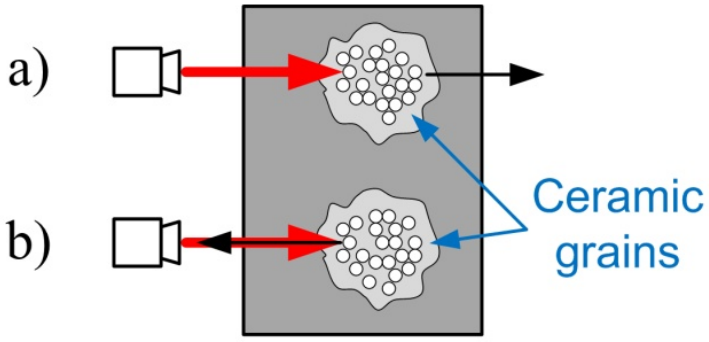

Figure 2.11.1. Ultrasonic methods: a) through-transmission, b) pulse-echo techniques.

UT was applied on many occasions for "green" state ceramics inspection during sintering [229], determination of the porosity, orientation, shape and number of pores in ceramic thermal barrier coatings (TBC) [224, 228, 230, 231], turbine blades inspection [232], and detection of defects in high temperature ceramics [233]. The rapid growth in the field of optics has lead to new developments of a non-contact and a non-destructive laser-based ultrasonics (LU). In LU the ultrasonic waves are generated during the laser beam material interaction and then are subsequently detected with a laser [234-237]. LU was used for the inspection of mechanical properties of ceramic spray coatings and consequently described the mechanism for the appearance of stresses and cracks in these coatings [234, 237].

2.11.2. Acoustic emission technique

Acoustic Emission (AE) is a natural phenomenon which occurs in a material after it has been excited externally. This excitation generates acoustic waves which appear due to the release of energy in the material under the stress (see Figure 2.11.2). This produces acoustic waves in the range of up to several MHz [238, 239]. Defect generation is one of the examples when AE appears in the material [240]. The energy released during this type of event can be generated not directly by the crack itself but by the structural changes in proximity to the crack where friction appears.

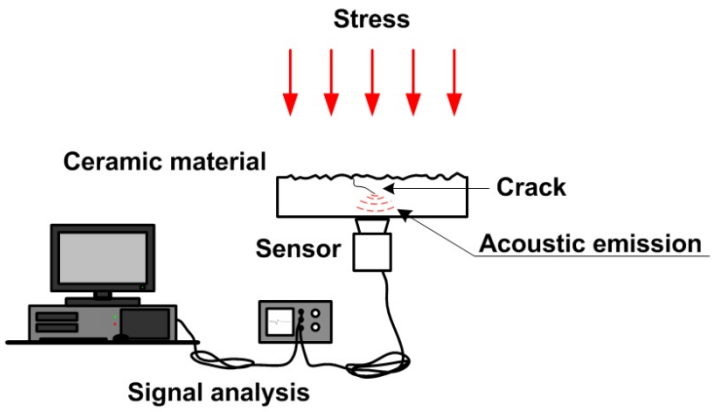

Figure 2.11.2. Simple acoustic emission detection system.

The AE technique is designed to monitor acoustic emission waves produced within the material during failure, rather than transmitting and collecting ultrasonic waves after they have travelled through the material. By measuring the amplitude distribution and number of counts (events) appearing during the measurement, detection of the cracks is achievable [241]. There are two main types of signals which can be detected with AE

techniques: continuous and burst-type emissions [238]. Continuous emission is usually caused by a plastic deformation of the material [239] and a burst-type signal can result from microcracking in brittle solids, phase transformation and other fracture processes [239, 242]. Crack generation mechanisms in ceramic coatings are the main area of application for the AE technique [238, 239, 243, 244]. AE observations were also used at elevated temperatures during TBC manufacturing processes to investigate the microfracture during coating cooling [245], to investigate the influence of the plasma spray parameters on mechanical properties of TBCs [246], to measure the ceramic materials strength [247] and thermal shock behaviour [248].

Apart from traditional AE inspection Oishi introduced Scanning Laser Acoustic Microscopy (SLAM) (see Figure 2.11.3) for non-destructive evaluation of structural ceramics [249]. This technique uses acoustic waves which propagate through the sample and generate a ripple which is proportional to the localized sound pressure on one of the specimen surfaces. This ripple is then observed by the detector which acquires the laser beam reflected from the surface. In ceramics SLAM is mainly used to measure mechanical properties but also to detect defects in the bulk material.

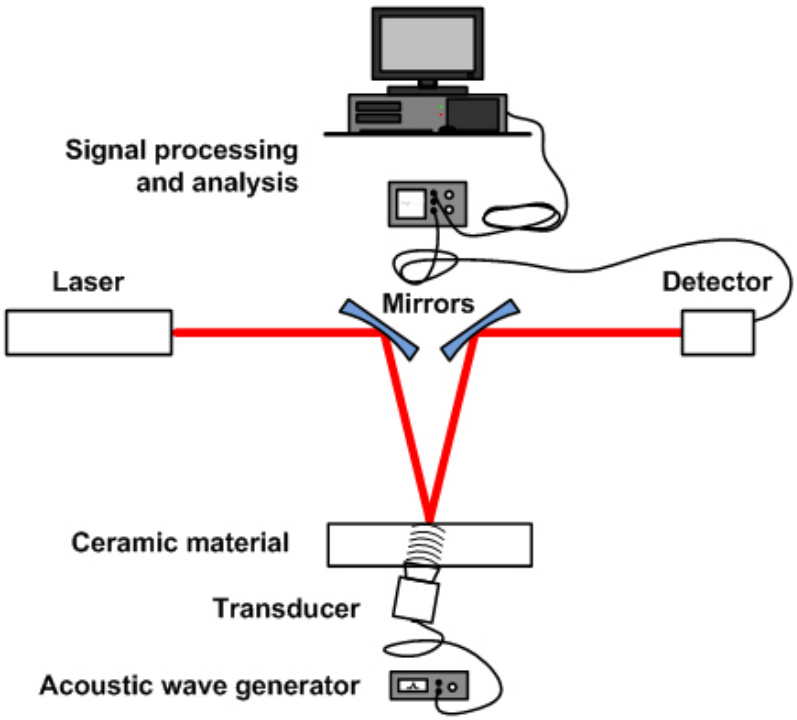

Figure 2.11.3. SLAM setup[249].

2.11.3. Optical profilometry

The remaining techniques presented in section 2.11 are optical inspection techniques. A key characteristic of all optical testing techniques is their non-contact nature. Similarly to some ultrasonic techniques [234-237, 249] the optical testing can be much faster than the conventional contact methods because the sample can be examined in-situ in an automated environment, where high speed, high accuracy and low cost are required [250]. Optical techniques can provide information about the shape, surface roughness and imperfections by detecting changes in the light which is reflected, transmitted, absorbed or scattered by the material.

The optical profilometry technique provides an accurate, relatively slow measurement due to involving a one-dimensional profile scanning (compared to non-scanning techniques). However, optical profilometers generally operate faster than their mechanical stylus counterparts [251]. Improved lateral resolution is an additional attribute of optical profilers. Either laser coherent beam (see Figure 2.11.4) or white light is applied in optical profilometry [251]. There are various system configurations depending on the application: Confocal Microscopy (CM) [252, 253], Scanning Near-Field Optical Microscopy (SNOM) [251], white light profilometry [254] and laser profilometry [255] are just a few examples of the techniques currently available.

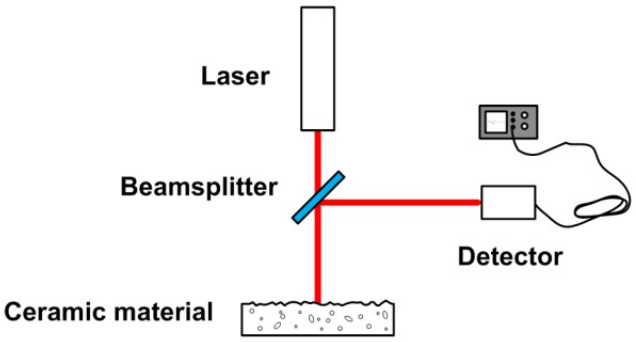

Figure 2.11.4. Simple laser optical profilometer.

Surface topography and wear mechanism investigations [256] are the main applications for optical profilometry in ceramics. Due to low cost and high raster scanning speed (compared with a mechanical approach), optical profilometry often accompanies other techniques in determining failure and wear mechanisms in ceramics. Confocal laser profilometry was used during the investigation of corrosion mechanisms in dental ceramics [257]. 3D optical profilometry based on interference microscopy was applied during the analysis of the wear mechanisms of hip joint ceramics. Alumina, 3Y-TZP

and alumina-Zirconia composites were tested to directly measure the worn volume [258]. The optical profilometry was also used during investigation of plasma sprayed ceramic coatings for the surface roughness and wear [259], elastic modulus [260] and coating thickness measurements [261] where it illustrated and helped to explain the surface roughness and wear mechanisms of the ceramic coatings.

2.11.4. Visible light camera and microscopy imaging

The most cost-effective solution is using visible light for inspecting the ceramic parts where the specimen is simply illuminated by the light source and the camera or the microscope allows for the specimen observation. This is due to the wide availability of visible light cameras and microscopes. Particularly for the visible light camera for which the field of view can be easily adjusted the cost is very low.

Another approach is to use visible light Confocal Microscopy (CM) [262-264]. The main advantage of CM is an ability to accurately produce a 3D map of the scanned sample due to a point-by-point scanning. This enhances the acquired image contrast, particularly in thick specimens. Furthermore, by restricting the observed volume, the technique restricts overlying or nearby scatterers from contributing to the detected signal. The disadvantage of CM is the time of the measurement which may be substantial depending on the inspection requirements. It is possible to use multi-point scanning to reduce the scanning time, however this process is still considerably slower than standard camera imaging. Another disadvantage of confocal imaging is a very limited signal traversing through the pinhole due to its size because the pinhole operates as a spatial filter. The main field of applications for CM is medicine [264] where shallow depth of field is required to image only a particular area of interest. CM was for example applied successfully for a characterisation of the small channels topology which were machined in Zirconia [265].

Although the above techniques present high flexibility in material inspection capabilities the main disadvantages is the optical transmittance incompatibility of the visible wavelengths with the optical characteristics of the measured Zirconia-based ceramics due to highly scattering nature in visible (see section 2.4). However, if the visible light inspection is carried out on the Zirconia parts a skilled operator is required to quantify any changes in the light structure. Unfortunately, there is a high risk of omitting some of the flaws due to variation in the operator's skills over time.

2.11.5. Thermal Wave Imaging

Thermal Wave Imaging (TWI) technique uses thermal waves to obtain information about the parameters and defects in the material. The intensity of the emitted thermal energy depends on the object and it varies with the temperature and the radiation wavelength. If the object is colder than about 500ºC then the emitted radiation can only be detected within infrared wavelength region [266]. Due to the properties of thermal waves, a significant majority of thermal wave imaging techniques use a modulated infrared source (heat flashing) to increase the speed and to improve the resolution of the measurement. The cooling rate of the heated object varies and it depends on the material thermal properties, thickness and number of defects in the component [267, 268]. The cooling rate and the cooling curve determine how fast and how accurately the component can be measured. There are two main groups of thermal wave imaging techniques: transmission based and reflection based techniques (see Figure 2.11.5) [183]. The transmission technique monitors heat transmission through the material. The considerable disadvantage of this technique is the fact that both sides of the sample have to be accessible, which often is not feasible in a practical component or application. The reflection technique on the other hand monitors the heat waves which are reflected back either from the surface or from the discontinuities in the bulk material. This solution is more feasible for ceramic coatings applications where only one side of the part can be accessed.

The TWI technique was applied during the characterisation of droplet impact on plasma spraying of Zirconia particles [269-271], to assess the efficiency of the coating deposition and to observe the coating failure modes [268, 272, 273]. The other applications involve the determination of material porosity, the presence of voids and corrosion detection [273, 274]. Integrity and thickness of TBCs was also investigated with TWI [275]. It should be noted that TWI has a limited applicability due to difficulties in controlling the flash heat source, complex analysis of thermal transients in the material, very restricted depth of penetration and long time required for the measurement. These factors reduced the implementation of TWI in the industrial environment.

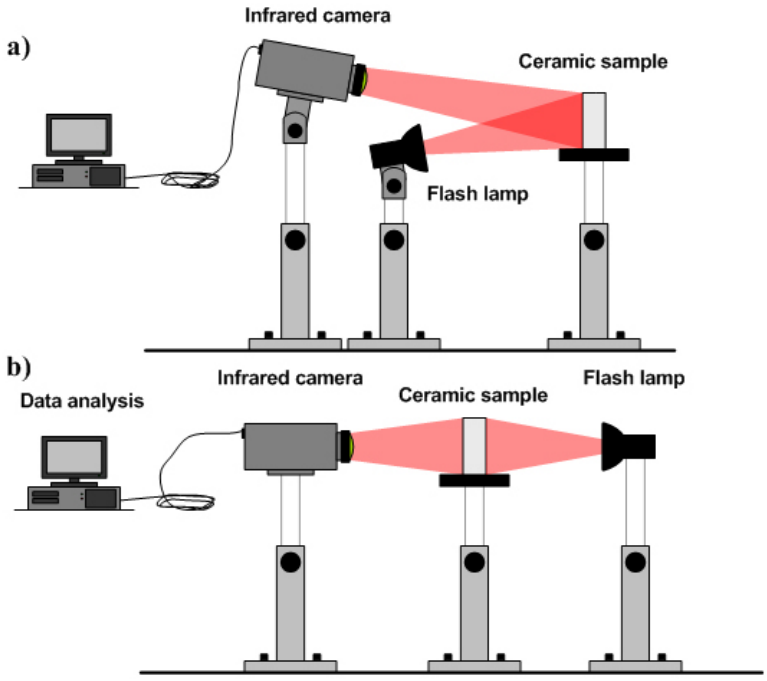

Figure 2.11.5. Infrared thermography: a) reflection; b) transmission technique.

2.11.6. Optical coherence Tomography

Optical Coherence Tomography (OCT) was introduced in the early nineties for depth-resolved high resolution imaging in transparent and turbid media [276, 277]. The majority of research activity in the OCT area is associated with biomedical science [278]. OCT systems usually consist of a Michelson or Mach-Zehnder interferometer which uses the light interference between the reflected/scattered from the sample and the reference light beams giving high depth-resolved data even in strongly scattering media (see Figure 2.11.6).

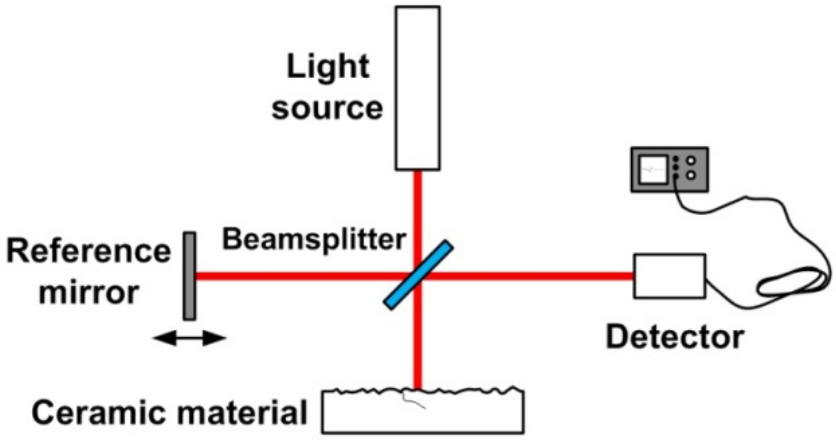

Figure 2.11.6. Schematic of OCT system [277].

Several modifications of OCT were presented depending on the application and the type of the measurement [278, 279]. Significant developments in the optics field allowed OCT techniques to be applied to study highly scattering materials such as ceramic TBCs [280, 281], dental ceramics [282-284] and other ceramic materials [278, 285]. A significant amount of research to determine the maximum detection depth of void structures using OCT in silicon nitride ceramics was implemented by Bashkansky's group [286, 287]. They reported depth of resolution of 10 μm and an imaging depth of 500 μm were sufficient to evaluate sub-surface cracks introduced by the indenter. The same group used the OCT to detect micropipe defects in silicon carbide [288, 289] and studied Hertzian C-shaped cracks in silicon nitride ceramic balls for bearings [290].

OCT as a non-destructive tool is mainly applied in biomedical studies. Ceramics are still very difficult materials for inspection due to the multicrystalline structure. Introducing new types of light sources which could mitigate the light scattering and expand the operating wavelength for OCT systems is desirable. In addition further developments to enhance accuracy and reduce the cost of the OCT systems have to be exploited if these techniques are to become commonplace.

2.11.7. Mid-Infrared Reflectance Imaging

The disadvantages of the thermographic inspection lead to new developments in infrared imaging techniques. Eldridge [135, 291] presented a novel Mid-Infrared Reflectance Imaging (MIR) technique (see Figure 2.11.7) for inspection of TBCs which offers the advantage of reduced light scattering, thus a greater depth of penetration during the inspection of Zirconia-based TBCs compared to thermography. The author applied the MIR technique to observe failure mechanisms which emerge due to the formation and growth of the crack network on the interfaces between the TBC layers. The MIR technique allows the detection of the crack occurrence due to the increasing light reflection and scattering caused by the increasing number of cracks in the material. The air gaps become the scattering and reflection centres which guide the light back towards the top surface of the coating. Unfortunately, the identification of delamination regions and cracks in the material becomes difficult as the coating thicknesses reaches 300 μm due to light scattering. In addition, particularly for TBCs, the sintering process of the coating, surface contamination and influence of the specimen reflectance have to be considered during the measurements, thus the sample analysis becomes complex.

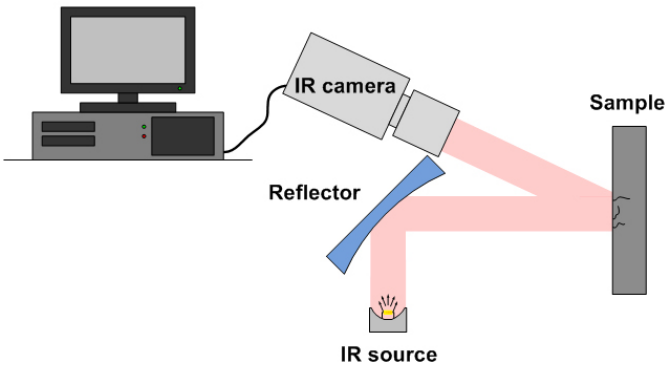

Figure 2.11.7. MIR reflection system setup [135].

2.11.8. Overview of Inspection techniques

Table 2.1 presents a comprehensive comparison of the techniques presented in the previous sections which were applied of inspection of Zirconia ceramics. The table compares the maximum depth of penetration, cost, and advantages/disadvantages of each of the techniques when inspecting highly scattering Zirconia ceramics. The flaws which size is above 1 mm are defined as macro scale cracks and below 1 mm there are micro cracks. Table 2.1 clearly shows that there is a gap in the market for inspection techniques of thick (above 1 mm in thickness), highly scattering ceramics for micro scale cracks detection.

Table 2.1. Comparison of the presented inspection technique.

Technique	Crack detection depth limit	Pros	Cons	Price
Sectioning	**Unlimited**	**Simple, cheap**	**Time consuming, destructive**	**< £1,000**
Dye-penetration	**Surface and subsurface**	**Simple, cheap**	**Can be destructive, time consuming, only for thin samples**	**< £1,000**
Ultrasonic testing	**Several hundred micrometres**	**Non-destructive, high axial resolution (up to 5 µm)**	**Low lateral resolution (100 µm), in literature used only for thermal barrier coatings inspection**	**< £15,000**
Acoustic emission	**Surface and subsurface**	**Easy critical for the part cracks detection, non-destructive**	**Microcracking difficult to detect, can only be used to monitor cracks generation during part machining**	**< £15,000**
Optical profilometry	**Surface**	**Vertical resolution in nanometre scale, non-destructive, non-contact**	**Expensive, scanning technique hence can be time consuming**	**< £50,000**
Visible light inspection	**< 1 mm – micro scale flaws > 1 mm – macro scale flaws**	**Cheap, equipment widely available, easy to set up, can be fast**	**Not suitable for highly scattering ceramics, difficulties in automatic focus adjustment, slow with scanning techniques**	**> £100**
Thermal wave imaging	**Few hundred microns – in literature**	**Can penetrate deeper into material than visible wavelengths**	**Expensive – thermal camera, slow, limited resolution**	**> £10,000**
Optical Coherence Tomography	**2 mm for highly scattering materials, 500 µm for micro cracks**	**Sub-micrometre resolution, 3D image acquisition, measurement in seconds**	**Expensive, not yet applicable in industrial environment**	**< £50,000**
Mid-Infrared Reflectance Imaging	**300 µm for micro cracks detection**	**Simple setup, fast measurement**	**Expensive – infrared camera, limited depth for cracks detection, resolution limited by the camera**	**> £10,000**

References:

[1] W. Burger, H. G. Richter, C. Piconi, R. Vatteroni, A. Cittadini and M. Boccalari: 'New Y-TZP powders for medical grade zirconia', *Journal of Materials Science-Materials in Medicine*, 1997, **8**(2), 113-118.

[2] L. L. Hench and W. June: 'An Introduction to Bioceramics'; 1993, World Scientific Publishing Co Pte Ltd.

[3] Z. Özkurt and E. Kazazoğlu: 'Clinical Success of Zirconia in Dental Applications', *Journal of Prosthodontics*, 2010, **19**(1), 64-68.

[4] C. H. Liebert: 'Tests of NASA ceramic thermal barrier coating for gas turbine engines', *Thin Solid Films*, 1979, **64**(2), 329-333.

[5] X. Q. Cao, R. Vassen, F. Tietz and D. Stoever: 'New double-ceramic-layer thermal barrier coatings based on zirconia-rare earth composite oxides', *Journal of the European Ceramic Society*, 2006, **26**(3), 247-251.

[6] J. Vleugels: 'Fabrication, wear and performance of ceramic cutting tools', *Ind. Ceram.*, 2008, **28**(2), 145-152.

[7] A. S. Kumar, A. R. Durai and T. Sornakumar: 'Yttria ceramics: cutting tool application', *Materials Letters*, 2004, **58**(11), 1808-1810.

[8] I. Denry and J. R. Kelly: 'State of the art of zirconia for dental applications', *Dental Materials*, 2008, **24**(3), 299-307.

[9] B. Cales: 'Y-TZP Zirconia Ceramics Hip Joint Heads Key-Issues for a High Reliability', Fourth Euro-Ceramics, Faenza (Italy), 1995, Gruppo Editoriale Faenza Editrice S.p.A., Riccione, Italy, 45–52.

[10] B. Cales: 'Zirconia as a Sliding Material: Histologic, Laboratory, and Clinical Data', *Clin. Orthoped. Related Res.*, 2000(October [379]), 94-112.

[11] C. B. Carter and M. G. Norton: 'Ceramic Materials: Science and Engineering'; 2007, New York, Springer-Verlag.

[12] T. Bayanova: 'Baddeleyite: A promising geochronometer for alkaline and basic magmatism', *Petrology*, 2006, **14**(2), 187-200.

[13] O. Ruff and F. Ebert: 'Refractory Ceramics: 1, The Forms of Zirconium Dioxide', *Zeitschrift für anorganische und allgemeine Chemie*, 1929, **180**(1), 19-41.

[14] O. Ruff and F. Ebert: 'Contributions to the Ceramics of Highly Refractory Materials: II, System Zirconia-Lime', *Zeitschrift für anorganische und allgemeine Chemie*, 192, **180**(1), 215-224.

[15] P. Duwez and F. H. Brown: 'Zirconia-Yttria System', *Journal of The Electrochemical Society*, 1951, **98**(9), 356-362.

[16] C. J. Howard and R. J. Hill: 'The polymorphs of zirconia: phase abundance and crystal structure by Rietveld analysis of neutron and X-ray diffraction data', *J. Mater. Sci.*, 1991, **26**(1), 127-134.

[17] H. G. Scott: 'Phase Relationships in Zirconia-Yttria System', *J. Mater. Sci.*, 1975, **10**(9), 1527-1535.

[18] C. Piconi and G. Maccauro: 'Zirconia as a ceramic biomaterial', *Biomaterials*, 1999, **20**(1), 1-25.

[19] R. H. J. Hannink, P. M. Kelly and B. C. Muddle: 'Transformation toughening in zirconia-containing ceramics', *J. Am. Ceram. Soc.*, 2000, **83**(3), 461-487.

[20] R. C. Garvie and M. V. Swain: 'Thermodynamics of the tetragonal to monoclinic phase transformation in constrained zirconia microcrystals', *J. Mater. Sci.*, 1985, **20**(4), 1193-1200.

[21] R. R. Prasad and B. S. S. Daniel: 'Cryogenically Synthesized Mechanically Alloyed Calcia Stabilized Zirconia', *Advanced Materials Research*, 2009, **67**(1), 271.

[22] A. H. H. A. G. Evans: 'REVIEW--Transformation Toughening in Ceramics: Martensitic Transformations in Crack-Tip Stress Fields', *J. Am. Ceram. Soc.*, 1980, **63**(5-6), 241-248.

[23] B. Basu: 'Toughening of yttria-stabilised tetragonal zirconia ceramics', *Int. Mater. Rev.*, 2005, **50**(4), 239-256.

[24] A. G. Evans and A. H. Heuer: 'Transformation Toughening in Ceramics - Martensitic Transformations in Crack-Tip Stress-Fields', *J. Am. Ceram. Soc.*, 1980, **63**(5-6), 241-248.

[25] R. C. Garvie, R. H. Hannink and R. T. Pascoe: 'Ceramic Steel?', *Nature*, 1975, **258**, 703-704.

[26] P. M. Kelly and C. J. Wauchope: 'The Tetragonal to Monoclinic Martensitic Transformation in Zirconia', *Key Engineering Materials*, 1998, **153-154**, 97-124.

[27] F. J.: 'Zirconium Oxcide Restorators with the DCS Precident System', *International Journal of Computerized Dentistry* 2003(6), 193-201.

[28] P. V. v. Steyern: 'All-Ceramic Fixed Partial Dentures', *Swedish Dental Journal Supplement*, 2005(173).

[29] M. Hadfield, T. A. Stolarski, R. T. Cundill and S. Horton: 'Failure modes of ceramic elements with ring-crack defects', *Tribology International*, 1993, **26**(3), 157-164.

[30] E. C. Panagiotopoulos, A. G. Kallivokas, I. Koulioumpas and D. E. Mouzakis: 'Early failure of a zirconia femoral head prosthesis: Fracture or fatigue?', *Clinical Biomechanics*, 2007, **22**(7), 856-860.

[31] F. Snijkers, A. de Wilde, S. Mullens and J. Luyten: 'Aqueous tape casting of yttria stabilised zirconia using natural product binder', *Journal of the European Ceramic Society*, 2004, **24**(6), 1107-1110.

[32] P. Duran, M. Villegas, F. Capel, J. Fernandez and C. Moure: 'Nanostructured and near defect-free ceramics by low-temperature pressureless sintering of nanosized Y-TZP powders', *J. Mater. Sci.*, 1997, **32**(17), 4507-4512.

[33] C. Piconi, G. Maccauro, L. Pilloni, W. Burger, F. Muratori and H. Richter: 'On the fracture of a zirconia ball head', *Journal of Materials Science: Materials in Medicine*, 2006, **17**(3), 289-300.

[34] H. Wang and X. Hu: 'Surface Properties of Ceramic Laminates Fabricated by Die Pressing', *J. Am. Ceram. Soc.*, 1996, **79**(2), 553-556.

[35] K. Tsukuma and M. Shimada: 'Hot isostatic pressing of Y2O3-partially stabilized zirconia', *American Ceramic Society Bulletin*, 1985, **64**, 310-313.

[36] M. Trunec: 'Fabrication of zirconia- and ceria-based thin-wall tubes by thermoplastic extrusion', *Journal of the European Ceramic Society*, 2004, **24**(4), 645-651.

[37] B. J. Kellett, C. Carry and A. Mocellin: 'High-Temperature Extrusion Behavior of a Superplastic Zirconia-Based Ceramic', *J. Am. Ceram. Soc.*, 1990, **73**(7), 1922-1927.

[38] P. H. Rieth, J. S. Reed and A. W. Naumann: 'Fabrication and flexural strength of ultrafine-grained yttria-stabilized zirconia', *Journal Name: Am. Ceram. Soc. Bull.; (United States); Journal Volume: 55:8*, 1976, Medium: X; Size: Pages: 717-721.

[39] R. Moreno, J. Requena and J. S. Moya: 'Slip Casting of Yttria-Stabilized Tetragonal Zirconia Polycrystals', *J. Am. Ceram. Soc.*, 1988, **71**(12), 1036-1040.

[40] H. Taguchi, H. Miyamoto and Y. Takahashi: 'Slip casting of partially stabilized zirconia', *Journal Name: Am. Ceram. Soc. Bull.; (United States); Journal Volume: 64:2*, 1985, Medium: X; Size: Pages: 325.

[41] M. Boaro, J. M. Vohs and R. J. Gorte: 'Synthesis of Highly Porous Yttria-Stabilized Zirconia by Tape-Casting Methods', *J. Am. Ceram. Soc.*, 2003, **86**(3), 395-400.

[42] M. P. Albano and L. B. Garrido: 'Aqueous tape casting of yttria stabilized zirconia', *Materials Science and Engineering: A*, 2006, **420**(1-2), 171-178.

[43] L. Samuel I-En: 'Near-net-shape forming of zirconia optical sleeves by ceramics injection molding', *Ceramics International*, 2001, **27**(2), 205-214.

[44] J. H. Song and J. R. G. Evans: 'The injection moulding of fine and ultra-fine zirconia powders', *Ceramics International*, 1995, **21**(5), 325-333.

[45] J. Y. Kim, S. Okamoto, N. Uchida and K. Uematsu: 'Hot isostatic pressing of Y-TZP powder compacts', *J. Mater. Sci.*, 1990, **25**(11), 4634-4638.

[46] J. Li, H. Liao and L. Hermansson: 'Sintering of partially-stabilized zirconia and partially-stabilized zirconia—hydroxyapatite composites by hot isostatic pressing and pressureless sintering', *Biomaterials*, 1996, **17**(18), 1787-1790.

[47] T. Masaki: 'Mechanical properties of toughened ZrO2-Y2O3 Ceramics', *J. Am. Ceram. Soc.*, 1986, **69**(8), 638-640.

[48] L. Gao, W. Li, H. Z. Wang, J. X. Zhou, Z. J. Chao and Q. Z. Zai: 'Fabrication of nano Y–TZP materials by superhigh pressure compaction', *Journal of the European Ceramic Society*, 2001, **21**(2), 135-138.

[49] T. Tepper, C. A. Ross and G. F. Dionne: 'Microstructure and optical properties of pulsed-laser-deposited iron oxide films', *Magnetics, IEEE Transactions on*, 2004, **40**(3), 1685-1690.

[50] G. S. A. M. Theunissen, A. J. A. Winnubst and A. J. Burggraaf: 'Sintering kinetics and microstructure development of nanoscale Y-TZP ceramics', *Journal of the European Ceramic Society*, 1993, **11**(4), 315-324.

[51] P. Durán, M. Villegas, F. Capel, P. Recio and C. Moure: 'Low-temperature sintering and microstructural development of nanocrystalline Y-TZP powders', *Journal of the European Ceramic Society*, 1996, **16**(9), 945-952.

[52] W. Li and L. Gao: 'Rapid sintering of nanocrystalline ZrO2(3Y) by spark plasma sintering', *Journal of the European Ceramic Society*, 2000, **20**(14-15), 2441-2445.

[53] K. W. Schlichting, N. P. Padture and P. G. Klemens: 'Thermal conductivity of dense and porous yttria-stabilized zirconia', *J. Mater. Sci.*, 2001, **36**(12), 3003-3010.

[54] K. Kwak and C. Kim: 'Viscosity and thermal conductivity of copper oxide nanofluid dispersed in ethylene glycol', *Korea-Australia Rheology Journal*, 2005, **17**(2), 35-40.

[55] A. J. Allen, J. Ilavsky, G. G. Long, J. S. Wallace, C. C. Berndt and H. Herman: 'Microstructural characterization of yttria-stabilized zirconia plasma-sprayed deposits using multiple small-angle neutron scattering', *Acta Mater.*, 2001, **49**(9), 1661-1675.

[56] X. Q. Cao, R. Vassen and D. Stoever: 'Ceramic materials for thermal barrier coatings', *Journal of the European Ceramic Society*, 2004, **24**(1), 1-10.

[57] N. P. Padture, M. Gell and E. H. Jordan: 'Thermal Barrier Coatings for Gas-Turbine Engine Applications', *Science*, 2002, **296**(5566), 280-284.

[58] L. Pawlowski: 'The Science and Engineering of Thermal Spray Coatings'; 2008, Wiley-Blackwell; 2nd Edition edition.

[59] A. Syed, Z. Ilhan, J. Arnold, G. Schiller and H. Weckmann: 'Improving plasma-sprayed yttria-stabilized zirconia coatings for solid oxide fuel cell electrolytes', *Journal of Thermal Spray Technology*, 2006, **15**(4), 617-622.

[60] J. M. Lee and G. M. Choi: 'Oxygen-permeating zirconia membrane: The effect of thickness and surface coating', *Journal of the European Ceramic Society*, 2007, **27**(13-15), 4219-4222.

[61] L. Shi, K.-C. Tin and N.-B. Wong: 'Thermal stability of zirconia membranes', *J. Mater. Sci.*, 1999, **34**(14), 3367-3374.

[62] C. G. Levi: 'Emerging materials and processes for thermal barrier systems', *Current Opinion in Solid State and Materials Science*, 2004, **8**(1), 77-91.

[63] D. D. Hass: 'Directed Vapor Deposition of Thermal Barrier Coatings', PhD thesis, University of Virginia, 2000.

[64] E. A. Jarvis and E. A. Carter: 'The role of reactive elements in thermal barrier coatings', *Computing in Science & Engineering*, 2002, **4**(2), 33 – 41.

[65] B. G. Nair, J. P. Singh and M. Grimsditch: 'Stress analysis in thermal barrier coatings subjected to long-term exposure in simulated turbine conditions', *J. Mater. Sci.*, 2004, **39**(6), 2043-2051.

[66] Y. H. Sohn, E. Y. Lee, B. A. Nagaraj, R. R. Biederman and R. D. Sisson: 'Microstructural characterization of thermal barrier coatings on high pressure turbine blades', *Surface and Coatings Technology*, **146-147**, 132-139.

[67] A. Christensen, E. A. Asche and E. A. Carter: 'Atomic-level Properties of Thermal Barrier Coatings: Characterization of Metal-Ceramic Interfaces', *Advanced Series in Physical Chemistry series*, 2001.

[68] R. T. Chiroff, R. A. White, E. W. White, J. N. Weber and D. Roy: 'The restoration of articular surfaces overlying replamineform porous biomaterials', *Journal of Biomedical Materials Research*, 1977, **11**(2), 165-178.

[69] P. Zeng: 'Biocompatible alumina ceramic for total hip replacements', *Tribology - Materials, Surfaces & Interfaces*, 2008, **2**(2), 109-120.

[70] L. PrÖBster: 'Four year clinical study of glass-infiltrated, sintered alumina crowns', *Journal of Oral Rehabilitation*, 1996, **23**(3), 147-151.

[71] M. Kern and J. R. Strub: 'Bonding to alumina ceramic in restorative dentistry: clinical results over up to 5 years', *Journal of Dentistry*, 1998, **26**(3), 245-249.

[72] T. W. Kelley, L. D. Boardman, T. D. Dunbar, D. V. Muyres, M. J. Pellerite and T. P. Smith: 'High-Performance OTFTs Using Surface-Modified Alumina Dielectrics', *The Journal of Physical Chemistry B*, 2003, **107**(24), 5877-5881.

[73] J. Veres, S. Ogier, G. Lloyd and D. de Leeuw: 'Gate Insulators in Organic Field-Effect Transistors', *Chemistry of Materials*, 2004, **16**(23), 4543-4555.

[74] B. E. Raahauge and W. S. Maley: 'Process and apparatus for the production of alumina', Patent, 2005.

[75] B. D. Flinn, R. K. Bordia, A. Zimmermann and J. Rödel: 'Evolution of defect size and strength of porous alumina during sintering', *Journal of the European Ceramic Society*, 2000, **20**(14-15), 2561-2568.

[76] T. K. Gupta: 'Crack Healing and Strengthening of Thermally Shocked Alumina', *J. Am. Ceram. Soc.*, 1976, **59**(5-6), 259-262.

[77] A. H. De Aza, J. Chevalier, G. Fantozzi, M. Schehl and R. Torrecillas: 'Crack growth resistance of alumina, zirconia and zirconia toughened alumina ceramics for joint prostheses', *Biomaterials*, 2002, **23**(3), 937-945.

[78] H. Huang and Y. C. Liu: 'Experimental investigations of machining characteristics and removal mechanisms of advanced ceramics in high speed deep grinding', *International Journal of Machine Tools and Manufacture*, 2003, **43**(8), 811-823.

[79] G. Brandt: 'Flank and crater wear mechanisms of alumina-based cutting tools when machining steel', *Wear*, 1986, **112**(1), 39-56.

[80] N. N. Greenwood and A. Earnshaw: 'Chemistry of the Elements'; 1984, Oxford: Pergamon.

[81] A. E. Goresy, M. Chen, L. Dubrovinsky, P. Gillet and G. Graup: 'An Ultradense Polymorph of Rutile with Seven-Coordinated Titanium from the Ries Crater', *Science*, 2001, **293**(5534), 1467-1470.

[82] F. Dachille, P. Y. Simons and R. Roy: 'Pressure-Temperature Studies Of Anatase, Brookite, rutile and TiO_2-II', *The American Mineralogist*, 1968, **53**.

[83] N. Osterwalder, C. Capello, K. Hungerbühler and W. Stark: 'Energy Consumption During Nanoparticle Production: How Economic is Dry Synthesis?', *Journal of Nanoparticle Research*, 2006, **8**(1), 1-9.

[84] E. Reck and M. Richards: 'TiO2 manufacture and life cycle analysis', *Pigment & Resin Technology*, 1999, **28**(3), 149-157.

[85] L. G. Phillips and D. M. Barbano: 'The Influence of Fat Substitutes Based on Protein and Titanium Dioxide on the Sensory Properties of Lowfat Milks', *Journal of Dairy Science*, 1997, **80**(11), 2726-2731.

[86] A. Fujishima, K. Hashimoto and T. Watanabe: 'TiO2 photocatalysis. Fundaments and Applications'; 1999, BKC, Inc.

[87] S. Bakardjieva, V. Stengl, J. Subrt, V. Tyrpekl and J. Brown: 'Photocatalytic Activity of Rare Earth Doped TiO2 Nanoparticles', *Microscopy and Microanalysis*, 2007, **13**(SupplementS02), 650-651.

[88] T. Kosmac, C. Oblak, P. Jevnikar, N. Funduk and L. Marion: 'The effect of surface grinding and sandblasting on flexural strength and reliability of Y-TZP zirconia ceramic', *Dental Materials*, 1999, **15**(6), 426-433.

[89] T. Kosmac, C. Oblak and L. Marion: 'The effects of dental grinding and sandblasting on ageing and fatigue behavior of dental zirconia (Y-TZP) ceramics', *Journal of the European Ceramic Society*, 2008, **28**(5), 1085-1090.

[90] H. H. K. Xu, S. Jahanmir and L. K. Ives: 'Effect of Grinding on Strength of Tetragonal Zirconia and Zirconia-Toughened Alumina', *Machining Science and Technology*, 1997, **1**(1), 49-66.

[91] H. H. K. Xu, S. Jahanmir and L. K. Ives: 'Material Removal and Damage Formation Mechanisms in Grinding Silicon Nitride', *Journal of Materials Research*, 1996, **11**(7), 1717-1724.

[92] T. N. Farris and S. Chandrasekar: 'On the Characterization and Contol of Surface Finishing Damage in Ceramics', *Journal of Mechanical Working Technology*, 1989, **20**, 69-78.

[93] M. Shuji, I. Satoshi, K. Masanobu and K. Ryuzo: 'Changes of Bending Strength and Structure in Ground Surface of Y-TZP', *Report of the Industrial Technology Institute, Yamaguchi Prefectural Government*, 1999(11), 1-7.

[94] W. Konig, L. Cronjager, G. Spur, H. K. Tonshoff, M. WVigneau and W. J. Zdeblick: 'Machining of New Materials', *Annals of the CIRP*, 1990, **39**(2), 673-681.

[95] H. Huang: 'Machining characteristics and surface integrity of yttria stabilized tetragonal zirconia in high speed deep grinding', *Materials Science and Engineering A*, 2003, **345**(1-2), 155-163.

[96] H. Han, L. Yuchan, T. P. Luan and L. K. Hwee: 'High Speed Deep Grinding of Tetragonal Zirconia', Singapore Institution of Manufacturing Technology, 2001.

[97] N. V. Novikov, O. A. Rozenberg, A. G. Mamalis and S. V. Sokhan: 'Finish diamond machining of ceramic femoral heads', *International Journal of Advanced Manufacturing Technology*, 2005, **25**, 244–247.

[98] W. M. Steen and J. N. Jamulu: 'Materials Processing: Theory and Practice', in 18-29; 1983, Berlin.

[99] S. Copley, M. Bass, B. Jau and R. Wallace: 'Shaping Materials with lasers', *Laser Materials Processing*, 1983, 297-336.

[100] I. Nettleship and R. Stevens: 'The effect of Cooling Rate on the Phase Transformations in Mg-PSZ', *British Ceramic Transactions and Journal*, 1987, **86**(6), 183-186.

[101] P. Affolter and H. G. Schmid: 'Processing of new ceramics materials with solid state laser radiation', *SPIE-High Power lasers and their industrial applications*, 1987(801), 120-129.

[102] R. F. Firestone and E. J. Vesely Jr.: 'High Power Laser Bean Machining of structural Ceramics', *ASME Symposium on Machining of Advanced Ceramic Materials*, 1988, 215-227.

[103] F. C. Dear: 'Laser Machining Of Medical Grade Zirconia Ceramic For Dental Reconstruction Applications', PhD thesis, Heriot Watt University, Edinburgh, 2008.

[104] F. C. Dear, J. D. Shephard, X. Wang, J. D. C. Jones and D. P. Hand: 'Pulsed laser micromachining of yttria-stabilized zirconia dental ceramic for manufacturing', *International Journal of Applied Ceramic Technology*, 2008, **5**(2), 188-197.

[105] X. Wang, J. D. Shephard, F. C. Dear and D. P. Hand: 'Optimized nanosecond pulsed laser micromachining of Y-TZP ceramics', *J. Am. Ceram. Soc.*, 2008, **91**(2), 391-397.

[106] K. J. Bowman, F. E. Pfefferkorn and Y. C. Shin: 'Recrystallization textures during laser-assisted machining of zirconia ceramics', *Materials Science Forum*, 2002, **408-412**, 1669-1674.

[107] P. A. Rebro, F. E. Pfefferkorn, Y. C. Shin and F. P. Incropera: 'Comparitive Assessment of Laser-Assisted Machining for various Ceramics', *Transactions of NAMRI/SME*, 2002, **30**, 153-160.

[108] K. Werelius and P. Weigl: 'Ceramic dentures manufactured with ultra-short laser pulses', *Commercial and Biomedical Applications of Ultrafast Lasers IV*, 2004, **SPIE 5340**, 127-132.

[109] P. Weigl, A. Kasenbacher and K. Werelius: 'Dental Applications', *Topics In Applied Physics*, 2004, **96**, 167-187.

[110] P. Weigl and A. Ka: 'Topics In Applied Physics', 2004, **96**(2004), 167-187.

[111] N. Bärsch, S. Barcikowski and K. Baier: 'Ultrafaser-laser-processed zirconia and its adhesion to dental cement', Proceedings of LPM2007 - the 8th International Symposium on Laser Precision Microfabrication, 2007.

[112] B. Hitz: 'Fiber laser generates 1.6 W in single longitudinal mode - Potential applications in telecommunications and in sensing', *Photonics Spectra*, 2005, **39**(12), 110-111.

[113] A. Babushkin, N. S. Platonov and V. P. Gaponstev: 'Multi-kilowatt peak power pulsed fiber laser with precise computer controlled pulse duration for materials processing', Fiber Lasers Ii: Technology, Systems, and Applications, 2005, 98-102.

[114] J. A. Alvarez-Chavez, L. D. May, A. Martinez-Rios, I. Torres-Gomez and F. Martinez-Pinon: 'High power Er3+/Yb3+-doped fiber laser suitable for medical applications', Mep 2006: Proceedings of Multiconference on Electronics and Photonics, 2006, 77-79.

[115] J. Parry, R. Ahmed, F. Dear, J. Shephard, M. Schmidt, L. Li and D. Hand: 'A Fiber-Laser Process for Cutting Thick Yttria-Stabilized Zirconia: Application and Modeling', *International Journal of Applied Ceramic Technology*, 2010, no-no.

[116] S. Yoshioka and T. Miyazaki: 'Blackening of Zirconia Ceramics in Groove-Making by Q-Switched YAG Laser ', *Bulletin Of The Japan Society Of Precision Engineering*, 1990, **24**(4), 258-262.

[117] C. M. Choy, Q. F. Li and M. H. Myo: 'Feasibility Study Using Y-TZP Ceramic Stamping Punch Made by Powder Injection Moulding Technology', Singapore Institute of Manufacturing Technology, 2003.

[118] J. Chevalier: 'What future for zirconia as a biomaterial?', *Biomaterials*, 2006, **27**(4), 535-543.

[119] A. R. Studart, F. Filser, P. Kocher and L. J. Gauckler: 'Fatigue of zirconia under cyclic loading in water and its implications for the design of dental bridges', *Dental Materials*, 2007, **23**, 106-114.

[120] P. Pittayachawan: 'Comparative study of physical properties of Zirconia based dental ceramics', PhD thesis, University College London, London, 2008.

[121] J. Eichler, J. Rödel, U. Eisele and M. Hoffman: 'Effect of Grain Size on Mechanical Properties of Submicrometer 3Y-TZP: Fracture Strength and Hydrothermal Degradation', *J. Am. Ceram. Soc.*, 2007, **90**(9), 2830-2836.

[122] D. Munz and T. Fett: 'Ceramics: mechanical properties, failure behaviour, materials selection'; 1999, Berlin, Springer-Verlag.

[123] R. H. Dauskardt, W. Yu and R. O. Ritchie: 'Fatigue Crack Propagation in Transformation-Toughened Zirconia Ceramic', *J. Am. Ceram. Soc.*, 1987, **70**(10), C-248-C-252.

[124] J. Chevalier, C. Olagnon and G. Fantozzi: 'Subcritical Crack Propagation in 3Y-TZP Ceramics: Static and Cyclic Fatigue', *J. Am. Ceram. Soc.*, 1999, **82**(11), 3129-3138.

[125] C. F. Bohren and D. R. Huffmann: 'Absorption and Scattering of Light by Small Particles'; 1998, New York, Wiley.

[126] E. Hecht: 'Optics (4th Edition)'; 2002, Addison Wesley.

[127] A. M. Rao, P. C. Eklund, S. Bandow, A. Thess and R. E. Smalley: 'Evidence for charge transfer in doped carbon nanotube bundles from Raman scattering', *Nature*, 1997, **388**(6639), 257-259.

[128] S. Durant, O. Calvo-Perez, N. Vukadinovic and J.-J. Greffet: 'Light scattering by a random distribution of particles embedded in absorbing media: diagrammatic expansion of the extinction coefficient', *J. Opt. Soc. Am. A*, 2007, **24**(9), 2943-2952.

[129] H. C. v. d. Hulst: 'Light Scattering by Small Particles'; 1981, Dover Publications.

[130] A. T. Young: 'Rayleigh Scattering', *Physics Today*, 1982, **35**(1), 42-48.

[131] S. Heiroth, R. Ghisleni, T. Lippert, J. Michler and A. Wokaun: 'Optical and mechanical properties of amorphous and crystalline yttria-stabilized zirconia thin films prepared by pulsed laser deposition', *Acta Mater.*, 2011, **59**(6), 2330-2340.

[132] A. Dietrich, R. B. Heimann and G. Willmann: 'The colour of medical-grade zirconia (Y-TZP)', *Journal of Materials Science-Materials in Medicine*, 1996, **7**(9), 559-565.

[133] D. L. Wood and K. Nassau: 'Refractive-Index of Cubic Zirconia Stabilized with Yttria', *Appl. Optics*, 1982, **21**(16), 2978-2981.

[134] D. L. Wood, K. Nassau and T. Y. Kometani: 'Refractive-Index of Y2o3 Stabilized Cubic Zirconia - Variation with Composition and Wavelength', *Appl. Optics*, 1990, **29**(16), 2485-2488.

[135] J. I. Eldridge, C. M. Spuckler and R. E. Martin: 'Monitoring delamination progression in thermal barrier coatings by mid-infrared reflectance imaging', *International Journal of Applied Ceramic Technology*, 2006, **3**(2), 94-104.

[136] J. I. Eldridge, C. M. Spuckler, K. W. Street and J. R. Markham: 'Infrared Radiative Properties of Yttria-Stabilized Zirconia Thermal Barrier Coatings', *CERAMIC ENGINEERING AND SCIENCE PROCEEDINGS*, 2002, **23**, 417-430.

[137] J. I. Eldridge, C. M. Spuckler, J. A. Nesbitt and K. W. Street: 'Health Monitoring of Thermal Barrier Coatings by Mid-Infrared Reflectance', in '27th Annual Cocoa Beach Conference on Advanced Ceramics and Composites: A: Ceramic Engineering and Science Proceedings, Volume 24, Issue 3', (ed. H.-T. L. Waltraud M. Kriven), 511-516; 2008.

[138] A. Krell, T. Hutzler and J. Klimke: 'Transmission physics and consequences for materials selection, manufacturing, and applications', *Journal of the European Ceramic Society*, 2009, **29**(2), 207-221.

[139] N. T. McDevitt and W. L. Baun: 'Infrared Absorption Spectroscopy in Zirconia Research', *J. Am. Ceram. Soc.*, 1964, **47**(12), 622-624.

[140] J. E. Alaniz, F. G. Perez-Gutierrez, G. Aguilar and J. E. Garay: 'Optical properties of transparent nanocrystalline yttria stabilized zirconia', *Optical Materials*, 2009, **32**(1), 62-68.

[141] H. N. Yoshimura and H. Goldenstein: 'Light scattering in polycrystalline alumina with bi-dimensionally large surface grains', *Journal of the European Ceramic Society*, 2009, **29**(2), 293-303.

[142] D. H. Woodward: 'Multiple Light Scattering by Spherical Dielectric Particles', *J. Opt. Soc. Am.*, 1964, **54**(11), 1325-1330.

[143] R. Apetz and M. P. B. van Bruggen: 'Transparent alumina: A light-scattering model', *J. Am. Ceram. Soc.*, 2003, **86**(3), 480-486.

[144] J. G. J. Peelen and R. Metselaar: 'Light scattering by pores in polycrystalline materials: Transmission properties of alumina', *J. Appl. Phys.*, 1974, **45**(1), 216-220.

[145] L. A. Dombrovsky, H. K. Tagne, D. Baillis and L. Gremillard: 'Near-infrared radiative properties of porous zirconia ceramics', *Infrared Physics & Technology*, 2007, **51**(1), 44-53.

[146] J. Kim, M. Miyashita, M. Inoue, N. Uchida, K. Saito and K. Uematsu: 'Characterization of internal structure in Y-TZP powder compacts', *J. Mater. Sci.*, 1992, **27**(3), 587-591.

[147] F. F. Lange and M. Metcalf: 'Processing-Related Fracture Origins: II, Agglomerate Motion and Cracklike Internal Surfaces Caused by Differential Sintering', *J. Am. Ceram. Soc.*, 1983, **66**(6), 398-406.

[148] E. Anastassakis, B. Papanicolaou and I. M. Asher: 'Lattice dynamics and light scattering in Hafnia and Zirconia', *Journal of Physics and Chemistry of Solids*, 1975, **36**(7-8), 667-676.

[149] M. Matysiak, J. P. Parry, J. G. Crowder, D. P. Hand, J. D. Shephard, N. Jones, K. Jonas and N. Weston: 'Development of Optical Techniques for Noncontact Inspection of Y–TZP Parts', *International Journal of Applied Ceramic Technology*, 2011, **8**(1), 140-151.

[150] M. Matysiak, J. P. Parry, J. G. Crowder, N. Jones, K. Jonas, N. Weston, D. P. Hand and J. D. Shephard: 'Development of an optical, non-destructive technique for inspection of Zirconia ceramic parts', Lasers and Electro-Optics 2009 and the

European Quantum Electronics Conference. CLEO Europe - EQEC 2009. European Conference on, 14-19 June 2009, 2009, 1-1.

[151] M. Boulouz, L. Martin, A. Boulouz and A. Boyer: 'Effect of the dopant content on the physical properties of Y2O3-ZrO2 and CaO-ZrO2 thin films produced by evaporation and sputtering techniques', *Materials Science and Engineering B*, 1999, **67**(3), 122-131.

[152] J.-Y. Kim, M. Inoue, Z. Kato, N. Uchida, K. Saito and K. Uematsu: 'Direct observation of internal structure in spray-dried yttria-doped zirconia granule', *J. Mater. Sci.*, 1991, **26**(8), 2215-2218.

[153] H. Lin, C.-L. Fan and J.-N. Gui: 'Infrared transmission of sintered 3 mol% Y₂O₃-ZrO₂ gel', *J. Mater. Sci.*, 1996, **31**(9), 2339-2343.

[154] A. Bucholtz: 'Rayleigh-scattering calculations for the terrestrial atmosphere', *Appl. Opt.*, 1995, **34**(15), 2765-2773.

[155] M. Sneep and W. Ubachs: 'Direct measurement of the Rayleigh scattering cross section in various gases', *Journal of Quantitative Spectroscopy and Radiative Transfer*, 2005, **92**(3), 293-310.

[156] B. R. Holstein: 'Blue skies and effective interactions', *American Journal of Physics*, 1999, **67**(5), 422-427.

[157] L. Dombrovsky, J. Randrianalisoa and D. Baillis: 'Modified two-flux approximation for identification of radiative properties of absorbing and scattering media from directional-hemispherical measurements', *J. Opt. Soc. Am. A*, 2006, **23**(1), 91-98.

[158] L. A. Dombrovsky: 'Radiation Heat Transfer in Disperse Systems'; 1996, Begell House.

[159] T. J. Hendricks and J. R. Howell: 'Absorption/Scattering Coefficients and Scattering Phase Functions in Reticulated Porous Ceramics', *Journal of Heat Transfer*, 1996, **118**(1), 79-87.

[160] J. Modersitzki: 'FAIR: Flexible Algorithms for Image Registration'; 2009, Society for Industrial and Applied Mathematics.

[161] R. J. Schalkoff: 'Digital image processing and computer vision'; 1989, John Wiley & Sons.

[162] G. J. Grevera and J. K. Udupa: 'Shape-based interpolation of multidimensional grey-level images', *IEEE Transactions On Medical Imaging*, 1996, **15**(6), 881-892.

[163] A. N. Netravali and B. G. Haskell: 'Digital Pictures: Representation, Compression and Standards (Applications of Communications Theory)'; 1995, Kluwer Academic / Plenum Publishers.

[164] M. Unser, A. Aldroubi and M. Eden: 'Fast B-Spline Transforms for Continuous Image Representation and Interpolation', *IEEE Transactions on Pattern Analysis and Machine Intelligence*, 1991, **13**(3), 277-p285.

[165] www.efg2.com.

[166] S. C. Park, M. K. Park and M. G. Kang: 'Super-resolution image reconstruction: a technical overview', *Signal Processing Magazine, IEEE*, 2003, **20**(3), 21-36.

[167] S. Borman and R. L. Stevenson: 'Super-resolution from image sequences-a review ', Circuits and Systems, Notre Dame, IN , USA, 1998, 374 - 378

[168] Q. Tian and M. N. Huhns: 'Algorithms for subpixel registration', *Computer Vision, Graphics, and Image Processing*, 1986, **35**(2), 220-233.

[169] E. Carmi, S. Liu, N. Alon, A. Fiat and D. Fiat: 'Resolution enhancement in MRI', *Magnetic Resonance Imaging*, 2006, **24**(2), 133-154.

[170] C. L. L. Hendriks and L. J. van Vliet: 'Improving resolution to reduce aliasing in an undersampled image sequence [3965-23]', 2000, SPIE, 214-222.

[171] P. Cheeseman, R. Kanefsky, R. Kraft, J. Stutz and R. Hanson: 'Super-Resolved Surface Reconstruction From Multiple Images', *FUNDAMENTAL THEORIES OF PHYSICS*, 1996, **62**, 293-308.

[172] R. C. Hardie, K. J. Barnard and E. E. Armstrong: 'Joint MAP registration and high-resolution image estimation using a sequence of undersampled images ', *Image Processing, IEEE*, 1997, **6**(12), 1621 - 1633

[173] P. E. Eren, M. I.Sezan and A. M. Tekalp: 'Robust, object-based high-resolution image reconstruction from low-resolution video ', *Image Processing, IEEE*, 1997, **6**(10).

[174] M. Irani and S. Peleg: 'Improving resolution by image registration', *CVGIP: Graphical Models and Image Processing*, 1991, **53**(3), 231-239.

[175] L. Chih-Lung: 'An approach to adaptive infrared image enhancement for long-range surveillance', *Infrared Physics & Technology*, 2011, **54**(2), 84-91.

[176] W. K. Pratt: 'Digital Image Processing', 720; 1991, John Wiley & Sons; .

[177] C. Beck: 'Image edge enhancement', *Optics & Laser Technology*, 1979, **11**(5), 275-278.

[178] J. A. Stark: 'Adaptive image contrast enhancement using generalizations of histogram equalization', *IEEE Transactions on Image Processing*, 2000, **9**(5), 889-896.

[179] A. M. Reza: 'Realization of the Contrast Limited Adaptive Histogram Equalization (CLAHE) for Real-Time Image Enhancement', *Journal of VLSI Signal Processing*, 2004, **38**, 35-44.

[180] B. D. Guenther: 'Modern Optics'; 1990, John Wiley & Sons.

[181] D. l. Huang, D. z. Yao, W. Liu, Y. q. Sun and Y. y. Hua: 'Development of Intelligent Night Vision CCD Monitoring System', *INFRARED TECHNOLOGY*, 2009, **31**, 390-394.

[182] K. Babak, Y. Vicky, Y. Cheng, G. Warren and G. John Peter: 'Infrared thermal imaging: A review of the literature and case report', *Neuroimage*, 2009, **47**, T154-T162.

[183] G. Busse: 'Imaging with Optically Generated Thermal Waves', *Philosophical Transactions of the Royal Society of London Series a-Mathematical Physical and Engineering Sciences*, 1986, **320**(1554), 181-186.

[184] C. Xiao and W. Chenliang: 'Ultrasonic Measurement System with Infrared Communication Technology', *Journal of Computers*, 2011, **6**(11), 2468.

[185] T. Töpfer, K. P. Petrov, Y. Mine, D. Jundt, R. F. Curl and F. K. Tittel: 'Room-temperature mid-infrared laser sensor for trace gas detection', *Appl. Opt.*, 1997, **36**(30), 8042-8049.

[186] G. M. Peavy, L. Reinisch, J. T. Payne and V. Venugopalan: 'Comparison of cortical bone ablations by using infrared laser wavelengths 2.9 to 9.2 μm', *Lasers in Surgery and Medicine*, 1999, **25**(5), 421-434.

[187] A. K. Dubey and V. Yadava: 'Laser beam machining—A review', *International Journal of Machine Tools and Manufacture*, 2008, **48**(6), 609-628.

[188] C. P. Arora: 'Thermodynamics'; 2001, Tata McGraw-Hill Education.

[189] M. A. Heald: 'Where is the "Wien peak"?', *American Journal of Physics*, 2003, **71**(12), 1322-1323.

[190] A. I. Fisenko and S. N. Ivashov: 'Determination of the true temperature of emitted radiation bodies from generalized Wien's displacement law', *Journal of Physics D: Applied Physics*, 1999, **32**(22), 2882.

[191] R. Siegel and J. R. Howell: 'Thermal radiation heat transfer'; 2002, Taylor & Francis.

[192] B. Ferguson and X.-C. Zhang: 'Materials for terahertz science and technology', *Nat Mater*, 2002, **1**(1), 26-33.

[193] A. J. Fitzgerald, V. P. Wallace, M. Jimenez-Linan, L. Bobrow, R. J. Pye, A. D. Purushotham and D. D. Arnone: 'Terahertz Pulsed Imaging of Human Breast Tumors1', *Radiology*, 2006, **239**(2), 533-540.

[194] M. T. McCulloch, E. L. Normand, N. Langford, G. Duxbury and D. A. Newnham: 'Highly sensitive detection of trace gases using the time-resolved frequency downchirp from pulsed quantum-cascade lasers', *J. Opt. Soc. Am. B*, 2003, **20**(8), 1761-1768.

[195] R. E. Fisher, B. Tadic-Galeb and P. R. Joder: 'Optical System Design, Second Edition'; 2008, McGraw-Hill Professional.

[196] D. J. Spencer, G. C. Denault and H. H. Takimoto: 'Atmospheric Gas Absorption at Df Laser Wavelengths', *Appl. Optics*, 1974, **13**(12), 2855-2868.

[197] P. W. Kruse: 'A comparison of the limits to the performance of thermal and photon detector imaging arrays', *Infrared Physics & Technology*, 1995, **36**(5), 869-882.

[198] A. Rogalski: 'Infrared detectors: status and trends', *Progress in Quantum Electronics*, 2003, **27**(2-3), 59-210.

[199] A. Rogalski: 'Assessment of HgCdTe photodiodes and quantum well infrared photoconductors for long wavelength focal plane arrays', *Infrared Physics & Technology*, 1999, **40**(4), 279-294.

[200] A. Rogalski: 'Infrared detectors: an overview', *Infrared Physics & Technology*, 2002, **43**(3-5), 187-210.

[201] A. Rogalski and J. Piotrowski: 'Intrinsic infrared detectors ', *Progress in Quantum Electronics 12*, 1988, 87-289.

[202] P. L. Richards: 'Bolometers for infrared and millimeter waves ', *J. Appl. Phys.*, 1994, **76**(1), 1 - 24

[203] R. A. Wood: 'Chapter 3 Monolithic Silicon Microbolometer Arrays', in 'Semiconductors and Semimetals', (eds. W. K. Paul, et al.), 43-121d; 1997, Elsevier.

[204] R. Ambartzumian, L. Dorozhkin, G. Makarov, A. Puretzky and B. Chayanov: 'Direct measurement of multiphoton molecular absorption of IR laser radiation by pyroelectric detector', *Applied Physics A: Materials Science & Processing*, 1980, **22**(4), 409-413.

[205] M. R. Webb: 'A millimeterwave pyroelectric detector', *International Journal of Infrared and Millimeter Waves*, 1991, **12**(10), 1225-1231.

[206] R. Lenggenhager, H. Baltes, J. Peer and M. Forster: 'Thermoelectric infrared sensors by CMOS technology ', *Electron Device Letters, IEEE* 1992, **13**(9), 454 - 456

[207] N. Sclar: 'Extrinsic silicon detectors for 3–5 and 8–14 μm', *Infrared Physics*, 1976, **16**(4), 435-448.

[208] W. F. Kosonocky: 'Review of Schottky-barrier imager technology', 1, 1990, SPIE, 2-26.

[209] B. F. Levine: 'Quantum-well infrared photodetectors ', *J. Appl. Phys.*, 1993, **74**(8).

[210] H. Schneider and H. C. Liu: 'Quantum well infrared photodetectors : physics and applications / H. Schneider, H.C. Liu. [eBook]'; 2007, Berlin ; New York : Springer, 2007.

[211] W. V. McLevige, G. M. Williams, R. E. DeWames, J. Bajaj, I. S. Gergis, A. H. Vanderwyck and E. R. Blazejewski: 'Variable-area diode data analysis of surface and bulk effects in MWIR HgCdTe/CdTe/sapphire photodetectors', *Semiconductor Science and Technology*, 1993, **8**(6S), 946.

[212] V. Gopal: 'Variable-area diode data analysis of surface and bulk effects in HgCdTe photodetector arrays', *Semiconductor Science and Technology*, 1994, **9**(12), 2267.

[213] A. Ambrozy: 'Electronic noise '; 1982, McGraw-Hill.

[214] S. Kogan: 'Electronic Noise and Fluctuations in Solids'; 1996, Cambridge University Press.

[215] J. Piotrowski and A. Rogalski: 'High-Operating-Temperature Infrared Photodetectors'; 2007, SPIE.

[216] P. R. Griffiths and J. A. D. Haseth: 'Fourier Transform Infrared Spectrometry'; 2007, Wiley-Interscience.

[217] D. J. Gardiner: 'Practical Raman spectroscopy'; 1989, Springer-Verlag.

[218] S. Hillier: 'Accurate quantitative analysis of clay and other minerals in sandstones by XRD: comparison of a Rietveld and a reference intensity ratio (RIR) method and the importance of sample preparation', *Clay Minerals*, 2000, **35**(1), 291-302.

[219] T. H. Ballinger, J. C. S. Wong and J. T. Yates: 'Transmission infrared spectroscopy of high area solid surfaces. A useful method for sample preparation', *Langmuir*, 1992, **8**(6), 1676-1678.

[220] J. Goldstein, D. E. Newbury, D. C. Joy, C. E. Lyman, P. Echlin, E. Lifshin, L. Sawyer and J. R. Michael: 'Scanning electron microscopy and x-ray microanalysis'; 2007, Springer, 2nd edition.

[221] L. Reimer: 'Scanning Electron Microscopy: Physics of Image Formation and Microanalysis '; 1998, Springer.

[222] G. D. Danilatos: 'Foundations of Environmental Scanning Electron Microscopy', in 'Advances in Electronics and Electron Physics', (ed. W. H. Peter), 109-250; 1988, Academic Press.

[223] B. J. Hulm and J. D. Parker: 'Evaluation of the mechanical performance of zirconia bioceramic based on the size of incipient flaw', *J. Mater. Sci.*, 2000, **35**(8), 1845-1855.

[224] A. Vincent and A. Moughil: 'Ultrasonic characterization of zirconia-based thermal barriers', *NDT International*, 1989, **22**(5), 283-291.

[225] K. Kirimoto, K. Nobugai and T. Miyasato: 'Ultrasonic attenuation in yttria-stabilized zirconia', *Physica B: Condensed Matter*, 1999, **263–264**(0), 759-761.

[226] J. Krautkramer: 'Ultrasonic Testing of Materials'; 1990, Springer-Verlag.

[227] T. Shen and P. Hing: 'Ultrasonic through-transmission method of evaluating the modulus of elasticity of Al2O3–ZrO2 composite', *J. Mater. Sci.*, 1997, **32**(24), 6633-6638.

[228] Q. Fan, J. Takatsubo and S. Yamamoto: 'Quantitative characterization of advanced porous ceramics based on a probabilistic theory of ultrasonic wave propagation', *J. Appl. Phys.*, 1999, **86**(7), 4023-4028.

[229] H-D Tietz, L. B. M Dietz and B. May: 'Non-destructive testing of green ceramic materials ', *Journal of Nondestructive Testing & Ultrasonics (Germany)*, 1998 **3**(11), 173.

[230] S. M. Meier, D. M. Nissley, K. D. Sheffler and T. A. Cruse: 'Thermal Barrier Coating Life Prediction Model Development', *Journal of Engineering for Gas Turbines and Power*, 1992, **114**(2), 258-263.

[231] C. G. Levi: 'Emerging materials and processes for thermal barrier systems', *Current Opinion in Solid State & Materials Science*, 2004, **8**(1), 77-91.

[232] B. T. Khuri-Yakub: 'Nondestructive Evaluation of Structural Ceramic Components', 1979 Ultrasonics Symposium, 1979, 1979, 309-320.

[233] D. S. Kupperman and M. Linzer: 'High temperature ultrasonic testing of materials for internal flaws', Patent, USA, 1988.

[234] R. S. Lima, S. E. Kruger and B. R. Marple: 'Towards engineering isotropic behaviour of mechanical properties in thermally sprayed ceramic coatings', *Surface and Coatings Technology*, 2008, **202**(15), 3643-3652.

[235] T. Matsumoto, Y. Nagata, T. Nose and K. Kawashima: 'Laser ultrasonics for measurements of high-temperature elastic properties and internal temperature distribution', *Review of Scientific Instruments*, 2001, **72**(6), 2777-2783.

[236] L. Kehoe, G. Coyle, S. Murray, C. M. Flannery and G. M. Crean: 'Laser ultrasonic surface wave inspection of alumina ceramics of varying density', *Ultrasonics*, 2000, **38**(1-8), 508-512.

[237] K. J. Singh, Y. Matsuda, K. Hattori, H. Nakano and S. Nagai: 'Non-contact sound velocities and attenuation measurements of several ceramics at elevated temperatures', *Ultrasonics*, 2003, **41**(1), 9-14.

[238] D. Andrews and J. Taylor: 'Quality control of thermal barrier coatings using acoustic emission', *Journal of Thermal Spray Technology*, 2000, **9**(2), 181-190.

[239] A. A. Pollock: 'Practical Guide to Acoustic Emission Testing', PhD thesis, Princeton, NJ, 1988.

[240] J. C. Radon and A. A. Pollock: 'Acoustic emissions and energy transfer during crack propagation', *Engineering Fracture Mechanics*, 1972, **4**(2), 295-310.

[241] S. K. Lee, R. Tandon, M. J. Readey and B. R. Lawn: 'Scratch damage in zirconia ceramics', *J. Am. Ceram. Soc.*, 2000, **83**(6), 1428-1432.

[242] J. R. Matthews: 'Acoustic emission'; 1983, Gordon and Breach Science Publishers.

[243] K. Konsztowicz: 'Crack Growth and Acoustic Emission in Ceramics During Thermal Shock', *J. Am. Ceram. Soc.*, 1990, **73**(3), 502-508.

[244] P. K. Panda, T. S. Kannan, J. Dubois, C. Olagnon and G. Fantozzi: 'Thermal shock and thermal fatigue study of alumina', *Journal of the European Ceramic Society*, 2002, **22**(13), 2187-2196.

[245] S. Nishinoiri and et al.: 'In situ monitoring of microfracture during plasma spray coating by laser AE technique', *Science and Technology of Advanced Materials*, 2003, **4**(6), 623.

[246] A. Kucuk, C. C. Berndt, U. Senturk and R. S. Lima: 'Influence of plasma spray parameters on mechanical properties of yttria stabilized zirconia coatings. II: Acoustic emission response', *Materials Science and Engineering: A*, 2000, **284**(1–2), 41-50.

[247] G. A. Gogotsi, A. V. Drozdov and M. Swain: 'Strength, fracture toughness, and acoustic emission of ceramics based on partially stabilized zirconium dioxide', *Strength of Materials*, 1991, **23**(1), 45-51.

[248] F. Mignard, C. Olagnon and G. Fantozzi: 'Acoustic emission monitoring of damage evaluation in ceramics submitted to thermal shock', *Journal of the European Ceramic Society*, 1995, **15**(7), 651-653.

[249] M. Oishi: 'Nondestructive evaluation of materials with the scanning laser acoustic microscope', *Electrical Insulation Magazine, IEEE*, 1991, **7**(3), 25-30.

[250] K. I. Jolic, C. R. Nagarajah and W. Thompson: 'Non-contact, optically based measurement of surface roughness of ceramics', *Measurement Science and Technology*, 1994(6), 671.

[251] A. Jalocha and C. Pieralli: 'A scanning optical profilometer using the SNOM architecture', *Pure and Applied Optics: Journal of the European Optical Society Part A*, 1994, **3**(5), 793.

[252] S. Guo and R. I. Todd: 'Confocal fluorescence microscopy in alumina-based ceramics: Where does the signal come from?', *Journal of the European Ceramic Society*, 2010, **30**(3), 641-648.

[253] C. Rousseau, S. Poland, J. M. Girkin, A. F. Hall and C. J. Whitters: 'Development of fibre-optic confocal microscopy for detection and diagnosis of dental caries', *Caries Research*, 2007, **41**(4), 245-251.

[254] C. Gorecki and et al.: 'Optical profilometer in white light', *Journal of Optics*, 1983, **14**(1), 19.

[255] A. E. Ennos and M. S. Virdee: 'Precision measurement of surface form by laser profilometry', *Wear*, 1986, **109**(1-4), 275-286.

[256] G. A. Carter, A. v. Riessen and R. D. Hart: 'Wear of zirconia-dispersed alumina at ambient temperature, 140 °C and 250 °C', *Journal of the European Ceramic Society*, 2006, **26**(16), 3547-3555.

[257] P. Milleding, A. Wennerberg, S. Alaeddin, S. Karlsson and E. Simon: 'Surface corrosion of dental ceramics in vitro', *Biomaterials*, 1999, **20**(8), 733-746.

[258] E. Serra, A. Tucci, L. Esposito and C. Piconi: 'Volumetric determination of the wear of ceramics for hip joints', *Biomaterials*, 2002, **23**(4), 1131-1137.

[259] G. Bolelli, V. Cannillo, L. Lusvarghi and T. Manfredini: 'Wear behaviour of thermally sprayed ceramic oxide coatings', *Wear*, 2006, **261**(11-12), 1298-1315.

[260] M. Eskner and R. Sandström: 'Measurement of the elastic modulus of a plasma-sprayed thermal barrier coating using spherical indentation', *Surface and Coatings Technology*, 2004, **177-178**, 165-171.

[261] A. A. Kamshilin and et al.: 'Dynamic-speckle profilometer for online measurements of coating thickness', *Journal of Physics: Conference Series*, 2007, **85**(1), 012021.

[262] H. W. Robert: 'Confocal optical microscopy', *Reports on Progress in Physics*, 1996, **59**(3), 427.

[263] R. L. Price and W. G. J. Jerome: 'Basic Confocal Microscopy'; 2011, Springer.

[264] J. Pawley: 'Handbook of Biological Confocal Microscopy'; 2006, Springer.

[265] D. J. Draeger and E. D. Case: 'Characterization of channels in zirconia ceramics using laser scanning confocal microscopy', *Journal of Materials Science Letters*, 2002, **21**(10), 787-791.

[266] D. C. Bursell, *IR Thermography – How It Works*, in *Photonics Online*. 2009.

[267] L. D. Favro, T. Ahmed, D. J. Crowther, H. J. Jin, P.-K. Kuo, R. L. Thomas and X. Wang: 'Infrared thermal-wave studies of coatings and composites', 1 Thermosense XIII, Orlando, FL, USA, 1991, SPIE, 290-294.

[268] G. Newaz and X. Chen: 'Progressive damage assessment in thermal barrier coatings using thermal wave imaging technique', *Surface and Coatings Technology*, 2005, **190**(1), 7-14.

[269] K. Shinoda, H. Murakami, S. Kuroda, K. Takehara and S. Oki: 'In Situ Visualization of Impacting Phenomena of Plasma-Sprayed Zirconia: From Single Splat to Coating Formation', *Journal of Thermal Spray Technology*, 2008, **17**(5), 623-630.

[270] K. Shinoda, H. Murakami, S. Kuroda, S. Oki, K. Takehara and T. G. Etoh: 'High-speed thermal imaging of yttria-stabilized zirconia droplet impinging on substrate in plasma spraying', *Appl. Phys. Lett.*, 2007, **90**(19), 194103-194103.

[271] K. Shinoda, Y. Kojima and T. Yoshida: 'In situ measurement system for deformation and solidification phenomena of yttria-stabilized zirconia droplets impinging on quartz glass substrate under plasma-spraying conditions', *Journal of Thermal Spray Technology*, 2005, **14**(4), 511-517.

[272] H. I. Ringermacher, D. R. Howard and B. Knight: 'Thermal imaging at general electric', *Review of Progress in Quantitative Nondestructive Evaluation, Vols 25A and 25B*, 2006, **820**, 523-528.

[273] R. Osiander and J. W. M. Spicer: 'Time-resolved infrared radiometry with step heating. A review', *Revue Générale de Thermique*, 1998, **37**(8), 680-692.

[274] K. No and J. F. McClelland: 'Thermal-wave imaging of voids in structural ceramics', *J. Appl. Phys.*, 1988, **64**(5), 2801-2803.

[275] B. Franke, Y. H. Sohn, X. Chen, J. R. Price and Z. Mutasim: 'Monitoring damage evolution in thermal barrier coatings with thermal wave imaging', *Surface and Coatings Technology*, 2005, **200**(5-6), 1292-1297.

[276] D Huang, EA Swanson, CP Lin, JS Schuman, WG Stinson, W Chang, MR Hee, T Flotte, K Gregory and CA Puliafito: 'Optical coherence tomography', *Science*, 1991, **254**(5035), 1178-1181.

[277] B. E. Bouma and G. J. Tearney: 'Handbook of Optical Coherence Tomography'; 2002, New York, Marcel Dekker.

[278] D. Stifter: 'Beyond biomedicine: a review of alternative applications and developments for optical coherence tomography', *Applied Physics B-Lasers and Optics*, 2007, **88**(3), 337-357.

[279] A. F. Fercher and et al.: 'Optical coherence tomography - principles and applications', *Reports on Progress in Physics*, 2003, **66**(2), 239.

[280] J. Veilleux, C. Moreau, D. Levesque, M. Dufour and M. I. Boulos: 'Optical Coherence Tomography for Inspection of Highly Scattering Ceramic Media: Glass Powders and Plasma-Sprayed Coatings', 2006, AIP, 1059-1066.

[281] J. Veilleux, C. Moreau, D. Lévesque, M. Dufour and M. Boulos: 'Optical Coherence Tomography for the Inspection of Plasma-Sprayed Ceramic Coatings', *Journal of Thermal Spray Technology*, 2007, **16**(3), 435-443.

[282] C. Sinescu, M. Negrutiu, M. Hughes, A. Bradu, M. Rominu, P. Laissue, G. Dobre and A. Podoleanu: 'Optical Coherence Tomography: Applications in Dentistry', *European Cells and Materials*, 2008, **16**, 10.

[283] C. Sinescu, M. Negrutiu, M. Romînu, C. Haiduc, E. Petrescu, M. Leretter and A. G. Podoleanu: 'En-Face Optical Coherence Tomography Combined with Fluorescence in Material Defects Investigations for Ceramic Fixed Partial Dentures', *World Academy of Science, Engineering and Technology*, 2009, **59**.

[284] C. Sinescu, M. Negrutiu, R. Negru, M. Romînu and A. G. Podoleanu: 'Material Defects Identification in Metal Ceramic Fixed Partial Dentures by En-Face Polarization Sensitive Optical Coherence Tomography', *World Academy of Science, Engineering and Technology*, 2009, **53**.

[285] M. R. Strakowski, J. Plucinski, M. Jedrzejewska-Szczerska, R. Hypszer, M. Maciejewski and B. B. Kosmowski: 'Polarization sensitive optical coherence tomography for technical materials investigation', *Sensors and Actuators A: Physical*, 2008, **142**(1), 104-110.

[286] M. Bashkansky, M. D. Duncan, M. Kahn, D. Lewis Iii and J. Reintjes: 'Subsurface defect detection in ceramics by high-speed high-resolution optical coherent tomography', *Opt. Lett.*, 1997, **22**(1), 61-63.

[287] M. Bashkansky, M. D. Duncan, M. Kahn, J. Reintjes and P. R. Battle: 'Subsurface defect detection in ceramic materials using an optical gated scatter

reflectometer′, Lasers and Electro-Optics, 1996. CLEO '96., Summaries of papers presented at the Conference on, 2-7 June 1996, 1996, 327-328.

[288] M. Duncan, M. Bashkansky and J. Reintjes: 'Subsurface defect detection in materials using optical coherence tomography', *Opt. Express*, 1998, **2**(13), 540-545.

[289] M. Bashkansky, M. D. Duncan and J. F. Reintjes: 'Optical gating techniques for material inspection′, 1 Sensors and Controls for Advanced Manufacturing, Pittsburgh, PA, USA, 1998, SPIE, 98-106.

[290] M. Bashkansky, D. Lewis Iii, V. Pujari, J. Reintjes and H. Y. Yu: 'Subsurface detection and characterization of Hertzian cracks in Si3N4 balls using optical coherence tomography', *NDT & E International*, 2001, **34**(8), 547-555.

[291] C. M. S. K. W. S. J. R. M. J. I. Eldridge: 'Infrared Radiative Properties of Yttria-Stabilized Zirconia Thermal Barrier Coatings', in '26th Annual Conference on Composites, Advanced Ceramics, Materials, and Structures: B: Ceramic Engineering and Science Proceedings, Volume 23, Issue 4', (ed. M. S. Hau-Tay Lin), 417-430; 2008.

3. Catalogue of samples tested

This chapter consists of the detailed analysis of the tested samples and their properties. To establish the imaging capabilities of the developed systems including visible light inspection, Mid-Infrared Transmission Imaging (MIR-TI), Confocal Mid-Infrared Transmission Imaging (CMIR-TI), Camera- and Confocal Mid-Infrared Reflection Imaging thorough analysis was required. At first the optical properties of 3mol% Yttria Stabilised Zirconia Polycrystal (3Y-TZP) were measured and the investigation of the results is presented in this chapter. Furthermore the investigation of Raman characteristics and the phenomena behind how the macro scale (above 1 mm in size) and micro scale (below 1 mm in size) features detected in the bulk of the measured samples was carried out. Finally the images and the description of all the samples used in this work were presented.

3.1. Measurement of the mid-infrared transmittance of 3Y-TZP

Very little data of optical characteristics of 3Y-TZP exists, hence the optical transmittance of the material was measured using Fourier Transform Infrared Spectroscopy (FTIR) described in section 2.9.1. Bruker IFS 66v/S FTIR system was utilised during the measurement (see Figure 3.1.1). The measurements were carried out in the air atmosphere.

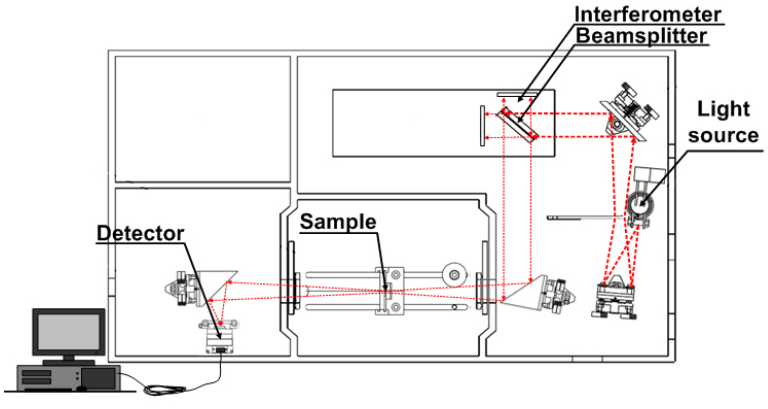

Figure 3.1.1. Schematic of Bruker IFS 66v/S FT-IR beam path.

At first the spectra between 333 nm and 25 μm was measured to acquire the broad optical transmittance spectra of 3Y-TZP ceramics. The measured spectral range was divided into three measurements: a) from 330 and 570 nm; b) from 650 nm to 1.9 μm;

c) from 1.7 to 25 µm. For the first two ranges a tungsten light source and a Gallium Phosphate (GaP) detector were used. For the third wavelength range a glow bar light source and a pyroelectric detector replaced the aforementioned components. The measurement could not be carried out at once for the whole spectral range (from 333 nm to 25 µm) because the available light sources and detectors were unable to operate in full spectral range with optimal optical sensitivity.

A first measurement of 300 µm thick sample is presented in Figure 3.1.2. In visible wavelength range low optical transmittance was observed. However, at mid-infrared wavelengths above 2 µm sharp optical transmittance rise was measured. At approximately 4.25 µm the carbon dioxide (CO_2) absorption was visible [1].

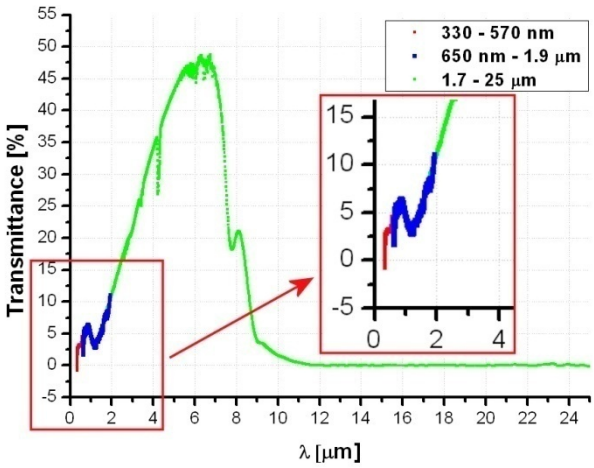

Figure 3.1.2. FTIR measurement of 3Y-TZP optical transmittance between 330 nm and 25 µm.

The mid-infrared optical transmittance window was present due to the material grain size being smaller than the incident wavelength [2-4]. An increased wavelength resulted in a reduced quantity of interactions between the material grains and the longer wavelength photons, therefore the scattering which significantly hampered the transmittance in visible wavelength region was reduced (see section 2.4). 3Y-TZP is non-porous (see section 2.1.1), therefore the main scattering centres were the grains and their interaction with light travelling through the material. The irregular polycrystalline structure of the material scattered the waves, thus the radiation traversing forward was reduced. Apart from forward scattering, there was also light reflection (back-scattering) caused by the changing angles of incidence between scattered photons and the grains [5].

It was observed that light scattering decreased with an increasing wavelength of illumination up to 7 – 8 μm. This conclusion was based on the discussions presented in the literature [6, 7] and the measured optical transmittance. Unfortunately, very little published material exists on the optical properties of 3Y-TZP, thus it was difficult to comment on the influence of the optical absorption in the mid-infrared region. However, it was assumed that the transmission edge at the short wavelength end was dictated by scattering due to the material grains size having comparable size to the wavelength. At the long wavelength end on the other hand the transmission window cut-off was dominated by absorption due to the lattice vibrational and rotational changes of the molecules but further experimental measurements/data is required to definitively determine this.

This reduction of scattering was a typical behaviour for radiation scattered by grains smaller than the wavelength (see section 2.4). The transmission window appeared above 2 μm, therefore it could be deduced that the light scattering in 3Y-TZP ceramics was dependent on the grains and their size which on average measured 500 nm (see Figure 2.4.1).

On the other side of the 3Y-TZP transmission peak, above 7 μm the transmittance drop was associated with the light absorption caused by the lattice vibrational and rotational changes of the molecules (see section 2.4). The low energy of infrared radiation was absorbed and transformed into lattice phonons. These phonons can appear as a rising temperature or as a sound or light emitted from the material [8, 9]. This drop was comparable with the results observed by Dombrovsky [6], Eldridge [10-12] and Wood [13, 14]. Above 10 μm 3Y-TZP showed no transmission. High absorption in the infrared was one of the reasons why the successful attempts of 3Y-TZP machining using CO_2 laser were carried out [7].

The measured optical transmittance of 3Y-TZP was initially carried out on a 300 μm thick sample. However, the components used in the dental industry often measure more than 600 μm in thickness. For that reason the FTIR measurements were repeated with thicker samples. Three samples measuring 300, 600 μm and 1.2 mm in thickness were used for the test (see Figure 3.1.3). Only the transmittance spectra in the mid-infrared was measured (see Figure 3.1.4) for these samples. The transmittance drop was observed with the increasing sample thickness still due to present light scattering. The mid-infrared wavelength was 10 times larger than the actual 3Y-TZP grains measuring

on average 500 nm, therefore the grains light scattering was only minimised because fewer interactions between the photons and the grains occurred.

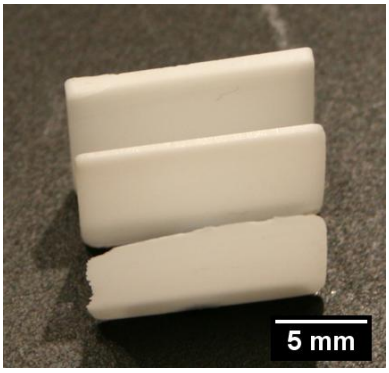

Figure 3.1.3. FTIR measurement of three 3Y-TZP samples: 300, 600 µm and 1.2 mm thick.

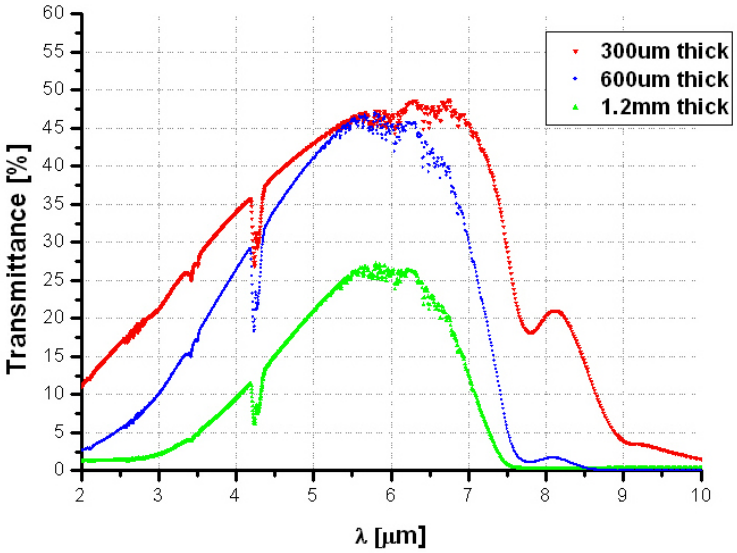

Figure 3.1.4. Mid-infrared optical transmittance of 300, 600 µm and 1.2 mm thick 3Y-TZP samples.

Apart from the decreasing optical transmittance with increasing thickness there was also a peak shift between the tested samples. All three samples were sliced from one 3Y-TZP block, however different optical characteristics were caused by the varying optical surface finish and this was the reason for the peak shift in the graph from Figure 3.1.4. The samples were cut using South Bay Technology model 650 low speed diamond saw, thus a surface was left by the diamond. However, the 300 µm thick specimen had one surface polished (the outer surface of the block) whilst the other surface was that which was left after the diamond saw cut. The remaining two samples measuring 600 µm and 1.2 mm in thickness had both surfaces machined by the diamond saw. These differences in surface finish affected the transmittance due to a change in surface scattering and reflection but this effect was not quantified. The measurements were

deemed suitable for this investigation as they clearly indicate a region of high transmission in the mid-infrared range and low transmission in the visible region.

3.2. Macro scale flaws samples

Due to the extensive number of samples used in the development and assessment of the imaging techniques it was necessary to produce a reference catalogue of the parts used repeatedly. At first the specimens used the macro scale flaws (above 1 mm in size) detection and their main parameters are presented (see Table 3.1).

A number was assigned to each sample and used to refer to it during the measurements. The flaws position in the samples varied between the samples therefore apart from geometrical parameters the position of them in reference to the surface from the camera/detector side was presented. The samples were machined using various laser systems including operating at 1064 nm GSI Lumonics JK705 Nd:YAG millisecond laser system, 1075 nm IPG YLR-1000-SM Ytterbium fibre laser system and 1064 nm Newport Spectra-Physics Inazuma Nd:YVO_4 laser system, however for the purpose of the post-machining inspection the information about the type of laser used to machine the sample was not necessary. The images of all the samples discussed in Table 3.1 are shown in Figure 3.2.1.

Sample 1 was a 3Y-TZP block which shattered in two pieces during laser machining. This sample was taped back together for the measurements. This simulated a critical crack which propagated through the whole thickness of the sample. The crack visible from both sides of the sample is highlighted in the inverted colour images in Figure 3.2.1(a).

Table 3.1. List of sample having macro scale flaws buried in them. The "machined holes position" is the depth of the holes in the bulk material measured from the sample surface positioned towards the camera or detector.

Sample number	Width [mm]	Height [mm]	Thickness [mm]	Machined holes position [mm]
1	60	20	8	N/A
2	18	8	6.9	3.5
3	18	8	2	1.2
9	18	8	6	3.5
10	12	10	7	5

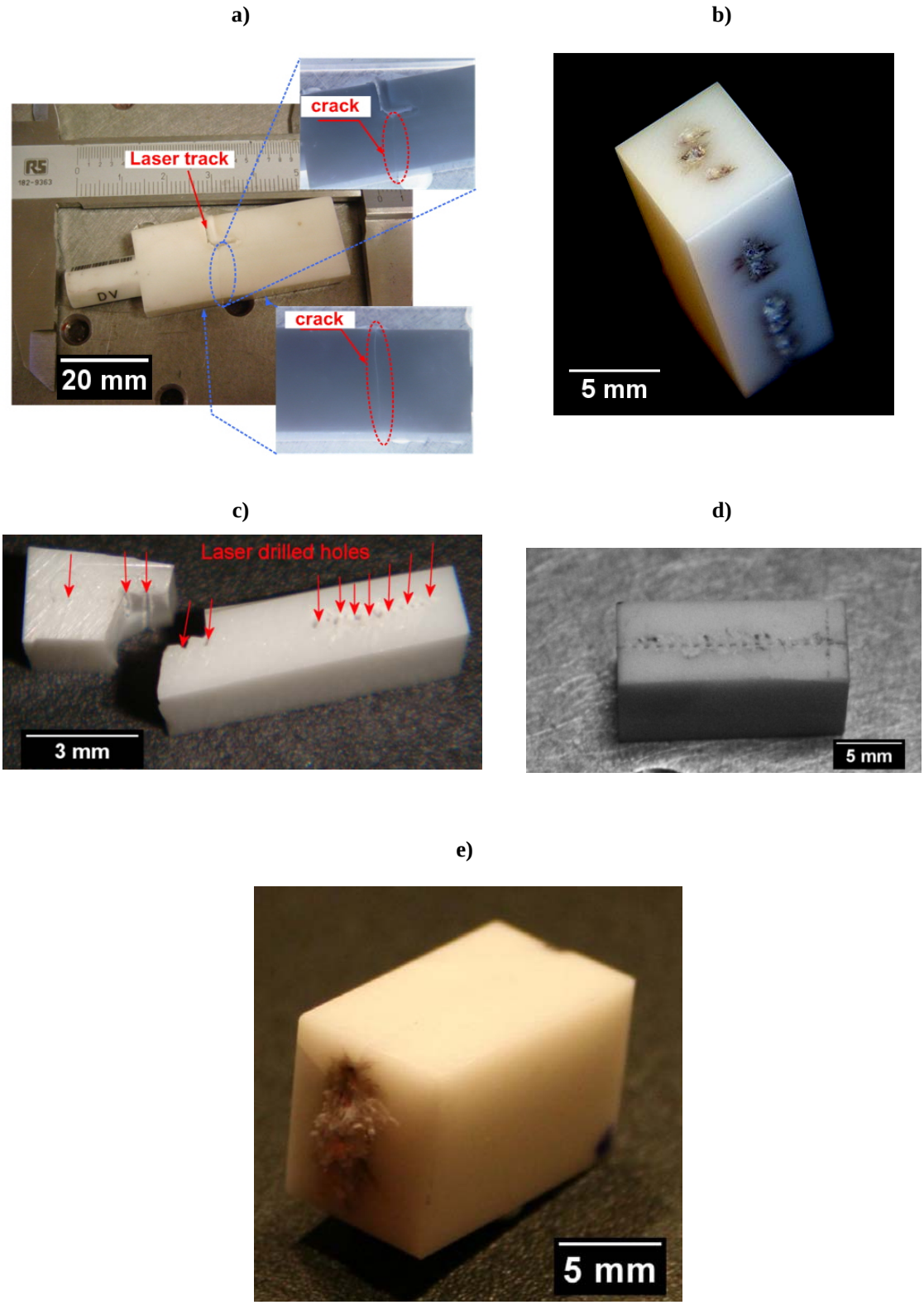

Figure 3.2.1. Macro scale flaws sample: a) 1; b) 2; c) 3; d) 9 and e) 10.

Sample 2 had a similar defect to sample 1 but in addition to the crack some blackening of the material appeared due to the laser machining (see section 2.2.2). The influence of the blackening on the mid-infrared imaging is presented later. Sample 3 on the other hand had multiple laser holes drilled from two sides of the sample. The sample did not

shatter during laser machining, therefore it was used to investigate if there were any cracks buried in the bulk of the sample.

Samples 9 was machined with an IPG YLR-1000-SM Ytterbium fibre laser system operating in pulsed mode. The fibre laser machining was exploited in the past as a quicker way of machining thick 3Y-TZP parts. It employs a controlled crack propagation technique to cut through thick sections of 3Y-TZP material [15]. This process substantially increased the thicknesses of 3Y-TZP components which could be machined in a single process. Multiple drilled holes were machined to initiate a controlled crack propagation (see section 2.2.2) through the sample which would result in sample separation. For this sample however, the laser machining did not break the sample into pieces, therefore it provided an ideal opportunity to inspect the macro holes and potential micro cracks which were introduced.

Samples 10 on the other hand was machined with a GSI Lumonics JK705 Nd:YAG millisecond pulse laser system operating at 1064 nm. The millisecond process was developed to enhance the speed of 3Y-TZP machining compared to traditional mechanical grinding. Although the laser process was considerably faster material cracking was a considerable problem because there was a significant thermal load induced during the millisecond laser pulse [7, 16].

3.2.1. Mechanism of macro scale cracks detection

One of the characteristic effects of laser machining of 3Y-TZP ceramics is blackening and the production of a glossy, or glass-like, finish occurring after re-solidification of the molten material [17]. The influence of surface changes after laser machining on the 3Y-TZP optical transmittance was examined using Fourier Transform Infrared (FTIR) spectroscopy [18] and Raman Scattering Spectroscopy. This experiment was performed to understand how the macro-scale features can be imaged within the volume of 3Y-TZP ceramics during mid-infrared inspection.

The darkening and the glossy finish noticeably influence the visible light transmission because the colour of the material changes from white to black in the visible. The darkening phenomenon of 3Y-TZP is caused by the oxygen vacancies that occur at high temperatures, during laser machining [19]. Oxygen vacancies are the absorption centres due to free electrons which absorb the incident radiation. The oxygen atoms are released after sub-stoichiometric dioxide formation where ZrO_2 becomes ZrO_{2-X} [17,

20]. The glossy finish on the other hand occurs after rapid re-solidification of the molten 3Y-TZP into a glassy layer [21, 22]. These two phenomena influence the optical properties of 3Y-TZP in the visible region; hence it is possible that optical properties of the laser machined region are also affected in mid-infrared.

The blackening of the 3Y-TZP ceramics caused by the oxygen vacancies can be reversed by heating up the sample. For that reason the sample was heated up to 1350ºC which allowed oxygen to diffuse back to the material vacancies rebuilding the crystalline structure and recovering the white colour of 3Y-TZP. The heat treatment ramp was carefully set to minimise any additional cracking during the sample colour recovery. The temperature ramp was set to 5ºC/min. Once the temperature reached 1350ºC it remained at that level for 30 min. Finally the sample was cooled back to room temperature at 5ºC/min. The image of sample 2 after heat treatment is presented in Figure 3.2.2. The sample is clearly whiter near the drilled holes, where previously the dark regions were present (see Figure 3.2.1(b)). The MIR-TI test of the blackened and whitened sample 2 is presented in Figure 3.2.3(b). From that image it was concluded that blackening has little impact on the detection of the drilled holes because no significant difference was observed in the infrared images.

Finally to confirm the presence of the laser drilled holes in sample 2 the specimen was sectioned along the line of the drilled holes using a South Bay Technology model 650 low speed diamond saw. The images of the sectioned pieces are presented in Figure 3.2.4. All the drilled holes detected with the MIR-TI technique were identified in the bulk of the sample. It should be noted that as the sectioning blade was 300 μm thick, some of the drilled holes seen in the MIR-TI images were not seen on sectioning due to part of machined area being removed by the diamond blade. This method of confirmation if all the detected flaws were present inside the samples was used for all the samples.

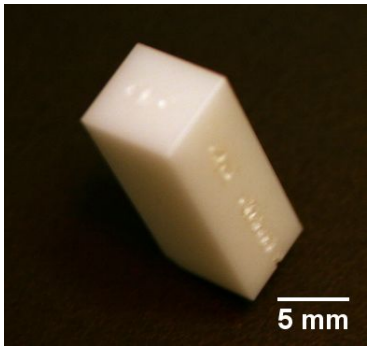

Figure 3.2.2. Sample 2 after heat treatment.

a)

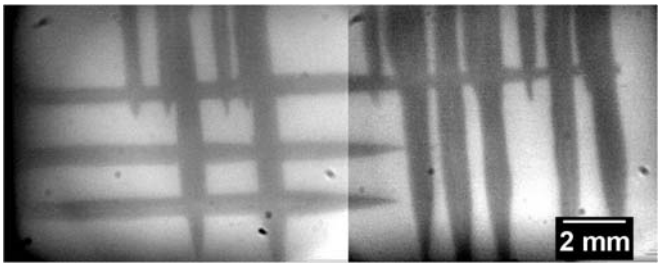

b)

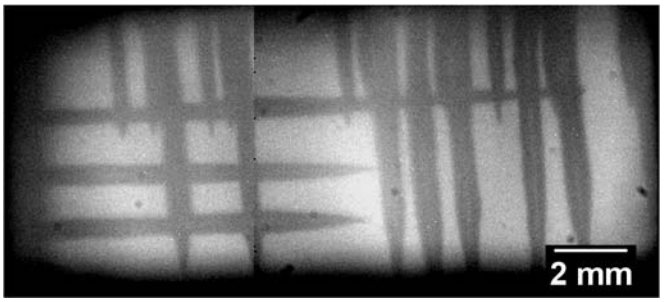

Figure 3.2.3. Sample 2: a) MIR-TI image before and b) MIR-TI image after heat treatment.

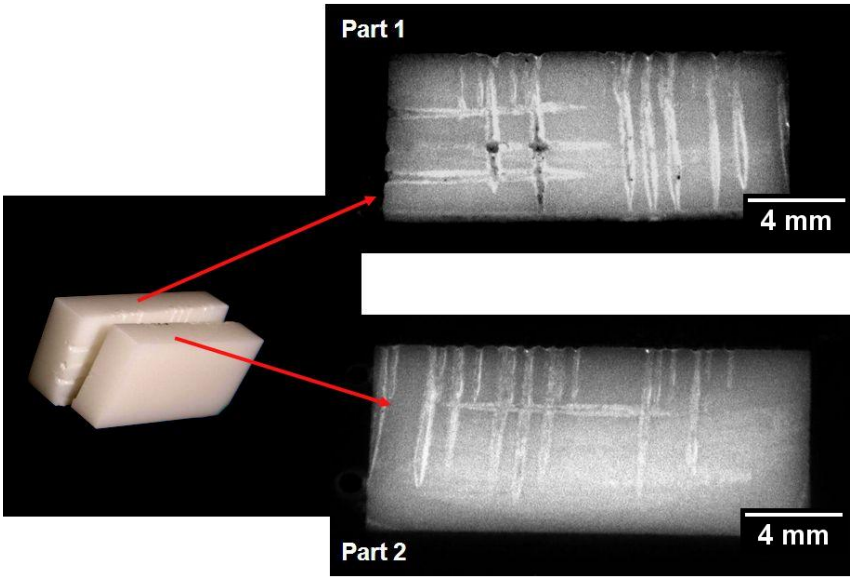

Figure 3.2.4. Sectioned sample 2.

To further investigate the blackening and glossy surface finish caused by laser machining of 3Y-TZP a 600 µm thick sample was marked on one side with a Spectra-Physics Inazuma Q-switched ns laser using 1.064 µm wavelength. The pictures of the 600 µm 3Y-TZP sample before and after laser machining are presented in Figure 3.2.5. A FEI Quanta 3D FEG Scanning Electron Microscope (SEM) was utilized to investigate the surface of the blackened, laser marked and post-laser marked heated sample. Apart from the black surface appearance grooves were left after laser marking, hence this also had to be considered when analysing the results (see Figure 3.2.6).

a) **b)**

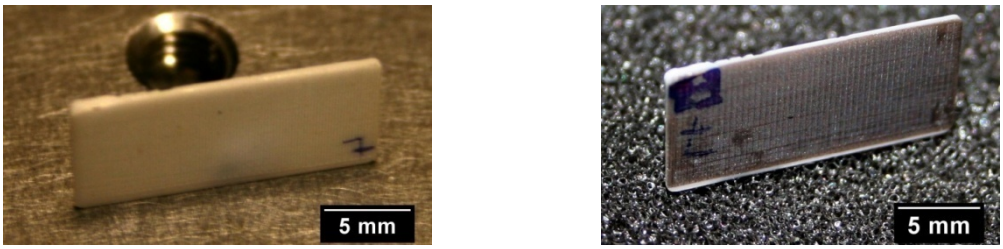

Figure 3.2.5. The images of 600 µm thick 3Y-TZP sample: a) before; b) after laser machining.

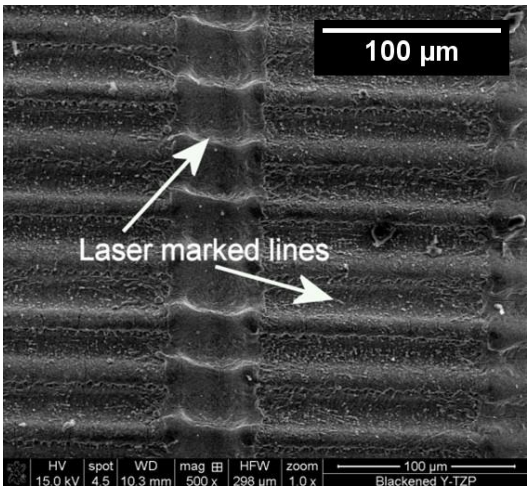

Figure 3.2.6. SEM image of the surface of sample from Figure 3.2.5(b) after laser marking.

The FTIR spectroscopy measurement was utilised to determine the optical transmittance properties of the sample before every step of the test (see Figure 3.2.7). The optical transmittance of the sample was measured through the 600 µm thickness of the sample. A considerable optical transmission drop was observed after the surface of the sample was laser marked but no optical transmittance recovery was detected after the specimen was heated up to recover the white colour of the specimen, hence in graph the transmittance spectra for black (laser marked sample) and white (heat treated sample) overlapped. Therefore, the blackening of the surface due to reduced oxygen atom concentration was not the dominating factor in reducing the optical transmittance in mid-infrared. The primary reason for a significant optical transmission drop was due to the increased surface roughness and the glassy surface appearance which together resulted in increased reflection, refraction and scattering.

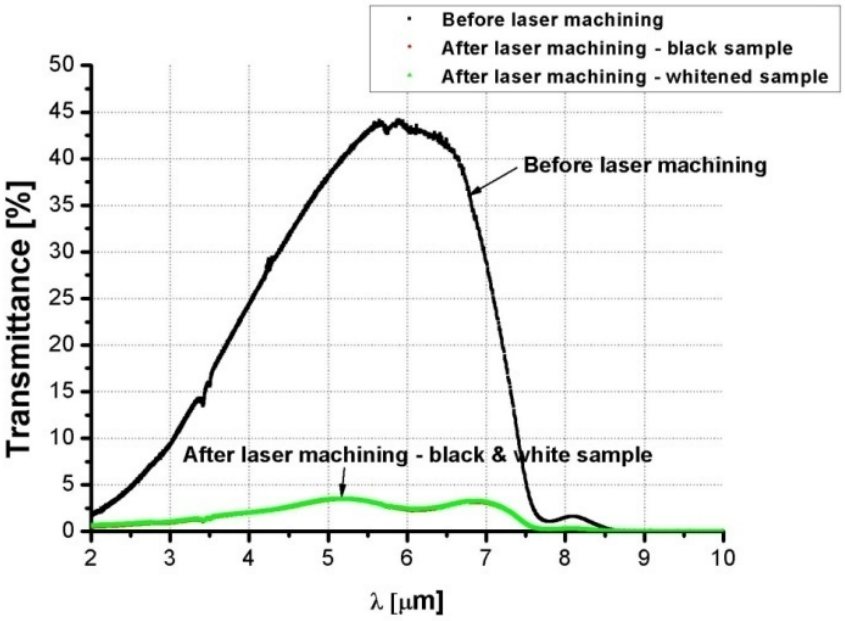

Figure 3.2.7. FTIR measurements of 600 μm thick 3Y-TZP sample: before laser machining, after laser machining and after heat treatment. The optical transmission of black and whitened sample are the same, therefore it cannot be seen in the figure.

The SEM images showed in Figure 3.2.8 presents the sample surface before and after the heat treatment process. The images show an area of one of the laser marked grooves. In Figure 3.2.8(b) the bright spots appeared in the image due to a charging effect, whereas in Figure 3.2.8(a) no charging effect was observed. The charging effect appears when the electron beam is incident on a non-conductive surface. Some of the electrons energy instead of being reflected is absorbed by the surface atoms causing the surface charging. The charged surface starts to deflect the electrons from the gun leading to bright spots and bright regions in the image [23, 24]. The bright spots in Figure 3.2.8(b) indicated that there was an additional layer of oxide on the surface which whitened its appearance, hence this confirmed that the oxygen diffused back onto the material surface.

Laser machining introduced considerable thermal gradients in the sample due to localised heating. This rapid melting and a subsequent cooling of the sample produced a translucent recast layer which consisted of the columnar structures generated parallel to the temperature gradient experienced in the material. This is another phenomenon which appears during laser machining of 3Y-TZP. This columnar structure growth (see Figure 3.2.9) of the material grains appears during the cooling and solidification [16] where the volume of the material shrinks by 3-5%. These columnar layers have also been observed in Alumina and Silicon Nitride ceramics [25, 26].

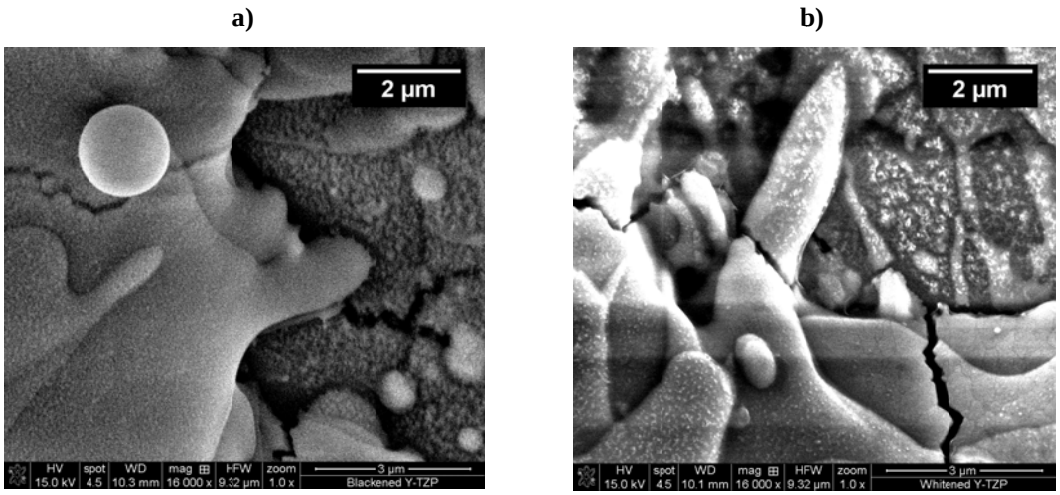

Figure 3.2.8. Sample surface after laser machining (a) and after heat treatment (b).

Apart from columnar structure generation rapid cooling of ceramics produces a glossy, fire polished surface finish of the recast layer. This feature is used during ceramic remelting processes to provide smooth surface finishes and to increase the optical transmittance of highly scattering ceramics [27]. A similar glossy surface was observed with zirconia ceramic coatings where polygonal grains of Zirconia were formed during laser remelting [28]. Due to the remelting of the surface the porosity of the material was decreased and the overall mechanical and thermal stability were enhanced. An example of the glossy appearance of the laser drilled holes is shown in Figure 3.2.10.

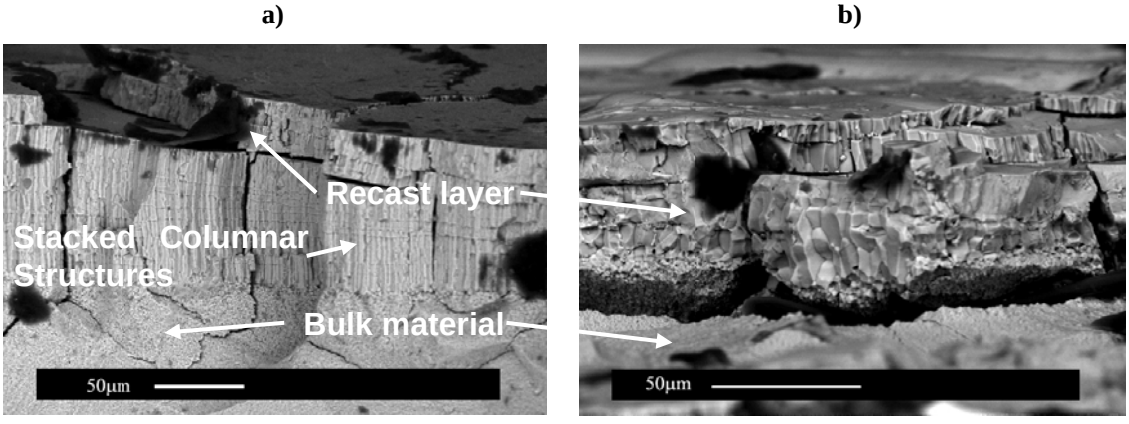

Figure 3.2.9. Re-crystallisation of 3Y-TZP ceramics through the thermal gradient [7].

The columnar structure of the material accompanied by the smooth fire polished surface allowed for the increased specular reflection. The presence of the elongated clusters in the material structure produces a more uniform surface and subsurface interfaces for the light to penetrate and reflect. Thus, the light scattering is reduced and the glossy surface appearance is highlighted. The grain size, grain distribution and the surface roughness

are the main scattering sources in 3Y-TZP and it was reported that the laser remelting process can potentially reduce the grain size, redistribute the grains and reduce the surface roughness [28-31]. Any structural changes to the material, particularly the grain size, grain distribution or the material porosity influence the optical properties. This laser remelting process reduced light scattering and increased optical reflection. For that reason the macro scale features buried in the bulk of 3Y-TZP ceramics could be detected by mid-infrared imaging techniques (see chapter 5 and 6).

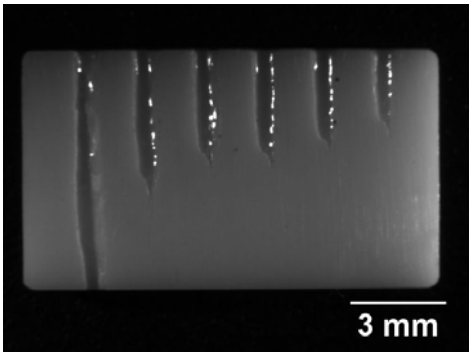

Figure 3.2.10. Glossy appearance of the laser drilled holes.

3.2.2. Raman scattering spectroscopy measurements

To investigate if during laser machining any structural changes appeared in the sample from Figure 3.2.5 a Raman Scattering spectroscopy measurement was employed (see Figure 3.2.11). The Raman spectroscopy technique is described in section 2.9.2. A Renishaw inVia Raman microscope with 514 nm excitation light was used during the tests. The exposure time was set to 10 seconds and the number of accumulations was 25. The laser output power was set to 25 mW during the experiment. The 3Y-TZP material phase was obtained from the Raman measurement. A 3Y-TZP ceramic contains mostly the tetragonal phase, hence little or no monoclinic phase should be observed for a non-machined sample. However, within the area measured using the Raman technique the monoclinic phase was identified even in the sample before laser marking. This was due to the fact that the surface of the sample was polished. The stresses introduced during the polishing process were high enough to transform the material surface into a monoclinic phase.

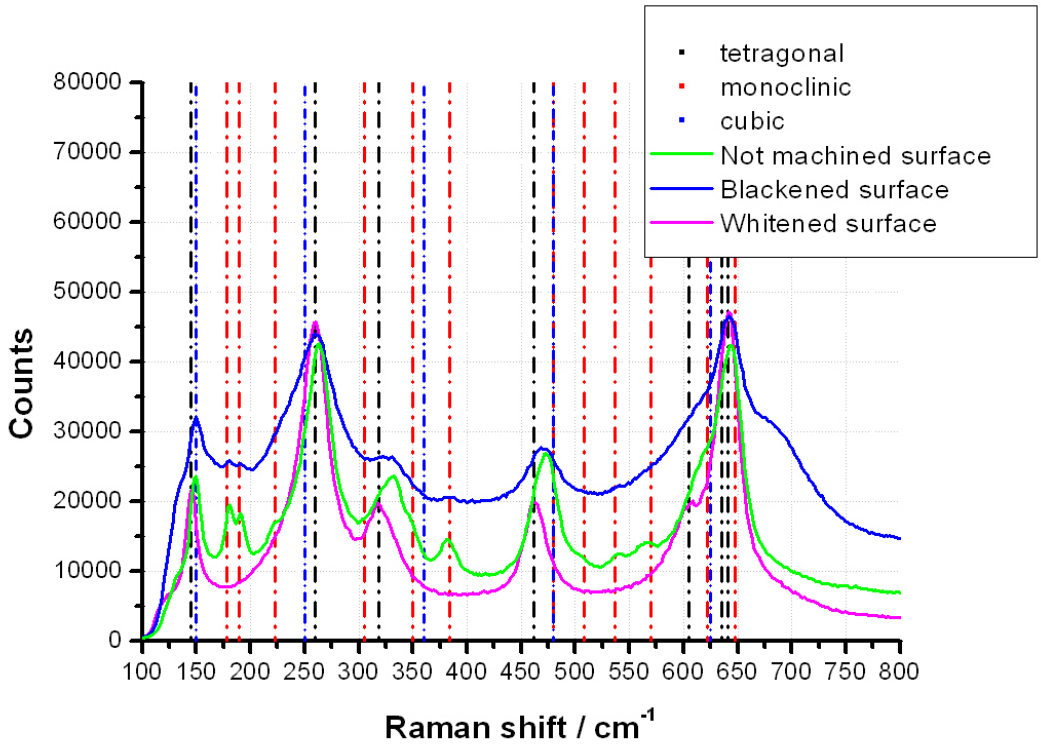

Figure 3.2.11. Raman scattering measurements of the sample before (surface of the sample), after laser machining (blackened) and after heat treatment (whitened).

The laser machined sample surface on the other hand resulted in noticeable broadening of the Raman shift spectrum which was due to an increased disorder of the crystalline structure. Tetragonal phase bands were still observed but the broadening was consistent with a material that has undergone a very rapid heating (due to the laser processing) and then cooling, i.e. rapid melting and re-crystallisation [32]. The monoclinic phase content dropped because the top polished material surface was removed during laser marking. After the sample was heated (the whitened surface) the Raman spectrum returned to a spectrum similar to that before the laser processing but without the monoclinic phase. The heat treatment released the stresses or annealed the material leading to phase equilibrium due to heating up and cooling down.

The whitening of the sample did not change the optical transmittance of the sample (see Figure 3.2.7) as was shown during this experiment. This highlighted the fact that the macro scale features could be detected in 3Y-TZP material due to the variation of the optical properties of the machined surface which was caused by the increased material reflectance and the change in surface roughness.

3.3. Micro scale flaws samples

Another group of tested samples include all the samples which had micro (below 1 mm in size) scale flaws buried in them. All the geometrical parameters of the samples are presented in Table 3.2, whereas samples images are shown in Figure 3.3.1.

Table 3.2. Parameters of the samples with micro scale flaws. The "machined holes position" is the depth of the holes in the bulk material measured from the sample surface positioned towards the camera or detector.

Sample number	Width [mm]	Height [mm]	Thickness [mm]	Machined holes position [mm]
4	13	5.5	2.6	N/A
5	13	5.5	3.76	N/A
6	7	7	3	N/A
7	13	8	2.7	Throughout
8	18	8	2.4/2.7	N/A
12	15	5	3	2

Samples 4 and 5 had laser marked lines on one of the surfaces. The marked lines in sample 4 and 5 measured between 50 μm (± 10 μm) and 150 μm (± 10 μm) in depth and between 80 μm (± 10 μm) and 130 μm (± 10 μm) in width. The parameters of the marked lines were evaluated with the microscope and an example of one of the machined lines measured with the microscope is shown in Figure 3.3.2.

An example of the indented sample was sample 6. The indented samples were using to determine if fine cracks could be detected with MIR-TI technique. The sample was indented using a 20 kg load which was held for 15 seconds. Sample 8 measured 2.7 mm thick (at the thickest section) and 2.4 mm (at the thinnest section). Multiple laser drilled holes were visible in the thinner section of the sample because during laser machining the sample shattered. A series of laser drilled holes were introduced in the sample which resulted in the specimen shattering. The regions in proximity of the drilled holes were not black because the sample was heated up in the furnace after laser machining. Figure 3.3.3 presents the microscope images of the cracks detected during the inspection using the MIR-TI inspection technique.

a)

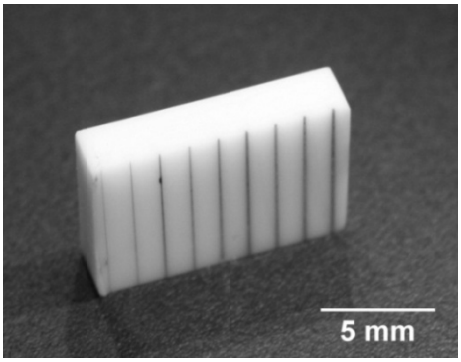

b)

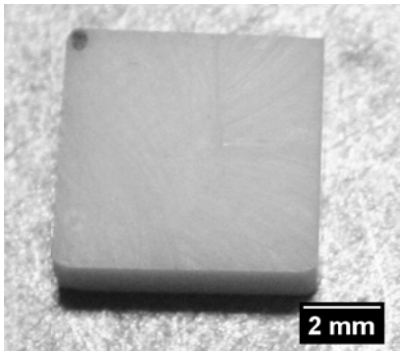

c)

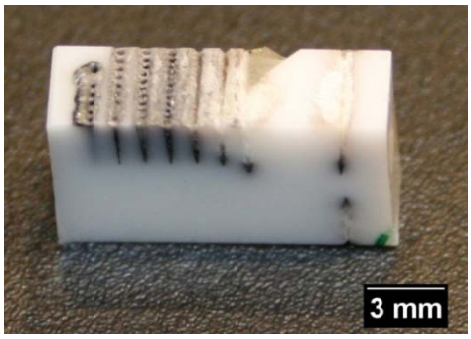

d)

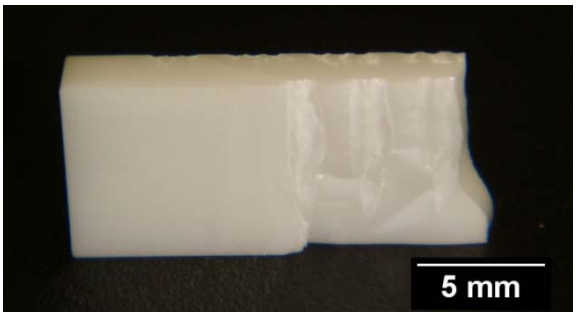

e)

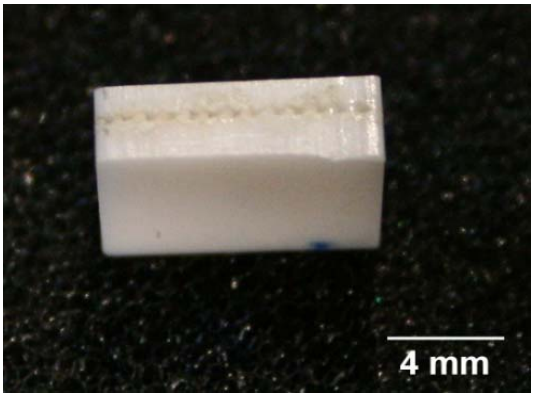

Figure 3.3.1. Micro scale flaws sample: a) 5; b) 6; c) 7; d) 8; e) 12.

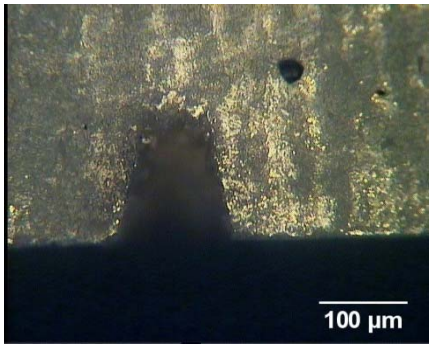

Figure 3.3.2. Laser machined lines measured with optical microscope. The image represents a side view of the specimen.

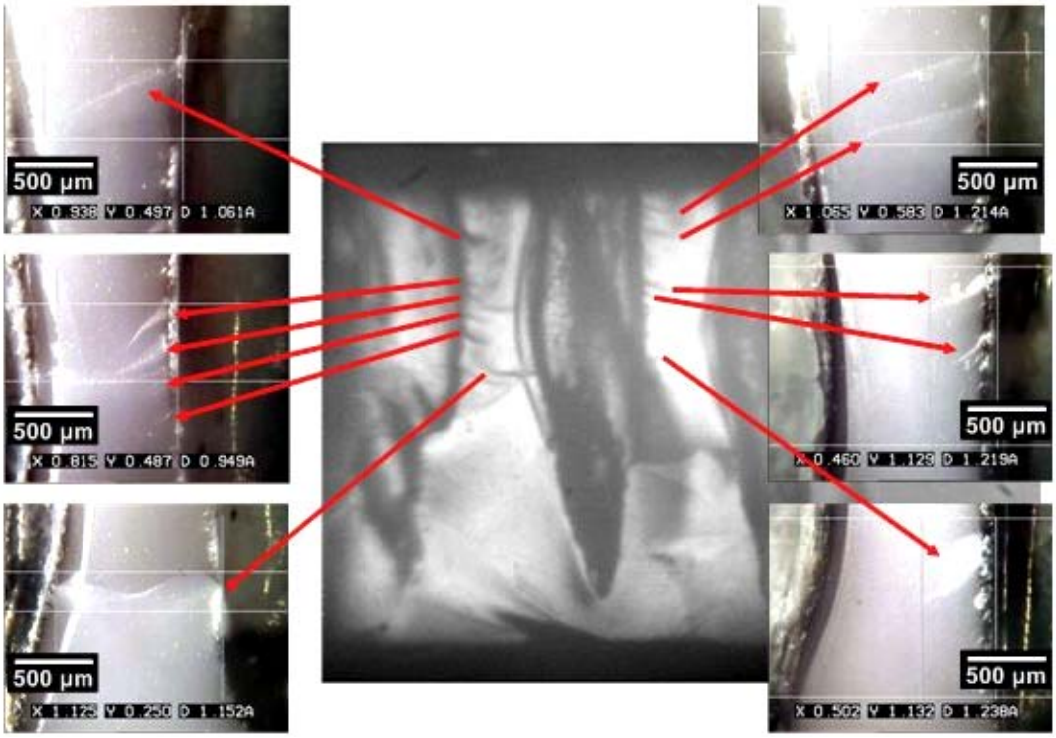

Figure 3.3.3. The microscope images of the crack edges in sample 8.

Sample 7 had multiple laser drilled holes machined from the top of the sample. During the inspection of the sample the laser machined side was placed at the bottom of the sample holder. Sample 12 was machined with the fibre laser and it was used to estimate the micro scale flaws imaging capabilities of MIR-TI and CMIR-TI inspection techniques.

3.3.1. Samples sectioning

As mentioned previously to confirm the presence of the detected flaws each sample was sectioned after it was imaged with mid-infrared imaging system. An example of sample sectioning is presented in this section. All the tested samples were sectioned with a diamond saw. Each sample was cut along the line of laser machined holes. During the cutting process, particularly the fibre laser machined samples shattered along the direction of the drilled holes due to a significant quantity of cracks introduced during laser machining and due to vibrations of the diamond saw (see Figure 3.3.4). As a high number of cracks were detected in the samples, it indicated that the controlled crack propagation process was initiated. However, as the process was not optimised for these samples the stresses generated during laser processing was not sufficient to drive the cracks and cause separation. Additionally, in this instance the hole pitch was not

optimised therefore the cracks did not progress along the laser track. Examples of the optimised process are reported elsewhere [15].

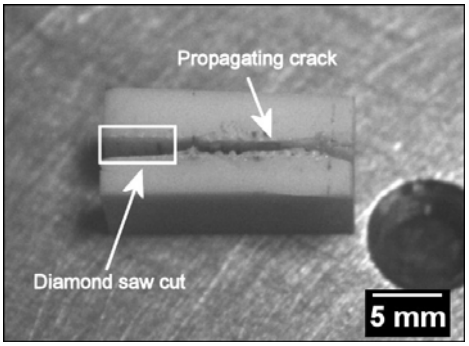

Figure 3.3.4. Sectioning process of sample 9. The shattered and diamond blade saw cut regions are highlighted in the picture.

Figure 3.3.5 presents the SEM images of the macro scale and vertical cracks detected with MIR-TI (see Figure 5.4.4(a)) and CMIR-TI (see Figure 6.3.3(b)) techniques in sample 12. Similar images of the flaws were also detected on the fractured surface of the remaining samples. The images from Figure 3.3.5 do not directly represent the cracks but the regions where the air gap of the cracks was generated causing the sample separation. The cracking in 3Y-TZP is an intergranular and transgranular effect [33] (see Figure 3.3.6), thus the existence and the position of the cracks could be confirmed if the exposed material grains were present in the ESEM images. The shear force driving the cracks led to separation of the grains as shown in Figure 3.3.7(a).

a) **b)**

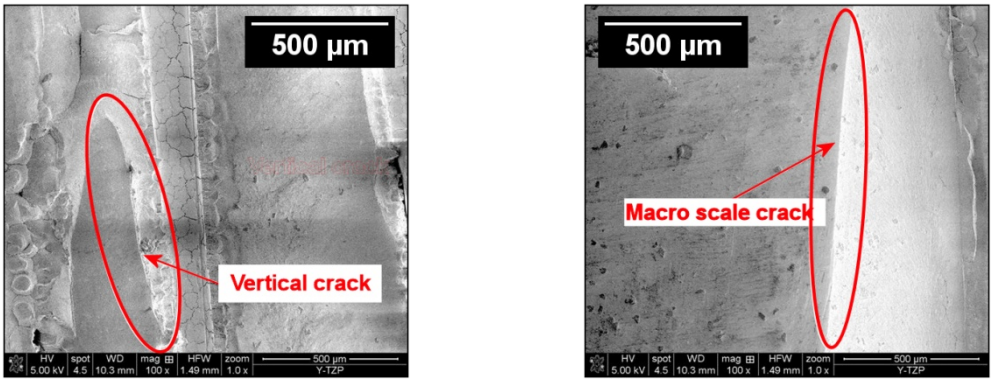

Figure 3.3.5. SEM images of the cracks detected in sample 12. Figure (a) presents one of the vertical cracks and figure (b) shows the edge of the macro scale crack.

The grain area over which the crack propagated had a different appearance compared to the rough 3Y-TZP surface (Figure 3.3.7(b)) or diamond saw cut surface (Figure 3.3.8). The different appearance of the grains in the cracked region, compared to the 3Y-TZP

surface, was due the fact that the cracked region resulted in a fresh fracture surface where grains are separated along the boundaries, whereas the outer surfaces were both cut and polished mechanically smoothing out some of this roughness. Therefore distinguishing the fractured area was relatively simple. The diamond saw cut surface appeared much smoother and no grains could be identified on the surface (see Figure 3.3.8) due to the polishing effect of the cutting blade. The polishing marks of the diamond blade can be seen on the surface in Figure 3.3.8.

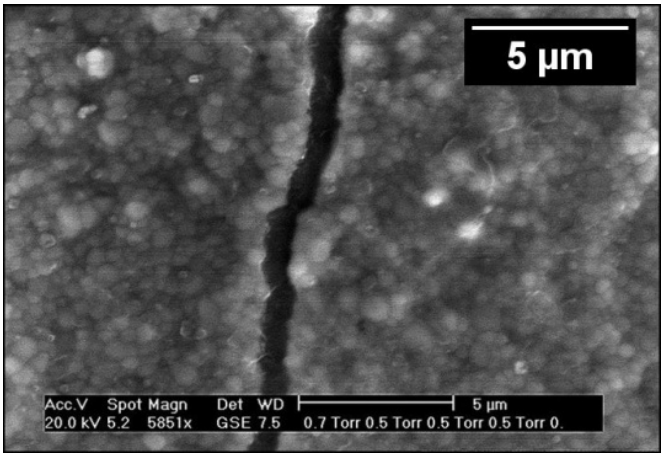

Figure 3.3.6. ESEM image of the crack propagating between the 3Y-TZP grains.

a) **b)**

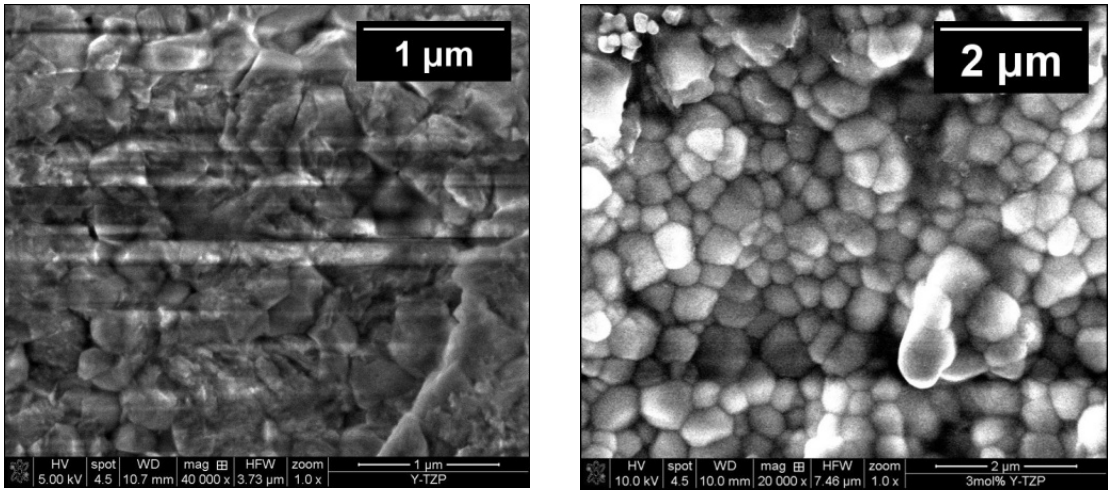

Figure 3.3.7. SEM images of: a) a rough crack area left after the sample separation; b) a rough surface of 3Y-TZP block.

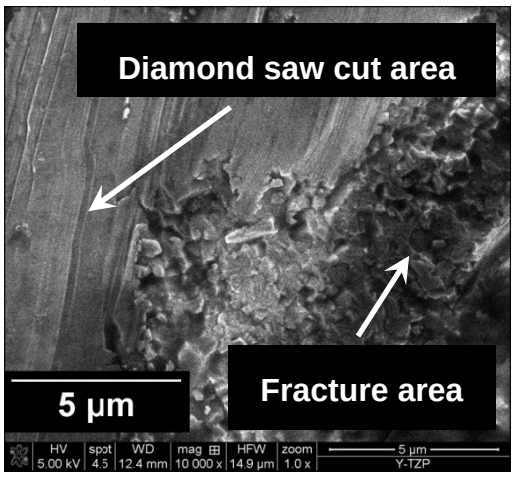

Figure 3.3.8. A SEM image of a diamond saw cut area.

Figure 3.3.9 present sharp edges of the cracks 1 and 2 detected in sample 9 using CMIR-TI technique (see section 6.3.2). The cracks were located approximately 3.5 mm from the front surface of the 7 mm thick sample.

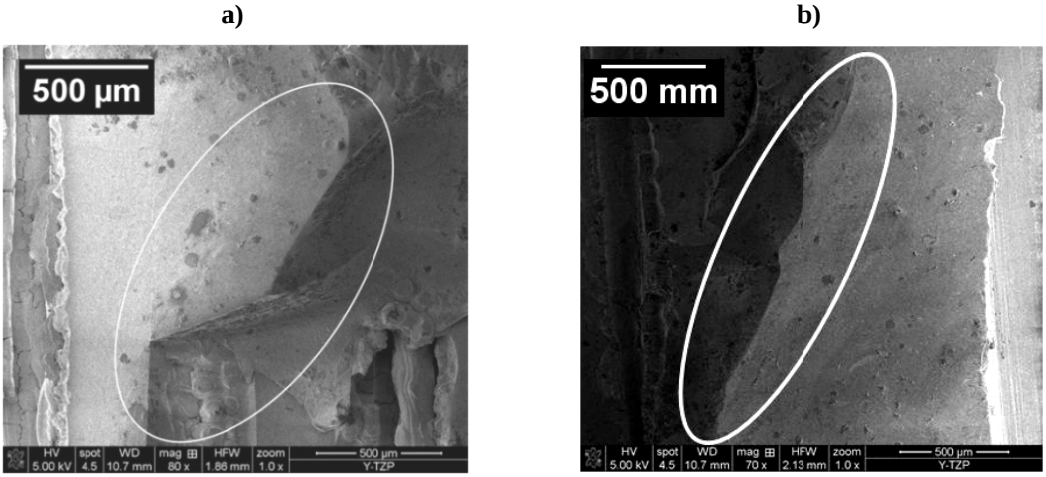

Figure 3.3.9. SEM images of the flaws highlighted in sample 9: a) crack 1; b) crack 2.

All of the tested samples, particularly the fibre laser machined ones were found to have a similar appearance in the fractured area to the one shown in Figure 3.3.7(a). The samples separated along the drilled holes while they were sectioned (apart from the millisecond laser machined samples) as a result of the micro scale cracks generated during laser machining.

Another very interesting sample was sample 7 due to its cracks detected in the bulk using MIR-TI (see Figure 5.4.2) and CMIR-TI (see Figure 6.3.3(a)) imaging. The Environmental Scanning Electron Microscope (ESEM) images in Figure 3.3.10 present the cracks on the back surface of the specimen. Figure 3.3.11(a) on the other hand

shows a magnified image of crack 1. From these images it can be seen that the cracks were long (few hundred microns) and thin (several microns air gap). Figure 3.3.11(b) presents the microscope image of crack 3 which turned out to be several cracks which propagated throughout the thickness of the sample.

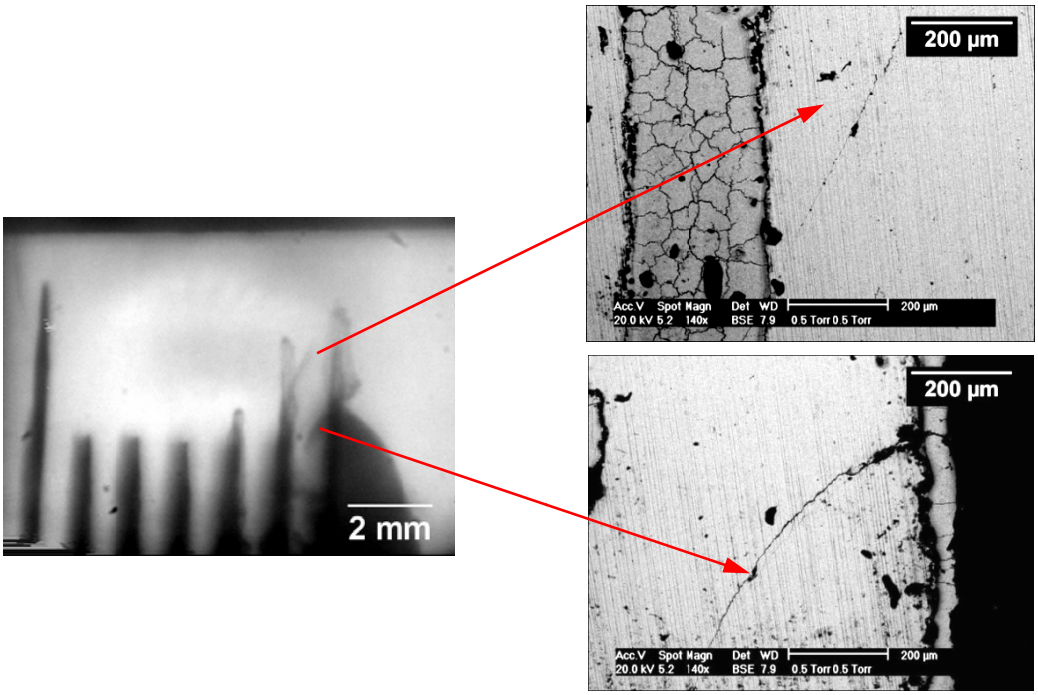

Figure 3.3.10. ESEM images of crack 1 and 4 detected at the back of sample 7 (infrared source side).

a) **b)**

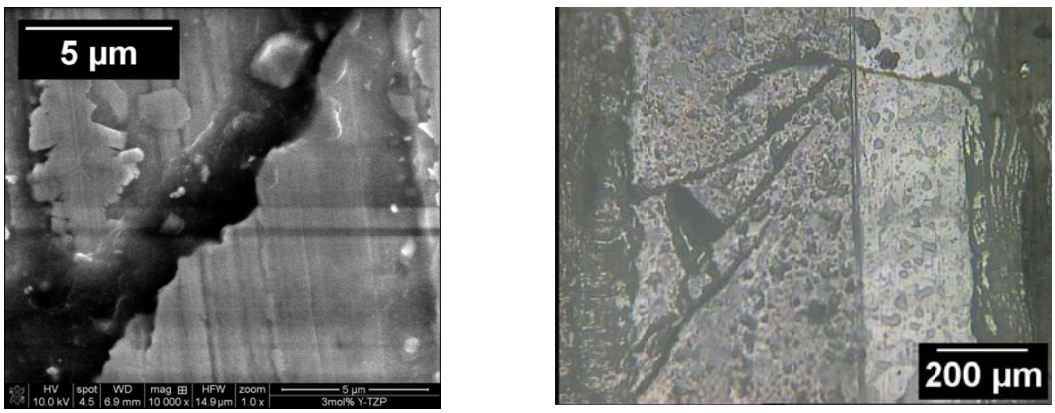

Figure 3.3.11. The magnified ESEM image of crack 1 clearly showing the air gap between the crack interfaces (a); microscope image of the crack 3 which consists of three cracks (b).

Figure 3.3.12 presents the image of the crack 2 that was observed after the sample was cut. The crack air gap appeared to be large due to damage which was caused by the cutting blade. The edges of the material in the proximity of the crack fractured during the sectioning leaving 10 µm wide pit which is shown in Figure 3.3.12(b). However,

the air gap at the bottom of the crater measured 500 nm which was closer to the expected crack size.

a) **b)**

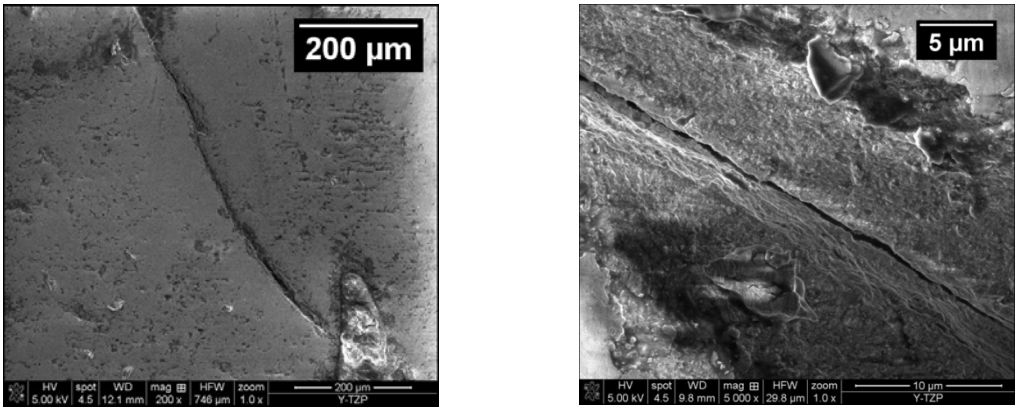

Figure 3.3.12. SEM images of crack 2: a) crack propagating away from the laser drilled hole; b) zoom in on the crack air gap.

Locating crack 2 to cut the sample and measure the crack was challenging due to the size of the flaw compared to the thickness of the diamond saw blade (300 µm). Incorrect positioning of the saw could potentially remove the flaw during cutting. The crack was located between 1.5 and 1.6 mm into the depth of the sample using MIR-TI inspection (see chapter 5). The sample was cut at 1.1 mm depth to include the thickness of the diamond blade measuring 300 µm and the MIR-TI technique depth of field (DOF) parameter error of 50 µm (see section 5.3.4). After the sample was sectioned, the remaining piece was measured with MIR-TI technique to confirm that the flaw was still present and that there were no additional cracks introduced during the cutting. The surface of the sample was then scanned with the SEM apparatus to locate the bulk crack.

After the SEM image of crack 2 was acquired the sample was polished until the crack disappeared to determine to actual crack thickness. After material was removed to a depth of 60 µm the crack could not be identified on the surface indicating the crack depth. The crack was exposed after the cutting due to the positioning error during the sectioning process. As crack 2 was already present on the surface after the sample was cut with a 300 µm thick diamond blade it created a challenge to determine how much of the crack was in the material removed by the blade. The sharp image of the flaw appeared at 1.5 mm from the front surface and the cut was done at 1.1 mm. After the sectioning, the sample was thinner by 130 µm from the anticipated thickness because

the diamond saw blade moved sideways during the cutting. Therefore the detected crack 2 thickness was estimated to be 240 μm which included the measured crack thickness of 60 μm (after polishing), the diamond blade position error of 130 μm and 50 μm MIR-TI technique DOF error.

The above examples highlighted how challenging and time consuming is the 3Y-TZP sectioning and why other alternatives, particularly due to the fact that it is a destructive means of testing should be developed.

3.4. Ceramic coatings samples

Another big group of samples which were measured in this study was ceramic coatings. These samples were tested using Camera- (Camera-MIRI) and Confocal Mid-Infrared Reflection Imaging (Confocal-MIRI) techniques. Outsourcing ceramic coatings with known defects was not feasible consequently, a thin 50 μm thick stainless steel sheet was used as a metallic substrate, with 3Y-TZP ceramic slices (200 ± 20 μm thick sample 13 and 500 ± 50 μm thick sample 14) to simulate a thin ceramic coating (see Figure 3.4.1). One side of the 3Y-TZP slice was polished to minimise the air gap between the steel substrate and the ceramic coating. The stainless steel substrate was laser marked with a Spectra-Physics Inazuma Q-switched ns laser at 1.06 μm wavelength to simulate a defect on the interface between the ceramic coating and the stainless steel substrate.

There were 3 groups of 4 lines machined on the stainless steel sheet. The depth and width of the laser machined marks was measured with an optical microscope (see Figure 3.4.2). The marked lines were machined by scanning the laser beyond the edge of the stainless steel sample so that the depth of each groove could be observed from the side of the metal sheet. The depth of the marks within each group varied due to varying number of scanning passes of the laser. The deepest groove in each group was performed with 10 laser passes, with other grooves machined with 5, 3 and 1 passes. The depth of the grooves ranged between 2 ± 0.2 and 44 ± 4 μm. Figure 3.4.3 presents the width of one of the grooves which varied between 50 ± 5 and 150 ± 15 μm depending on the number of laser line passes. The difference in width of the groove between the measurement from the side and from the top was due to not well defined edge of the machined mark.

a) **b)**

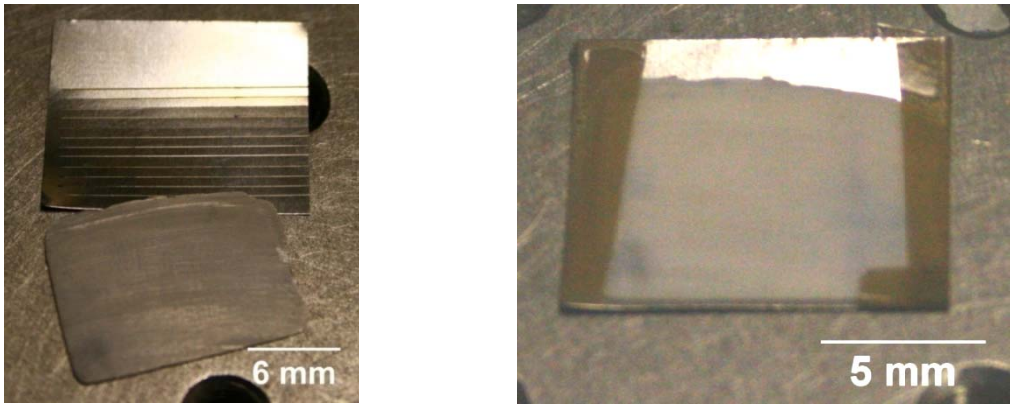

c)

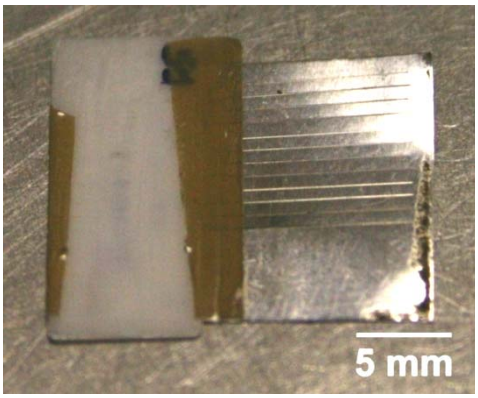

Figure 3.4.1. The investigation of the sub-surface inspection capabilities of the camera-MIRI system: a) laser marked stainless steel substrate and 200 µm thick 3Y-TZP ceramics slice; b) 200 µm thick ceramic slice taped to the stainless steel sheet – sample 13; c) 500 µm thick 3Y-TZP slice taped to the stainless steel sheet – sample 14.

a) **b)**

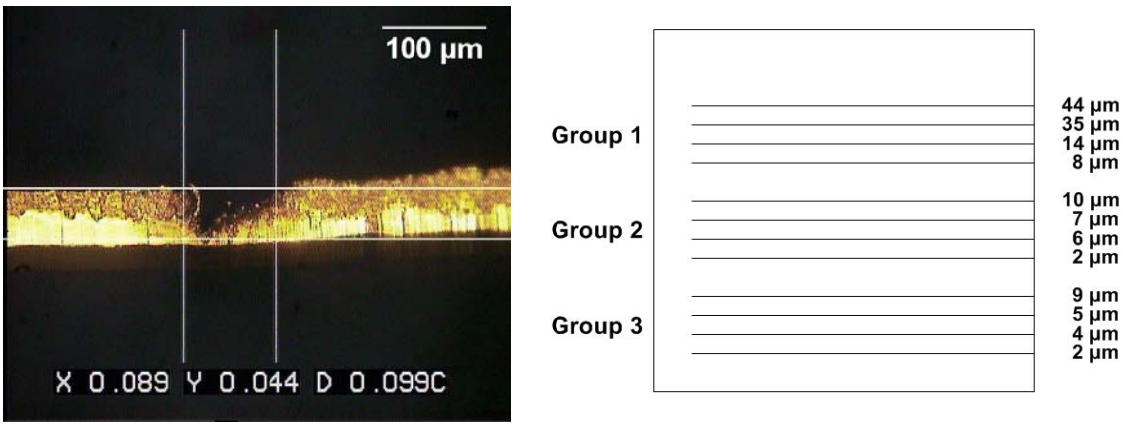

Figure 3.4.2. The measurement of the machined grooves: a) a microscope image of element 1 of group 1 from the side of the metal sheet, b) the depths of all the laser machined grooves on the surface of the metal sheet.

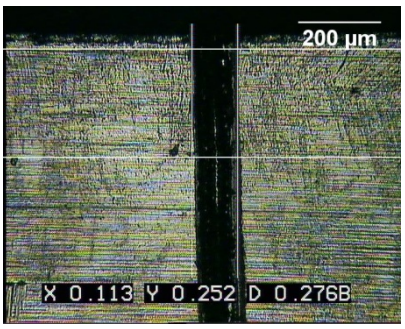

Figure 3.4.3. Microscope image used to measure the width of the marked groove. The width measured from the machined surface side.

Apart from the sample 13 and 14 real TBC samples 15, 16 and 17 presented in Figure 3.4.4 were inspected with reflection techniques. These samples were sectioned pieces of jet engine blades. The nickel superalloy substrate was coated with 150 µm Yttria-stabilized Zirconia (YSZ) coating consisting of 95 mol% of ZrO_2 and 5 mol% of Y_2O_3 using Electron Beam Physical Vapour Deposition (EB-PVD) [34] technique. Before the YSZ coating was deposited a thin 3 to 5 µm thermally grown oxide (TGO) layer of α-alumina was placed on the nickel superalloy to reduce the thermal properties mismatch between the substrate and the ceramic coating. The EB-PVD coatings are more durable compared to the other Air-Plasma Sprayed (APS) [35, 36] coatings but also are more expensive to manufacture due to more sophisticated equipment required. They are used primarily in the most severe applications, such as turbine blades and vanes in aircraft engines due to columnar structure which provides high flexibility which can accommodate high level of stresses due to thermal expansion mismatch between the substrate and the ceramic coating.

Several indentations were introduced from the top and bottom metallic side of samples 15 and 16 to simulate the spallation effect of TBC. The spallation is a cracking effect initiated by the thermal properties mismatch between the ceramic coating, the Thermally Grown Oxide (TGO) and the substrate layers [37, 38]. TGO is a layer that forms between thermal barrier coating and bond coat. It develops considerable stresses because of growth and thermal expansion mismatch, causing the layer to become unstable against part displacements. Therefore the cracking is often instigated on the interface between the TGO and the ceramic coating.

After the coatings were inspected with Camera- and Confocal-MIRI the samples were inspected with SEM to confirm the existence of the detected features. There were some bright spot defects located in the centre of the sample 15 in Figure 3.4.4(a) which could be caused by debris hitting the coating and causing damage. The SEM images of the

damaged coating are presented in Figure 3.4.6. The reason it was deduced that the exposed surface was the TGO (as opposed to the metallic nickel superalloy substrate) was due to a charging effect appearing in the image during the SEM analysis which would not be observed with the exposed metal surface. The electron beam charging appears due to the electron energy being absorbed (instead of being reflected) by a non-conductive material. The charged surface deflected the electrons due to the electrostatic charge and produced bright spots in the image.

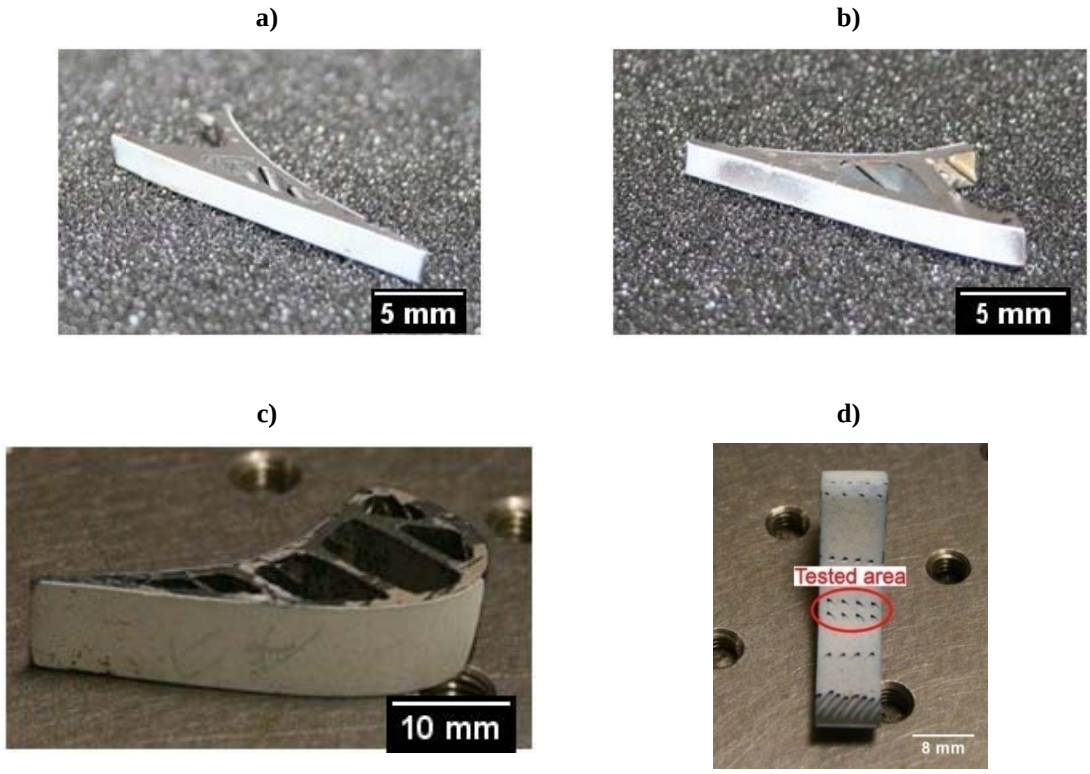

Figure 3.4.4. Jet Engine blade samples of a nickel superalloy substrate with YSZ 150 µm thick coating measured with the Camera-MIRI technique: a) sample 15; b) sample 16; c) sample 17; d) back surface of sample 17.

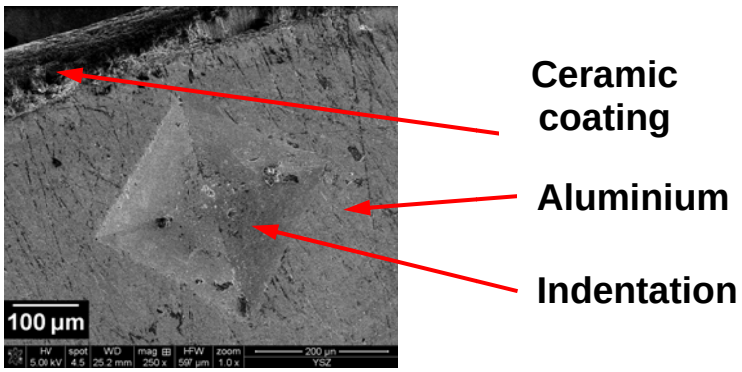

Figure 3.4.5. Indentation in nickel superalloy substrate of jet engine blade with 150 µm YSZ coating to simulate spallation defect.

a) **b)**

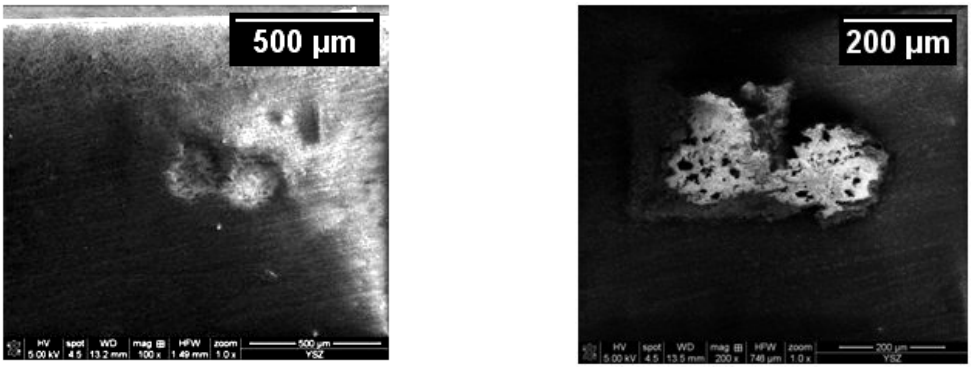

Figure 3.4.6. SEM images of sample 15: a) of the failed coating area; b) charging effect of the expose TGO layer.

The SEM image of one of the indentation defects is presented in Figure 3.4.7 where part of the coating was damaged or spalled off. On closer examination of the defect area using higher magnification the splat-like structure of the coating was observed. When the stress was applied to the coating (by the indenter) cracks propagated between the splats causing the material to shatter into pieces which subsequently peeled or spalled off from the surface resulting in the observed coating damage.

a) **b)**

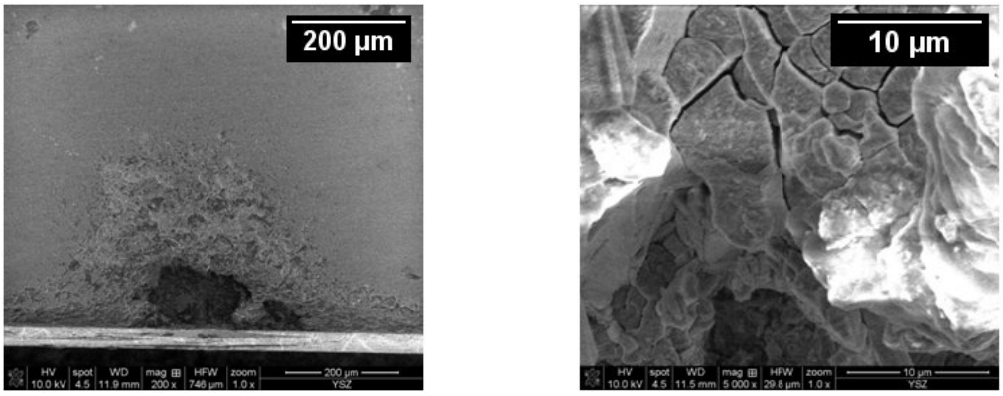

Figure 3.4.7. An SEM image of the failed coating due to the indentation from the side in the metallic substrate of sample 18: a) indentation; b) splat structure of the coating.

Figure 3.4.4(c) presents sample 17 made of the same material as samples 15 and 16 but this sample was aged to investigate the structural changes of the coating. Thermal cycling tests were conducted by a periodical heating up and cooling process which was controlled automatically. The sample was heated in the furnace and the temperature was maintained at 1150˚C. Immediately after being removed from the furnace the specimens were fan-cooled by the laboratory air. The specimens dwelled at the high

temperature for 20 hours and then stayed outside the furnace for 1 hour where they cooled down. The SEM image of the sample roughness is presented in Figure 3.4.8.

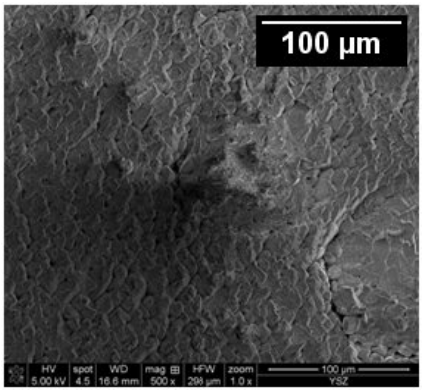

Figure 3.4.8. SEM image of the surface roughness of the sample 17.

In addition to the front side of the YSZ coating of the jet engine blade, thermal barrier coatings are also deposited from the back side where holes are drilled to provide the cooling for the engine components. One of the areas where the TBC performs a crucial role is near these exhaust nozzles. The picture of the nozzle area in sample 17 where the coating was deposited after the holes were drilled is presented in Figure 3.4.4(d). The SEM images of the nozzle area and its surface roughness are presented in Figure 3.4.9.

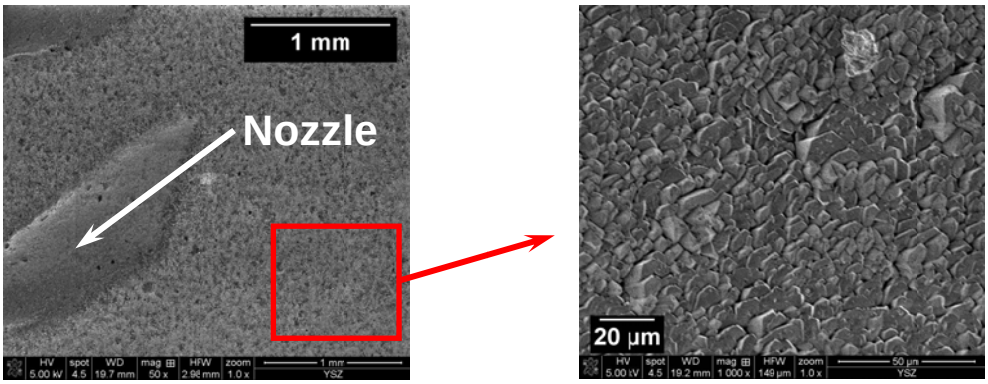

Figure 3.4.9. SEM image of the nozzle area in sample 17.

Another group of the ceramic coating samples tested is presented in Figure 3.4.10. These coatings were sprayed on an aluminium substrate using Air-Plasma Spraying (APS) technique [35, 36]. The coatings were prepared by the Centre of Thermal Spray Research (State University of New York). Three different types of coatings were investigated: Al_2O_3 (sample 18) as wear resistant coating and insulation for electronics applications, 8 mol% of Y_2O_3YSZ (8-YSZ) coating (sample 19) which is used as

thermal barrier coatings and TiO_2 is used for photocatalytic applications (sample 20). The spraying technique used to manufacture the coatings resulted in splat-type, rough surface with the material density between 80 and 90%. The dense YSZ coating density was between 90 and 95%. The exposed metal areas on the samples (see Figure 3.4.10) were present due to the sample clamping tool which held the sample during the coating deposition. On the surface of sample 19 there was no metallic substrate exposed because this sample was cut out from the larger sheet used during the deposition. The SEM images of the surface of the coatings from Figure 3.4.10 are presented in Figure 3.4.11, Figure 3.4.12, and Figure 3.4.13.

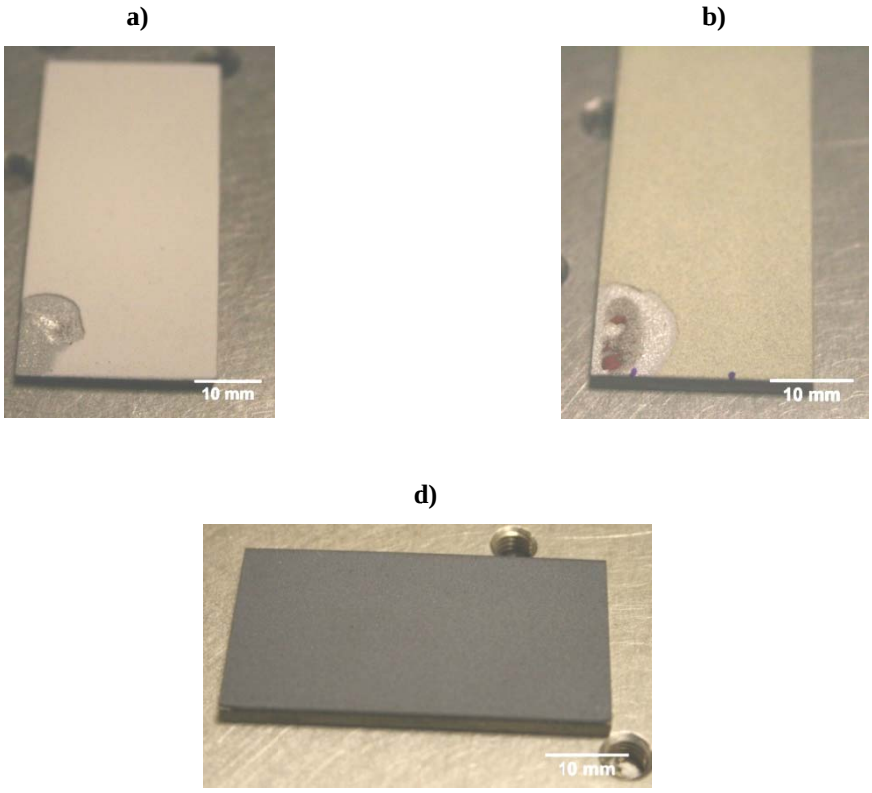

Figure 3.4.10. Ceramic coatings: a) sample 18; b) sample 19; c) sample 20.

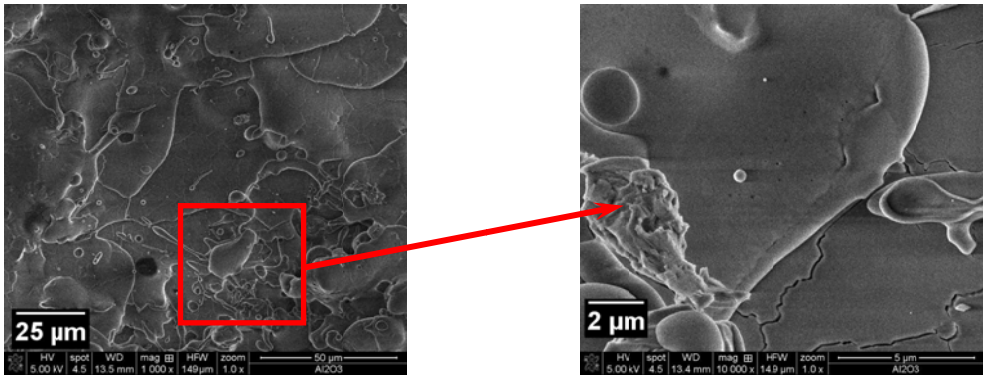

Figure 3.4.11. SEM image of the surface of sample 18 from Figure 3.4.10(a).

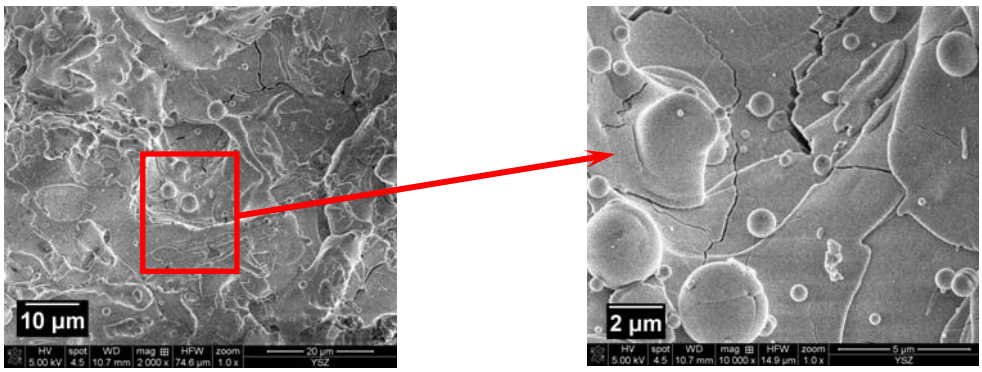

Figure 3.4.12. SEM image of the surface of sample 19 from Figure 3.4.10(b).

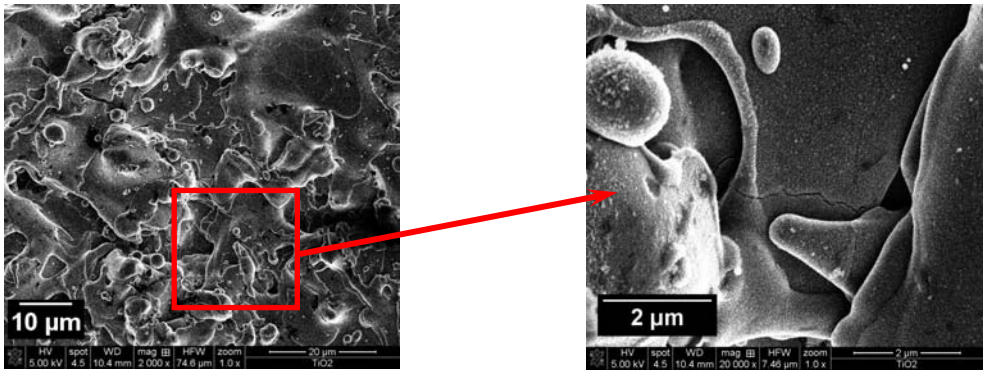

Figure 3.4.13. SEM image of the surface of sample 20 from Figure 3.4.10(c).

A piece of 400 µm thick YSZ free-standing coating similar to the sample 19 from Figure 3.4.10(b) was also investigated with FTIR spectroscopy to measure its optical transmittance (see Figure 3.4.14). This was to compare the results with 3Y-TZP optical transmittance. The measurement resulted in a low optical transmittance which was caused by scattering from the surface roughness and the material structure. The lower material density led to the increased light scattering which reduced the depth of penetration and the optical transmission of the mid-infrared radiation.

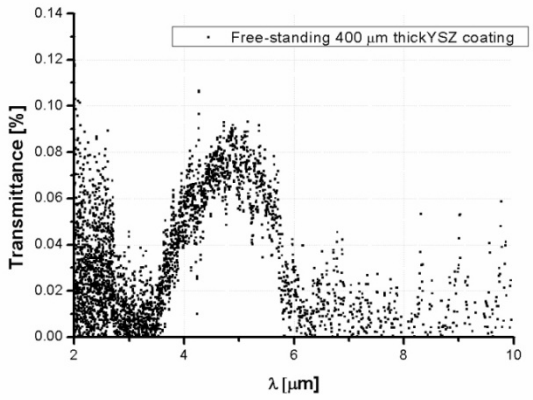

Figure 3.4.14. Measured optical transmittance using FTIR of 400 µm YSZ coating.

3.5. Other tested samples

In this section the remaining samples used during the analysis are presented. At first sample 21 which was a 3Y-TZP dental bridge which cracked (see Figure 3.5.1) during the hard-state grinding. High thermal load introduced during grinding left a rough internal surface which created challenges in inspecting the part as it was difficult to differentiate the surface roughness from any potential defects. Only the section where the crack appeared was investigated. The sample measured typically between 0.6 and 1 mm in thickness.

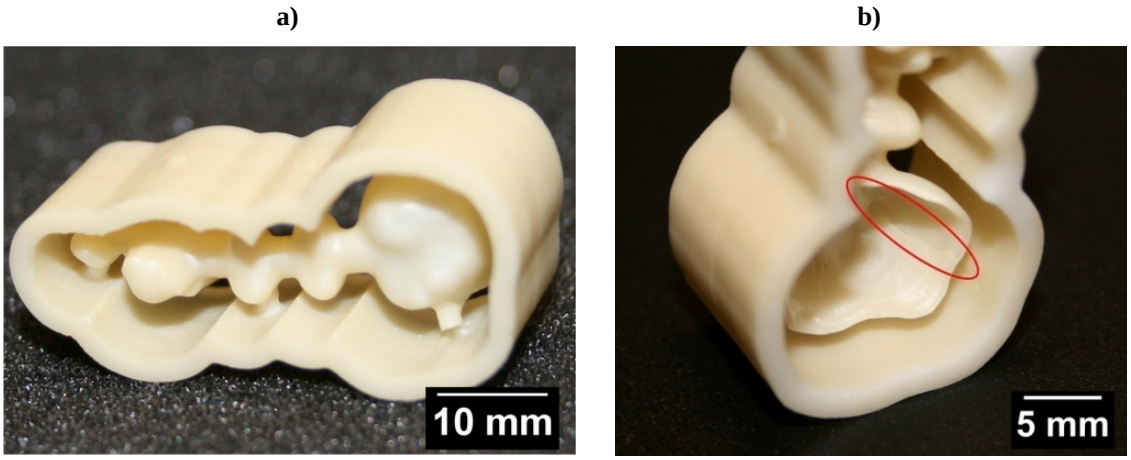

Figure 3.5.1.Dental bridge (sample 21) (a), crack visible in sample 21 (b).

The last group of samples tested were the pre-sintered "brown" stated 3Y-TZP ceramics. The "brown" state grain structure is similar to the "green" state 3Y-TZP ceramics. Both forms are not fully sintered with soft, low density structures (see section 2.1.3). An SEM image of the "brown" state 3Y-TZP is shown in Figure 3.5.2. The material is friable, hence the machining process requires less time and is more cost effective due to significantly reduced tool wear. On the other hand it is more challenging because the material is very brittle and in addition final sintering leads to the reduced volume of the final part thus getting the exact shape required is more difficult. Despite of all the difficulties the soft state ceramic machining is being developed as a viable process route for dental parts manufacturing.

Figure 3.5.2(b) presents 500 µm (sample 22), 1.1 mm (sample 23) and 1.6 mm (sample 24) thick "brown" state specimens. The optical transmittance of the samples was measured using FTIR (see Figure 3.5.3). Due to the lower density of "brown" state material (the exact density of "brown" 3Y-TZP is unknown, however the "green" state 3Y-TZP is 3 g/cm^3) compared to hard state 3Y-TZP the optical transmittance of the pre-

sintered slices was considerably reduced. Lower density implies a higher porosity or a higher number of air gaps between the material grains (see Figure 3.5.2(a)), thus the infrared radiation is more scattered than in the case for the hard state. These air spaces or pores between the grains acted similarly to the crack interfaces where the considerable refractive index change scattered and refracted the light. Therefore, significantly lower optical transmittance in mid-infrared was observed.

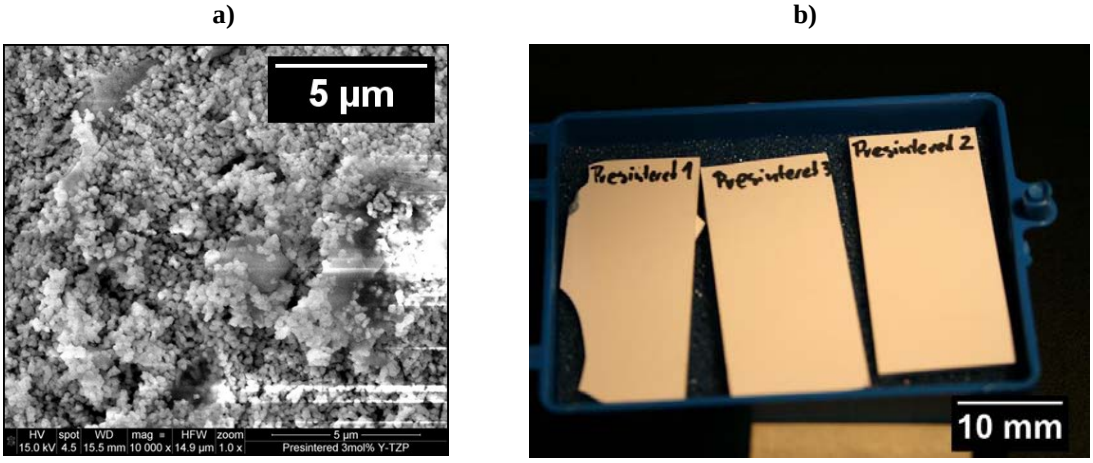

Figure 3.5.2. Pre-sintered "brown" state 3Y-TZP grains (a); three pre-sintered "brown" state 3Y-TZP specimens: sample 22, 23 and 24.

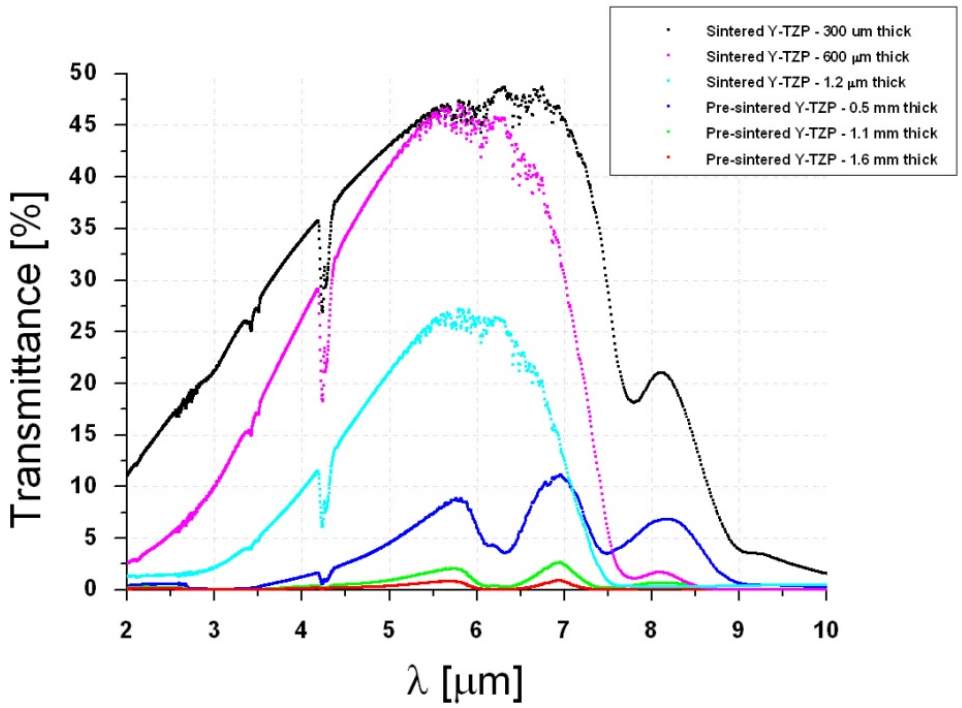

Figure 3.5.3. Optical transmittance of the pre-sintered samples measured with FTIR spectroscopy in comparison with hard state 3Y-TZP ceramics.

References:

[1] D. J. Spencer, G. C. Denault and H. H. Takimoto: 'Atmospheric Gas Absorption at Df Laser Wavelengths', *Appl. Optics*, 1974, **13**(12), 2855-2868.

[2] L. A. Dombrovsky: 'Radiation Heat Transfer in Disperse Systems'; 1996, Begell House.

[3] H. C. v. d. Hulst: 'Light Scattering by Small Particles'; 1981, Dover Publications.

[4] C. F. Bohren and D. R. Huffmann: 'Absorption and Scattering of Light by Small Particles'; 1998, New York, Wiley.

[5] E. Hecht: 'Optics (4th Edition)'; 2002, Addison Wesley.

[6] L. A. Dombrovsky, H. K. Tagne, D. Baillis and L. Gremillard: 'Near-infrared radiative properties of porous zirconia ceramics', *Infrared Physics & Technology*, 2007, **51**(1), 44-53.

[7] F. C. Dear: 'Laser Machining Of Medical Grade Zirconia Ceramic For Dental Reconstruction Applications', PhD thesis, Heriot Watt University, Edinburgh, 2008.

[8] M. A. Stroscio and M. Dutta: 'Phonons in Nanostructures'; 2001, Cambridge University Press.

[9] G. Zhdanov: 'The physics of phonons by J. A. Reissland', *Acta Crystallographica Section A*, 1974, **30**(3), 459-460.

[10] J. I. Eldridge, C. M. Spuckler and J. R. Markham: 'Determination of Scattering and Absorption Coefficients for Plasma-Sprayed Yttria-Stabilized Zirconia Thermal Barrier Coatings at Elevated Temperatures', *J. Am. Ceram. Soc.*, 2009, **92**(10), 2276-2285.

[11] J. I. Eldridge, C. M. Spuckler and R. E. Martin: 'Monitoring delamination progression in thermal barrier coatings by mid-infrared reflectance imaging', *International Journal of Applied Ceramic Technology*, 2006, **3**(2), 94-104.

[12] J. I. Eldridge and C. M. Spuckler: 'Determination of Scattering and Absorption Coefficients for Plasma-Sprayed Yttria-Stabilized Zirconia Thermal Barrier Coatings', *J. Am. Ceram. Soc.*, 2008, **91**(5), 1603-1611.

[13] D. L. Wood and K. Nassau: 'Refractive-Index of Cubic Zirconia Stabilized with Yttria', *Appl. Optics*, 1982, **21**(16), 2978-2981.

[14] D. L. Wood, K. Nassau and T. Y. Kometani: 'Refractive-Index of Y2o3 Stabilized Cubic Zirconia - Variation with Composition and Wavelength', *Appl. Optics*, 1990, **29**(16), 2485-2488.

[15] J. Parry, R. Ahmed, F. Dear, J. Shephard, M. Schmidt, L. Li and D. Hand: 'A Fiber-Laser Process for Cutting Thick Yttria-Stabilized Zirconia: Application and Modeling', *International Journal of Applied Ceramic Technology*, 2010, no-no.

[16] F. C. Dear, J. D. Shephard, X. Wang, J. D. C. Jones and D. P. Hand: 'Pulsed laser micromachining of yttria-stabilized zirconia dental ceramic for manufacturing', *International Journal of Applied Ceramic Technology*, 2008, **5**(2), 188-197.

[17] S. Yoshioka and T. Miyazaki: 'Blackening of Zirconia Ceramics in Groove-Making by Q-Switched Yag Laser', *Bulletin of the Japan Society of Precision Engineering*, 1990, **24**(4), 258-262.

[18] M. Matysiak, J. P. Parry, J. G. Crowder, D. P. Hand, J. D. Shephard, N. Jones, K. Jonas and N. Weston: 'Development of Optical Techniques for Noncontact Inspection of Y–TZP Parts', *International Journal of Applied Ceramic Technology*, 2011, **8**(1), 140-151.

[19] J. E. Alaniz, F. G. Perez-Gutierrez, G. Aguilar and J. E. Garay: 'Optical properties of transparent nanocrystalline yttria stabilized zirconia', *Optical Materials*, 2009, **32**(1), 62-68.

[20] J. Janek and C. Korte: 'Electrochemical blackening of yttria-stabilized zirconia - morphological instability of the moving reaction front', *Solid State Ionics*, 1999, **116**(3-4), 181-195.

[21] K. Ogata, N. Miyanagi, K. Suzuki, and Y. Shimomura: 'Ceramics Cutting with Pulsed Nd:Yag Laser', ICALEO, 1990, 261-270.

[22] C. Batista, A. Portinha, R. M. Ribeiro, V. Teixeira, M. F. Costa and C. R. Oliveira: 'Morphological and microstructural characterization of laser-glazed plasma-sprayed thermal barrier coatings', *Surface & Coatings Technology*, 2006, **200**(9), 2929-2937.

[23] Y. Mizuhara: 'Quantitative measurement of surface potential and amount of charging on insulator surface under electron beam irradiation', *J. Appl. Phys.*, 2002, **92**(10), 6128.

[24] T. Ichinokawa, M. Iiyama, A. Onoguchi and T. Kobayashi: 'Charging Effect of Specimen in Scanning Electron Microscopy', *Japanese Journal of Applied Physics*, 1974, **13**(8), 1272-1277.

[25] C.-H. Tsai and H.-W. Chen: 'Laser cutting of thick ceramic substrates by controlled fracture technique', *Journal of Materials Processing Technology*, 2003, **136**(1-3), 166-173.

[26] C. H. Tsai and H. W. Chen: 'The laser shaping of ceramic by a fracture machining technique', *The International Journal of Advanced Manufacturing Technology*, 2004, **23**(5), 342-349.

[27] F. J. Ester, A. Larrea and R. I. Merino: 'Processing and microstructural study of surface laser remelted Al2O3-YSZ-YAG eutectic plates', *Journal of the European Ceramic Society*, 2010, **In Press, Corrected Proof**.

[28] A. R. B. Shankar, B. J.; Sole, R.; Mudali, U. K.; Khatak, H. S.: 'Laser remelting of plasma sprayed zirconia based ceramic coating for pyrochemical reprocessing applications', *Surface Engineering*, 2007, **23**, 147-154.

[29] A. R. M. Shankar, U. Kamachi: 'Laser surface modification of plasma sprayed yttria stabilised zirconia coatings on type 316L stainless steel', *Surface Engineering*, 2009, **25**, 241-248.

[30] J. Ouyang and X. Li: 'Laser remelting of plasma-sprayed yttria partially stabilized zirconia coatings', *Journal of Materials Engineering and Performance*, 2000, **9**(5), 516-521.

[31] M. F. Morks, C. C. Berndt, Y. Durandet, M. Brandt and J. Wang: 'Microscopic observation of laser glazed yttria-stabilized zirconia coatings', *Applied Surface Science*, 2010, **256**(21), 6213-6218.

[32] L. Fangxin, Y. Jinlong and Z. Tianpeng: 'Raman and Fourier-transform infrared photoacoustic spectra of granular ZrO_{2}', *Phys. Rev. B*, 1997, **55**(14), 8847.

[33] J. Alcalá and M. Anglada: 'High-temperature crack growth in Y-TZP', *Materials Science and Engineering A*, 1997, **232**(1-2), 103-109.

[34] N. P. Padture, M. Gell and E. H. Jordan: 'Thermal Barrier Coatings for Gas-Turbine Engine Applications', *Science*, 2002, **296**(5566), 280-284.

[35] K. Shinoda, Y. Kojima and T. Yoshida: 'In situ measurement system for deformation and solidification phenomena of yttria-stabilized zirconia droplets impinging on quartz glass substrate under plasma-spraying conditions', *Journal of Thermal Spray Technology*, 2005, **14**(4), 511-517.

[36] K. Shinoda, H. Murakami, S. Kuroda, K. Takehara and S. Oki: 'In Situ Visualization of Impacting Phenomena of Plasma-Sprayed Zirconia: From Single Splat to Coating Formation', *Journal of Thermal Spray Technology*, 2008, **17**(5), 623-630.

[37] K. Vaidyanathan, M. Gell and E. Jordan: 'Mechanisms of spallation of electron beam physical vapor deposited thermal barrier coatings with and without platinum aluminide bond coat ridges', *Surface and Coatings Technology*, 2000, **133-134**, 28-34.

[38] M. Gell, J. Eric, V. Krishnakumar, K. McCarron, B. Barber, Y.-H. Sohn and V. K. Tolpygo: 'Bond strength, bond stress and spallation mechanisms of thermal barrier coatings', *Surface and Coatings Technology*, 1999, **120-121**, 53-60.

4. Visible light inspection

4.1. Motivation

Visible light inspection is a very common technique. Optical inspection is used to monitor structural, geometrical and operational quality of parts [1-3]. The measurement is usually carried out non-destructively which leaves the tested component undamaged, and the equipment required for visible light inspection is widely accessible and comparatively low cost, therefore it is a method of choice in many industrial applications [4, 5].

The non-destructive nature is a significant advantage of optical inspection, hence this was the first technique that was considered for the inspection of 3 mol% Yttria-Stabilised Zirconia Polycrystal (3Y-TZP). The low cost of the setup was also advantageous, particularly as the developed technique was aimed at being applied widely applied in the industrial environment.

This chapter presents the results of 3Y-TZP blocks and dental parts with visible light inspection. The challenges of this inspection due to light scattering are discussed and the limitations of visible light inspection are determined.

4.2. Introduction

There are a number of techniques which successfully attempted an inspection of Zirconia-based ceramics (see chapter 2). Unfortunately, the sample thickness is limited to 500 µm, whereas for dental restorations for example minimum of 600 µm is required with many parts being considerably thicker (up to 2 mm). Figure 4.2.1 presents an example of Renishaw 3Y-TZP dental bridge. Clearly the techniques described in chapter 2 are not suitable for measurement of more than 500 µm thick part. For that reason introducing a novel, accurate and non-destructive inspection technique of 3Y-TZP ceramics is highly desirable.

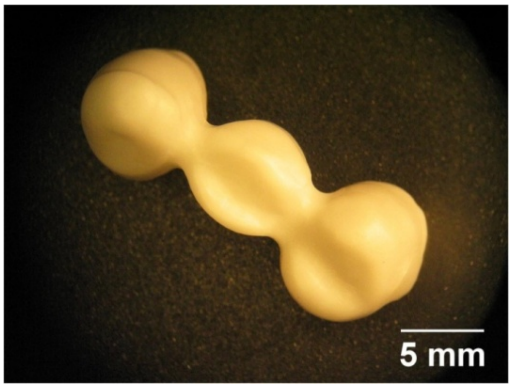

Figure 4.2.1. 3Y-TZP dental bridge machined using a conventional grinding technique provided by the Dental Products Division of Renishaw plc.

4.3. Visible light inspection setup

Despite a very low optical transmittance of 3Y-TZP in the visible wavelength region (see section 3.1), initial attempts to inspect the bulk of 3Y-TZP were carried out using visible light. The motivation of using visible light inspection was the low cost of components which was considerably lower compared to UV, NIR (near-infrared) and MIR (mid-infrared) wavelength regions.

In order to inspect the bulk of the material two approaches were considered:

a) Detecting the light transmitted through the sample. By detecting the changes of the light intensity the operator would be able to determine if any flaws were in the bulk of the inspected part,
b) Detecting the light reflected by the features in the bulk material. By observing the changes in the light reflected back the operator could potentially detect flaws. This technique would require a more powerful light source because the light would travelled through the material twice and the light reflected particularly from the sub-surface flaws would be much weaker compared to the light transmitted through the sample.

The first approach where the changes of the light transmitted through the material was more feasible for 3Y-TZP inspection due to the strong light scattering in visible and the sample thicknesses considered for the measurements.

Figure 4.3.1 presents the first setup developed for visible light inspection. Identifying the optimal visible light source for optical measurements of an opaque 3Y-TZP was a crucial element of the imaging system design. Another factor which was considered, since the inspection system was to be applied in industrial applications was the cost of the components. For that reason an LED was chosen for its low cost, efficiency and

reliability [6]. A red LED (625 nm) was chosen for the visible light inspection. The wavelength of the LED was not crucial because throughout the visible wavelength range the optical transmittance of 3Y-TZP was low (see section 3.1).

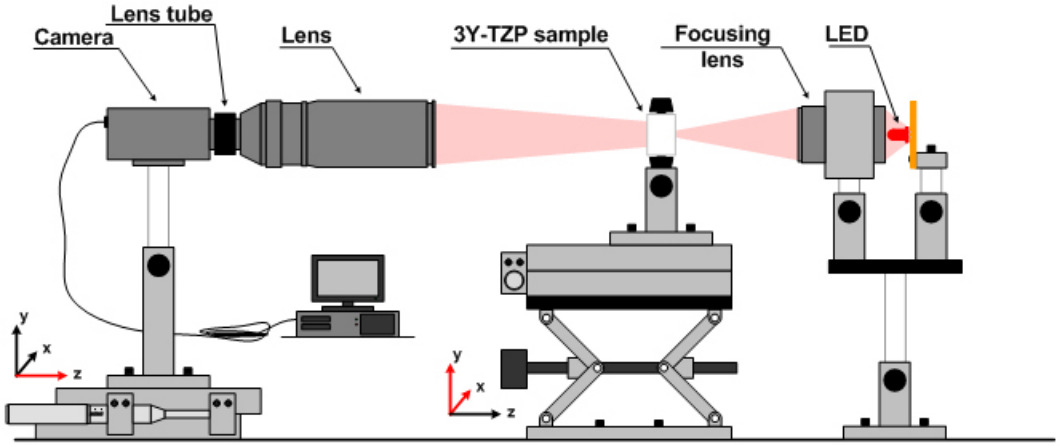

Figure 4.3.1. Visible light inspection setup using Spiricon beam profiling kit.

The initial setup consisted of a Pulnix TM-6CN camera used in combination with Spiricon beam profiling software. The Spiricon software provided light intensity contours of the acquired images, therefore for the initial tests it was easier to detect any changes in the light structure compared to the pictures acquired directly by the camera. Three light structures were investigated to check their feasibility in inspecting 3Y-TZP ceramics. The LED light had a form of a dot or a stripe illuminating part of the sample at any time or the LED illuminated the whole sample at once. The setup used for dot illumination is presented in Figure 4.3.1 and in Figure 4.3.2. The dot measuring between 2 and 3 mm in diameter was achieved by installing a Thorlabs LB1761 bi-convex lens and a Thorlabs LB1951 plano-convex lens as shown in Figure 4.3.3. The sample was placed approximately 25 mm away from the LB1951 lens. For the stripe illumination two Thorlabs lenses were replaced with a Thorlabs LJ1402L2 cylindrical lens with 50 mm focal length, therefore the sample was placed approximately 50 mm away from the lens. For the whole sample illumination, the LED was placed approximately 20 mm away from the sample. The overall length of the whole setup was approximately 900 mm.

During the measurements a Computar No. 250006 zoom lens was mounted on the camera. Depending on the light intensity an absorptive ND filter was mounted in front of the lens to protect the camera from saturation, especially when the inspected sample

was thin. The sample was mounted on three manual stages which allowed for sample movement in three axes.

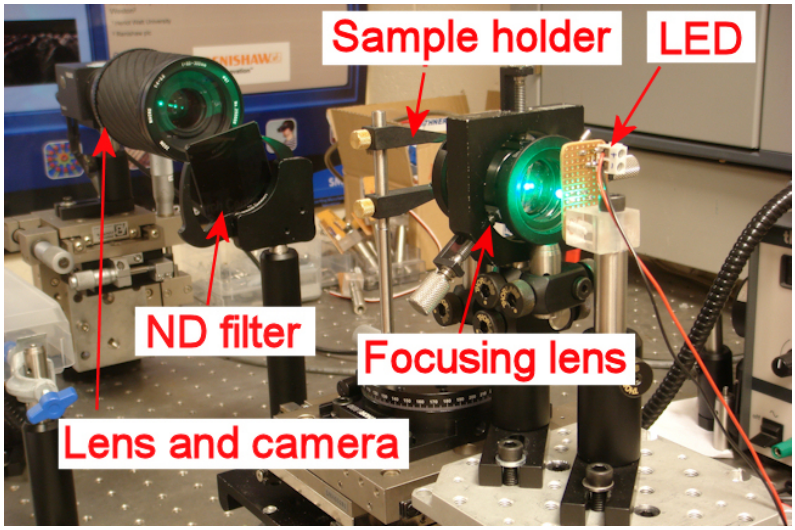

Figure 4.3.2. Real image of Spiricon beam profiling kit used for 3Y-TZP inspection. A green LED was installed in the system temporarily.

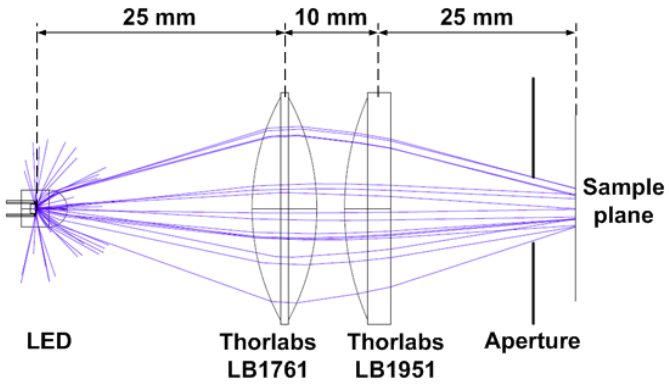

Figure 4.3.3. The lenses arrangement – dot sample illumination.

The initial tests showed no significant relationship between the illuminating light structure being a dot or a line and the quantity of cracks detected. For this reason the experimental section presents results from dot illumination and the whole sample illumination only. The dot illumination was used only occasionally because some of the presented features appeared more clearly. The advantage of whole sample illumination was a rapid measurement without the need to moving the sample.

4.4. 3Y-TZP blocks inspection

Sample 1 (see Figure 3.2.1(a)) was the first specimen tested. For the initial test both pieces of the block were taped back together. In Figure 4.4.1 the direction of sample

movement is shown and in Figure 4.4.2 a sequence of the acquired images is presented. The images presented were acquired while moving the sample stage in the x-axis (see Figure 4.3.1) across the LED dot illumination. A large crack due to an air gap between the shattered pieces was detected and it was highlighted with a white ellipse in the images.

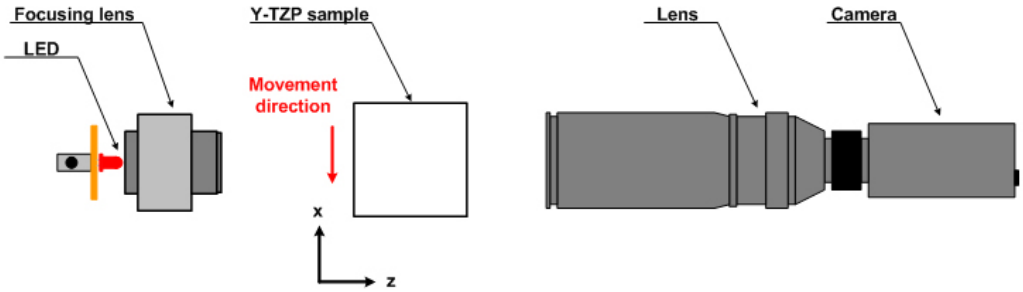

Figure 4.4.1. Sample direction of movement. Top view.

From the sequence of images distortion of the light intensity contour was noticeable. To automate the crack detection process a simple thresholding technique could be used so that below certain level of light intensity warning would be generated to inform about potential defect in the sample. The light incident on the crack was reflected and refracted at the crack-air gap interface due to rapid changes of the refractive index which consequently deviated the optical path of the photons propagating through the material. The schematic of the photons refracted and reflected at the crack interface are shown in Figure 4.4.3. The modified light contour helped to identify the presence of a crack. Even with such a thick sample (8 mm) identifying the presence of cracks was possible due to an air-gap between both taped parts of the sample.

Sample 2 (see Figure 3.2.1(b)) was another specimen tested. This sample did not shatter during laser machining, thus it was a good opportunity to investigate if any features such as laser machined holes or unidentified cracks, could be detected. One image from the visible light scanning is presented in Figure 4.4.4. This sample was fully illuminated at the same time as opposed to scanning the dot across the sample, therefore instead of presenting multiple images from the scanning sequence in x axis (see Figure 4.3.1) only a single image was required to image the sample. Apart from the crack, the sample had also some blackened regions in the proximity of the laser machined area, hence in the visible wavelength region the increased absorption of light was present. Again due to light scattering no micro scale cracks were detected.

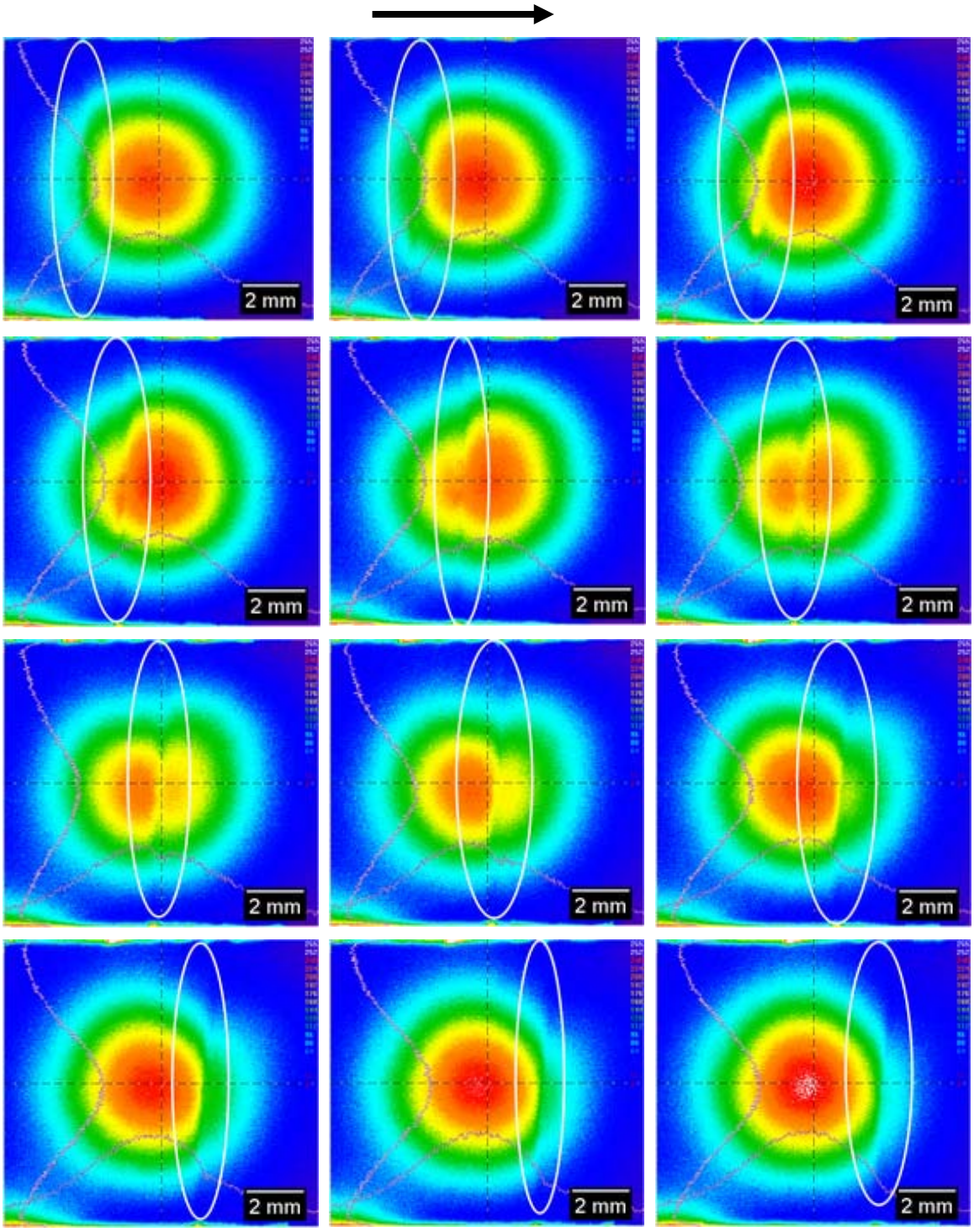

Figure 4.4.2. Crack detection in sample 1 using Spiricon beam profiling – changes of the light contour indicated the presence of the crack. The arrow indicates the movement direction of the sample. White ellipse highlights the crack area. The x movement step size is approximately 1 mm.

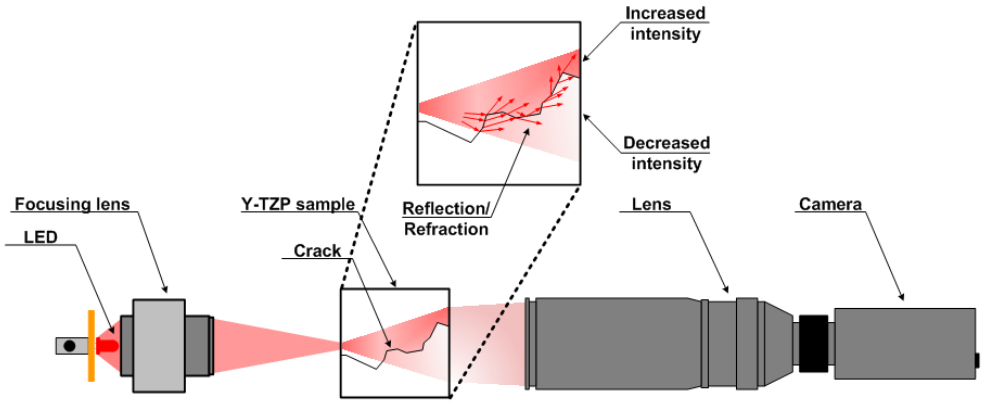

Figure 4.4.3. Light reflection and refraction within the crack region.

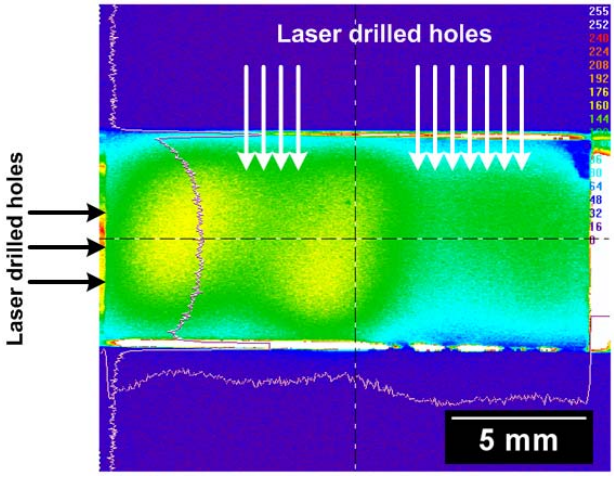

Figure 4.4.4. Visible inspection of sample 2. The arrows indicate the positions of the laser drilled holes.

After the samples were inspected with the visible light it immediately became apparent that visible light was not suitable for the inspection of thick (in the order of 8 mm) 3Y-TZP samples inspection due to light scattering. In addition the light absorption in the blackened region was another factor hampering the visible light imaging capabilities. The presented figures showed that there were some macro scale (above 1 mm in size) features buried in the bulk but it was impossible to measure the size and quantity these features. No micro scale (below 1 mm in size) features were detected with the visible light inspection. For that reason the visible light inspection was very limited.

Samples from 1 and 2 measured above 6.9 mm in thickness and the main factor influencing the visible light measurements was light scattering. To investigate if similar behaviour appeared in thinner samples, sample 3 (see Figure 3.2.1(c)) measuring 2 mm was tested with the visible light. Similarly to sample 2 only one image of the sample is presented because the whole sample was illuminated at once (see Figure 4.4.5). The

sample was mounted in the setup upside down, therefore the smaller shattered piece was from the opposite (right hand) side to the position in Figure 3.2.1(c). Sharp light intensity changes detected in the image were caused by the structure of the cracks in the sample. In addition, each boundary was more evident compared to the thicker samples inspected previously due to lower thickness of the part. However, there was still no indication of the remaining laser drilled holes which were buried in the bulk.

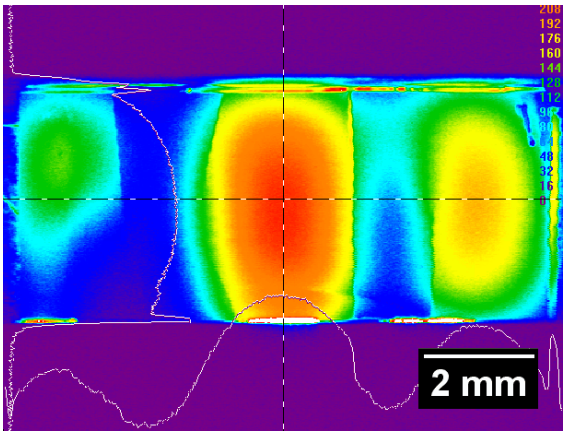

Figure 4.4.5. Visible light inspection of sample 3.

Another sample, sample 5 (see Figure 3.3.1(a)) had laser marked lines (measuring between 50 and 150 µm in depth and between 80 and 130 µm in width) machined on one surface. Sample 5 was inspected to confirm that detection of micro scale features (below 1 mm in size) was not feasible. The marked lines were from the light source side and Figure 4.4.6 confirmed that none of the marked lines were detectable with the visible light.

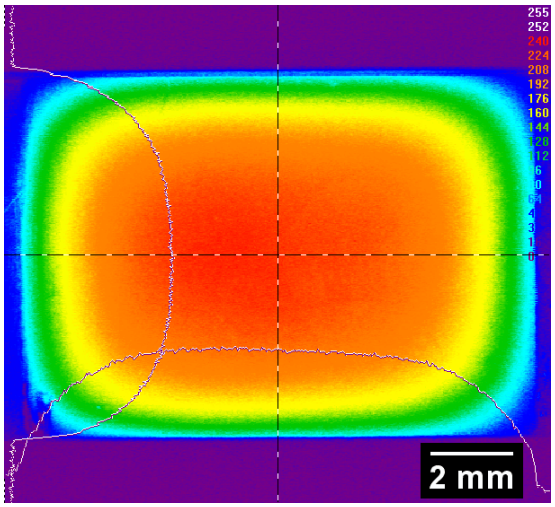

Figure 4.4.6. Visible light inspection of sample 5.

The setup presented in Figure 4.3.2 used Pulnix camera. The Pulnix camera was later replaced with a Basler A600f camera operated from a BCAM viewer software. The system was changed to further reduce the cost of the setup and to investigate if monitoring the images directly from the camera could provide more information about the features inside the sample. Sample 7 (see Figure 3.3.1(c)) was inspected with the modified setup (see Figure 4.4.7).

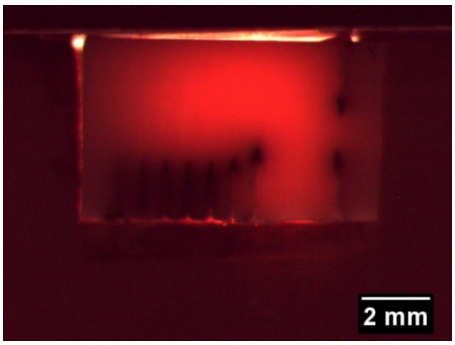

Figure 4.4.7. Visible light inspection of sample 7. Only the features on the surface of the sample were detected.

This sample was used extensively in a feasibility study of the MIR-TI and the Confocal Mid-Infrared Transmission Imaging (CMIR-TI) techniques described later. There were multiple holes drilled from one side of the sample throughout its thickness, thus clearly they were visible in the image. However, the visible light inspection of sample 7 did not manage to detect any cracks in the bulk. In contrast, when the sample was later inspected with the MIR-TI and the CMIR-TI techniques in addition to the machined holes the micro-cracks between the holes were also detected. Due to the fact that there were multiple holes in the sample there was a change to the transmitted light contour, however these changes were on a macro scale (above 1 mm) and it was impossible to acquire detailed information about the holes.

The results with the modified setup (new camera) did not provide any improvement in the visible light imaging capabilities of 3Y-TZP ceramics. Although a general indication that some macro scale features were present in the sample was achievable, the visible light measurements failed to indicate micro scale cracks. As these micro scale cracks are the main source of premature or in service 3Y-TZP part failure, there is a need to detect them and clearly that was not the case with visible light inspection.

4.5. 3Y-TZP dental part inspection

In this section a visible light inspection of a dental bridge (sample 21 – see Figure 3.5.1) is presented (see Figure 4.5.1). Traditionally the 3Y-TZP dental parts are machined using grinding techniques. Mechanical grinding provided a high quality surface finish on the outer, visible surface, however the internal surfaces were left rough. That was one of the main complications in the analysis of the acquired images because a crack would be difficult to distinguish from these grinding marks. However, as dental 3Y-TZP parts often are no more than 0.6 – 2 mm thick, the visible light inspection was possible.

With the sample outer surface positioned towards the camera (the sample was positioned as in Figure 3.5.1(a) towards the camera, however it was positioned vertically) the crack was detected immediately (see Figure 4.5.1) because it was visible on the surface. The same area of the bridge was also inspected from the inside i.e. the camera viewed the tooth from the inside of the cavity (as in Figure 3.5.1(b)) and the result is shown in Figure 4.5.2. In this configuration the same crack could not be found during the inspection due to the structure of the sample and the light scattering. The light reflected and scattered off the walls of the tooth cavity did not penetrate the side-walls, hence they appeared black in the images. The above mentioned phenomena made the crack detection not viable particularly due to light scattering and the internal tooth cavity surface roughness. The light intensity contour of image from Figure 4.5.2(a) is shown in Figure 4.5.2(b) to highlight that any surface roughness changes complicate the optical detection of cracks buried inside the material. This was one of the challenges which made the visible light inspection difficult and sometimes impossible.

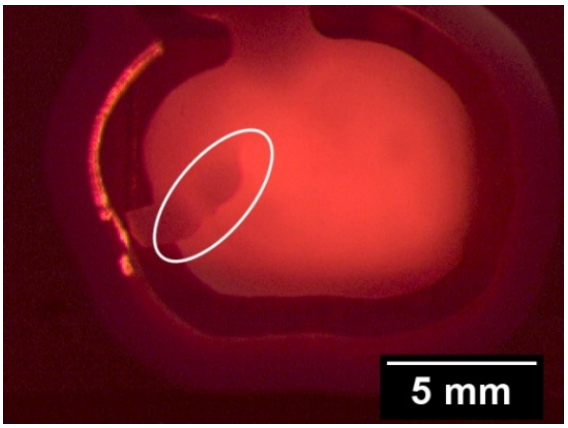

Figure 4.5.1. Visible light inspection of sample 21. Crack detected on the outer surface of the sample.

a) **b)**

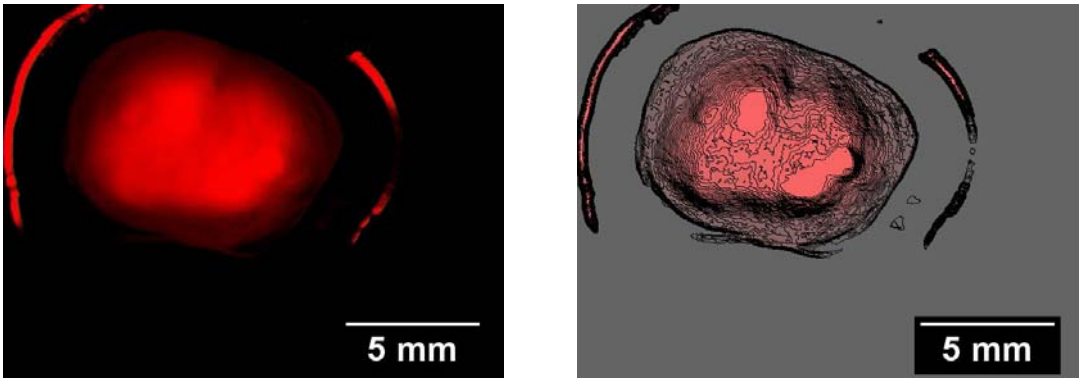

Figure 4.5.2. Sample 21: a) no cracks detected from the inside of the bridge; b) contour line of the image.

4.6. Conclusion

The feasibility of the visible light inspection of 3Y-TZP ceramics was investigated in this chapter. The FTIR results and the results presented in the literature suggest that light scattering in 3Y-TZP was the main source of the reduced optical transmittance in the visible and near-infrared regions. The FTIR results of the 3Y-TZP presented in chapter 3 confirmed a partial light transmission in the mid-infrared but considerable light scattering in the visible wavelength region.

Table 4.1 presents a list of all the samples tested in chapter 4 and summarises the feasibility of visible inspection technique to detect various types of features buried in these samples. The definition of a "critical crack" in the table is a crack which propagates through the whole thickness of the sample. Macro scale cracks measured above 1 mm in size, whereas micro cracks measured less than 1 mm. From these results the visible light inspection proved to be insufficient for the detection of flaws in the bulk of 3Y-TZP ceramics. Strong light scattering, particularly for thick 3Y-TZP samples limited the inspection capabilities. In some cases, for large, macro scale flaws, it was possible to establish their existence inside the sample, however precise information about these flaws was no possible. In addition, a skilled operator was required to detect the flaws. Unfortunately, no micro scale cracks were detected and therefore a more accurate 3Y-TZP inspection method is required. The main advantage of the visible light system was the cost which did not exceed £1000.

Table 4.1. List of the samples tested in chapter 4. Colours indicate: green – suitable to use, orange – limited feedback about the features, red – visible inspection of the features not possible.

Sample	Features inside the sample	VIS inspection feasibility	
1	**1. Critical crack**	**1. Possible**	●
2	**1. Laser drilled holes**	**1. Limited feedback about the features size, however the light structure has changed**	●
3	**1. Laser drilled holes** **2. Critical cracks**	**1. Limited feedback** **2. Possible**	● ●
5	**1. Laser marked lines – micro scale**	**1. Not possible**	●
7	**1. Laser drilled holes** **2. Macro scale cracks** **3. Micro scale cracks**	**1. Possible – only near the surface** **2. Not possible** **3. Not possible**	● ● ●
21	**1. Macro scale cracks**	**1. Limited – crack must be on the surface**	●

References:

[1] E. N. Malamas, E. G. M. Petrakis, M. Zervakis, L. Petit and J.-D. Legat: 'A survey on industrial vision systems, applications and tools', *Image and Vision Computing*, 2003, **21**(2), 171-188.

[2] F. Chen: 'Overview of three-dimensional shape measurement using optical methods', *Opt. Eng.*, 2000, **39**(1), 10.

[3] P. G. Cien: 'Optical Techniques for Industrial Inspection', 732; 1997, Tokyo, SPIE Press.

[4] W. Osten: 'Optical inspection of microsystems'; 2007, CRC/Taylor & Francis.

[5] P. K. Rastogi and D. Inaudi: 'Trends in Optical Non-Destructive Testing and Inspection'; 2000, Elsevier Science.

[6] J. Kovac, L. Peternai and O. Lengyel: 'Advanced light emitting diodes structures for optoelectronic applications', *Thin Solid Films*, 2003, **433**(1-2), 22-26.

5. Mid-Infrared Transmission Imaging

5.1. Motivation

As discussed previously in chapter 4 the use of a visible light technique for inspection of thick 3mol% Yttria-Stabilised Zirconia Polycrystal (3Y-TZP) components was not viable due to considerable light scattering. This chapter presents the development and evaluation of a Mid-Infrared Transmission Imaging (MIR-TI) technique for detection of flaws in the bulk 3Y-TZP ceramics [1].

Fourier Transform Infrared Spectroscopy (FTIR) measurements of Zirconia ceramics revealed a transmission window in mid-infrared wavelength region (see Figure 4.3.2). The development process and the results achieved with the MIR-TI technique are described for the various defects buried in the volume of 3Y-TZP ceramics. The investigations into the limitations of the technique are also presented, with the intention being to determine the potential for application in the industrial environment.

5.2. Introduction

As discussed in chapters 2 and 4 the optical properties of 3Y-TZP ceramics within the visible wavelength region restricted the penetration of light into the material making inspection of cracks or flaws buried in the bulk difficult. In addition to the visible wavelength inspection techniques examined in the previous chapter (see chapter 4) other optical [2-11], thermal [12-16] and acoustic inspection [17, 18] approaches have limited capabilities in terms of the depth of penetration and the quality of the data acquired from such inspection. Mid-infrared radiation on the other hand, as shown with the (FTIR) results (see Figure 4.3.2), was transmitted through the 3Y-TZP. Although the light absorption and scattering was still present in the mid-infrared the results were more promising than for visible light transmission. The challenge of the infrared imaging approach arose from the cost and limited availability of the components compared to the visible or near-infrared region, particularly between 3 μm and 8 μm.

The complexity of semiconductor structures for mid-infrared devices is apparent in the field of infrared detectors and cameras. Due to the low energy carried by the infrared radiation [19], infrared detectors require sophisticated material structures to prevent thermal noise from swamping the signal during the device operation [20]. Objects emit

infrared radiation themselves [21], therefore in order to eliminate background noise the detectivity of the infrared detector is extremely important and optimising it by careful and sophisticated material structure design provides a quality image of the observed object. Apart from the detectors the availability of powerful mid-infrared light sources is also limited to thermal filaments [22], low power diodes and lasers [23]. All these factors had to be considered, predominantly when developing an infrared imaging system for industrial applications where as well as the compactness and reliability, low cost was an essential requirement.

5.3. Instrument characterisation

5.3.1. MIR-TI setup

In order to measure flaws buried in the bulk of the material light had to pass through the volume of the specimen tested. Therefore the most simplistic approach was to mount the sample between the infrared source and the detector. Light scattering of 3Y-TZP was still present in the mid-infrared and limited availability of powerful mid-infrared sources required careful design to maximise the light transmitted through the optical system. Reducing the number of optical components used in the setup proved to be crucial in minimising the surface reflections and maximising the light reaching the detector.

The MIR-TI setup is presented in Figure 5.3.1. The design was simple and compact, thus the alignment procedure was simplified and the cost of the components was minimised. A thermal emitter Scitec IR-12K 11 W was chosen as an infrared source due to its long lifetime, low cost and optical stability which was also dependant on the stability of the power supply. According to the manufacturer specification the emissivity of the infrared source reached 80% of the perfect blackbody spectral radiance in a wide infrared range between 1 μm and 22 μm (Figure 5.3.2).

The infrared source was mounted in the Scitec MC-234 parabolic reflector to collimate the infrared radiation and to provide a uniform illumination of the sample. The image of the infrared source mounted in the reflector is presented in Figure 5.3.3. In front of the sample a mask cut out of a 300 μm sheet of stainless steel was positioned to avoid light passing around the sample and reaching the camera. High intensity light could

lead to the camera saturating and the detection of a defect within the bulk could be compromised. The infrared source was positioned 20 mm from the sample mask.

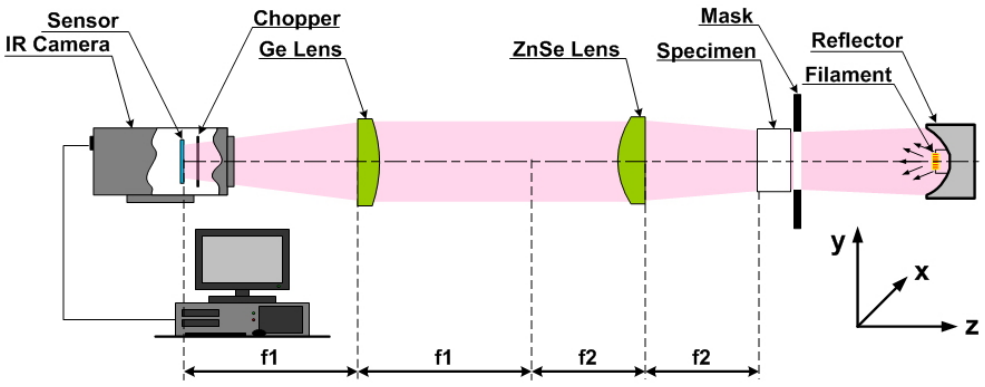

Figure 5.3.1. MIR-TI setup.

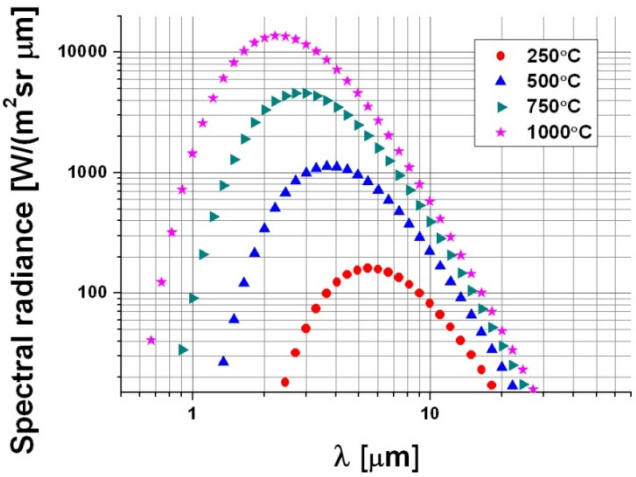

Figure 5.3.2. Spectral radiance of perfect blackbody at different temperatures – IR-12K source produce approximately 80% of these curves in the 1µm to 22µm range [22].

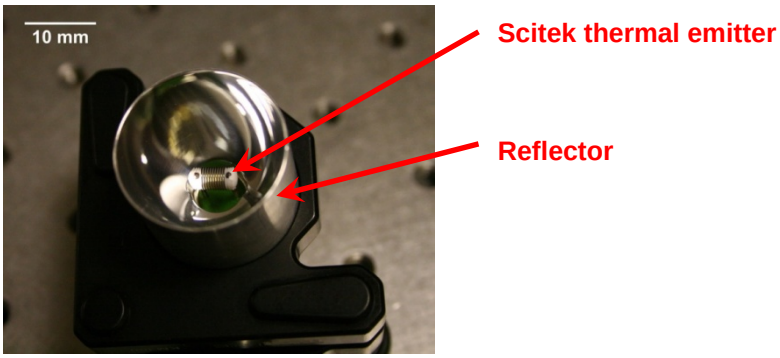

Figure 5.3.3. Scitec IR-12K infrared source mounted in the Scitec MC-234 parabolic reflector.

Each sample for inspection was mounted on the manual translation stages which allowed for sample position adjustments. This manual stage adjustment was required

due to the limited field of view (11 by 7 mm) of the MIR-TI system. One of the key objectives of the MIR-TI technique development was compact design, therefore a 4-f optical setup was introduced. The 4-f lens setup was required because using camera lens only required the sample to be positioned at least 450 mm from the camera which would not result in a compact system [24]. The 4-f system allowed adjustment of the image magnification, which depended on the ratio of lens focal lengths, and in addition it allowed the distance between the imaged object and the camera sensor to be reduced [25]. Due to the considerable cost of the infrared optics the 4-f system was also the most cost effective solution because it involved using only two lenses. The lens mounted on the sample side was a Zinc Selenide (ZnSe) aspheric lens, anti-reflection coated at 10.6 μm with 38.1 mm diameter and with 38.1 mm focal length (f_2). From the camera side anti-reflection coated at 10.6 μm Germanium (Ge) lens with 50 mm diameter and with 50 mm focal length (f_1) was installed. The magnification (M) of the imaging system with the assembled 4-f setup was 1.31 according to equation (5.1).

$$M = \frac{f_1}{f_2} \tag{5.1}$$

The designed setup, although more expensive due to the additional ZnSe lens reduced the overall size of the MIR-TI device from 900 mm to approximately 400 mm in length. Introducing the additional lens provided a smaller field of view and higher magnification which for the inspected parts was more suitable.

The 4-f system imaged the light transmitted through the sample onto the Electrophysics PV320-L2E infrared camera. This particular model of infrared camera was chosen due to the broad infrared detection spectra and affordability [24]. Although the sensitivity of the camera was low between 4 and 8 μm the initial results with the Electrophysics camera were promising. Low sensitivity in the mid-infrared range compared to 8 to 12 μm wavelength region was due to the fact that the camera was designed specifically for 8 to 12 μm which was a better suited region for surveillance where the detection of the objects above -30ºC is necessary. In addition the emitted energy from the sun in 3 to 5 μm is significantly higher than the radiation in 8 to 12 μm, thus to reduce ambient noise the camera was designed for the longer wavelength range [24]. Due the absorption of H_20 and CO_2 [26] designing the infrared camera for 3 μm to 8 μm region is considerably more difficult, consequently more expensive.

Apart from the low sensitivity of the camera, other challenges of using the Electrophysics camera, predominantly when attempting to detect micro-scale flaws in the 3Y-TZP material, were the low resolution (320 by 240 pixels) and relatively large pixel size of 48.5 μm of the camera sensor. These were the practical constraints which limited the resolution capabilities of the MIR-TI system.

The infrared camera was connected with Labview software written to acquire the image frames. The frequency of frame acquisition was limited by the software to a maximum of 10 Hz. The data acquisition and the image post-processing techniques are explained in the next sections.

5.3.2. Illumination stability measurement

Fluctuations in the intensity of the illumination could potentially introduce additional noise which, particularly when testing thick samples, could have a detrimental impact on the flaw detection. Therefore, the stability of the infrared source and the power supply was established. The measurement was performed with the Vigo infrared detector described in chapter 6. During the noise measurement a 1 mm thick 3Y-TZP block was mounted in the sample holder to protect the infrared detector from saturation. The measurement revealed signal fluctuations of ± 3% from an average value. The result was based on the Relative Standard Deviation (RSD) parameter (equation (5.2)) measured during a 30 minute trial.

$$\mathrm{RSD} = \frac{100 \cdot \sigma}{\mathrm{Mean}}[\%] \qquad (5.2)$$

where σ is the standard deviation and Mean is the average value of the acquired signal. The RSD is an accurate signal noise level indicator. It represents signal deviation from the signal mean value. The result achieved was satisfactory and confirmed that the infrared source was stable during the measurements. The criteria were based on the observed light intensity changes when detected flaws buried in the bulk of 3Y-TZP were detected on a bright background (see appendix E)

5.3.3. Data acquisition and manipulation

The image acquisition process was controlled from a Labview program developed for that purpose. During the measurements the data was saved as a sequence of image frames and the frequency of acquisition was set to 10 Hz. Due to the limited response time of the Labview program the maximum frequency of data acquisition was 10 Hz which was satisfactory for the purpose of the measurements. The program allowed for the adjustments of the data acquisition frequency, the acquisition time, the filename and the filename location. The images were saved in uncompressed tiff format. The images generated and acquired during the measurement had the additional counter added to the filename to more easily distinguish the sequence and order of their acquisition.

After the data was saved a series of the acquired images was post-processed in the Matlab package to enhance the contrast of the images. The batch of the images was uploaded to the program and with the built-in "imadjust" Matlab command the contrast of the images was increased. The "imadjust" command mapped the intensity values in the greyscale image to new values resulting in 1% of data being saturated at low and high intensities. Therefore grey colours in the image were stretched between two extremes of white and black to cover the entire image dynamic range. The "imadjust" method uses a linear scaling of the original data, hence no image information is lost other than the original pixel intensities. An example of the image of sample 12 before and after Matlab processing is presented in Figure 5.3.4. A considerable contrast enhancement as seen in the figure was achieved after processing the image in Matlab, therefore this process was used to improve the contrast of all the images acquired by the MIR-TI technique.

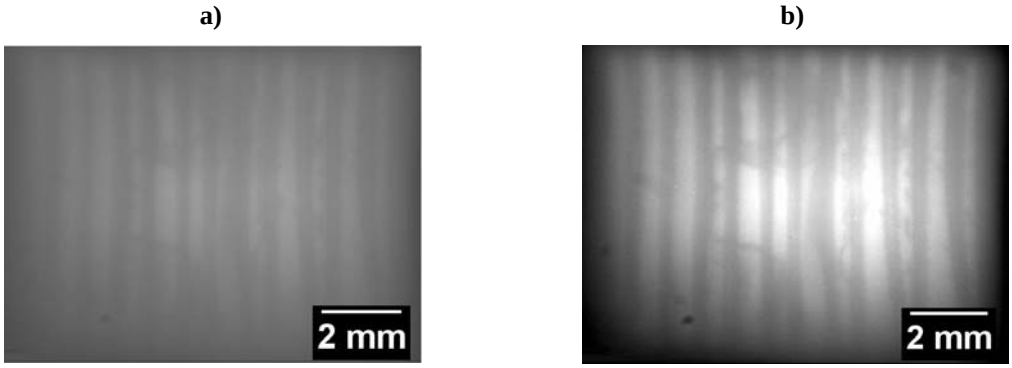

Figure 5.3.4. Sample 12 image Matlab processing: a) the image before the contrast enhancement; b) the image after "imadjust" script was applied.

The image contrast enhancement was quantified based on the image histogram changes. The histograms of the images from Figure 5.3.4 are presented in Figure 5.3.5. The improved image contrast used a considerably wider pixel intensity spectra and this could be seen from the image appearance. A wider pixel intensity range resulted in lower standard deviation of the quantity of pixels for all the pixel intensities (from 0 to 255 range) (defined as M_{pixel}). This was an indicator that the pixel intensity range was expanded, thus the image contrast was improved. For the Figure 5.3.4(a), the M_{pixel} was approximately 1916 and for Figure 5.3.4(b) the value was only 579. This was a considerable difference which highlighted how much the image contrast had changed. This method was used to quantify how the contrast was improved compared to the original image.

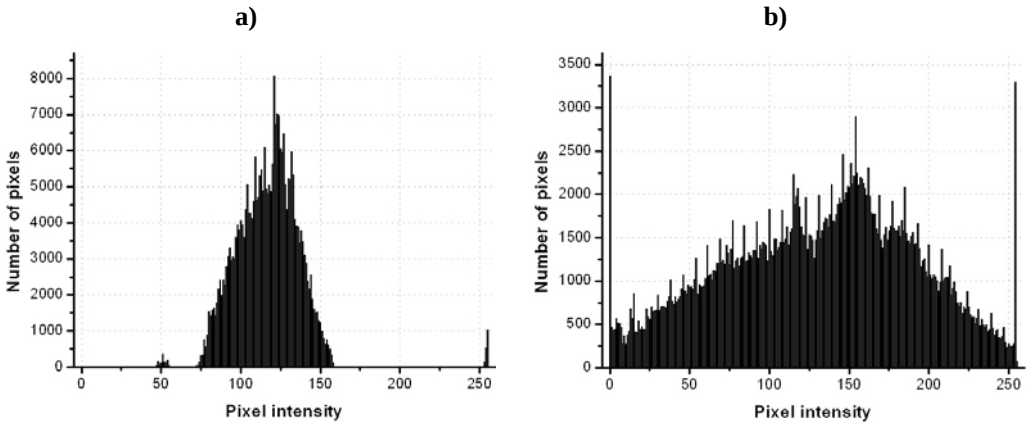

Figure 5.3.5. The histograms of the images from a) Figure 5.3.4(a) and b) Figure 5.3.4(b).

In addition to the "imadjust" command the "adapthisteq" Matlab command was evaluated. Both approaches perform a contrast-limited adaptive histogram equalization (CLAHE) described in section 2.5.3. The "adapthisteq" command showed comparable results to the "imadjust" image although the noise level in the images was higher (see Figure 5.3.6). The image intensity profile was more uniform across the whole image in comparison to "imadjust" image but at a cost of the reduced image contrast and the increased noise level. The "adapthisteq" algorithm splits the image into smaller regions in which the contrast in enhanced. Finally once all the regions are combined together to produce the whole image a bilinear interpolation (see section 2.5.1) applied to eliminate the artificially induced boundaries.

The image histogram from Figure 5.3.6 is shown in Figure 5.3.7. The M_{pixel} value was 1200. For the "adapthisteq" the peak has moved towards brighter limit. This is apparent in the image (see Figure 5.3.6(b)), especially close to the edges where there is

very little black area. Unfortunately a higher number of bright pixels resulted in a more grey appearance of the image which may have a detrimental impact on the detection of small flaws, particularly in the bright regions of the image. The "adapthisteq" and the "imadjust" Matlab plotting techniques were used to present the acquired images in the experimental part the choice of algorithms depending on which provided a better result.

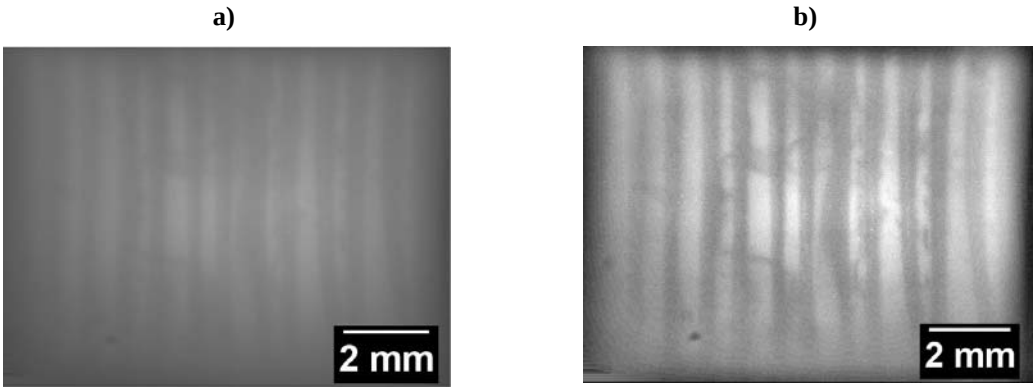

Figure 5.3.6. Matlab image processing of the image of sample 12: a) a non-processed image; b) "adapthisteq" image enhancement.

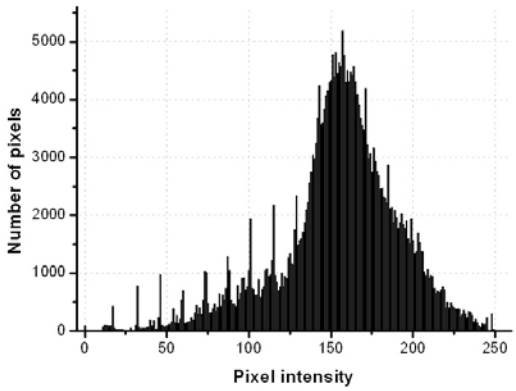

Figure 5.3.7. The "adapthisteq" histogram of the image from Figure 5.3.6(b).

5.3.4. Depth of field of MIR-TI system

The camera and the lenses were fixed to a manual stage which allowed the imaging part of the MIR-TI system to be translated, thus in-depth scanning of the samples was possible. To determine what thickness of the specimen tested was covered by one acquired image the depth of field (DOF) parameter was estimated from equation (5.3) [27]:

$$DOF = \frac{\lambda_0 \cdot n}{(NA)^2} \cdot \frac{n \cdot e}{M \cdot NA} \qquad (5.3)$$

where

$$e = \frac{\lambda_0}{2 \cdot NA} \tag{5.4}$$

where λ_0 was the wavelength of the illuminating light (set to 6 µm), n was the refractive index of the medium (air n = 1) between the sample and the objective front lens element, NA equalled to ZnSe lens numerical aperture [28] and M was the lateral magnification of the optical system (M = 1.31). The effective numerical aperture of ZnSe lens was calculated to be 0.45, using equation (5.5), where dia was its diameter and f_x was the focal length of the ZnSe lens [19].

$$NA = \sin[\arctan(\frac{dia}{2 \cdot f_x})] \tag{5.5}$$

The depth of field for the MIR-TI system was calculated to be 39 µm. The NA of the ZnSe lens was calculated based on the experiment which involved placing the 2 inch aperture in front of the lens. While closing the aperture the light intensity changed was observed in order to estimate what area of the ZnSe lens was used by the MIR-TI system. The change of light intensity was observed immediately when the open aperture size was equal to the lens size which is 38.1 mm. With dia = 38.1 mm and f_x = 38.1 mm the effective NA was 0.45.

The DOF parameter calculation was necessary to estimate the volume which was in focus during the MIR-TI system scanning. It was also essential to determine the DOF in order to precisely locate and estimate the size of the features detected. The above results gave an indication of the DOF for the MIR-TI system.

Before the samples were inspected with the MIR-TI technique the accuracy of the depth of field parameter calculated from equation (5.3) was measured experimentally. Two samples 2.6 (sample 4) and 3.76 mm thick (sample 5) were used for these experiments. The machined side of the sample was positioned at the infrared source side such that the lines were observed through the thickness of the sample (see Figure 5.3.8).

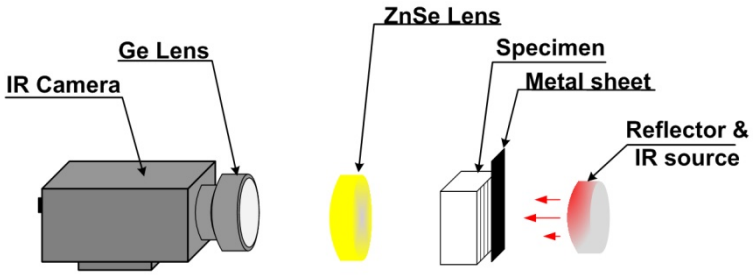

Figure 5.3.8. Laser marked sample inspected by the MIR-TI system.

The thickness of the sample was first estimated using the MIR-TI technique. This was the first measurement which helped to determine the accuracy of the DOF parameter calculated above. For that experiment a piece of thin metal sheet was adhered to the back of the sample (at the infrared source side) covering a partial area of the specimen in order to allow detection of the back surface more easily (see Figure 5.3.8). The rear surface position was established when sharp edge of the metal sheet was detected (see Figure 5.3.9(a)). The front surface position on the other hand was determined by detecting the sharp features on the surface of the specimen (see Figure 5.3.9(b)). Based on the z positions of the acquired images the thickness of 3.4 mm was measured for sample 5. This resulted in a 10% difference between the actual size of the sample and the size measured with MIR-TI system. Another laser marked sample 4 measuring 2.6 mm had the thickness measured to be 2.4, thus the measured thickness error was estimated to be in a region of 8%. Therefore there was a decrease in the thickness error with the changing sample thickness. This was anticipated due to still present light scattering which hampered the readings. Also, the measurement relied on the operator's perception of the detected features, thus additional error could be introduced.

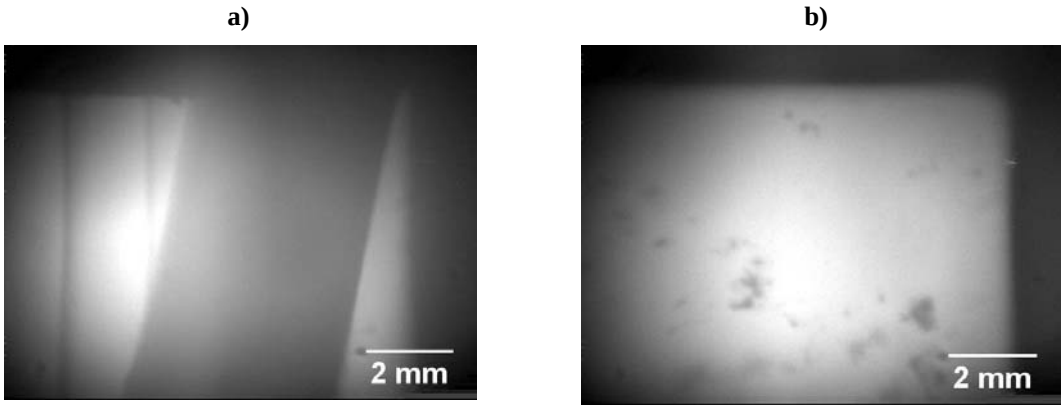

Figure 5.3.9. MIR-TI depth of field inspection: a) a sharp edge of the metal sheet at the back of sample 5 and b) sharp features on the front surface of sample detected.

To further investigate the accuracy of the calculated DOF, the depth of the laser marked lines machined on the sample surface was measured. The images of the lines at the point where they appeared sharp and then at the point before they begin to blur out or become defocused were acquired (see Figure 5.3.10). For the purpose of the test a line 150 µm deep was chosen because its depth allowed for determining sharp and blurred out appearance of the line during sample scanning. The image positions where the line first appeared sharp and then when the line is on the point of being out of focus were noted on the manual stage. The sharpness of the lines appearing on the screen was judged by the operator. The difference indicated a measurement of the DOF value plus the thickness of the marked line. For sample 4 a difference of 200 µm between the two positions were measured for the 150 µm deep marked line. For sample 5 on the other hand a difference of 210 µm was measured.

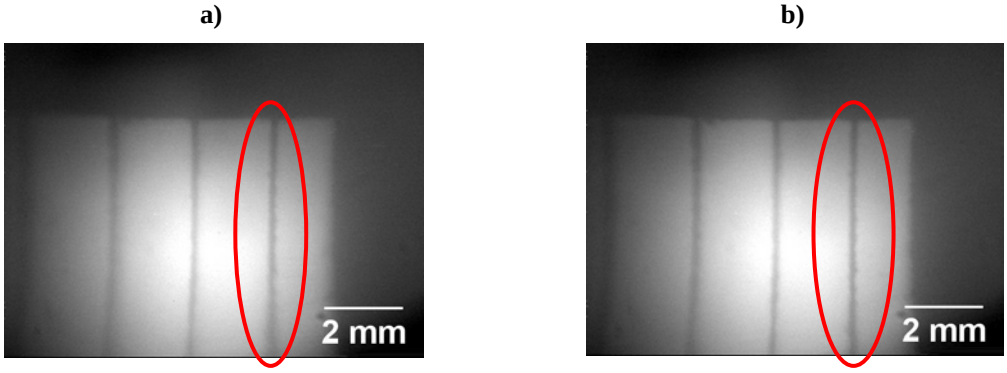

Figure 5.3.10. 150 µm deep marked line in sample 5 used to estimate the depth of field of MIR-TI system. The images of the sharp marked line at the depth of: a) 3.55 and b) 3.76 mm from the front sample surface.

Based on the DOF calculations from equation (5.3) the marked line depth measured with MIR-TI system should be approximately 190 µm which was the DOF value plus the actual depth of the marked line. Clearly, this is not the case for the above results. The inconsistency in the measurement was 5% for 2.6 mm thick sample and 10% for sample 5. The difference in the results was due to an inaccuracy in deciding where the marked line was in focus and an error in the measured depth of the marked line using an optical microscope (see chapter 3). The depths of the grooves were only measured from the side of the sample. Even small variation in laser output power could change the depth of the machined line.

The DOF calculations and the above experimental results were used to quantitatively assess the DOF. The calculated DOF was 39 µm. If the higher 10% error estimated experimentally was included, the DOF was approximately 43 µm, therefore a DOF of

50 μm was determined a working value for the system. During the sample scanning the MIR-TI image acquisition step size was set to 50 μm to maximise sample coverage and to minimise the time required for the measurement.

5.3.5. USAF standard resolution measurements

One of the key objectives for the developed MIR-TI imaging technique was providing sharp images which could enhance the detection of flaws, thus high imaging resolution which exceeds the flaws size was required. This is particularly challenging when the scale of the features which are to be investigated lie in sub-mm scale. The imaging resolution does not have a unique definition. It refers to a vanishing resolution which is defined as the highest spatial frequency where the bar chart pattern is visible. Often the USAF standard testing target is employed for such resolution measurements. The methodology used here to determine the resolution of the imaging system using a USAF testing target is described in detail in section 2.5.2. The smallest bars which can be resolved by the observer determine the group and the element of the bars and based on this the resolution is estimated from equation (2.7).

To establish the resolution of the MIR-TI system a standard positive USAF testing target was mounted on the sample holder. The picture of the target was taken with the MIR-TI system and then the contrast of the image was adjusted using the Matlab script (Figure 5.3.11). The smallest bars which could be resolved were the fourth element in the third group giving 44 μm resolution. A resolution in this order was expected due to the pixels size of the infrared camera which measured 48.5 μm. A 12% error margin should be considered when analysing the results. This is because the measurement relies on the observer and different observers may deduce that an adjacent element in the same group is the smallest that can be resolved. The error of 12% is approximately the difference between each adjacent element within the same group.

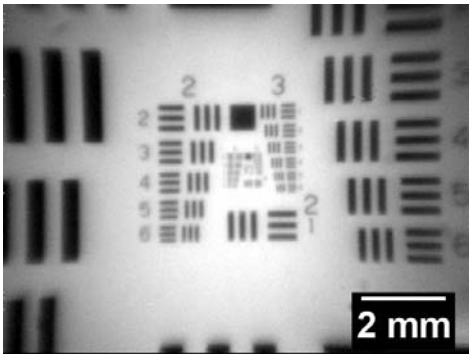

Figure 5.3.11. USAF target image acquired with the MIR-TI system.

The above measurement with the USAF target was not suitable for the infrared camera resolution inspection due to the limited infrared transmission of the soda lime glass (see appendix D) used to manufacture the target. Therefore to establish the resolution of the MIR-TI system in the mid-infrared wavelength region the USAF infrared target was developed based on USAF 1951 T-20 target (according to MIL-STD-150A standard) – see appendix D.

The resolution of the MIR-TI system was measured using the USAF infrared target mounted on the sample holder. The infrared image of the target is presented in Figure 5.3.12. The resolution calculated from the infrared target was 39.4 μm (group 3, element 5). However, this apparent improved resolution for the infrared target was attributed to the fact that the machined bars on the USAF infrared target were 9% smaller giving a larger spacing between the bars, thus allowing a smaller element to be resolved. Taking into account this effect the resolution of the MIR-TI system in mid-infrared was approximately 43 ± 5 μm (plus 12% error) which was similar to the resolution in the near infrared regime (44 μm) where the standard USAF target was used. Therefore the MIR-TI technique imaging resolution did not significantly deviate with the changing wavelength. Large camera pixels size and small amount of pixels in the camera sensor were limiting any further resolution improvements [24].

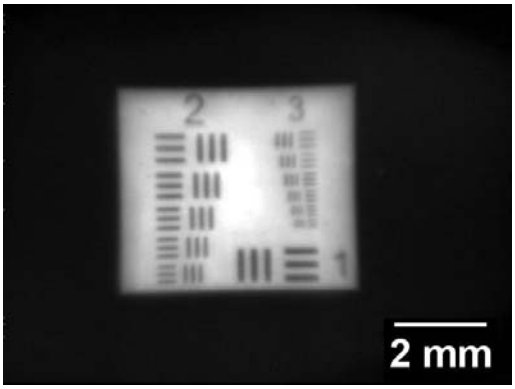

Figure 5.3.12. USAF infrared target resolution measurement of the MIR-TI system.

5.3.6. Resolution measurements with infrared filter

All of the above measurements were carried out over the entire spectral range of the infrared source and the infrared camera. Due to the limited optical transmittance of the 3Y-TZP ceramics (see Figure 4.3.2), the material acted as a filter for the MIR-TI system. To investigate if there was any influence of the broad optical spectra of operation of the MIR-TI system an infrared band-pass filter (Figure 5.3.13) was

mounted in front of the sample at the side of the infrared source. The optical transmittance of the MIR-TI system with the band-pass filter was limited to the range between 3 and 6 μm. The images of the USAF infrared target with the installed filter are presented in Figure 5.3.14. The standard USAF target was not tested due to the limited optical transmission in mid-infrared.

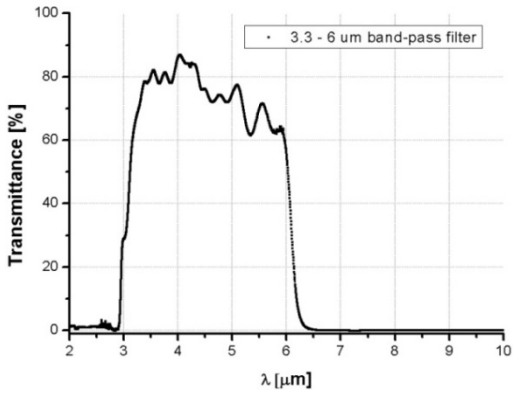

Figure 5.3.13. The optical transmittance spectra of infrared band-pass filter.

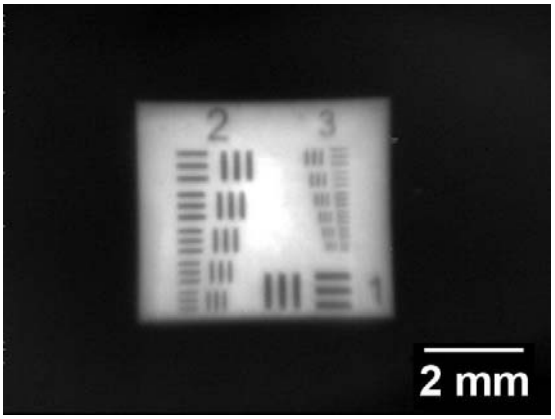

Figure 5.3.14. The resolution measurement performed with the infrared band-pass filter using USAF infrared target.

The resolution measured using the USAF infrared target with the band-pass filter in place was 39 μm (group 3, element 5) which with 9% error resulted in resolution of 42 ± 5 μm. This was an equivalent to the measurement without the filter. The resolution enhancement was not present when using an infrared band-pass filter because the normalised optical detectivity (see section 6.2) of the camera sensor in the mid-infrared was low [24]. Poor camera detectivity between 4 and 6 μm negated any resolution improvement with the band-pass filter due to reduced SNR [29]. Consequently any potential effects of reduced chromatic aberrations were not measurable. Table 5.1 presents the resolution results achieved for all USAF target measurements

Table 5.1. The comparison of all the resolution results for MIR-TI technique.

Target used	Resolution [µm]
USAF target	**44 ± 5**
USAF infrared target	**43 ± 5**
USAF infrared target with the infrared band-pass filter	**42 ± 5**

5.4. Results

In order to determine the MIR-TI technique inspection capabilities multiple samples where measured with macro (above 1 mm in size) and micro (below 1 mm in size) scale features buried in the bulk. Each sample was scanned and the acquired images were then enhanced using Matlab software. Finally, the operator evaluated the existence and then the size and the position of the features. Once the samples were tested they were sectioned to confirm the presence of the detected cracks. Based on the acquired results the sample thickness and the flaws size limits for all the tested samples and for the MIR-TI system were evaluated.

5.4.1. Macro scale features detection

This section covers the inspection of macro scale flaws buried in the samples. The samples were mounted in the sample holder and the image frames were grabbed through the thickness by scanning in the z axis (see Figure 5.3.1). An example of the MIR-TI scanning sequence of sample 7 is presented in appendix C.

To compare the results between the visible light inspection and the infrared imaging techniques the 6.9 mm thick sample 2 from Figure 3.2.1(b) was inspected with the MIR-TI system. The visible inspection did not provide detailed information about the features buried in the volume of the 3Y-TZP block (see Figure 4.4.4). The shadows in the images indicated the presence of some of the features but it was difficult to determine their parameters (size, position or depth). The MIR-TI measurement on the other hand resulted in a more promising result (see Figure 3.2.3). The presented image is the combination of two images due to the size of the sample being larger than the imaging area of the MIR-TI system. All the laser machined holes were clearly distinguishable in the image. In addition the position and the depth of each hole could be determined from the acquired images based on the evaluated DOF and the micrometre screw position. Precise information about the features machined in the bulk

sample without sectioning the components significantly reduced the time for the inspection of 3Y-TZP parts but what was more important was that the measurement was non-destructive, thus if the component passes the test it could be further processed or used as a final part.

One of the key parameters of the MIR-TI technique which had to be determined was the maximum sample thickness which could be inspected with the system. To quantify the maximum thickness of the sample at which macro scale features could still be detected a series of laser machined samples were tested including samples 9 (see Figure 3.2.1(d)) and 10 (see Figure 3.2.1(e)). The MIR-TI images of the samples 9 and 10 are presented in Figure 5.4.1. As can be seen from the images the macro scale features were detected in all the samples. Still present light scattering in mid-infrared wavelength range diffused the light and impaired the ability to detect the macro scale features for samples above 6 ± 0.1 mm in thickness. The low optical output power of the infrared source combined with the level of scattering present in a thick sample reduced the image contrast. This however could be changed significantly if more powerful light source and better resolution camera were used.

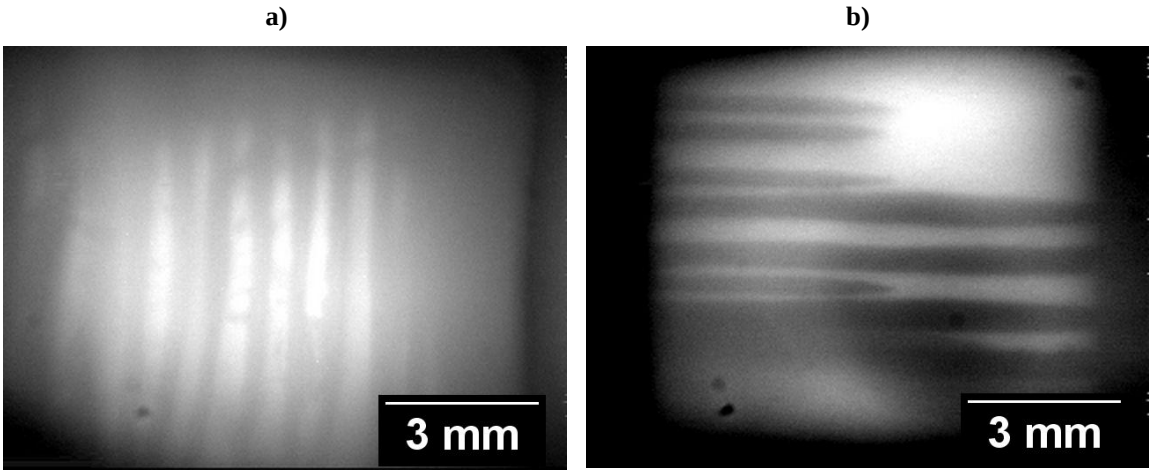

Figure 5.4.1. MIR-TI images of sample: a) 9 and b) 10.

The presented examples of the macro scale features detected by MIR-TI technique confirmed improved imaging capabilities compared to the visible light inspection technique presented in the previous chapter (see chapter 4). For the visible wavelength inspection the most detrimental effect was the light scattering. This scattering, although present was much reduced at wavelengths above 3 μm. However, at wavelengths above 7 μm strong light absorption dominated and became the main factor reducing the optical transmission of 3Y-TZP (see Figure 3.1.4).

Despite the much improved imaging capabilities of the MIR-TI system (compared with the visible technique) the infrared camera used in the MIR-TI system had a limited sensitivity in the 3 to 6 μm transmission region which was of most interest to inspect 3Y-TZP ceramics. Consequently, the combination of the low power infrared source and reduced spectral response of the camera were the two factors which limited the maximum depth of the sample which could be inspected.

5.4.2. Micro scale feature detection

The MIR-TI system was designed to detect the micro scale flaws measuring below 1 mm in size which might be present in 3Y-TZP ceramics after machining. Micro scale cracks have a negative effect on material mechanical stability which, especially in medical applications, is highly undesirable. The crack detection capabilities were tested using a series of samples: 7 (Figure 3.3.1(c)), 12 (Figure 3.3.1(e)) and others not presented in this study. Similarly to macro scale features samples, these samples had defects introduced during laser machining. The samples were ideal candidates for testing the flaw detection capabilities of the MIR-TI technique due to the introduced large number of cracks.

At first sample 7 was inspected with the MIR-TI system and the images of the cracks detected are presented in Figure 5.4.2. Three images pitched by approximately 200 μm along z axis are shown to highlight the cracks detected. High thermal input introduced into the sample due to the millisecond laser pulse resulted in several cracks being generated.

What can be seen from the images in Figure 5.4.2 is that cracks propagated away from the drilled holes. Therefore, the mechanism which makes these cracks visible in the picture was not due to the change of material properties after its solidification, as was the mechanism that allows macro scale flaw to be detected (section 5.4.1). The micro scale cracks in contrast, were detected due to a significant refractive index change in the material which appeared after the crack air gap was produced. The air filling the gap had a refractive index of 1, whereas the refractive index of 3Y-TZP ceramics was close to 2 [30, 31]. Therefore the significant refractive index change produced a reflective and refractive interface for the light highlighting the cracks. These cracks appeared as dark regions in the images within the crack area because direction of light propagation changed, thus the light intensity profile changed. Furthermore, light propagating from

high refractive index zirconia n ≈ 2 to air undergone 11% reflection for 6 µm wavelength [1] for light propagating perpendicular to the crack interface.

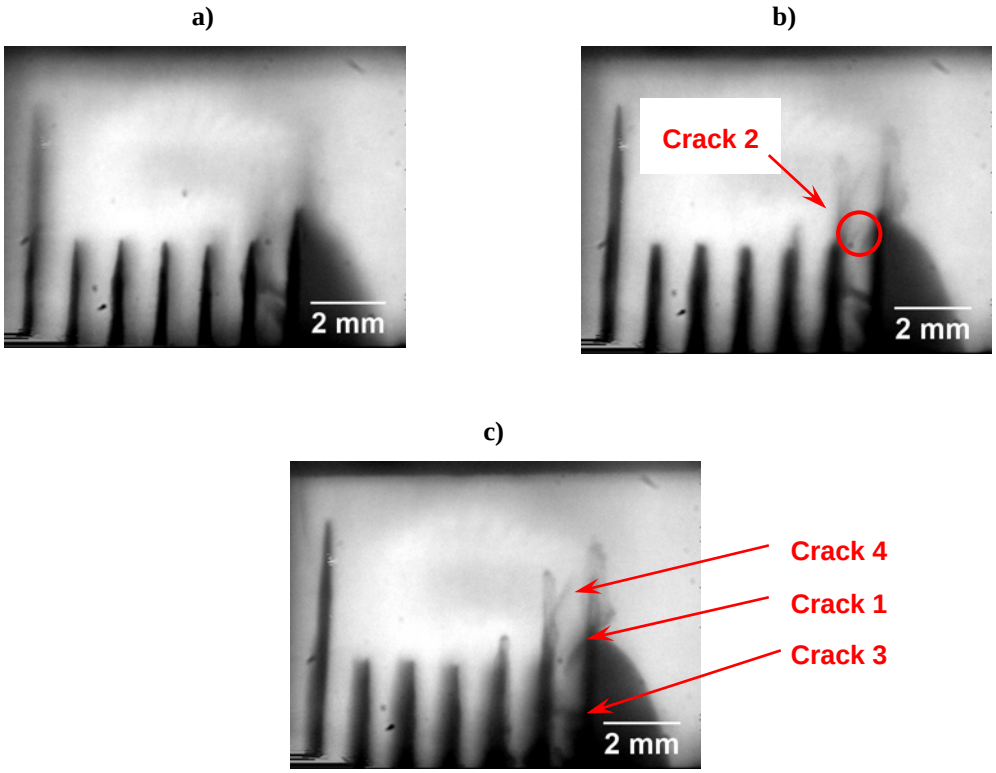

Figure 5.4.2. The sequence of images acquired during scanning of sample 7. The images are spaced 200 µm from each other.

In sample 7 there were several features identified as cracks. Crack 1 (Figure 5.4.2) appeared 2 mm from the front surface, whereas crack 4 appeared 2.2 mm from the front surface (at the camera side) during MIR-TI scanning. However, closer investigation revealed that cracks 1 and 4 were actually present on the back surface (at the infrared source side) of the sample. The ESEM images of the flaws from Figure 3.3.10 showed that the cracks were elongated and measured a few hundred microns, but the air gaps of these cracks were between 1 and 4 microns in thickness (see Figure 3.3.11(a)). As both the camera resolution and the DOF parameter were in the range of tens of microns, it was surprising that such fine features could be detected by MIR-TI technique. However, in the infrared image, these cracks appeared much larger due to the presence of the shadows which indicated that the actual cracks propagated deeper in the material. The sharp image of the cracks appeared 500 and 750 µm from the back surface of the sample for crack 1 and 4 respectively, thus indicating that the cracks penetrated into the sample to a depth which was estimated to be 500 and 750 µm (taking into account the

DOF discussed above). Therefore the actual crack size was much higher than the MIR-TI system resolution limit, hence these apparent fine surface cracks were detected.

In Figure 5.4.2(a) there were also several shadows detected at the bottom of the sample below crack 1. These shadows indicated the presence of crack 3 in the MIR-TI images. Crack 3 appeared at the start of the scanning sequence suggesting that this feature was positioned near the front surface of the sample. After a 500 μm slice of the sample was mechanically cut the crack 3 detected by the MIR-TI technique turned out to be a group of three fine micro cracks close to each other. The microscope image in Figure 3.3.11(b) shows the identified cracks and it was determined that these features were present throughout the whole thickness of the sample. The strong shadows in the images provided strong indication as to the size of these flaws. In fact during a subsequent cutting processes the material volume underneath these cracks separated from the sample indicating how detrimental these cracks were to the overall material integrity.

One feature which was not identified on the surface of the sample was crack 2 which appeared 1.5 mm from the front surface of the sample and disappeared at approximately 1.6 mm during the scanning. This suggested that it was a much finer feature compared to the other detected cracks. Crack 2 was located in the sample and the whole process is described in chapter 3. Figure 3.3.12 presents the image of crack 2 that was observed after the sample was cut. The crack 2 size was estimated to be 240 μm which was above the resolution limit of the MIR-TI system, hence it was not surprising that the flaw was detected.

The experiment carried out above highlighted how difficult the inspection was using conventional sectioning of the sample because there is always a risk of removing some cracks without observing them. With the MIR-TI system the crack depth was determined accurately, whereas with sample sectioning the whole process had to be carried out carefully. Furthermore, the crack thickness could only be deduced to be within a certain range which included the errors dependent on the inspection process.

The discussed cracks (cracks 1 – 4) detected with the MIR-TI system were elongated and deep but the air gaps were very fine. The MIR-TI technique provided an image of the crack volume rather than just imaging a single plane of the feature. Therefore, a crack with a 1 μm air gap could be detected when at least two dimensions of the crack were above the MIR-TI technique resolution limit. To identify what effect the crack depth had on the ability of the MIR-TI set up to detect cracks, several samples were

indented with a Vickers indenter to introduce very fine flaws (see Figure 3.3.1(b) for an example of the indented sample 6).

The MIR-TI image of sample 6 is presented in Figure 5.4.3. The indent was highlighted with a circle but no cracks were detected in the proximity of the indent. The ESEM image of the indented area from Figure 5.4.3 show the cracks which propagated from the edges of the diamond tip. These cracks were very fine and only one of the dimensions (crack length) was above the MIR-TI system resolution limit. The diamond tip itself had all three dimensions above the resolution limit, hence it was detected. The measurement confirmed that the observation of flaws in the bulk of 3Y-TZP ceramics was possible as long as at least two out of three dimensions of the feature were above the MIR-TI resolution limit.

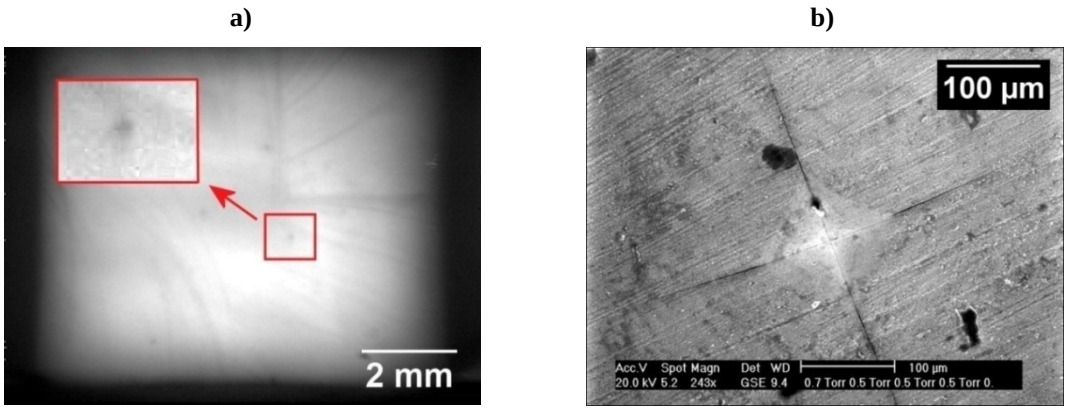

Figure 5.4.3. The MIR-TI (a) and ESEM (b) images of the sample 6.

To determine the maximum thickness of the sample which allowed for the detection of micro scale cracks samples 12 was also investigated. The MIR-TI images of the measured samples are presented in Figure 5.4.4. The images of fibre laser machined samples showed a high quantity of micro scale cracks which facilitated the controlled sectioning of thick 3Y-TZP blocks [32]. These cracks were produced in the heat affected zone (HAZ) surrounding the drilled hole and were driven by the stress occurring near the bottom of the hole during the drilling process. To generate the cut these cracks should propagate through the material between each laser drilled hole. Figure 5.4.4 shows an example in which a deviation of the crack propagation path appeared for sample 12. One of the cracks propagated away from the direction of drilled holes. This crack had a significant size which is shown in Figure 5.4.4 as a macro scale crack. There were also multiple small cracks propagating in the vertical direction which was different from the cracks propagating between the other holes.

Unfortunately the laser machining parameters which generated this crack behaviour are unknown, hence they cannot be compared.

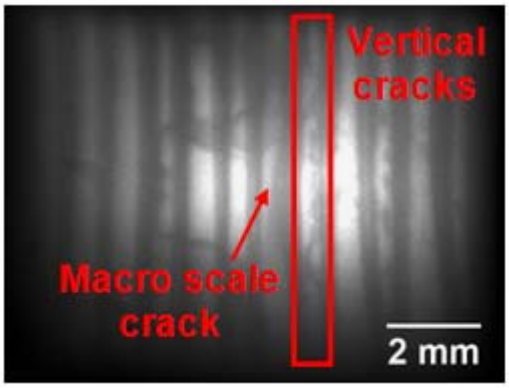

Figure 5.4.4. Laser machined sample 12.

Increasing sample thickness reduced the contrast between the background illumination and the features buried inside, compared to the thinner samples. Consequently spotting the cracks between the holes was becoming more difficult, however still feasible and it required a skilled operator who could identify the changes in light illumination in the image. The inspection of thicker than sample 12 samples showed that the 3Y-TZP thickness limit was 6 mm (sample 9 and other samples tested) which was established by still present light scattering and reduced pixel size of the infrared camera. The image was blurred by the scattered photons and due to large camera pixel size (approximately 50 μm), hence detecting micro scale cracks was limited.

In order to confirm the presence and the size of the detected flaws all the tested samples were sectioned with a diamond saw. An example of the sectioned sample is shown in Figure 3.3.4. The detailed analysis of the method used to determine the cracks existence is presented in chapter 3 (see section 3.3.1). The existence of all the detected cracks was confirmed by samples sectioning. The MIR-TI technique was able to detect cracks resulting from the laser drilling process which provided useful information about the fracture mechanism. The cracks could be detected providing the size was above the measured resolution limit for at least two dimensions of the feature and the maximum thickness for the detection of flaws on the micro scale was limited to 6 mm.

5.4.3. Dental parts inspection

Cracks identified in 3Y-TZP ceramics with the MIR-TI technique were detected due to the localised change in material optical properties in the crack area. The crack/air gap

interface, which introduced a significant refractive index change, led to a change in the spatial profile of the light transmitted through the sample, therefore highlighting or imaging the feature. This phenomenon was presented in section 5.4.2 where the detected cracks consisted of two 3Y-TZP surfaces separated by the air gap.

The effect of a large refractive index difference between the air and the 3Y-TZP explained also what happened when the light was incident on a rough 3Y-TZP surface. An example of how the surface roughness variation influenced the light intensity profile transmitted through sample 8 (see Figure 3.3.1(d)) is presented in Figure 5.4.5. Several features in Figure 5.4.5 (the highlighted regions) were detected by MIR-TI and appeared to be cracks which propagated between the laser drilled holes. Sharp edges on the surface of the sample led to the similar light reflection and refraction effects as cracks buried in the bulk material. The light propagation was deviated which appeared as dark lines in the image which consequently highlighted sharp edges on the surface of the sample.

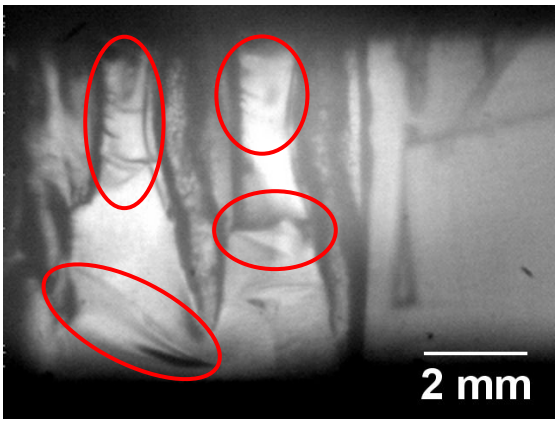

Figure 5.4.5. Light intensity profile on the rough surface of sample 8. In red, the areas where the surface roughness changes were observed.

The microscope images of the potential cracks detected by the MIR-TI technique (see Figure 3.3.3) appeared as cracks, although in fact they only represented the sharp edges of the regions where cracks were propagating. The observed features confirmed that there was a significant impact of the surface position in reference to the light direction of propagation. The discontinuity of the refractive index accompanied by the changing angle of the 3Y-TZP surface enabled the highlighted features to be detected as cracks. The observed edges appeared exactly the same as edges detected after sectioning the fibre laser machined samples. An example of the edges indicating that the crack was propagating between the holes is show in Figure 3.3.5.

The effect of changing angular position of the sample surface with respect to the light travelling through the sample created a challenge of how to distinguish between the buried in the bulk cracks and the surface roughness variation. Due to the low DOF of the MIR-TI system and thanks to in-depth sample scanning, the differentiation of the aforementioned features was possible if the flaws were away from the surface. The situation was more complex when the cracks propagated from the surface into the bulk of the sample. However, if the inspected part had either flaws or burrs on the surface and they were detected by the MIR-TI technique, further inspection could be applied to establish if the detected feature could be detrimental to the sample integrity.

This challenge was brought into prominence with complex dental samples which have many geometrical variables including varying thickness, surface roughness or texture and a complex overall shape. Sample 21 (see Figure 3.5.1) is an example of a 3Y-TZP dental bridge mounted in the billet where a crack was detected. The crack appeared during the sintering stage of manufacturing where the part was transformed into a final hard state. The most common cause for cracking during parts manufacturing are the inhomogeneities in the green state (pre-sintered) material including varying pore sizes, chemical inhomogeneities and density gradients which are transformed into cracks during sintering [33].

Cracks appearing during sintering significantly reduce the strength of the parts, thus the MIR-TI technique was used to attempt to detect these features as a possible means of non-destructive testing and quality control. Figure 5.4.6 presents three MIR-TI images spaced by approximately 1 mm in z axis (in depth). Unfortunately the surface variation impaired the ability to detect the crack, therefore distinguishing it from the background was difficult. The most noticeable feature observed in the images was a considerable roughness of the internal surface of the part. These were grinding marks left by the grinder used to drill out the inner cavity of the part.

The presented example shows that detecting any flaws in the bulk material of a fabricated dental part with a rough surface was challenging because it was difficult to differentiate between the crack and the surface roughness. One of the possible solutions for further investigation is to use multiple illumination points and angles to achieve more uniform light structure. Even with this solution the burrs on the surface would still be visible. The issue may be solved by finding an angle of illumination and an angle for camera where the rough surface marks are not interfering with the MIR-TI

inspection, thus they would not hide any cracks which might be below the grinding marks.

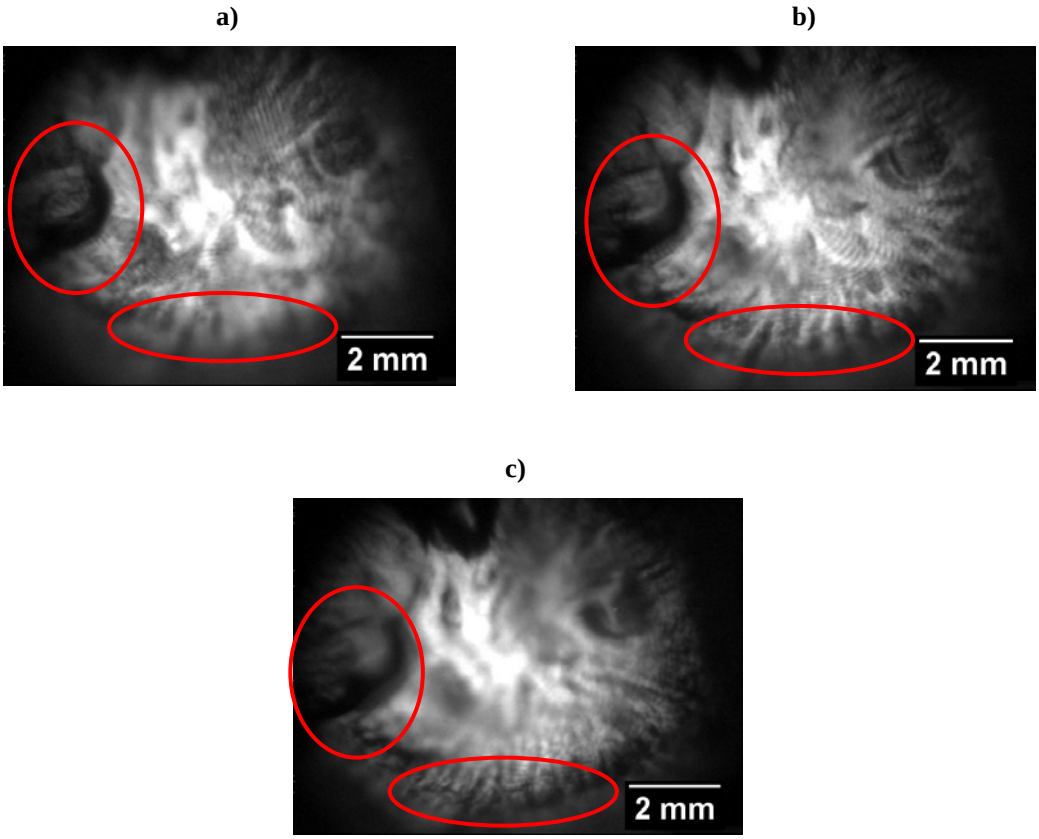

Figure 5.4.6. MIR-TI images of sample 1 spaced by 1 mm in z axis. In red the area where the crack should be detected.

5.4.4. Pre-sintered "brown" state ceramics inspection

The above MIR-TI measurements were performed for the fully sintered hard state ceramics where density reaches 6.02 g/cm^3 [34]. The disadvantage of the hard state 3Y-TZP machining is the time required and the resulting tool wear in achieving the anticipated shape [35]. In addition the heat introduced during machining increases the probability of introducing flaws introduction into the material [36, 37]. This is highly undesirable, hence there is a requirement for an alternative way to machine 3Y-TZP parts.

A possible alternative solution for the fabrication of 3Y-TZP parts is machining the components in the "green" state (see section 2.2) [38, 39]. In order to investigate the feasibility of the MIR-TI technique in inspecting the pre-sintered "brown" state 3Y-TZP ceramics, three samples: 22, 23 and 24 were prepared for the test. Figure 3.5.2(b) presents the "brown" states specimens used during the test. The MIR-TI images of the

"brown" state samples are shown in Figure 5.4.7. To measure the maximum thickness of the sample which could be inspected with the MIR-TI technique black marker labels written on the samples were utilised.

Due to the significantly increased light scattering above the thickness of 1.6 mm, detecting the macro scale label measuring between 1 and 2 mm in width was difficult. Lower material density, pores, and other organic compounds between the grains increased the light scattering (see section 2.4). Therefore the maximum thickness of pre-sintered 3Y-TZP part which can be inspected with MIR-TI technique was reduced by a factor of four compared to hard state 3Y-TZP components. However, dental parts manufactured from 3Y-TZP ceramics rarely reach the thickness above 2 mm [40], thus inspection of pre-sintered dental parts is still feasible.

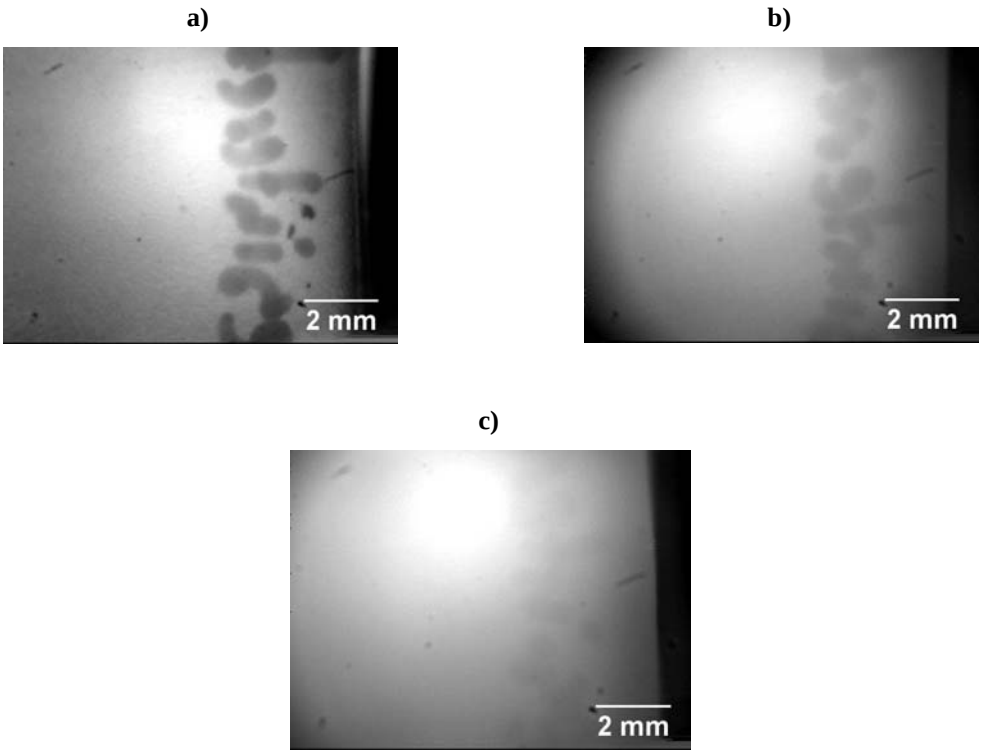

Figure 5.4.7. MIR-TI results for: a) sample 22; b) sample 23 and c) sample 24. Black marker labels written on the samples were used to determine the MIR-TI techniques capabilities in inspecting pre-sintered Y-TZP.

5.5. Conclusions

The MIR-TI technique provided a considerable improvement over visible light inspection. The cost of the MIR-TI system was estimated to be approximately £18,000 for which the most expensive component was Electrophysics infrared camera (approximately £12,000).

The imaging resolution of the MIR-TI system was calculated using a USAF standard measurement with a custom manufactured infrared target. The imaging resolution of 42 ± 5 μm was measured with the USAF infrared target and with the infrared band-pass filter. The main component limiting the MIR-TI technique performance was the infrared camera. Reducing the pixel size could potentially lead to much enhanced imaging capabilities although may add significant cost

In the mid-infrared wavelength region an optical transmission window allowed for the inspection of the 3Y-TZP parts. Successful detection of macro and micro scale features at a depth of up to 6 ± 0.1 mm was feasible. Table 5.2 presents the list of samples tested and the suitability of the MIR-TI technique for 3Y-TZP parts inspection. Details of all the tested samples can be found in chapter 3.

Table 5.2. List of the samples tested with the MIR-TI technique. Colours indicate: green – suitable for 3Y-TZP inspection, orange – limited feedback about the detected feature, red – MIR-TI inspection of the features not possible. Macro features measure more than 1 mm in size and micro scale features measure below 1 mm in at least two dimensions.

Sample	Features inside the sample	MIR-TI inspection feasibility	
6	**1. Micro scale flaws**	**1. Indenter diamond tip detected**	●
7	**1. Macro scale cracks** **2. Micro scale cracks**	**1. Possible** **2. Possible**	● ●
9	**1. Macro scale cracks** **2. Micro scale cracks**	**1. Possible** **2. Possible**	● ●
10	**1. Macro scale cracks**	**1. Possible**	●
12	**1. Macro scale cracks** **2. Micro scale cracks**	**1. Possible** **2. Possible**	● ●
21	**1. Macro scale cracks**	**1. Not possible due to surface roughness**	●
22-24	**1. Macro scale cracks**	**1. Possible – 1.6 mm sample thickness limit – sample 24**	●

In addition to the hard state samples, three pre-sintered parts were inspected. The thickness had to be reduced to 1.6 mm (four times lower than for hard state 3Y-TZP) to detect macro scale features. Furthermore, inspection of a dental bridge with the MIR-TI system was not viable due to high surface roughness of the internal cavities of the tooth.

References:

[1] M. Matysiak, J. P. Parry, J. G. Crowder, D. P. Hand, J. D. Shephard, N. Jones, K. Jonas and N. Weston: 'Development of Optical Techniques for Noncontact Inspection of Y–TZP Parts', *International Journal of Applied Ceramic Technology*, 2011, **8**(1), 140-151.

[2] J. I. Eldridge, C. M. Spuckler and J. R. Markham: 'Determination of Scattering and Absorption Coefficients for Plasma-Sprayed Yttria-Stabilized Zirconia Thermal Barrier Coatings at Elevated Temperatures', *J. Am. Ceram. Soc.*, 2009, **92**(10), 2276-2285.

[3] J. I. Eldridge, C. M. Spuckler and R. E. Martin: 'Monitoring delamination progression in thermal barrier coatings by mid-infrared reflectance imaging', *International Journal of Applied Ceramic Technology*, 2006, **3**(2), 94-104.

[4] J. I. Eldridge, C. M. Spuckler, J. A. Nesbitt and K. W. Street: 'Health Monitoring of Thermal Barrier Coatings by Mid-Infrared Reflectance', in '27th Annual Cocoa Beach Conference on Advanced Ceramics and Composites: A: Ceramic Engineering and Science Proceedings, Volume 24, Issue 3', (ed. H.-T. L. Waltraud M. Kriven), 511-516; 2008.

[5] M. Bashkansky, M. D. Duncan, M. Kahn, D. Lewis Iii and J. Reintjes: 'Subsurface defect detection in ceramics by high-speed high-resolution optical coherent tomography', *Opt. Lett.*, 1997, **22**(1), 61-63.

[6] M. Bashkansky, M. D. Duncan, M. Kahn, J. Reintjes and P. R. Battle: 'Subsurface defect detection in ceramic materials using an optical gated scatter reflectometer', Lasers and Electro-Optics, 1996. CLEO '96., Summaries of papers presented at the Conference on, 2-7 June 1996, 1996, 327-328.

[7] M. Bashkansky, M. D. Duncan and J. Reintjes: 'Rapid, high-resolution optical coherence tomography (OCT) for defect detection in materials', Lasers and Electro-Optics, 1997. CLEO '97., Summaries of Papers Presented at the Conference on, 18-23 May 1997, 1997, 328-329.

[8] M. Bashkansky, M. D. Duncan and J. F. Reintjes: 'Optical gating techniques for material inspection', 1 Sensors and Controls for Advanced Manufacturing, Pittsburgh, PA, USA, 1998, SPIE, 98-106.

[9] M. Bashkansky, D. Lewis Iii, V. Pujari, J. Reintjes and H. Y. Yu: 'Subsurface detection and characterization of Hertzian cracks in Si3N4 balls using optical coherence tomography', *NDT & E International*, 2001, **34**(8), 547-555.

[10] M. Bashkansky and J. Reintjes: 'Statistics and reduction of speckle in optical coherence tomography', *Opt. Lett.*, 2000, **25**(8), 545-547.

[11] J. Veilleux, C. Moreau, D. Lévesque, M. Dufour and M. Boulos: 'Optical Coherence Tomography for the Inspection of Plasma-Sprayed Ceramic Coatings', *Journal of Thermal Spray Technology*, 2007, **16**(3), 435-443.

[12] G. Newaz and X. Chen: 'Progressive damage assessment in thermal barrier coatings using thermal wave imaging technique', *Surface and Coatings Technology*, 2005, **190**(1), 7-14.

[13] M. K. Ferber, A. A. Wereszczak, M. Lance, J. A. Haynes and M. A. Antelo: 'Application of infrared imaging to the study of controlled failure of thermal barrier coatings', *J. Mater. Sci.*, 2000, **35**(11), 2643-2651.

[14] S. Marinetti, V. Vavilov, P. G. Bison, E. Grinzato and F. Cernuschi: 'Quantitative infrared thermographic nondestructive testing of thermal barrier coatings', *Materials Evaluation*, 2003, **61**(6), 773-780.

[15] B. Franke, Y. H. Sohn, X. Chen, J. R. Price and Z. Mutasim: 'Monitoring damage evolution in thermal barrier coatings with thermal wave imaging', *Surface and Coatings Technology*, 2005, **200**(5-6), 1292-1297.

[16] B. Franke, Y. H. Sohn, X. Chen, J. R. Price and Z. Mutasim: 'Thermal Wave Imaging Application in Thermal Barrier Coatings', in 'Advances in Ceramic Coatings and Ceramic-Metal Systems: Ceramic Engineering and Science Proceedings, Volume 26, Number 3', (ed. K. P. Dongming Zhu), 112-119; 2008.

[17] K. J. Singh, Y. Matsuda, K. Hattori, H. Nakano and S. Nagai: 'Non-contact sound velocities and attenuation measurements of several ceramics at elevated temperatures', *Ultrasonics*, 2003, **41**(1), 9-14.

[18] D. Andrews and J. Taylor: 'Quality control of thermal barrier coatings using acoustic emission', *Journal of Thermal Spray Technology*, 2000, **9**(2), 181-190.

[19] E. Hecht: 'Optics (4th Edition)'; 2002, Addison Wesley.

[20] J. Piotrowski and A. Rogalski: 'High-Operating-Temperature Infrared Photodetectors'; 2007, SPIE.

[21] A. Rogalski: 'Infrared Detectors, Second Edition'; 2010, CRC Press.

[22] www.scitec.uk.com.

[23] www.roithner-laser.com.

[24] www.electrophysics.com.

[25] S. Durant, O. Calvo-Perez, N. Vukadinovic and J.-J. Greffet: 'Light scattering by a random distribution of particles embedded in absorbing media: full-wave Monte Carlo solutions of the extinction coefficient', *J. Opt. Soc. Am. A*, 2007, **24**(9), 2953-2962.

[26] D. J. Spencer, G. C. Denault and H. H. Takimoto: 'Atmospheric Gas Absorption at Df Laser Wavelengths', *Appl. Optics*, 1974, **13**(12), 2855-2868.

[27] www.microscopyu.com.

[28] C. P. Schillaber: 'Photomicrography In Theory and Practice'; 1944, New York, J. Wiley & Sons, Inc.; London, Chapman & Hall, Limited.

[29] M. Matysiak, J. P. Parry, F. Albri, J. G. Crowder, N. Jones, K. Jonas, N. Weston, D. P. Hand and J. D. Shephard: 'Infrared confocal imaging for inspection of flaws in yttria-stabilized tetragonal zirconia polycrystal (Y-TZP)', *Measurement Science and Technology*, 2011, **22**(12), 125502-125511.

[30] D. L. Wood, K. Nassau and T. Y. Kometani: 'Refractive-Index of Y2o3 Stabilized Cubic Zirconia - Variation with Composition and Wavelength', *Appl. Optics*, 1990, **29**(16), 2485-2488.

[31] D. L. Wood and K. Nassau: 'Refractive-Index of Cubic Zirconia Stabilized with Yttria', *Appl. Optics*, 1982, **21**(16), 2978-2981.

[32] J. Parry, R. Ahmed, F. Dear, J. Shephard, M. Schmidt, L. Li and D. Hand: 'A Fiber-Laser Process for Cutting Thick Yttria-Stabilized Zirconia: Application and Modeling', *International Journal of Applied Ceramic Technology*, 2010, no-no.

[33] P. Duran, M. Villegas, F. Capel, J. Fernandez and C. Moure: 'Nanostructured and near defect-free ceramics by low-temperature pressureless sintering of nanosized Y-TZP powders', *J. Mater. Sci.*, 1997, **32**(17), 4507-4512.

[34] R. Singh, C. Gill, S. Lawson and G. P. Dransfield: 'Sintering, microstructure and mechanical properties of commercial Y-TZPs', *J. Mater. Sci.*, 1996, **31**(22), 6055-6062.

[35] F. C. Dear: 'Laser Machining Of Medical Grade Zirconia Ceramic For Dental Reconstruction Applications', PhD thesis, Heriot Watt University, Edinburgh, 2008.

[36] T. Kosmac, C. Oblak, P. Jevnikar, N. Funduk and L. Marion: 'The effect of surface grinding and sandblasting on flexural strength and reliability of Y-TZP zirconia ceramic', *Dental Materials*, 1999, **15**(6), 426-433.

[37] T. Kosmac, C. Oblak and L. Marion: 'The effects of dental grinding and sandblasting on ageing and fatigue behavior of dental zirconia (Y-TZP) ceramics', *Journal of the European Ceramic Society*, 2008, **28**(5), 1085-1090.

[38] R. M. C. Sasahara, H. N. Yoshimura, C. Fredericci, A. Calasans, P. F. Cesar and A. L. Molisani: 'Development of Y-TZP Pre-Sintered Blocks for CAD-CAM Machining of Dental Prostheses', *Advanced Powder Technology Vi*, 2008, **591-593**, 712-716.

[39] X. Wang, J. D. Shephard, F. C. Dear and D. P. Hand: 'Optimized Nanosecond Pulsed Laser Micromachining of Y-TZP Ceramics', *J. Am. Ceram. Soc.*, 2008, **91**(2), 391-397.

[40] N. Jones: Personal communication, 2010.

6. Confocal Mid-Infrared Transmission Imaging

6.1. Introduction

This chapter presents the development process for a Confocal Mid-Infrared Transmission Imaging (CMIR-TI) [1] technique and the results subsequently obtained with this new system. The MIR-TI technique presented in the previous chapter provided significantly enhanced capabilities in inspection of highly scattering 3Y-TZP ceramics. Nevertheless, the high cost of MIR-TI technique components, particularly the camera, and the limited resolution for the crack detection due to infrared camera pixels size provided an opportunity for further improvements in 3Y-TZP ceramics inspection.

Confocal microscopy for high resolution imaging has been introduced into a variety of fields, particularly in biology and medicine where highly scattering materials are common and has proven to be an accurate and robust inspection tool [2-5]. Highly scattering 3Y-TZP ceramics present similar imaging challenges compared to substances measured in biology, therefore the CMIR-TI technique has the potential for high resolution imaging of thick 3Y-TZP ceramic components. However, the main drive in approaching the confocal imaging was the potential to significantly reduce the cost of the whole system. The most expensive component in the Mid-Infrared Transmission Imaging (MIR-TI) system was the camera. Here, by using a much smaller size detector, the cost of the system was considerably reduced.

6.2. Instrument characterisation

Confocal imaging provides several advantages over conventional optical imaging. The main advantage of the confocal technique, particularly for detecting flaws in the bulk material, is the ability to collect a series of optical sections from thick specimens. Slicing the volume of the tested sample during imaging has a significant advantage. To add more the depth of each slice is well controlled, thus the out of focus light is rejected and the imaging quality is improved. In this paragraph the developed Confocal Mid-Infrared Transmission Imaging (CMIR-TI) setup is discussed. The system components and the main parameters are presented and calculated.

6.2.1. CMIR-TI setup

The developed setup is based on the MIR-TI system (see Figure 5.3.1). Other than the infrared source, which was mounted in the elliptical reflector (instead of the parabolic reflector used in MIR-TI setup) to focus down the infrared beam, the two lenses imaging the sample onto the pinhole were arranged identically to the MIR-TI technique. The infrared camera (detectivity of 1×10^{9} cm·Hz$^{1/2}$/W) was replaced with a high detectivity (5×10^{11} cm·Hz$^{1/2}$/W) Vigo PVI-2TE-8 infrared detector [6]. The detector was based on a $Hg_{1-x}Cd_xTe$ photodiode with an absorber structure. The response time of the detector was below 7 ns. The active region measured 300 µm x 300 µm and was optically immersed in a high refractive index GaAs hyperhemispherical lens (refractive index of the lens n = 3.3) [7]. A hyperhemispherical lens is characterised by a wide field of view (FOV) reaching theoretically 180º but in practice was limited by the detector casing and the optics. For the detector used in the experiments the available light cone was approximately 70º.

The 300 µm x 300 µm detector area allowed some flexibility in choosing the pinhole size used during sample scanning. In addition the CMIR-TI system alignment was simplified due to the large detector active region. On the other hand the light intensity reaching the detector (that passes thorough a small pinhole) was dissipated over a relatively large region (compared to the pinhole size used) which led to reduced signal-to-noise (SNR) value, particularly when the signal was weak. However, for the feasibility study of CMIR-TI technique and the flexibility in investigating various pinhole sizes the 300 µm square detector was chosen. Figure 6.2.1 presents the detectivity [8] and Figure 6.2.2 shows the picture of the whole Vigo system including the power supply.

The detectivity, D, of the sensor was the reciprocal of the Noise Equivalent Power (NEP) [9]. NEP is the incident power on the detector generating an output signal equal to the root mean square (RMS) output noise, i.e. the signal level that produces a SNR of 1. NEP is proportional to the square root of the detector signal which is proportional to the detector area A_d. Normalised detectivity D* , which depends on detector area, A_d, was used to compare the MIR-TI technique infrared camera and Vigo sensors and is defined by equation (6.1) [9].

$$D^* = \frac{(A_d \Delta f)^{1/2}}{NEP} \qquad (6.1)$$

where Δf is effective noise bandwidth. The advantage of D* is the fact that it allowed detectors of different active regions to be compared. The detector used in the CMIR-TI had a higher detectivity compared to that of the camera sensor used in the MIR-TI and consequently this led to a higher SNR and therefore an improved resolution.

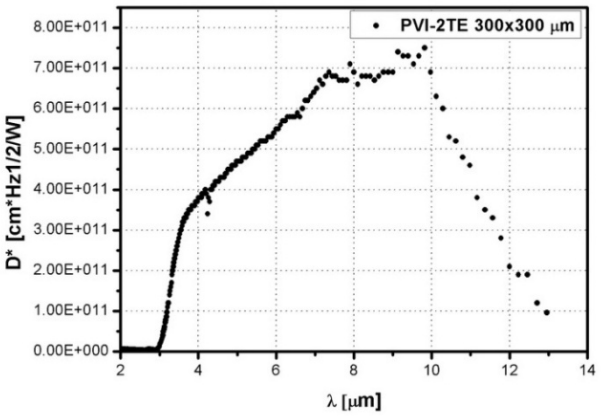

Figure 6.2.1. Operating wavelength range of Vigo PVI-2TE-8 detector; detectivity as a function of wavelength.

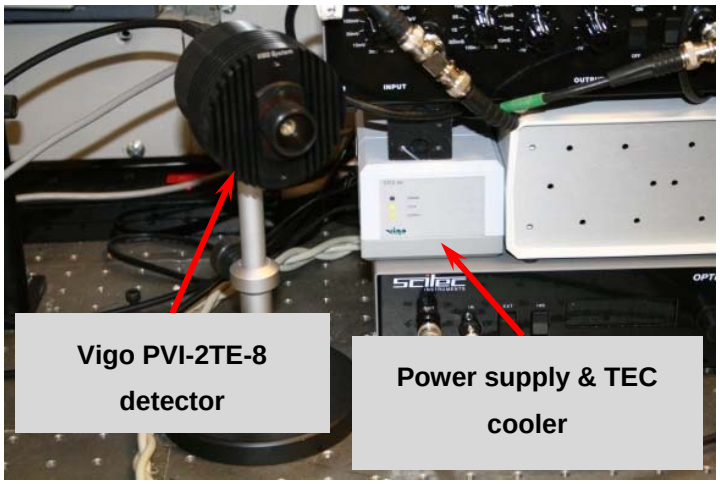

Figure 6.2.2. Vigo PVI-2TE-8 system.

The detector operated between 3 µm and 9 µm which was suitable for 3Y-TZP ceramics inspection given the measured transmission window (see Figure 3.1.4). The detector was cooled with a thermoelectric cooler (TEC) which was integrated into the casing. The chopped AC signal captured by the detector was amplified by an integrated, custom bandwidth (200 Hz to 10 kHz) preamplifier. The detector operated in AC mode to reduce any heat related noise influenced by the constant DC operation. Therefore, the signal reaching the detector was modulated using a Scitec 300CD mechanical chopper. Depending on the chopping disc mounted the frequency ranged between 0.015 Hz and

40 kHz. The pre-amplified output signal of the detector was expressed in volts. The chopper and the detector were connected to the analogue lock-in amplifier (Scitec Instruments Model 420) which was introduced to further enhance the signal stability, reduce any external noise and to amplify the input signal. The lock-in amplifier gain helped to enhance the signal from the background and it filtered out some of the background noise and increases the SNR of the whole system. The gain and the lock-in integration time were the two parameters which had to be optimised to enhance the CMIR-TI system response. The optimisation process of the lock-in amplifier is described later after the optimisation of pinhole size is determined.

Confocal imaging uses pinhole light filtering which combined with a pinhole or sample movement allows for pixel-by-pixel imaging of the whole specimen. The pinhole is an integral part of the confocal system and it determines the resolution and the quality of the imaging. Initially a 50 µm pinhole, which is similar in diameter to the MIR-TI camera pixel size of 48.5 µm, was mounted in the system to compare the results between CMIR-TI and MIR-TI techniques.

At first the confocal setup presented in Figure 6.2.3 was considered for 3Y-TZP inspection. The pinhole mounted in front of detector limited the light reaching the detector and the chopper provided an AC signal as required. The optimal distance of 820 µm (Figure 6.2.4) between the detector and the pinhole, was calculated in order to maximise the light acquired by the detector. Maximising the coverage of the detector active region was important due to the reduced noise because the non-illuminated detector area was minimised, therefore there was no random signal contributing to the overall light acquired.

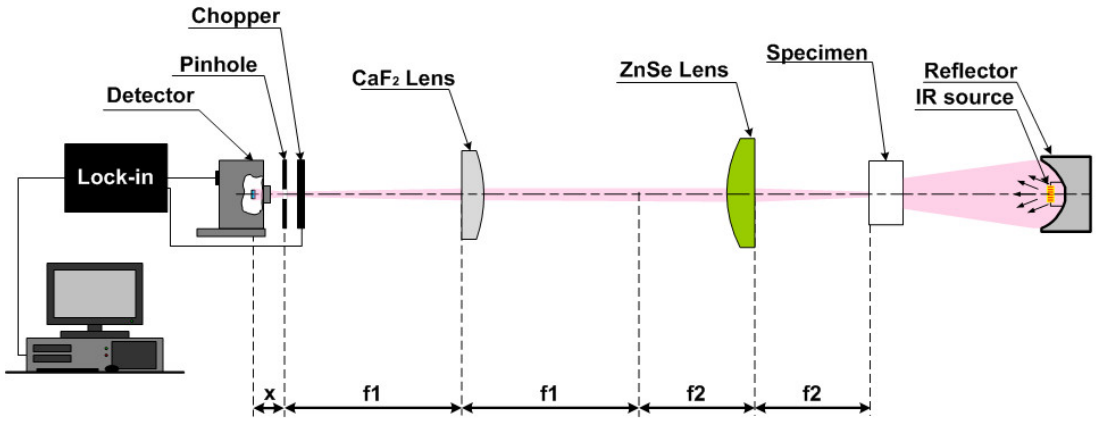

Figure 6.2.3. Initial CMIR-TI setup. The focal lengths of the lenses were as follows: f1 = 50 mm, f2 = 38.1 mm.

Figure 6.2.4 presents the experimental setup where the pinhole is mounted in front of the infrared detector. The light cone area on the CaF_2 lens was estimated from equations below but first a 1 inch aperture in front of the lens was introduced to estimate the effective numerical aperture NA of the CaF_2 lens. The aperture was positioned 1 mm from the curved optical surface of the CaF_2 lens on the optical axis of the CMIR-TI system. While closing the aperture a drop in light intensity was observed. The aperture was closed at 18 mm, where a 5% drop in signal was observed. This value of 18 mm was taken as the aperture of the CaF_2 lens.

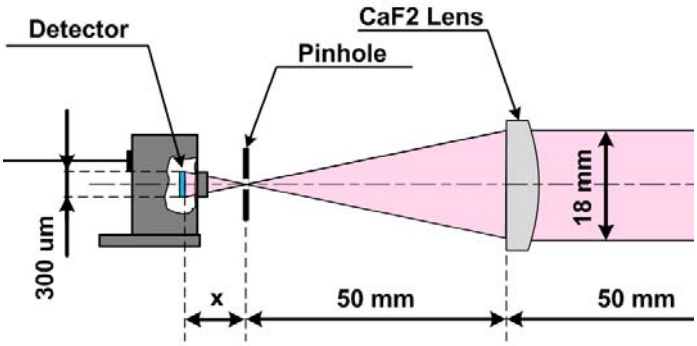

Figure 6.2.4. An estimation of the optimal distance between the pinhole and the infrared detector active region.

The effective numerical aperture NA of CaF_2 of 0.18 was then estimated from equation (5.5), where dia was 18 mm and f_x was the focal length of the CaF_2 lens. To simplify the calculations the diffraction on the pinhole was ignored. Therefore, the effective NA of the light reaching the detector was 0.18 and the distance x between the pinhole and the detector was calculated from equation (6.2) to be 820 µm.

$$NA = \sin[\arctan(\frac{A_d}{2 \cdot x})] \qquad (6.2)$$

where A_d was the diameter of the detector area. Due to the construction of the TE-8 detector packaging the active region was 9 mm away from the BaF_2 front window. The calculated distance between the pinhole and the active region on the other hand should be 820 µm to capture most of the light transmitted through the pinhole. Such a high difference required some changes in the CMIR-TI setup. Therefore, an additional 4-f lens setup was introduced to extend the required distance between the pinhole and the detector. The setup with the additional 4-f lenses is shown Figure 6.2.5.

The additional 4-f lens setup consisted of two CaF_2 lenses (1" and 0.5" diameter lenses) which imaged the pinhole onto the detector with an image magnification of 2. The magnification was calculated using equation (5.1). The magnified pinhole image reduced the irradiance of the infrared radiation reaching the detector (reduced SNR) but on the other hand the detector was less susceptible to picking up any external noise, including the temperature and lighting variations in the lab because the active region was illuminated. Irradiance is the power of electromagnetic radiation per unit surface area [10]. Therefore an increased area of illumination causes reduced light intensity at the detector.

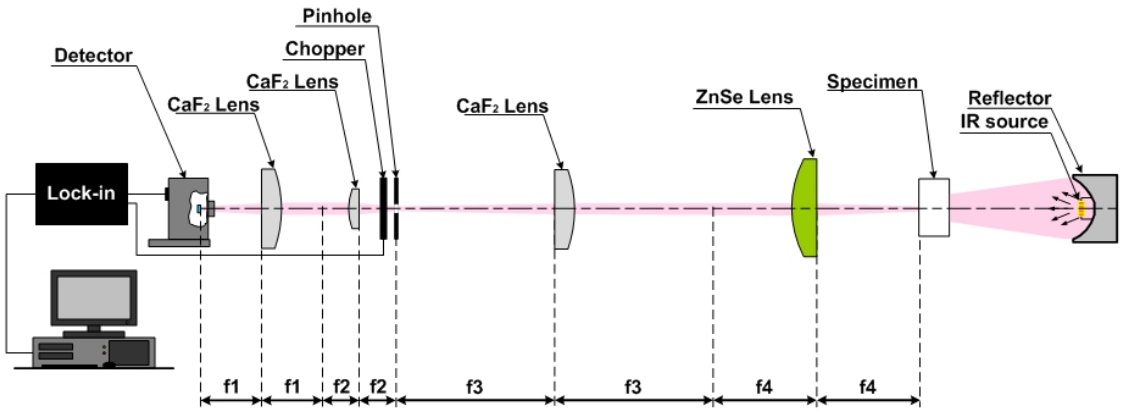

Figure 6.2.5. CMIR-TI setup. Focal lengths of the lenses were as follows: f1 = 40 mm, f2 = 20 mm, f3 = 50 mm, f4 = 38.1 mm.

The developed CMIR-TI system used a controlled movement of the sample to scan the whole area of the samples. Consequently, during the measurements the samples were mounted on three Standa 8MT173-30DCE (DC) motorised translation stages with 30 mm travel. The stages provided xyz movement of the samples during the scanning process with resolution of 100 nm. The minimum motion step was 140 nm and the bi-directional repeatability reached 400 nm. During the measurements the speed of movement of the stages was set to 160 μm/s and the movement sequence was controlled via a Labview program. Additionally, the Labview program also controlled the DC lock-in output acquisition via a USB-6008 12-bit National Instruments data acquisition card.

Figure 6.2.6 presents the stages arrangement and the scanning technique sequence (the number order in the figure) chosen for the CMIR-TI system. In this instance raster scanning chosen for the CMIR-TI technique allowed for fast imaging of the xy planes. It also reduced the z position error and it decreased the wear of y and z stages carrying

more weight. Throughout the experiments there were substantial issues with the reliability of the Standa stages, hence to maximise the lifetime of the motorised stages the movement algorithm had to be analysed and optimised in great detail. The x stage was the stage that failed most frequently as it was the stage which was moving back and forth constantly throughout the scans (see Figure 6.2.6).

With this setup the x stage was carrying the weight of the stage itself, the sample holder and the specimen tested so it was not thought that there was excessive load on the stage. The possible cause of poor stage reliability was their design. An excessive heat generated in the motor when the stage was operating for more than several hours was observed. All the stage failures were caused by the motor failure. The manufacturer replaced the stages several times but failures still occurred. For future systems an alternative motorised stage should be implemented.

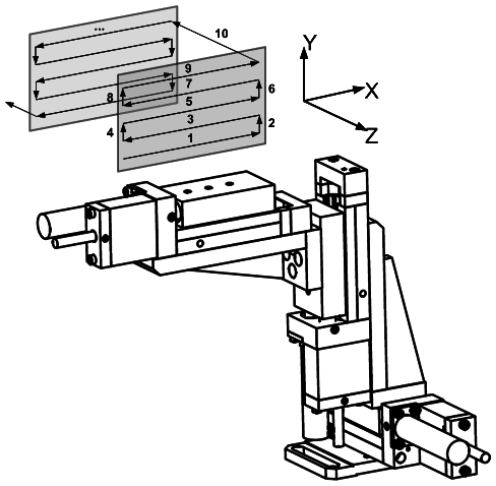

Figure 6.2.6. CMIR-TI scanning sequence. The numbers represent the sequence of the xyz stages movement.

6.2.2. CMIR-TI pinhole size optimisation

The CMIR-TI technique used a pinhole scanning technique to produce a pixel-by-pixel image of the tested sample. Pinhole size had a big impact on the acquired image quality, particularly when measuring highly scattering ceramics. It acted as a filter which cut out the scattered photons, and the out of focus light, thus the pinhole increased the image contrast. At the same time the pinhole reduced the signal reaching the detector due to the limited aperture for light to pass through (see Figure 6.2.7), therefore there was balance between image contrast and signal strength when selecting the pinhole size.

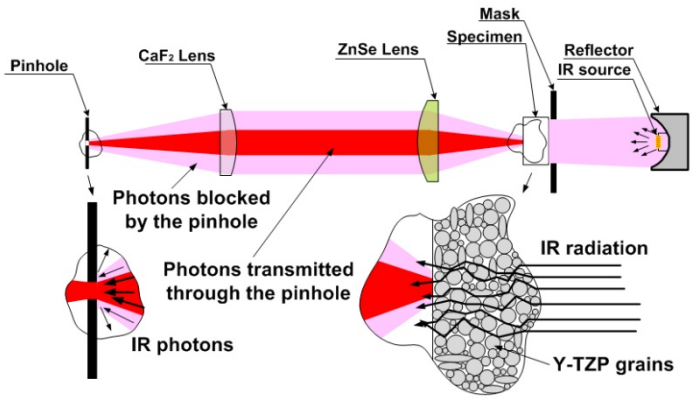

Figure 6.2.7. Schematic of the photons scattered by 3Y-TZP grains and blocked by the pinhole.

Three pinhole sizes: 100 µm (Thorlabs P100S), 50 µm (Thorlabs P50C) and 25 µm (Thorlabs P25C) were tested to investigate the smallest pinhole size which provided high resolution, high contrast images. A reduction of the pinhole diameter by a factor of two reduced the area of the pinhole by a factor of four. This resulted in a fourfold reduction of signal level.

To determine the optimal pinhole size sample 7 from Figure 3.3.1(c) was used as the test target. Three step size scanning methods 50, 25 and 10 µm were used during the experiment. For steps smaller than the actual pinhole size the step overlapping technique was applied. The results of the scanning process for 100 and 50 µm pinhole configurations are presented in Figure 6.2.8. There are no results shown for 25 µm because the images appeared black due to too low signal reaching the detector.

The reduction of the pinhole size offered improved image sharpness as did the reduced step size. The scanning process with 100 µm pinhole and 10 µm steps provided a comparable result to the 50 µm pinhole and 10 µm scanning but the blurring effect was more noticeable with the 100 µm pinhole. The reduced pinhole size provided sharper images due to the decreased amount of out-of-focus photons contributing to the blurring effect as shown in Figure 6.2.9. On the other hand the decreased number of photons reduced the maximum sample thickness which could be tested.

The reduction of the pinhole size to 25 µm led to significant signal decay where nothing was visible in the image and implied a pinhole size limit for the CMIR-TI setup. Apart from photon filtration the enhanced image quality was also influenced by an increased number of data points acquired. Each data point was used to generate the image as a light intensity map acquired during the measurement. For the purpose of the experimental part, based on the results presented in Figure 6.2.8, a 50 µm pinhole was applied for all the measurements.

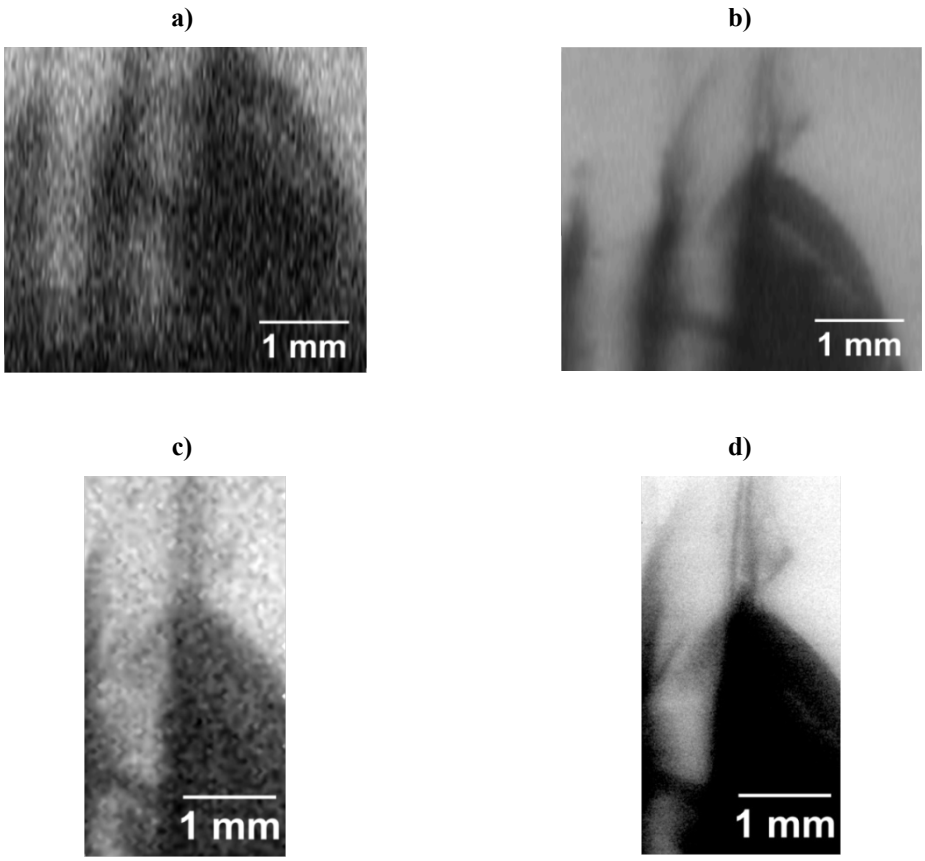

Figure 6.2.8. The results of CMIR-TI scanning of sample 7 with: a) 100 µm pinhole, 100 µm scanning steps in x and in y axis; b) 100 µm pinhole, 10 µm scanning steps; c) 50 µm pinhole and 50 µm scanning steps; d) 50 µm pinhole and 10 µm scanning steps.

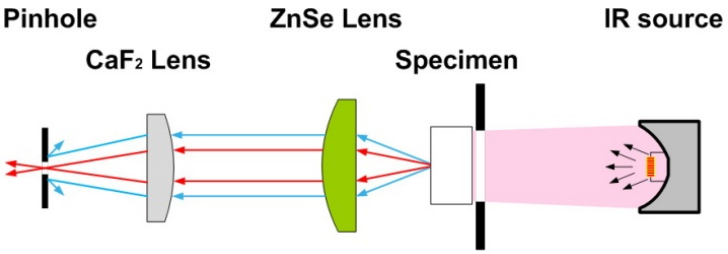

Figure 6.2.9. Confocal pinhole scanning. Photons which were out of focus were blocked by the pinhole.

6.2.3. Optimisation of lock-in amplifier parameters

Lock-in amplifiers are used to detect and measure low level, noisy signals [11]. By only applying a specific modulation to the signal of interest this signal is amplified and detected. In practice noise still contributes in the signal amplification, thus the low level signal acquisition capabilities of lock-in amplifiers are limited. The Scitec Instruments Model 420 lock-in amplifier employed in the CMIR-TI setup operated as a filter before the signal was acquired and stored by data acquisition software. Lock-in amplifiers use a technique known as phase-sensitive detection [12] to single out the

component of the signal at a specific reference frequency and phase. Signals at frequencies other than the reference frequency, are rejected and do not influence the measurement. The lock-in input consists of the desired signal and the unwanted noise. The noise is represented as varying signals at all frequencies. The ideal lock-in filtering responds only to the noise at the reference frequency. The noise at other frequencies is removed by the low-pass filter.

In order to maximise the efficiency of lock-in signal filtering the optimisation process was carried out. It was necessary to evaluate the optimal sensitivity S and integration time $T_{lock\text{-}in}$ of the device to maximise the SNR of the signal. The S parameter determined the lock-in input signal gain (g). S is the value of the input signal required to give 1 V output signal. A lower value of S gave a higher gain. For example, with S = 300 μV the signal gain was 3333 (i.e. 300 μV input signal resulted in a 1 V output signal) compared to a gain of 10 000 for S = 100 μV (i.e. 100 μV input signal resulted in a 1 V output signal). This was expressed as:

$$V_0 = \frac{V_1}{g} \tag{6.3}$$

where V_0 was the lock-in input voltage , V_1 was the lock-in output voltage and g was the lock-in signal output gain. In addition to the signal itself the noise buried in the amplified signal and the noise from the lock-in were also amplified. For that reason choosing the optimal gain which resulted in an improved ratio between the measured signal and the noise was crucial to enhance the CMIR-TI technique capabilities.

The integration time $T_{lock\text{-}in}$ was another fundamental lock-in parameter which determined over what time period a single lock-in output data point was acquired. Increasing the value of $T_{lock\text{-}in}$ led to longer data acquisition and the measured signal was averaged by longer period of time. With longer data acquisition the noise and signal stability could be enhanced. Chopping frequency $f_{chopper}$ determined by Scitec 300CD chopper was another lock-in parameter which was interdependent with lock-in integration time $T_{lock\text{-}in}$. It determined the number of input signal periods N acquired in fixed amount of time per single output data point. Equation (6.4) presents the relation between the three aforementioned parameters.

$$N = T_{lock-in} \cdot f_{chopper} \tag{6.4}$$

The higher the N value the better the image quality because signal level deviation is reduced with an increased number of samples acquired due to an increased signal averaging. To enhance the SNR of the acquired signal a 1.6 kHz chopping frequency was set throughout the experiments because more stable operation of the chopper motor was observed compared to the lower frequencies. In addition, this frequency was chosen to minimise the 1/f noise produced in the detector (see section 2.8).

To determine the optimal $T_{lock\text{-}in}$ and S parameters for CMIR-TI technique the system was tested with sample 7 with the infrared source current set to 1.8 A. The chopping frequency was fixed at 1.6 kHz and only $T_{lock\text{-}in}$ and S parameters were changed. The data for each of the settings was acquired for approximately 12 seconds using a custom Labview program. The data was saved into a text file. Each data point was acquired at an interval determined by the lock-in integration time $T_{lock\text{-}in}$. For example if $T_{lock\text{-}in}$ was set to 30 ms, the program acquired the data points every 30 ms.

Figure 6.2.10 presents the signal characteristics for the range of S and $T_{lock\text{-}in}$ values. With the S values of 300 μV and 1 mV the detected signal was close to 0 because the lock-in gain was too low for this particular light intensity transmitted through the sample. The increased gain with the reduced lock-in S value from 1 mV to 30 μV significantly increased the signal level. However, this highlighted how much the signal was fluctuating. Increasing the lock-in averaging time improved the signal stability. Particularly noticeable was the difference in signal stability between $T_{lock\text{-}in}$ = 30 and 100 ms.

In Figure 6.2.10(c) the lock-in amplifier was overloaded due to too high a DC noise component. For $T_{lock\text{-}in}$ = 100 ms and S = 30 μV a significant increase of DC signal offset was observed due to the ambient thermal noise. The DC noise was attributed to infrared radiation being reflected from the chopping disc. The light reflecting off the chopping disc was guided towards the detector and because the reflection was from the chopping disc this noise was modulated with the same frequency as the reference signal. The DC component was therefore reduced by mounting the chopper at an angle (Figure 6.2.11).

The CMIR-TI setup was installed on a bench near the electronic equipment which heated up during operation. In addition, the chopping motor heated up significantly during the measurements. Therefore, these were other possible sources of noise. The detector operated up 9 μm, which based on Wien's displacement law [10] would result in temperature of 322 K (48.82°C) and higher for a perfect black body. The infrared

radiation reflected and chopped by the chopping disc had exactly the same frequency as the measured signal, hence it could not be filtered out. Increasing the lock-in gain increased the signal level including the DC noise component, thus a DC offset in the graphs is present, particularly in Figure 6.2.10(c).

a)

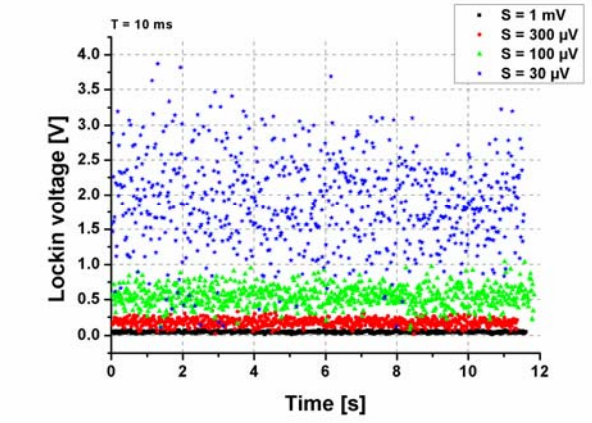

b)

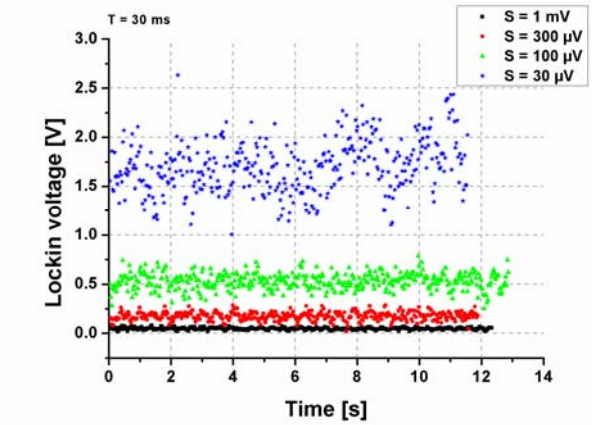

c)

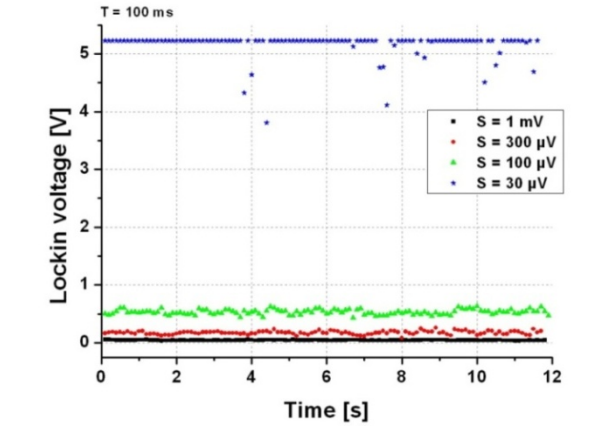

Figure 6.2.10. Signal level fluctuations as a function of varying sensitivity and lock-in integration time. Lock-in integration time: a) $T_{lock\text{-}in}$ = 10 ms; b) $T_{lock\text{-}in}$ = 30 ms; c) $T_{lock\text{-}in}$ = 100 ms.

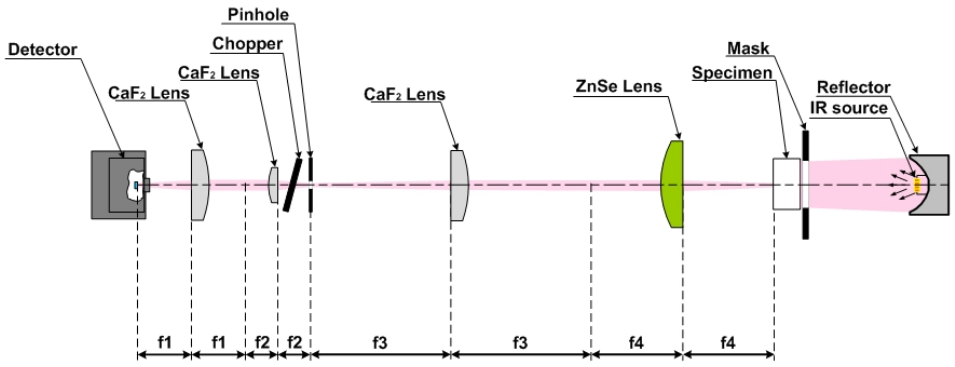

Figure 6.2.11. The top view of the CMIR-TI setup after mounting the chopper under an angle.

Other than heat generated by the nearby electrical devices, another source of noise was the changing ambient temperature in the lab. Therefore during further measurements the setup was isolated from the light illumination and changing ambient temperature by covering the whole setup with a cardboard box.

Table 6.1 presents the statistical analysis of the signals from Figure 6.2.10. The above observation that the most noticeable signal stability improvement was for $T_{lock\text{-}in}$ between 30 and 100 ms was confirmed by the Relative Standard Deviation (RSD) results which were calculated from equation (6.2). RSD is used as an accurate signal noise level estimator [13], thus the RSD results are presented in Table 6.1.

Table 6.1. Statistical analysis of the signals presented in Figure 6.2.10 for $f_{chopper}$ = 1.6 kHz.

$T_{lock\text{-}in}$ [ms]	S	Mean [V]	Standard Deviation (σ)	RSD [%]	SNR
10	1 mV	0.048	0.015	31	3.2
	300 µV	0.181	0.049	27	3.7
	100 µV	0.551	0.144	26	3.8
	30 µV	1.893	0.622	32	3.0
30	1 mV	0.048	0.012	25	4
	300 µV	0.180	0.043	24	4.2
	100 µV	0.530	0.08	15	6.6
	30 µV	1.704	0.266	16	6.4
100	1 mV	0.045	0.004	9	11.25
	300 µV	0.172	0.015	9	11.5
	100 µV	1.772	0.144	8	12.3
	30 µV	-	-	-	

Apart from RSD a Signal-to-Noise Ratio (SNR) was used to highlight output signal changes with the changing lock-in parameters (see Table 6.1). SNR (see equation (6.5)) is defined as the power ratio between a signal P_{signal} (meaningful information) and the background noise P_{noise} which can also be expressed as Mean of the signal to signal standard deviation σ. For the signal acquired by the CMIR-TI system the power of the signal and the noise was represented in volts.

$$SNR = \frac{P_{signal}}{P_{noise}} = \frac{Mean}{\sigma} \qquad (6.5)$$

The SNR values presented in Table 6.1 were calculated from equation (6.5). The RSD calculations presented in Table 6.1 showed a decrease in relative signal variation with reduced S value (increased gain) for S = 1 mV, 300 μV and 100 μV. The results confirmed the advantages of using a lock-in amplifier for low level signal detection because the increased gain provided lower signal fluctuation which was confirmed by the enhanced SNR of the signal. Unfortunately increasing the lock-in gain (reducing S) came at a cost of increased noise level due to the much higher sensitivity of the detector to any external and internal noise (see section 2.8), hence for S = 30 μV the RSD and SNR factors indicated that the signal quality deteriorated.

The results showed also that increasing the $T_{lock\text{-}in}$ improves the signal quality. $T_{lock\text{-}in}$ was set to 30 ms (because during the experiments no significant improvement in image quality was observed) to investigate the influence of varying the S parameter on the quality of the CMIR-TI technique images. Furthermore, the integration time of 30 ms provided a good quality signal and any additional reduction of $T_{lock\text{-}}$in was not necessary due to low speeds of the stages. If the stages moved faster the $T_{lock\text{-}in}$ parameter should be reduced in order to keep the same value of N.

With the velocity of the motorised stages set to 160 μm/s throughout all the experiments a value of N = 48 was calculated from equation (6.4). With the N value set the optimal sensitivity, S parameter, was investigated. The chopper frequency remained at 1.6 kHz and the lock-in integration time $T_{lock\text{-}in}$ was set to 30 ms. The step size of the stages was set to 10 μm in x and in y axes. The results for varying S are presented in Figure 6.2.12 where sample 7 with laser machined holes was inspected.

The results from Table 6.1 implied that changing the S value influences the signal stability. If S was set to 1 mV the SNR was reduced (see Table 6.1, $T_{lock\text{-}in}$ = 10, 30 and

100 ms). However if the gain was increased too much (S = 30 μV) it was observed that noise contributed more in the image. This can be seen particularly for T = 10 ms in Table 6.1 where for S = 30 μV the RSD increases and the SNR falls and in Figure 6.2.12(a) where the image quality is relatively poor. Good image quality was achieved for S = 100 μV and 300 μV. Increasing the gain to high (S = 30 μV) led to reduction in signal quality (see Table 6.1), however the reduction of image quality was more evident. It should be noted that the measurements from Figure 6.2.10 were carried out without any sample, where in Figure 6.2.12 sample 7 was inspected. This reduced the signal level acquired by the detector, thus it was more susceptible to noise. Furthermore, the RSD and SNR values calculated in Table 6.1 were estimated based on the average signal fluctuation values which aim was to indicate that with changing lock-in parameters the acquired signal characteristics change as well. The jitter noticeable in Figure 6.2.12(b) and (c) was caused by the poor bi-directional repeatability of the x motorised stage which failed later during the experiments.

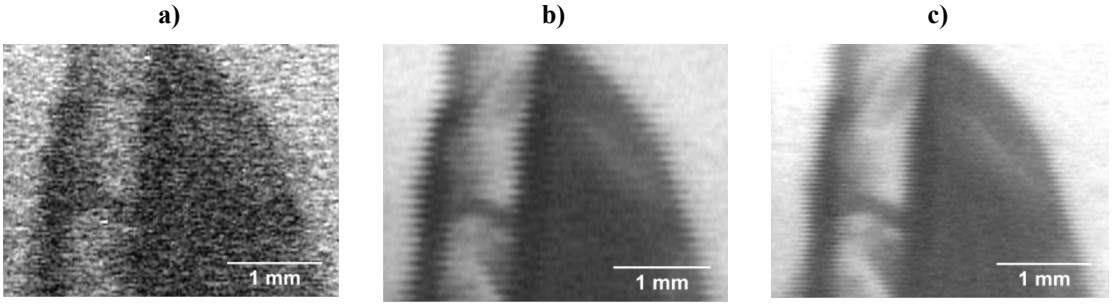

Figure 6.2.12. Image quality as a function of the lock-in sensitivity S: a) S = 30 μV; b) S = 100 μV; c) S = 300 μV for $f_{chopper}$ = 1.6 kHz and $T_{lock\text{-}in}$ = 30 ms.

The S = 100 μV and 300 μV were used interchangeably during the experiments depending on the sample thickness. Increasing the thickness of the sample resulted in a lower signal reaching the detector. For the 4 mm thick samples above the value of S that produced an acceptable image contrast was 100 μV without the need to use higher gain. For the sample 7, S = 300 μV was the most optimal value because the image in Figure 6.2.12(c) was of best quality. The lock-in gain of 3333 (S = 300μV) produced the output signal in a range between 0.1 and 0.5 V. Therefore the actual signal before the lock-in amplifier was between 30 and 150 μV based on equation (6.3). For $f_{chopper}$ = 1.6 kHz, S = 300 μV and $T_{lock\text{-}in}$ = 30 ms the signal variation during the measurement reached ± 22% from the average value. With that level of signal variation for the signal voltage range between 30 and 150 μV, the noise level range was ± 6 to 33μV. Such

levels of noise were noticeable in the images, therefore choosing the correct plotting method which could potentially reduce the noise during image generation was essential.

6.2.4. CMIR-TI automation and control

The assembled CMIR-TI system was controlled from the developed Labview program. The software controlled the movement of the motorised stages and the data acquisition. It provided flexibility in choosing the movement sequence of the stages, the stage step size, step tolerance and the distance of travel. The step tolerance was introduced due to the limited response time of the software. The software repeatedly sent the stage position request and the response of the stage controller was limited by the serial port bandwidth. Therefore an additional ± 3 to 5 μm step tolerance depending on the stages velocity was introduced. This brought in additional challenges particularly when plotting the data because of the irregular pitch of the data points. The image plotting algorithm is presented in section 6.2.5.

In addition to the motorised stage control the Labview program was also responsible for the data acquisition. The voltage detected and amplified by the lock-in was acquired by the data acquisition card. Therefore, not only were the stage x, y, z positions saved but also at each step the signal voltage was stored in a text file. The text file where data was stored was defined in the program by the file name and the path to that file. The new file was generated every time the z axis stage position changed, thus in each file the data for a single sample slice (plane) was stored. Every time the z stage position changed a number next to the file name was incremented by one. This helped to plot the images of each of the sample slices acquired during the inspection.

6.2.5. CMIR-TI – processing of the acquired data

The CMIR-TI system operated in semi-automatic mode. The scanning process and the data acquisition were controlled automatically but the data processing and image generation were performed using Matlab software. Matlab provided flexibility in choosing the data plotting technique, therefore it was used to generate the images. Two approaches were considered as optimal image generation techniques: “griddata” and “scatter” commands. Both of them allowed for image generation from the acquired non-uniform grid of data points. This was caused by the step tolerance implemented during the stage movement (see section 6.2.4). A simple example of the plotting

process for several data points is presented in Figure 6.2.13 where "scatter" and "griddata" command results are presented.

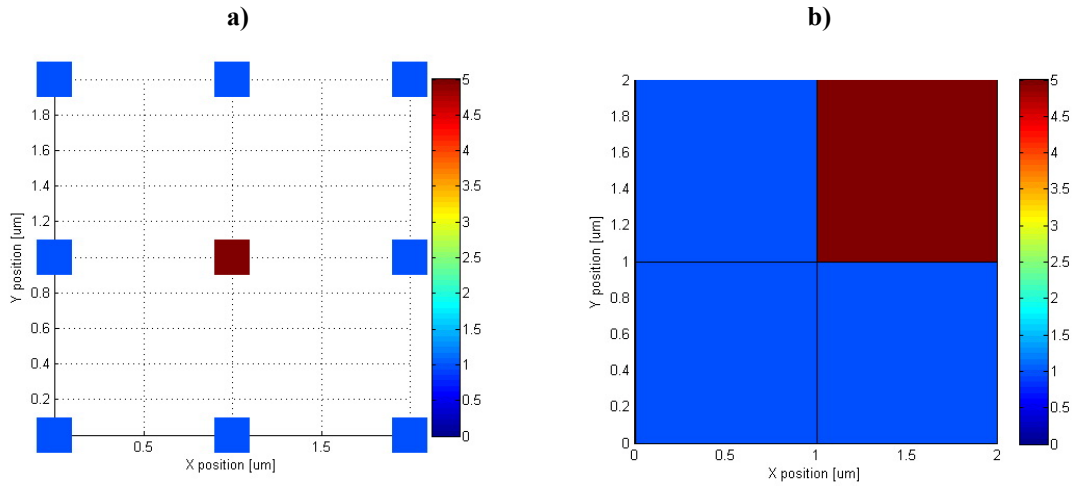

Figure 6.2.13. Matlab plotting techniques: (a) "scatter" and, (b) "griddata" interpolation.

The "scatter" command image presented in Figure 6.2.13(a) shows the data points as a coloured squares and gaps between them. The colours of the squares represent the real lock-in signal voltage acquired by the data acquisition card. The X and Y coordinates in the graph represent the x and y positions, therefore the distance between each data point was not always equal because of the step tolerance introduced as discussed above. The difficulty in using the "scatter" script was the requirement to set up the correct size of the square of data points in the image so that none of the points overlap and there is no gap between the points (which is not the case in Figure 6.2.13(a)). Usually several iterations were required and sometimes there was additional noise caused by the gaps between the points. To add more, it was more difficult to identify if the points overlap, especially with the high quantity of data points. The advantage of "scatter" command was that it plotted the direct data, therefore it did not require additional time to process and interpolate the data between the data points. This was the case with "griddata" command where the data interpolation required considerably more computer resources in order to generate the images.

With a high volume of points the data point square size was usually set to 1 point. Matlab information did not provide an exact definition of the point size in image pixels. Experimentally it was determined that 1 point defined in Matlab script resulted in 1 pixel in the plotted image. Unfortunately increasing the point number resulted in a non-linear increase in the image pixels size, thus this was another difficulty which extended the time required to match the correct size of the plotted squares when using "scatter"

command if the point value was set to the value different than 1. Figure 6.2.14 presents a comparison of the changing square size. The values shown in caption of the figure are in Matlab points. With the square size set to 1 point (Figure 6.2.14(d)) the result was comparable to the interpolated image using "griddata" command (Figure 6.2.15). However, if the step size was too large and the points overlapped (Figure 6.2.14(a)) the image became less clear than the one in Figure 6.2.14(d). Consequently having the data points overlap or having an excessive gap between the points reduced the ability to detect flaws, thus it was necessary to adjust the data points size properly.

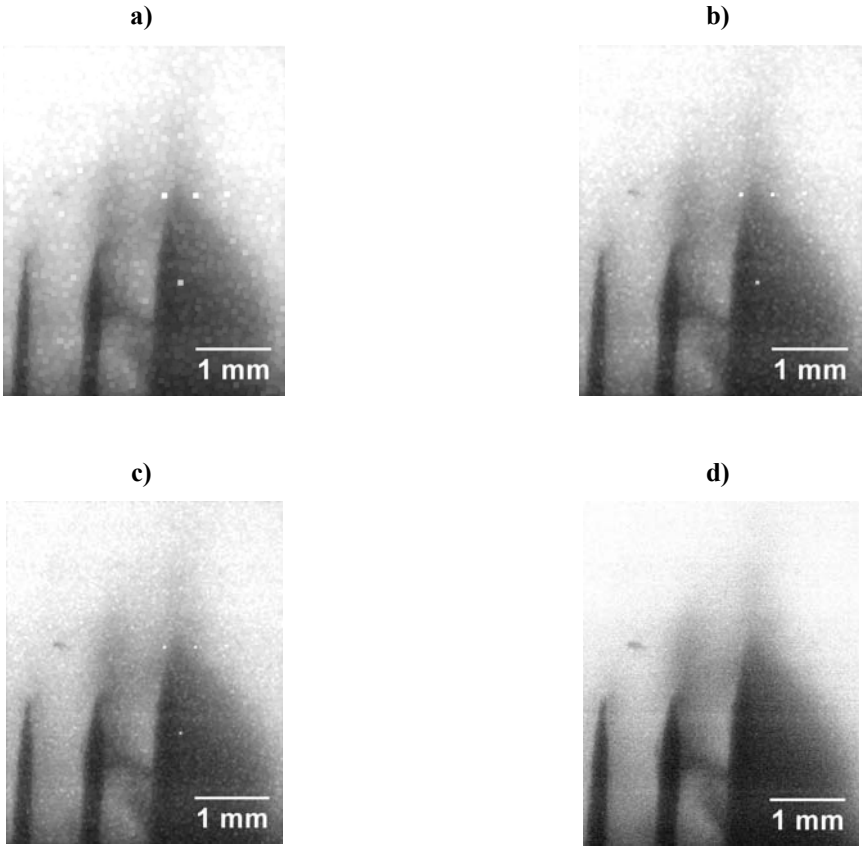

Figure 6.2.14. Optimising the plotting parameters using "scatter" command: a) 50; b) 25; c) 10; d) 1 point.

The second function used for data plotting was "griddata" command (Figure 6.2.13(b)). This command interpolated the surface between the acquired data points. Once the data for the image was interpolated a "surf" command was applied to plot the image. The advantage of this plotting method was the smoother appearance of the whole image. The cores of the "scatter" and "griddata" scripts were the same. The program generated a 3D map where the x and y coordinates were the x and y stage positions saved in the data files. The third component used to produce images was the acquired lock-in

amplifier voltage. The x and y image coordinate map was produced in a form of a mesh. The original data was non-uniformly spaced due to the stage step size tolerance.

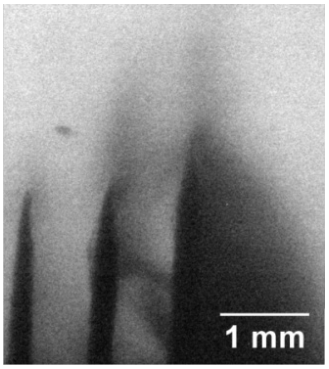

Figure 6.2.15. Matlab plotting of an image of sample 7 using "griddata" triangle-based cubic interpolation.

For the "griddata" script it was necessary to generate a uniform mesh to be able to create the image in Matlab. Two commands: "linspace" and "meshgrid" generated the uniform mesh of points. A uniform mesh of points increased the speed of plotting the data because data points were spaced regularly so the software data access was simplified.

In the next step the uniform mesh was triangulated with Delaunay triangulation (DT) [14, 15]. A 2D mesh of non-uniform data points was triangulated to the uniform mesh using Delaunay triangulation. DT minimised the discontinuities in the produced image, thus detecting flaws was easier. The light intensity value (voltage) for the generated mesh was then interpolated based on the triangle-based cubic convolution interpolation (CC) algorithm [16-19]. Interpolation is fundamental to many digital image processing applications, particularly in operations requiring image processing [18, 20-22]. It is used to magnify or reduce images and to correct spatial distortions. Interpolation is usually implemented by convolving the data points with a kernel function. The CC interpolation method closely approximates the theoretically optimum sinc(x) interpolation function using third-degree cubic polynomials with coefficients based on the acquired data points.

The results of both plotting methods for sample 7 were shown in Figure 6.2.14 and Figure 6.2.15. With "griddata" technique the image was less grainy and it appeared smoother. The jitter in Figure 6.2.15(b), noticeable in the proximity of the holes is due to poor bi-directional repeatability of the x motorised stage which eventually failed.

The image plotting algorithm required setting the range of the light intensity within which the data was plotted. Defining the correct scale was a crucial part of the plotting process because poor contrast of the produced image might suppress some of the flaws. The example shown in Figure 6.2.13 was plotted with a colour map scale between 0 and 5 units. The colour map was used to readily highlight the difference between the data point values. The images of the samples tested, on the other hand, were plotted in greyscale within the defined voltage scale so that the results could be compared with the MIR-TI technique images.

The voltage range used to plot the images could be calculated either automatically in Matlab, based on the maximum and minimum pixel intensities identified in the data set, or it could be set manually for every inspected sample. The manual adjustment of the plotting range allowed contrast enhancement which aided the detection of the flaws in the images. An example of sample 9 in Figure 6.2.16 presents automatically and manually optimised scales for the same data set. The manually set scale (Figure 6.2.16(b)) presented the enhanced image contrast highlighting the defects. The scale adjustment was particularly important with thick samples where signal level was low and image contrast was poor. The automatic scale adjustment on the other hand was highly susceptibility to noise which could interfere with the correct voltage range scaling.

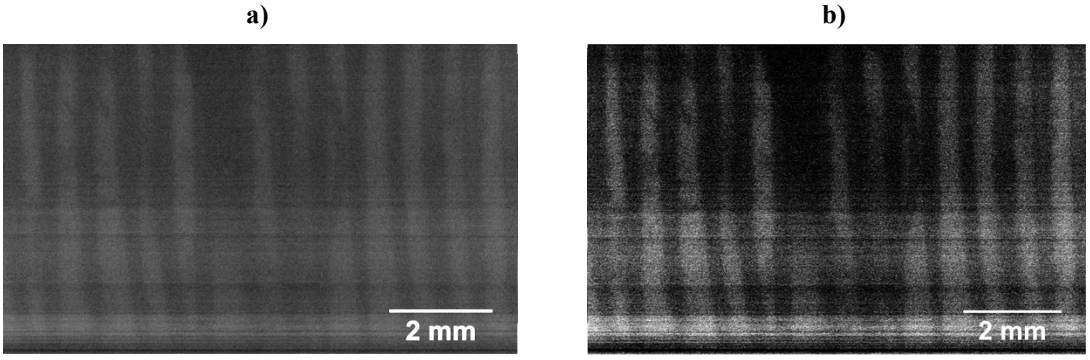

Figure 6.2.16. Matlab script image contrast adjustment: a) automatically; b) manually adjusted image scales for sample 9.

It should be noted that the horizontal bands observed in some of the plotted images (Figure 6.2.16) were caused by ambient temperature and lighting fluctuations in the laboratory. These fluctuations were particularly noticeable due to the measurement time (more than 18 hours measurement for a single plane). This was another reason for

covering the CMIR-TI setup with the cardboard box (section 6.2.3) minimising the influence of the environment fluctuations.

The image in Figure 6.2.13(b) shows the "griddata" interpolation technique where the number of grid points on the surfaces was equal to number of the acquired data points. In this particular example image smoothing was not noticeable due to the low number of the data points. The Matlab interpolation algorithm allowed for generation and plotting of an increased number of points in a mesh (in comparison to the number of the acquired data points) which could potentially enhance the image even further. An example of the same data as in Figure 6.2.13(b) but with two and six times as many grid points in the mesh as the acquired data points during scanning is presented in Figure 6.2.17(b) and (c) respectively. The region which required only one red rectangle in Figure 6.2.13 was smeared out over a larger area due to the interpolation and increased number of data points in the mesh, thus smoothing the feature appearance. Although some of the features could potentially be lost due this interpolation, the advantage was the reduction of the point-to-point fluctuations in the plotted image.

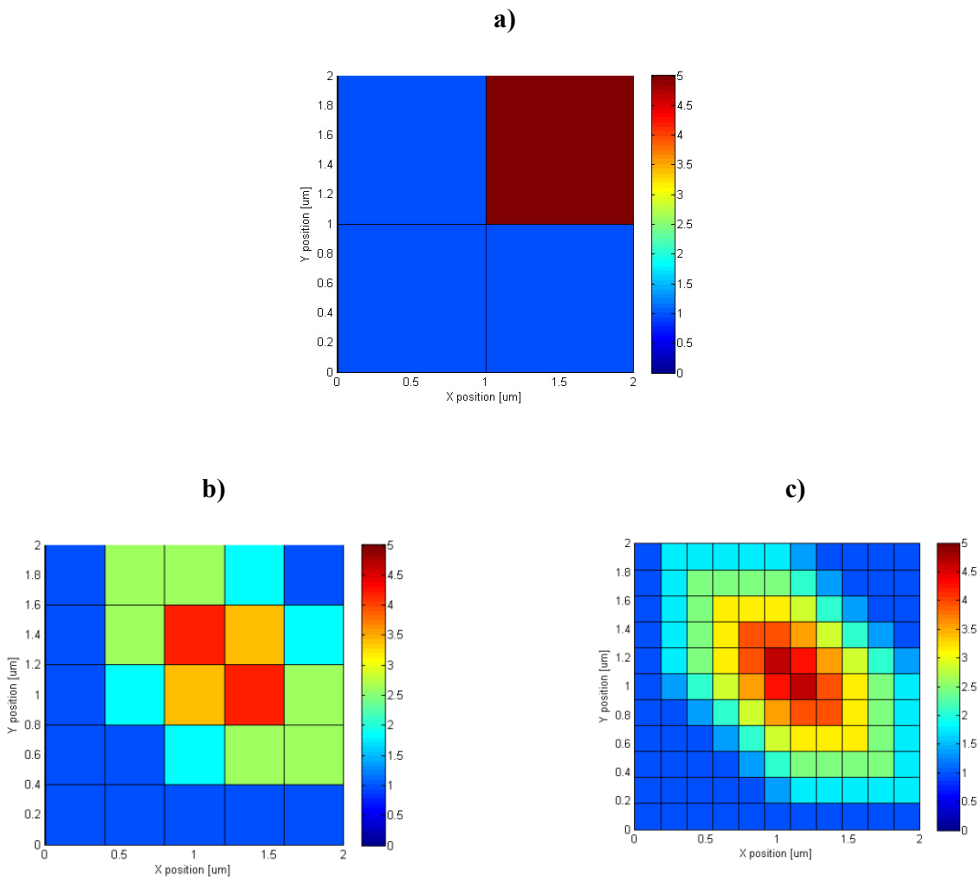

Figure 6.2.17. The increasing number of grid points smoothens the image surface and highlights the area of interest. Mesh consisting of a) equal amount; b) two and c) six times as many grid points as data points.

All the images achieved during the experimental measurements were comparable with the MIR-TI results as a result of implementing the appropriate Matlab plotting technique ("gridata") and the cubic-interpolation. The images presented in the experimental part were plotted using six times more grid points than the actual number of data points acquired which produced smoother images, particularly for thick samples where the images were noisy.

6.2.6. Depth of field of CMIR-TI system

Before any sample was inspected with the CMIR-TI technique the optimal step sizes for all three axes were investigated. Similarly to the MIR-TI technique, the CMIR-TI setup allowed for sample in-depth scanning where the in-focus distance was based on the depth of field (DOF) parameter. The major source of errors during confocal inspection is the mismatch between optical section thickness and the actual confocal system sampling interval, therefore the optimal step sizes were investigated.

There are many definitions for the DOF parameter available in literature [3, 23, 24]. The general rule for the confocal systems presented in literature is that a point light source is imaged at the object plane so that the illuminated in the object point and the light source are confocal. The image of the illuminated object point is imaged onto the pinhole which means that the illumination, object and pinhole points are confocal.

For the CMIR-TI system, however the light source geometry was large and the mid-infrared light illuminated a considerable area of the sample. Only a part of this area was imaged onto the pinhole which then was imaged onto the detector with additional optics to extend the distance between the pinhole and the detector. Therefore, a contribution of the scattered (by the ceramic material) photons in every data point acquired during sample scanning was feasible. Furthermore due to the thickness of the specimens tested the impact on the photons path should also be considered.

To estimate the DOF equation (6.6) [3] was used. DOF depends on NA of the objective lens, the wavelength of incident light (λ = 6 μm), the size of the aperture and the refractive index of the material (n ≈ 2).

$$\mathrm{DOF} = \frac{0.45 \cdot \lambda}{\mathrm{n} \cdot \left(1 - \cos\left(\sin^{-1}\left(\frac{\mathrm{NA}}{\mathrm{n}}\right)\right)\right)} \qquad (6.6)$$

where NA is the effective numerical aperture of the ZnSe lens calculated below. The NA of the ZnSe lens was different from the NA of the MIR-TI system which used the whole area of the lenses. Similar to the calculations from Figure 6.2.4 the effective NA of the ZnSe lens was measured using similar approach (see Figure 6.2.18). Again a 1 inch aperture was used during the experiment. The aperture was installed close to the ZnSe lens and it was closed until a 5% drop in signal was observed. The aperture diameter resulting in this 5% drop was measured with a precision calliper and found to be 20 mm which resulted in an effective NA of 0.25 calculated from equation (5.5) for the ZnSe lens with a focal length of 38.1 mm.

Therefore the DOF of CMIR-TI system calculated from equation (6.6) was approximately 172 µm. It should be noted that this value is for a confocal system where there is a point light source which is imaged into a point in the object volume. This point in object volume is then image onto a point on the pinhole. That is not the case for CMIR-TI system where non-confocal illumination and additional 4f system to image the pinhole onto the detector were used, hence the calculated DOF value should only be used as a guide.

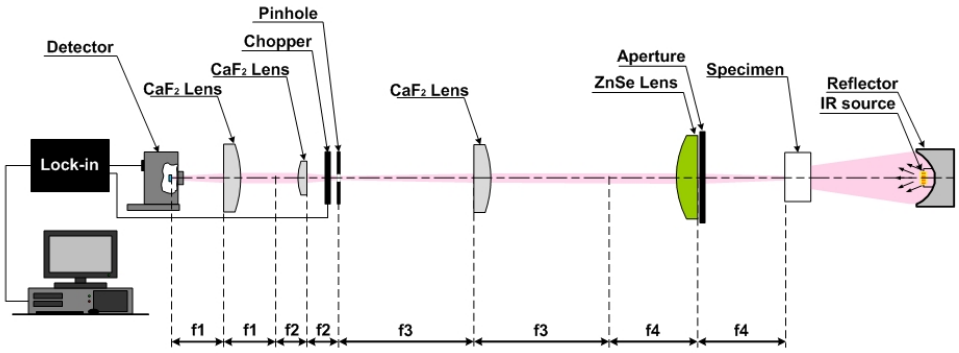

Figure 6.2.18. The NA parameter estimation of the ZnSe lens.

For that reason the DOF was determined experimentally, similarly to MIR-TI DOF estimation (see section 5.3.4). The DOF was used as a z stage step size during the measurements. From the experimental results presented in the section 6.3 the DOF of 150 µm was established. Locating the cracks buried in the sample during sectioning proved that the DOF of 150 µm was accurate (sample sectioning allowed to reach the cracks after their position was determined with the CMIR-TI technique).

6.2.7. Measurement of testing targets

Before any of the samples were inspected with the CMIR-TI technique the resolution of the system was determined using USAF resolution testing targets (see section 2.5.2). The experimental procedure for the CMIR-TI technique was similar to the MIR-TI resolution measurement where USAF target was used (sections 5.3.5 and 5.3.6). The testing targets were positioned in the sample holder and the area of the target was scanned with the CMIR-TI apparatus. At first the standard soda lime glass USAF target was used during the measurement.

The CMIR-TI technique provided flexibility in choosing both the pinhole and step sizes. The sample measurements in the experimental part were mainly carried out using a 50 μm pinhole and 50 μm, 25 μm and 10 μm step sizes for scanning. The resolution results for the CMIR-TI system for the three step sizes of 50 μm, 25 μm, 10 μm using the 50 μm pinhole are presented in Figure 6.2.19. As expected the reduction of the step size led to an improved image quality and higher image resolution due to an increased number of data points being acquired. The CMIR-TI resolution deduced from the images for 50 μm and 25 μm steps indicated that the smallest feature which can be detected was in a region of 44.3 ± 5 μm according to the USAF standard (group 3, element 4). Similarly to the USAF target results presented in chapter 5, 12% reading error was included in the results (see section 5.3.5). Again during the scanning, particularly for 25 μm steps (see Figure 6.2.19(b)) the jitter was present. This hampered the resolution because distinguishing smaller bars was more difficult, hence the resolution for 25 and 50 μm step scanning was the same. For 10 μm step scanning (see Figure 6.2.19(c)) on the other hand due to extended time of scanning the influence of the varying temperature in the lab was apparent in the image. This however did not influence the resolution measurement (31.3 ± 4 μm - group 4, element 1) due to large number of data points acquired. The resolution was calculated from equation (2.7) and equation (2.8).

The USAF testing target used during the above experiment had limited optical transmittance in the mid-infrared (see appendix B). Consequently to determine the CMIR-TI technique's resolution in the mid-infrared, measurements using a laser machined USAF infrared target (see appendix B) were carried out. The results for this target are shown in Figure 6.2.20.

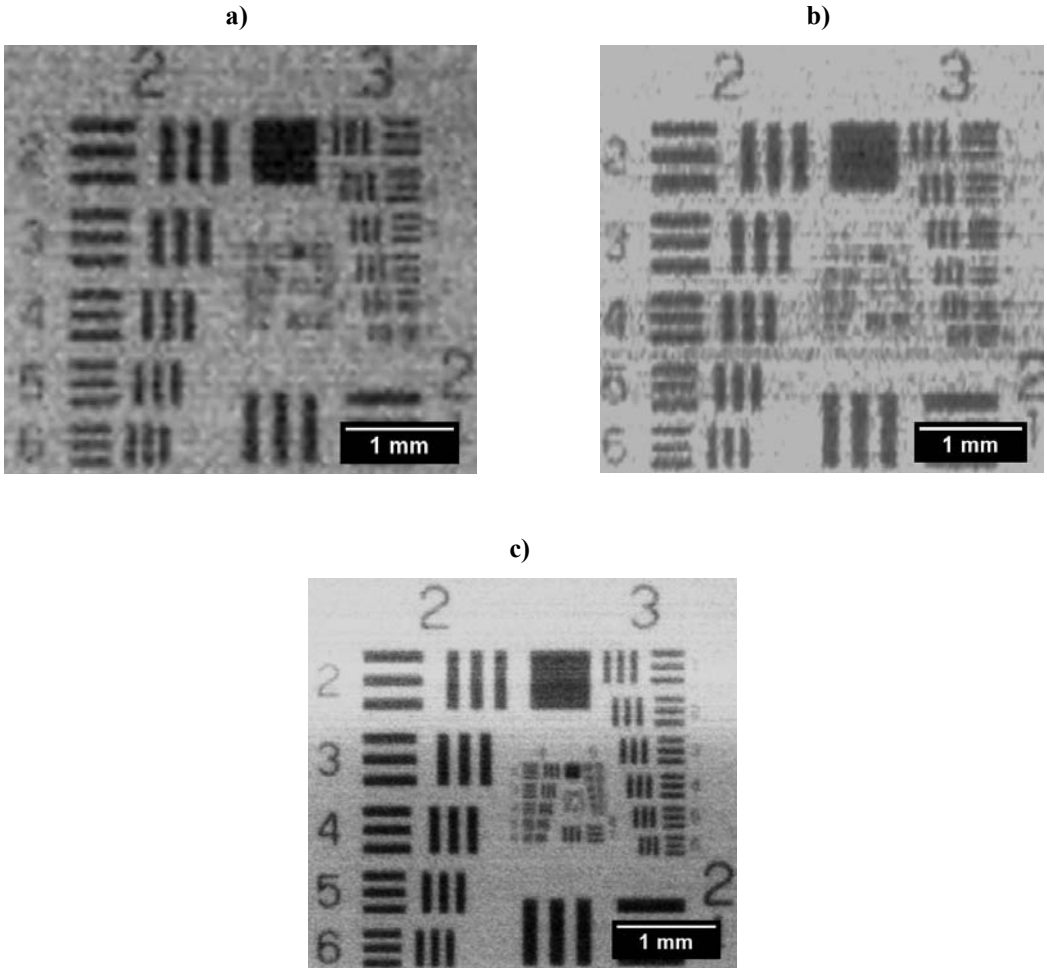

Figure 6.2.19. The standard USAF testing target images acquired with CMIR-TI technique using 50 μm pinhole and: a) 50 μm; b) 25 μm; c) 10 μm steps size.

The USAF infrared target was produced on a CaF_2 glass substrate which is transparent in the mid-infrared region (see appendix B). The bars on the infrared target were 9% smaller compared to the standard USAF due to inaccuracy in the laser machining process. The resolution calculated from the images for 50 μm steps was 49.5 μm (group 3, element 3) and for 25 μm and 10 μm steps it was 35 μm (group 3, element 6). With 9% error and similarly to the USAF target results presented in chapter 5, 12% error (see section 5.3.5) for 50 μm steps the resolution was 54.4 ± 7 μm and for 25 and 10 μm steps was 38.5 ± 5 μm.

The results achieved with USAF infrared target and the CMIR-TI technique were very close to the resolution limit achievable with the laser machining. The smallest infrared target features which could be accurately manufactured with the laser were in group 3. This was due to poor laser stability. For that reason distinguishing if there was any difference in the resolution between 25 μm and 10 μm steps, by imaging smaller bars, was not feasible.

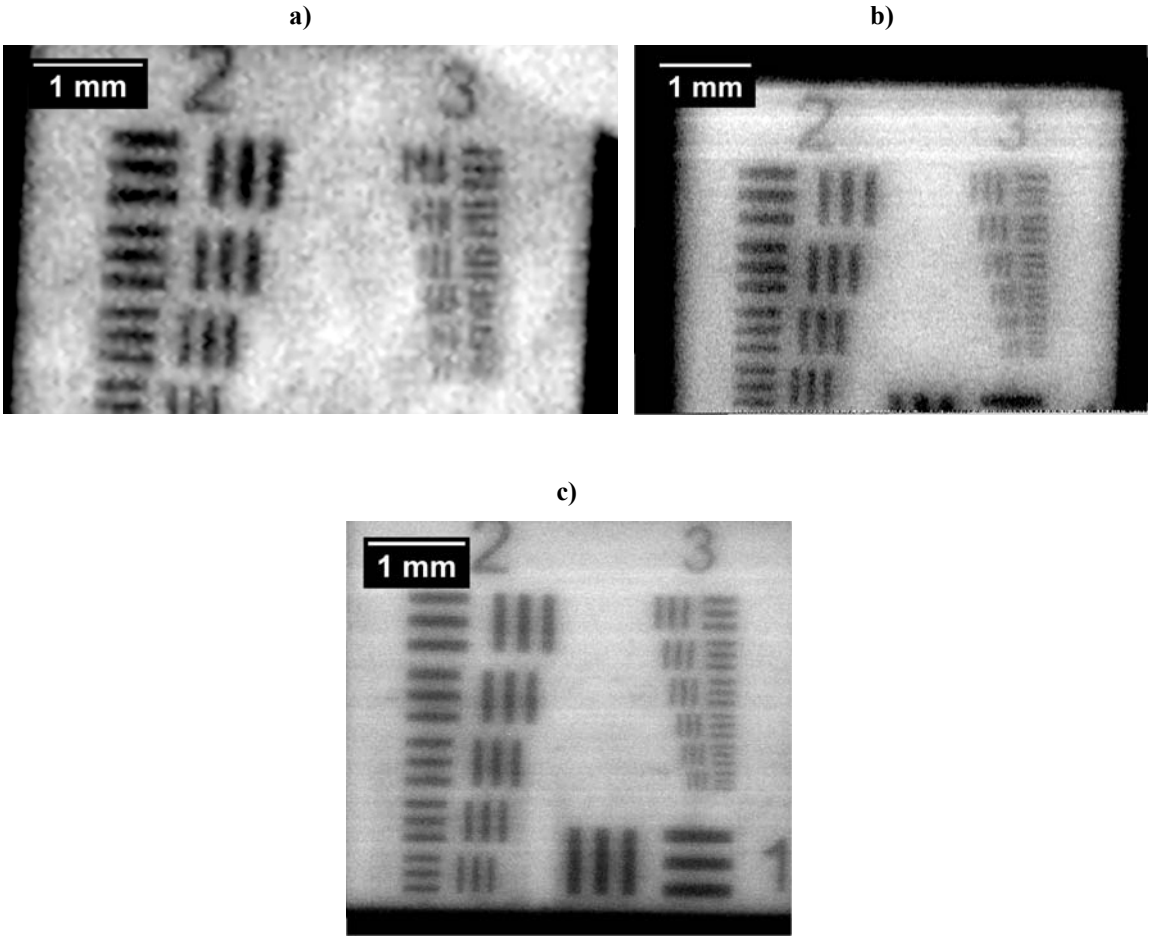

Figure 6.2.20. CMIR-TI resolution measurements using USAF infrared testing target for: a) 50 µm; b) 25 µm; c) 10 µm steps.

The resolution measurements with the USAF infrared target were performed over the entire wavelength range available from the infrared source, and the detector. The limiting component for the spectral range of CMIR-TI technique was the infrared detector which operated between 2.5 – 9 µm. However, such a wide spectral range introduces additional noise and chromatic aberrations. Therefore, a band-pass infrared filter was applied to investigate the resolution between 3 and 6 µm (see appendix B).

With the filter installed in front of the sample (from the detector side) a noticeable improvement in image sharpness, especially for 10 µm steps, was observed (see Figure 6.2.21). For 25 µm and 10 µm steps the resolution was at least 35 µm (group 3 element 6) or at least 38.5 ± 5 µm with 9% and 12% errors, whereas for 50 µm the resolution achieved was 44.3 ± 5 µm (group 3, element 4) and with the 9% bar size error was 48.5 ± 6 µm.

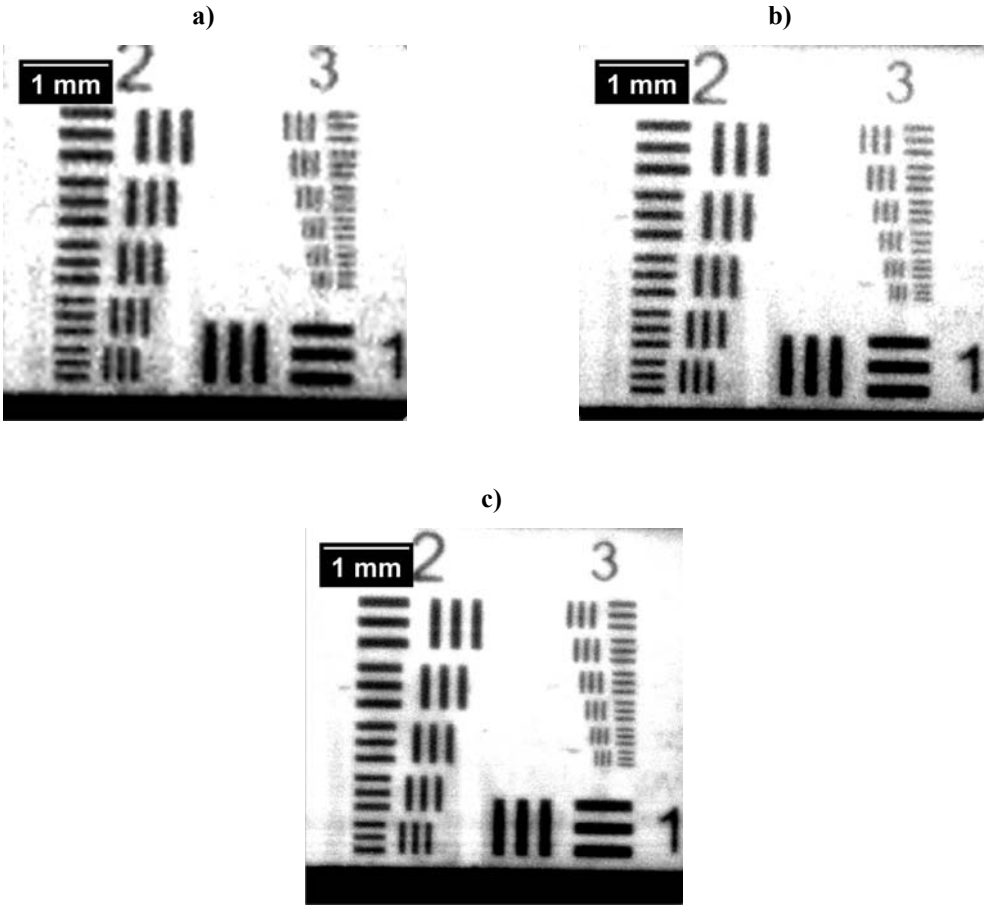

Figure 6.2.21. CMIR-TI resolution measurements using infrared testing target and infrared filter for: a) 50 µm; b) 25 µm; c) 10 µm steps.

The comparison of the resolution results achieved for the CMIR-TI system using the standard and the infrared USAF targets is presented in Table 6.2. The resolution of the CMIR-TI system measured with the standard USAF target was the same as the result for the MIR-TI technique (see section 5.3.5). Lower resolution was measured with the infrared testing target for 50 µm steps due to considerable noise present in the acquired image. This noise was a result of the instability of the motorised stages resulting in a lack of repeatability. This gave variations in the pitch and produced poor images. This was particularly noticeable for 50 µm step size where there was no overlapping technique used, thus any data point inaccuracy was spotted more easily. Reduction of the step size during scanning helped to compensate this noise because the data points overlap giving a higher number of data points averaging out the effect.

The enhanced image appearance of the USAF infrared testing target with infrared filter for all step sizes was caused by a reduction of lenses diffraction and aberrations effect due to the longer photons being stopped by the band-pass filter. The resolution enhancement was less observed with 25 and 10 µm steps compared to 50 µm steps due

to the step overlapping technique. The overlap provided a higher number of data points where each of them covered 50 μm area, thus it compensated for some of the loss of image sharpness due to optical aberrations and diffraction because the light intensity map was reconstructed more accurately. However, with the reduced spectral range (when using the infrared filter) these unwanted effects were reduced by the filter itself, thus the step overlapping had less of an effect. It may however, be possible to further improve the resolution, when using a 25 or 10 μm steps, by reducing the pinhole size.

Table 6.2. Resolution calculated for the CMIR-TI system using USAF and USAF infrared targets with and without the infrared band-pass filter.

Parameter / Step size	USAF target [μm] with 12% error	USAF infrared target [μm] Result with 9% and 12% errors	USAF infrared target with infrared filter [μm] Result with 9% and 12% errors
50 μm	44.3 ± 5	54.4 ± 7	48.5 ± 6
25 μm	44.3 ± 5	< 38.5 ± 5	< 38.5 ± 5
10 μm	31.3 ± 4	< 38.5 ± 5	< 38.5 ± 5

Apart from the pinhole and the step size, the quality of the images was also determined by a Matlab plotting technique. The developed plotting script allowed defining of the range in which the data was plotted, thus the brightness and contrast of the images could be adjusted. The plotting range was determined by the voltage range of the acquired data points. The plotting range adjustments could be carried out automatically or manually (section 6.2.5), however often the manual approach was chosen because it provided the better images for identifying cracks. To achieve high contrast the images often had a high number of saturated pixels.

For that reason the low contrast image from Figure 6.2.22 was compared with high contrast image from Figure 6.2.20(c). The reduced contrast resulted in resolution drop from 38.5 ± 5 μm (group 3, element 6) in Figure 6.2.20(c) where voltage range was between 0.25 V and 0.5 V to 44 ± 5 μm (group 3 element 4) in Figure 6.2.22 where voltage range was between 0 and 0.9 V. The greyscale values were spread over a wider range of intensities reducing the contrast and image resolution.

For that reason it was crucial to choose the optimal plotting range for the images because optimising the contrast could also aid the detection of flaws by optimising the

resolution. On the other hand, there is a risk of losing some of the low contrast features if the image contrast was set too high. These factors have to be balanced and that is why the contrast adjustment in the experimental part was carried out manually.

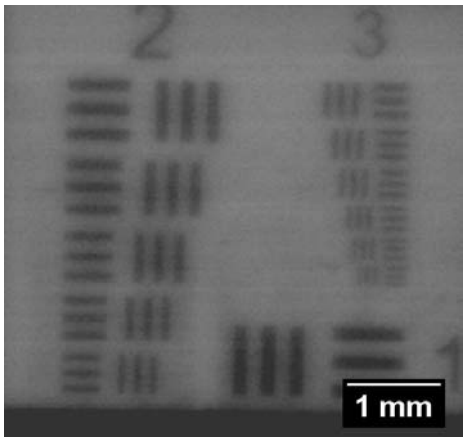

Figure 6.2.22. The influence of Matlab plotting parameters on the resolution of the CMIR-TI technique. Low contrast USAF infrared target image.

6.3. Results

To establish the CMIR-TI technique limitations a group of samples with macro scale (above 1 mm in size) and micro scale (below 1 mm in size) flaws were inspected. Plane-by-plane scanning of the samples provided extensive information about the flaws buried inside, however at a cost of considerably reduced signal reaching the detector. For that reason a series of samples was tested to establish the flaws detection limits and to compare the results of CMIR-TI imaging with the MIR-TI technique.

The setup used in the experimental part is presented in Figure 6.2.11, where 50 μm pinhole and 10 μm step scanning were applied. The chopper was set to 1.6 kHz, the stages velocity was 160 μm/s, $T_{lock\text{-}in}$ was 30 ms and S was between 100 and 300 μV (depending on sample thickness).

6.3.1. Macro scale feature detection

To validate if similar results to those achieved with the testing target measurements in terms of image quality enhancement (compared to MIR-TI) could be repeated with a series of samples including sample 9 (see Figure 3.2.1(d)), 10 (see Figure 3.2.1(e)) and other were tested. These samples were also inspected with the MIR-TI technique (see section 5.4.1). The results for CMIR-TI scanning of the aforementioned samples are shown in Figure 6.3.1. It should be noted in the following images produced with the

CMIR-TI technique represented only a single plane where sharp features in the bulk material were revealed. For the confocal system increasing the thickness of the sample did not have as significant effect on the appearance of the flaws hidden inside the sample as for MIR-TI technique due to the nature of confocal imaging which looked at a thin slice rather than the whole bulk (as in the MIR-TI technique) [23, 25, 26]. The flaws in the CMIR-TI technique appeared as dark regions in the image due to the significant material changes of the re-molten 3Y-TZP.

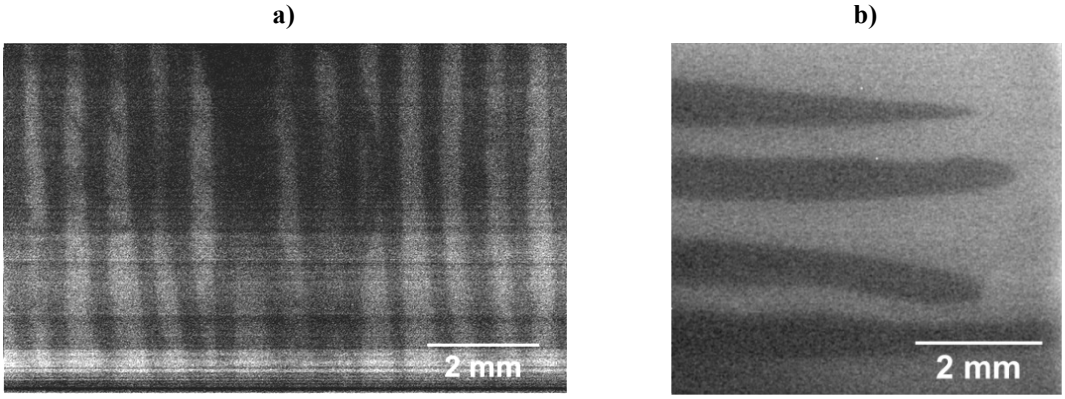

Figure 6.3.1. CMIR-TI scanning results for: a) sample 9; b) sample 10.

The tested samples had macro scale flaws introduced into the bulk volume of the 3Y-TZP material by the laser machining. The laser machining process, due to the high temperatures generated in the proximity of the laser beam, melted and vaporised 3Y-TZP ceramics. The material was ejected from the machined area [27-29] and after rapid cooling, once the laser beam moved away from the area, a fire polish or glassy appearance of the recast layer was produced as discussed in section 3.2.1. This modified surface structure allowed for macro scale features detection using MIR-TI system, therefore a similar outcome was predicted when using the CMIR-TI technique.

The disadvantage of using pinhole imaging was the significantly reduced light intensity, due to the pinhole, which had a direct impact on the thickness of the sample which could be inspected with CMIR-TI system. Additionally, despite the significantly reduced light scattering in the mid-infrared, there were still some losses due to multi-crystalline nature of 3Y-TZP which was the main scattering source (see section 3.1), thus the light scattering was still present. The reduced signal level reduced the SNR which impacted the images contrast. Low SNR made the acquired signal more susceptible to noise, therefore distinguishing any features in the image was a challenge. Regardless of the aforementioned challenges, to test the CMIR-TI technique, macro

scale features were investigated (see Figure 6.3.1) in 9 (see Figure 3.2.1(d)), 10 (see Figure 3.2.1(e)) and others) up to 8 mm thick. For 8 mm thick sample (not presented in this study) the laser drilled holes were difficult to locate precisely because there was only a shadow of them present. This showed that 8 mm thick sample was too thick to be inspected with CMIR-TI technique.

The advantage of confocal imaging was demonstrated by the remaining samples. CMIR-TI provided acceptably clear images of the features from various depths throughout samples 9 and 10. With sample 10 shown in Figure 6.3.1(b) the drilled holes placed 5 mm from the front surface of the sample were easily imaged and they appeared sharp. Therefore demonstrating that the CMIR-TI technique can inspect macro scale features in relatively thick 3Y-TZP components. Clear images highlighting the machined holes were also presented for 9 (Figure 6.3.1(a)) which was thinner than sample 10, thus the CMIR-TI inspection provided satisfactory results. For that reason sample 10 measuring 7 ± 0.1 mm in thickness was determined to be the limit for macro scale features detection for CMIR-TI technique. For features in 8 mm thick sample (see Figure 6.3.1(c)), the image sharpness deteriorated significantly and affected the ability to detect the features reliably. Detection of macro scale features in thicker samples may however be possible with a more powerful infrared source.

This experiment showed that to be able to inspect thicker samples increasing the power of the infrared source is a key. Up to the thickness limit, there was no significant difference in the appearance of holes at various depths. This was due to the fact that confocal imaging took an optical slice of the sample imaging it plane-by-plane.

6.3.2. Micro scale feature detection

The significant material modification of the re-molten 3Y-TZP enabled the CMIR-TI technique to detect macro scale features. The increased light reflection altered the intensity of the light and this allowed features above 1 mm to be detected, despite being buried in the bulk of the highly scattering material. In the micro scale, detection of flaws was dependent on a different mechanism. The cracks which appeared, due to the highly localised thermal load, propagated from the solidified 3Y-TZP molten layer deeper into the bulk material. Consequently the crack detection was not based on the optical difference between the bulk 3Y-TZP and re-molten layer as was the case for macro scale flaws but on a considerable refractive index change on the crack air gap and 3Y-TZP material which resulted in an interface at which the light was reflected and

refracted [30]. The air gap size varied from few microns to hundreds of microns depending on the heat load and its distribution in the material during either laser machining or any other means of material processing [31-33].

To determine the maximum thickness of the samples which allowed for micro scale features to be detected laser machined samples including samples: 7 (Figure 3.7), 12 (Figure 3.13) and others were examined. The same samples were used during MIR-TI inspection to compare the results. The CMIR-TI results were carried out with the same setup as during macro scale features detection for three examined samples are shown in Figure 6.3.2. Each image presents a single scanned plane hence some features, not in that plane, appeared not as sharp as the other cracks. Although the confocal pinhole rejected out-of-focus photons there was a limit to this, based on the finite size of the pinhole, consequently out-of-focus features could still be seen albeit with a blurred appearance. To add more the detected cracks propagated inside the sample in three dimensions and the shadows represented the size in all three dimension.

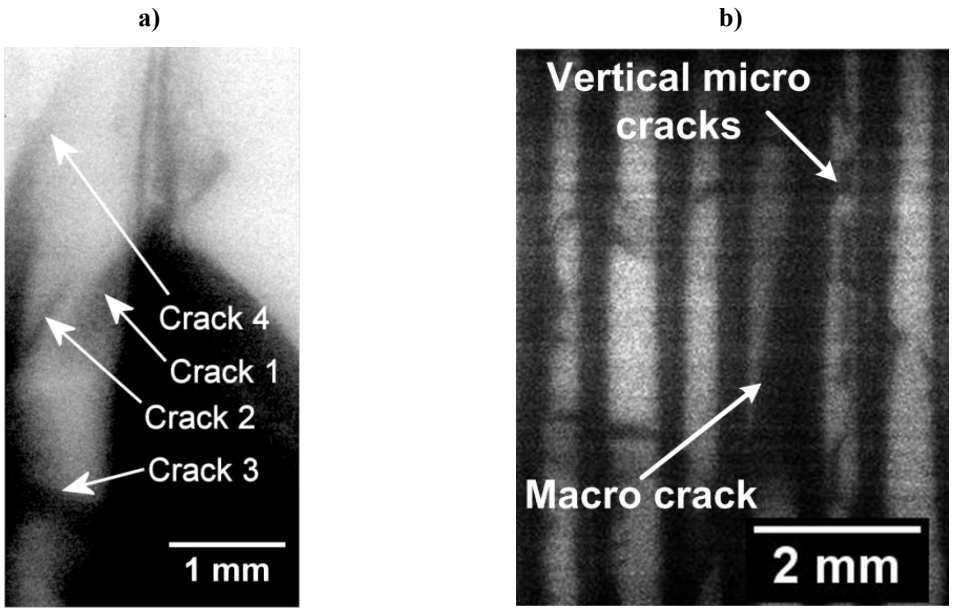

Figure 6.3.2. CMIR-TI images of: a) sample 7; b) sample 12.

For example in sample 7 (Figure 6.3.2(a)) cracks 1 and 4 appeared blurred due to being out-of-focus. In addition the shadow represented a 3D structure of the crack in the bulk material. The sequence of CMIR-TI images of sample 7 is shown in appendix D where sharper cracks 1 and 4 were spotted. Samples 12 in Figure 6.3.2(b) had cracks introduced intentionally to aid the machining of the ceramic using a crack separation technique [34, 35]. These cracks appeared between drilled holes to allow the controlled crack propagation phenomenon to separate the sample along the path of the holes. This

technique was developed to increase the thickness of 3Y-TZP samples which can be machined with laser [29] which provided a potential increase in machining speed of 3Y-TZP ceramics [34, 36]. Fortunately these samples had a large quantity of cracks which was ideal to determine the CMIR-TI technique capabilities.

The micro scale flaws detected by the CMIR-TI technique in sample 7 from Figure 6.3.2(a) had fine air gaps in region of 1 μm in thickness (see Figure 3.3.11 and Figure 3.3.12). However, due to the overall crack dimensions, particularly in depth, these cracks were much larger than the resolution limitation of CMIR-TI technique. Consequently, the identification of these features was feasible. There were several cracks identified during the inspection. The detected flaws were characterised in chapter 3. The results for the CMIR-TI technique were very similar to the MIR-TI results although the images contrast was higher with the CMIR-TI imaging. Cracks and drilled holes appeared sharper due to the relative advantages of the confocal pinhole scanning. After sample 7 was inspected with MIR-TI and CMIR-TI techniques it was sectioned to precisely characterise the flaws buried in the bulk. Determining the accurate positions of the flaws in the bulk was possible due to confocal plane-by-plane scanning. Employing the MIR-TI for this process was also possible, however lower imaging resolution of the MIR-TI imaging would result in lower accuracy of the measurement.

Cracks 1 and 4 (Figure 6.3.2(a)) were identified as being surface cracks. The cracks were present on the back surface of the specimen from the infrared source side. Similar to the MIR-TI technique, Cracks 1 and 4 appeared sharper at approximately 2.1 mm from the sample surface from detector side. There was 100 μm difference between the MIR-TI and the CMIR-TI result. This difference was caused by the error in reading the position where both features appeared sharp and the larger step size of the CMIR-TI technique steps. Cracks 2 and 3 on the other hand again were not found on the surface of the sample. Therefore the depths of cracks 2 and 3 were calculated based on the z positions of the acquired images (the scanning position). The specimen was sectioned at this depth to verify the presence of the flaws. Crack 2 was 1.5 mm below the surface which for 2.7 mm thick sample resulted in crack depth of 1.2 mm. Crack 3 on the other hand appeared 300 μm below the surface from the detector side and its thickness was estimated to be 2.4 mm. Additionally, closer investigation revealed that crack 3 consisted of three smaller cracks which propagated throughout most of the sample thickness. Significant reflection and refraction of the light in the region of crack 3

reduced contrast to such an extent that the three individual features could not be separately imaged. A Scanning Electron Microscope (SEM) and an Environmental Scanning Microscope (ESEM) were used to measure the size of the cracks detected and full crack characteristics are presented in section 3.3.1.

One of the key differences with the CMIR-TI technique compared to the MIR-TI approach was the noticeably different depth of field. This particular feature had both advantages and disadvantages. The CMIR-TI technique had a lower NA of the imaging lens, therefore the depth of field was increased and a thicker section of the inspected volume could be measured at once. It was possible to speed up the inspection because fewer sections were required to scan the full depth. Consequently if the inspection was carried out to simply identify the presence of a single or few flaws within an otherwise pristine sample then reducing the measurement time was feasible due to the increased depth of inspection in a single plane scan. However, if there were many features and the aim of the inspection was to quantify how many features were present, the size and shape, and the locations of these features in the specimen, a thicker optical section could be disadvantageous. Some features could potentially be hidden behind some other flaws within the same optical section, hence they could be missed and the accuracy of the position would be restricted to the depth of field.

For medical purposes identifying if any cracks are present in the material is of more significance as opposed to quantitatively measuring the position and size of the flaws. Not only do macro scale flaws have a significant impact on the material strength but also small, micro scale cracks which can grow and create a network of cracks during the lifetime of the part critically affect material strength [31, 32, 37-41]. Hence if any flaws are detected the part is likely to fail inspection and be rejected. The precise location of these flaws is not important, just identification of whether they are present or not.

Therefore the CMIR-TI technique was developed to identify the presence of any flaws which could be detrimental to the strength and reliability of 3Y-TZP parts. Increasing the thickness of the inspected part introduced a challenge due to low signal reaching the detector which subsequently produced low contrast images. This was particularly evident for sample 13 in Figure 6.3.2(c) where the image has very low contrast. The small pinhole diameter reduced the light reaching the infrared detector, therefore imaging any micro cracks was difficult. Crack 1 in this instance was difficult to identify due to low contrast. Crack 2 on the other hand, due to the large size, could be identified more clearly. The overall shapes of the flaws could be ascertained from the

image but during an inspection it was feasible to believe that these features could easily be missed.

Cracks 3 and 4 for example for sample 13 (not detected by the MIR-TI technique) were even more difficult to detect. Reduced contrast with thicker components was again caused by the light scattering which blurred the images. The scattering combined with the low optical power of the infrared source reduced the contrast and made the detection of cracks difficult. In Figure 6.3.2(b) the image contrast was still acceptable and the multiple cracks were highlighted in the bright background between the laser drilled macro holes. The dimensions of these flaws were above the CMIR-TI resolution limit, therefore they could be identified.

Sample 9 (see Figure 6.3.3) measuring 7 ± 0.1 mm in thickness was inspected with CMIR-TI technique and apart from macro scale cracks (see section 6.3.1) the micro scale cracks 1 and 2 were detected in this sample. There was a significant amount of dark artefacts in the image in addition to the highlighted flaws, but these two features appeared sharp. They appeared sharp because the edges of the crack inspected with SEM (see chapter 3) were sharp. In addition they were positioned approximately 3.5 mm from the front surface of the 7 mm thick sample 9. Hence this showed that in some cases where there are sharp crack edges or there is an increased air gap, micro flaws could still be detected in samples of the order of 7 mm thick.

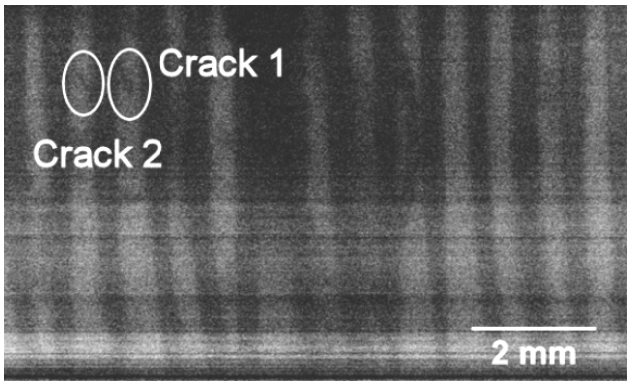

Figure 6.3.3. Cracks detected in sample 9.

The inspection of the 3Y-TZP samples assisted in establishing the maximum thickness which allowed for detection of micro scale (cracks with an approximately 1 μm air gap) flaws. The cracks which were positioned 3.5 ± 0.1 mm away from the sample surface (see Figure 6.3.3), in thick 3Y-TZP components having buried cracks measuring between 240 μm (crack 2 for sample 7) and 1 mm in any of the dimensions could be clearly identified. Smaller size cracks were not found in the inspected samples. The

component thickness limit of 3.5 mm was based on the crack detection capabilities from the acquired images. The image contrast was higher for thinner samples because the area around the crack (background) was brighter (higher light intensity) in thinner samples. To quantify this, the histograms of various regions in the images were investigated in appendix E.

Overall, the detection of micro scale features was limited by the pinhole size, scanning step size and by the signal losses due to light scattering. The increasing thickness of the sample significantly reduced the quantity of photons reaching the detector because there were more interactions between the material grains and the photons. Introducing a more powerful light source and a larger pinhole could enhance the SNR of the CMIR-TI setup. There is however a trade-off between the light reaching the detector (i.e. sample thickness which can be inspected and the pinhole size) and the imaging resolution. Another solution is increasing the pinhole size to 100 μm which could provide four times higher signal reaching the detector.

Most of the features identified in the volume of the presented samples have been identified after sectioning of all the specimens. In some cases, due to excessive amount of cracks and their size, identification of all the features was not feasible. The presented results for micro scale features detection confirmed an improved CMIR-TI imaging resolution due to the confocal pinhole scanning technique. In addition the increased number of data points acquired during scanning, due to the overlapping technique, contributed to the improved imaging capabilities.

6.4. CMIR-TI technique optimisation

The results presented in the experimental part were performed using low speed motorised stages and low chopping frequencies. To investigate the principles of the confocal mid-infrared technique it was unnecessary to use high speed scanning. Furthermore, during the development of the scanning software the limited response time of the Labview software was also one of the factors limiting the maximum allowable scanning speed.

The measurement times calculated with the low speed stages were high, which, particularly in the industrial environment, is not viable. Thus, to simulate the ultimate potential capabilities of the CMIR-TI technique, if the higher specification components were used, the predicted scanning times were estimated. The main factor which had to

be considered when increasing the scanning speed was the quality of the acquired signal which depended on several parameters:

a) Signal-to-Noise (SNR) ratio of the signal reaching the detector,
b) Lock-in sensitivity S,
c) Chopping frequency $f_{chopper}$,
d) Lock-in integration time $T_{lock\text{-}in}$,
e) Detector response time.

The SNR of the acquired signal was determined by the CMIR-TI pinhole size, the optical power of the infrared light source, the losses on the optical surfaces, the quality of the system alignment and by the specimen thickness (light scattering). Lock-in sensitivity, S, set the gain of the lock-in amplifier for the input signal. The lower the signal level the higher the gain was required to differentiate the signal from the background noise. The sensitivity was set carefully because signal amplification was also accompanied by noise amplification. In addition, with higher gain, additional noise from the lock-in control electronics was introduced.

The lock-in integration time, $T_{lock\text{-}in}$, was another parameter which determined the noise level in the output signal. The increased integration time, resulted in increased signal averaging and hence better point-to-point data stability, which in turn resulted in reduced noise. Therefore noise was critical in determining the maximum speed at which the CMIR-TI technique could operate.

6.4.1. Number of signal periods per data point

The first parameter investigated was the number of periods of the detector signal per single data point N (equation (6.4)) at the output of the lock-in amplifier. In the experimental part this parameter was set to N = 48 as there were no requirements for high scanning speed. This high value of N was chosen to reduce noise in the images.

The Imatest infrared testing target [42, 43] produced using the same method as USAF infrared testing target discussed in appendix B was used to investigate the minimum acceptable N value. Due to the many variables of the CMIR-TI technique scanning it was decided to fix the value of S during the experiment to S = 300 μV (which resulted in a gain of 3333). For this sensitivity range the images plotted appeared similar to the MIR-TI images and no unexpected noise was present. The infrared source power

supply was set to I = 0.9 A which was half of the maximum allowable value due to high optical transmittance of the CaF_2 target glass.

The chopping frequency and the lock-in integration time were changed to sweep through a wide range of N values. The measured N range was between 1 and 78 periods of input signal per single output data point and the results are presented in Figure 6.4.1. The measurement range was determined by the maximum available chopping frequency $f_{chopper}$ (4 kHz) and the minimum integration time $T_{lock\text{-}in}$ (1 ms).

The images helped to establish that with N between 5 and 6 the background noise was reduced but with N = 7.8 the noise was considerably lower. Therefore, N = 8 was set to be a limiting value for reduced noise in the CMIR-TI signal. After each of the images was acquired the lock-in signal was grabbed for a further 10 seconds in a stationary position to estimate the statistical parameters of the captured signals. Similarly to Figure 6.4.1 during the 10 second signal acquisition it was observed that increasing $f_{chopper}$ and $T_{lock\text{-}in}$ led to an improved SNR. Increased $T_{lock\text{-}in}$ allowed for longer signal averaging, therefore reduced signal noise was expected. Higher $f_{chopper}$ on the other hand increases the number of signal samples which could be acquired during the same period of time, thus further image stability improvement was possible.

The statistical signal analysis results are shown in Table 6.3. For N = 7.8 the relative standard deviation (RSD) [12] of ± 6.7 % according to equation (5.2) and SNR of 15 was achieved. The RSD value indicated that the CMIR-TI output signal varied ± 6.7% from the average value. For N >7.8 the RSD parameter dropped less rapidly, however the SNR was increasing. The N = 7.8 provided a satisfactory signal quality. In addition further significant increase of N did not result in a significant image quality enhancement.

The signal changes of ± 6.7% from the average value were then compared with the signal changes when a flaw in the material was detected. The purpose of this experiment was to investigate if this pixel intensity change is more significant than the RSD for N = 7.8. Signal variation between the background pixel intensity and the cracks hidden in the bulk of 3Y-TZP samples Pix_{avg} were calculated previously and the results are shown in appendix E. It was clear that the signal variation of ± 6.7% was lower even compared to the sample 9 or 13 for example where the crack detection became difficult, therefore for N = 8 the signal variation was acceptable.

a) N= 1.6 samples, $T_{lock\text{-}in}$ = 1 ms, $f_{chopper}$ = 1.6 kHz.

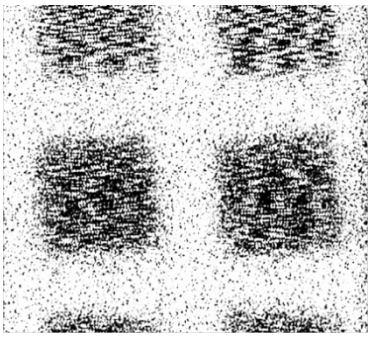

b) N= 2.1 samples, $T_{lock\text{-}in}$ = 1 ms, $f_{chopper}$ = 2.1 kHz.

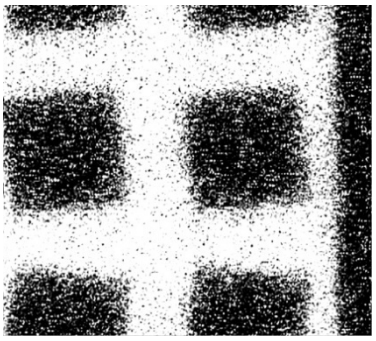

c) N= 2.6 samples, $T_{lock\text{-}in}$ = 1 ms, $f_{chopper}$ = 2.6 kHz.

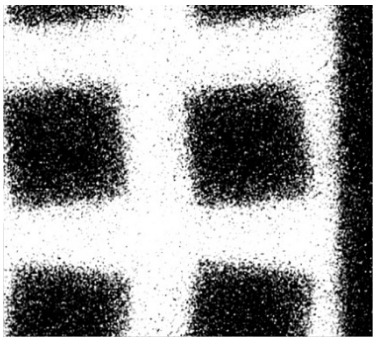

d) N= 4.8 samples, $T_{lock\text{-}in}$ = 3 ms, $f_{chopper}$ = 1.6 kHz.

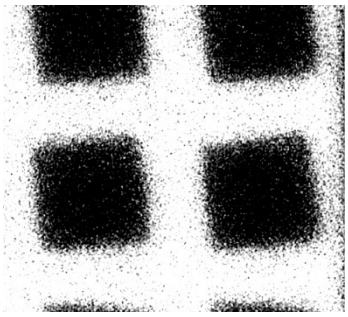

e) N= 6.3 samples, $T_{lock\text{-}in}$ = 3 ms, $f_{chopper}$ = 2.1 kHz.

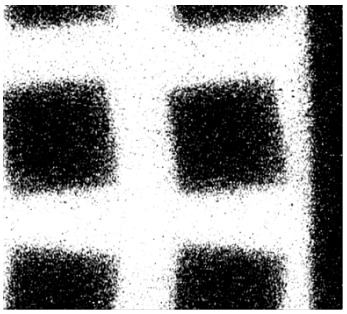

f) N= 7.8 samples, $T_{lock\text{-}in}$ = 3 ms, $f_{chopper}$ = 2.6 kHz.

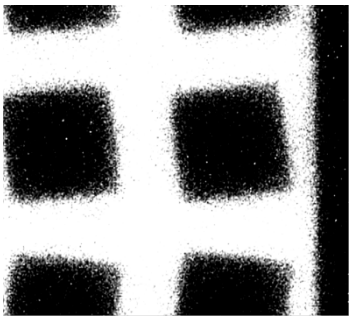

g) N= 16 samples, $T_{lock\text{-}in}$ = 10 ms, $f_{chopper}$ = 1.6 kHz.

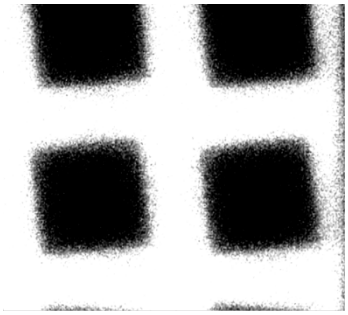

h) N= 21 samples, $T_{lock\text{-}in}$ = 10 ms, $f_{chopper}$ = 2.1 kHz.

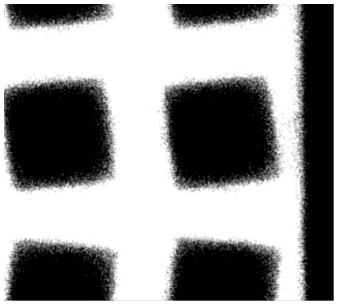

i) N= 26 samples, $T_{lock\text{-}in}$ = 10 ms, $f_{chopper}$ = 2.6 kHz.

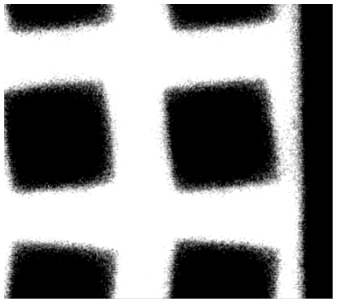

j) N= 48 samples, $T_{lock\text{-}in}$ = 30 ms), $f_{chopper}$ = 1.6 kHz.

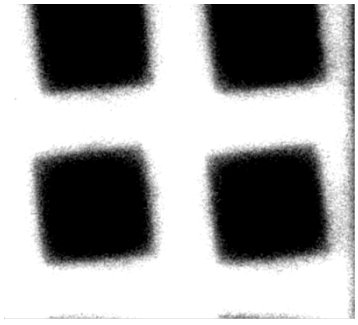

k) N= 63 samples, $T_{lock\text{-}in}$ = 30 ms, $f_{chopper}$ = 2.1 kHz

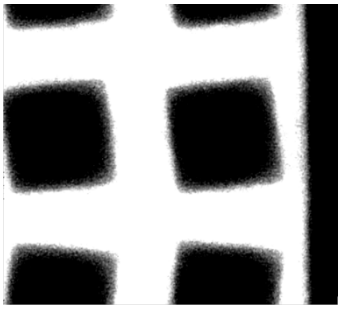

l) N= 78 samples, $T_{lock\text{-}in}$ = 30 ms, $f_{chopper}$ = 2.6 kHz

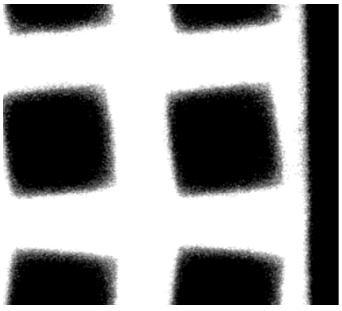

Figure 6.4.1. The optimal N parameter determination.

Table 6.3. Statistical analysis of the signals acquired when the stages were stationary.

Analysed signal parameters	N	Mean [V]	Standard Deviation (σ)	RSD [%]	SNR
$f_{chopper}$ = 1.6 kHz, $T_{lock\text{-}in}$ = 1 ms	1.6	0.84	**0.41**	**48.81**	**2**
$f_{chopper}$ = 2.1 kHz, $T_{lock\text{-}in}$ = 1 ms	2.1	0.95	**0.19**	**20.00**	**5**
$f_{chopper}$ = 2.6 kHz, $T_{lock\text{-}in}$ = 1 ms	2.6	1.01	**0.18**	**17.82**	**6**
$f_{chopper}$ = 1.6 kHz, $T_{lock\text{-}in}$ = 3 ms	4.8	0.83	**0.08**	**9.64**	**10**
$f_{chopper}$ = 2.1 kHz, $T_{lock\text{-}in}$ = 3 ms	6.3	0.93	**0.08**	**8.60**	**12**
$f_{chopper}$ = 2.6 kHz, $T_{lock\text{-}in}$ = 3 ms	7.8	1.05	**0.07**	**6.67**	**15**
$f_{chopper}$ = 1.6 kHz, $T_{lock\text{-}in}$ = 10 ms	16	0.93	**0.05**	**5.37**	**19**
$f_{chopper}$ = 2.1 kHz, $T_{lock\text{-}in}$ = 10 ms	21	0.88	**0.04**	**4.54**	**22**
$f_{chopper}$ = 2.6 kHz, $T_{lock\text{-}in}$ = 10 ms	26	1.09	**0.05**	**4.59**	**22**
$f_{chopper}$ = 1.6 kHz, $T_{lock\text{-}in}$ = 30 ms	48	0.93	**0.03**	**3.23**	**31**
$f_{chopper}$ = 2.1 kHz, $T_{lock\text{-}in}$ = 30 ms	63	0.90	**0.02**	**2.22**	**45**
$f_{chopper}$ = 2.6 kHz, $T_{lock\text{-}in}$ = 30 ms	78	1.09	**0.03**	**2.75**	**36**

The first five rows indicate an unacceptable, noisy signal.

6.4.2. Estimation of CMIR-TI speed

The developed CMIR-TI system was limited by the motorised stage velocity, data acquisition speed, the chopping frequency and the developed Labview software. If these parameters could be improved the speed of scanning for CMIR-TI technique could be significantly increased. With N = 7.8 ≈ 8 the speed of scanning for the CMIR-TI system was simulated in a range of scenarios. For the purpose of these calculations currently available components were used to estimate the potential improvement possible for the CMIR-TI technique capabilities. Before the results for N = 8 are presented the calculations of the scanning times for the original CMIR-TI system were calculated.

The CMIR-TI technique used raster scanning to image the samples. The sequence is shown in Figure 6.2.6. Each picture was produced from the lines in the x axis pitched

by a single step in the y axis. Based on the raster scanning approach and step size the time required to scan different areas was estimated using equation (6.7). Three areas of 1 x 1 mm^2, 5 x 5 mm^2 and 10 x 10 mm^2 were used to calculate the scanning times and the remaining parameters used for the calculations were: $T_{lock\text{-}in}$ = 30 ms, $f_{chopper}$ = 1.6 kHz, therefore N was 48 and the stages velocity v was 160 µm/s.

$$t = n_y \cdot (t_x + t_y) \tag{6.7}$$

where t is the CMIR-TI system scanning time, n_y is the number of iterations/steps in y axis, t_x and t_y are the times of single line scan in x axis and single step in y axis respectively. The scanning times for the area of 1 x 1 mm^2, 5 x 5 mm^2 and 10 x 10 mm^2 are presented in Table 6.4. With the increasing area of scanning the scanning time increase significantly, therefore finding a more rapid scanning is required.

Table 6.4. Stages speed calculated for the CMIR-TI setup used in this study.

Scanning steps d / Scanning area	**10 µm**	**25 µm**	**50 µm**
1 x 1 mm	562 µs	250 s	22 µs
5 x 5 mm	260 min.	101 min.	52 min.
10 x 10 mm	1042 min.	416 min.	208 min.

The first scenario considers an ideal situation where CMIR-TI system can operate at frequencies close to the detector response time $t_{detector}$ = 7 ns [6]. For a single data point at the output of CMIR-TI system, eight periods of the input signal were acquired (N = 8), therefore the lock-in integration time $T_{lock\text{-}in}$ was 56 ns and chopping frequency $f_{chopper}$ was:

$$t_{chopper} = 8 \cdot t_{detector} = 8 \cdot 7\ \text{ns} = 56\ \text{ns} = T_{lock-in} \tag{6.8}$$

$$f_{chopper} = \frac{1}{t_{detector}} \approx 143\ \text{MHz} \tag{6.9}$$

For the given chopping frequency and the lock-in integration time the required velocities for 10 µm, 25 µm and 50 µm steps were calculated from equation (6.10):

$$v = \frac{d}{t_{chopper}} = d \cdot f_{chopper} \left[\frac{m}{s}\right] \qquad (6.10)$$

where v is the stages velocity, d is the scanning step size. The stages velocities for all steps sizes are presented in Table 6.5 and the scanning times for three areas of 1 x 1 mm^2, 5 x 5 mm^2 and 10 x 10 mm^2 based on equation (6.7) are shown in Table 6.6. These results were theoretically limited by the detector response time. However these scanning speeds were not achievable because such high stages velocity (see Table 6.5), signal modulation frequency and short integration times are not practical.

Table 6.5. Stages speed calculated from the estimated chopping frequency of 143 MHz.

Scanning step size d	Stages velocity v
10 µm	178 m/s
25 µm	446 m/s
50 µm	892 m/s

Table 6.6. Calculation of the scanning time for the given area for 10 µm, 25 µm and 50 µm scanning steps. Lock-in integration time is $T_{lock\text{-}in}$ = 56 ns.

Scanning steps d / Scanning area	10 µm	25 µm	50 µm
1 x 1 mm	562 µs	90 µs	22 µs
5 x 5 mm	14 ms	2 ms	570 µs
10 x 10 mm	56 ms	9 ms	2 ms

To identify a practical limit on the CMIR-TI system several component configurations were considered. The main scanning speed limit in the CMIR-TI system were the motorised stages. Although they provided high precision movement the maximum speed was limited to 160 µm/s. One of the fastest motorised stages available on the market is the Aerotech ABL1000 air bearing stage. The velocities of 300 mm/s and a high accuracy of 0.5 nm were within the specification of this product. The calculations below were carried out based on a stage velocity of v = 300 mm/s and N = 8. Consequently the lock-in integration time $T_{lock\text{-}in}$ was calculated according to equation (6.11) based on the above values:

$$T_{lock-in} = \frac{d}{v}\ [s] \qquad (6.11)$$

where d is the stage step size and v is the stage velocity. The results are presented in Table 6.7. These lock-in integration times ranging from tens to hundreds of microseconds are attainable with currently available lock-in amplifiers.

Table 6.7. Calculation of lock-in integration time $T_{lock-in}$ based on a stage velocity of 300 mm/s and varying step size.

Scanning step size d	$T_{lock-in}$
10 µm	33 µs
25 µm	83 µs
50 µm	166 µs

For the given step size and for N = 8 the chopping frequency was estimated from equation (6.13).

$$t_{chopper} = \frac{T_{lock-in}}{8}\ [s] \qquad (6.12)$$

$$f_{chopper} = \frac{1}{t_{chopper}}\ [Hz] \qquad (6.13)$$

The results for 10 µm, 25 µm and 50 µm CMIR-TI scanning are presented in Table 6.8. Unfortunately, such high chopping frequencies are difficult to reach with mechanical choppers due to the limited rotation speed of the chopper motor and the limited spacing between the holes on the chopping disc.

Table 6.8. Calculation of chopping frequency for the given step size, d, and lock-in integration time, $T_{lock-in}$, for 300 mm/s scanning speed.

Scanning step size d	$f_{chopper}$
10 µm	243 kHz
25 µm	96 kHz
50 µm	48 kHz

For the given stage velocity the scanning times were calculated according to equation (6.7) and the results are shown in Table 6.9. Scanning speeds allowing inspection of a single plane in a sample under 1 minute could be practical in the industrial environment. For example if a lower resolution with 50 µm step scanning was used with a 0.5 to 1 mm thick sample (a common thickness in dental components) then for DOF of 150 µm the time required to scan the part would be approximately 50 s for 10 x 10 mm area using 7 planes.

Table 6.9. Scanning times for a single image plane for 10 µm, 25 µm and 50 µm step scanning for the stages velocity of 300 mm/s.

Scanning steps d / Scanning area	10 µm	25 µm	50 µm
1 x 1 mm	333 ms	133 ms	66 ms
5 x 5 mm	8.3 s	3.3 s	1.7 s
10 x 10 mm	33.3 s	13.3 s	6.7 s

The scanning times of the same area for 10 and 25 µm steps would require approximately 1 minute and 33 seconds and almost 4 minutes respectively. These results could also be applied for the industrial inspection if the condition of the parts had to be measured accurately.

In the developed CMIR-TI system motorised stages were used to scan the whole area of the sample. An alternative technique could implement galvanometer light beam scanning [23, 24, 44-47] instead of moving the specimen. A Scanlab hurrySCAN II galvanometer with a speed of movement reaching 3.5 m/s and N = 8 was used to calculate the potential scanning speed capabilities of the CMIR-TI technique. The Lock-in integration times required for the 3.5 m/s scanning speed were calculated based on the previously presented equation (6.11). Similarly, the chopping frequency was estimated from equation (6.13) and the scanning times for 10 µm, 25 µm and 50 µm steps were calculated from equation (6.7). Table 6.10, Table 6.11 and Table 6.12 present the results for the above calculations for all three step sizes.

Table 6.10. Lock-in integration time $T_{lock\text{-}in}$ calculated based on 3.5 m/s galvanometer speed.

Scanning step size d	$T_{lock\text{-}in}$
10 µm	3 µs
25 µm	7 µs
50 µm	14 µs

Table 6.11. Chopping frequency for the given step size d and lock-in integration time $T_{lock\text{-}in}$ for 3.5 m/s scanning speed.

Scanning step size d	$f_{chopper}$
10 µm	2.78 MHz
25 µm	1.12 MHz
50 µm	556 kHz

Table 6.12. Scanning times for a single image plane for 10 µm, 25 µm and 50 µm step scanning for the galvanometer velocity of 3.5 m/s.

Scanning steps d / Scanning area	10 µm	25 µm	50 µm
1 x 1 mm	29 ms	12 ms	6 ms
5 x 5 mm	716 ms	287 ms	143 ms
10 x 10 mm	2.9 s	1.2 s	580 µs

A considerable scanning speed enhancement when using a galvanometer is feasible based on the results from Table 6.12. These results presented a promising opportunity for the CMIR-TI technique to be applied in the industrial environment. Unfortunately, the high signal modulation frequency required for the system with galvanometer scanner created a significant challenge. Similarly to the previous example the mechanical chopping becomes difficult above 100 kHz due to the limited chopper motor speed and the limited minimal gaps on the chopping disc.

Excluding the speed of movement of the motorised stages, one of the key parameters influencing the scanning speed of CMIR-TI system was the chopping frequency. The aforementioned examples confirmed that for the future development increasing the chopping frequency is one of the main challenges. Faster chopping could provide shorter integrations times which would lead to faster sample scanning with higher speed motorised stages or when using a galvanometer. The previously highlighted mechanical chopping limitations were the electric motor speed and the frequency (spacing) of the

gaps in the chopping disc. The maximum chopping frequencies which could be achieved with a conventional chopping motor reach 120 kHz with a Scitec 300D445 chopping disc. There are various issues with controlling such high chopping frequency. The heat from the motor and the action of the disc moving through the air causes the air to heat significantly because 50 W motor is used to rotate the disc at 130 m/s. A high power motor is required due to the high resistance between the disc edges and the air. The heat generated during disc rotation particularly for mid-infrared imaging is highly undesirable. Vibration is also an issue, thus it would be necessary to ensure that the chopping head is securely bolted to a secure surface at all times.

For that reason a lower frequency, 40 kHz, Scitec 300D200 disc was chosen for this part of the calculations to estimate the lock-in integration time and the stage velocity required. For N = 8 the lock-in integration time $T_{lock\text{-}in}$ for the set $f_{chopper}$ was calculated according to equation (6.14).

$$T_{lock-in} = 8 \cdot \frac{1}{F_{chopper}} = \frac{8}{40\text{kHz}} = 200\ \mu\text{s} \qquad (6.14)$$

The stage velocity v for the step size, d, of 10 µm, 25 µm and 50 µm was calculated from equation (6.15) and the results are presented in Table 6.13. The scanning times were calculated based on equation (6.7) and are presented in Table 6.14.

.

$$v = \frac{d}{T_{lock-in}}\ [\frac{m}{s}] \qquad (6.15)$$

Table 6.13. Motorised stage velocity, v, for the chopping frequency $f_{chopper}$ = 40 kHz and the step size, d.

Scanning step size d	Stages velocity v
10 µm	50 mm/s
25 µm	125 mm/s
50 µm	250 mm/s

The required stage velocities presented in Table 6.13 could be accomplished with the Aerotech stages presented in this paragraph. These stages could travel up to 300 mm/s, therefore the velocities presented in Table 6.13 were within their specification. Due to

40 kHz chopping frequency the scanning times were increased compared to the results presented previously.

Table 6.14. Scanning times for a single image plane for 10 µm, 25 µm and 50 µm step scanning for the given chopping frequency of 40 kHz.

Scanning steps d / Scanning area	10 µm	25 µm	50 µm
1 x 1 mm	2 s	320 ms	80 ms
5 x 5 mm	50 s	8 s	2 s
10 x 10 mm	200 s	32 s	8 s

The presented modifications to the CMIR-TI setup were used to establish how fast and how accurately the CMIR-TI system can operate. The first example of the calculations provided the results for the detector being the limiting component for CMIR-TI scanning speed which clearly was not the case. The calculations were repeated using parameter values based on currently available equipment to determine the system capabilities in an industrial environment. The sample scanning speed of 3.5 m/s was limited by the signal modulation technique. The significant challenge was reaching MHz frequencies in the mid-infrared wavelength region which could be possible if the infrared source and the chopper were replaced with a current modulated quantum cascade laser [48-50]. Another proposed solution would be to use a Pockels cell electro-optic modulation which potentially could provide similarly fast signal modulation [51-53].

The examples with the 300 mm/s stages velocity or with 40 kHz chopping frequency present the potential to be employed in the industrial environment. A chopping frequency of several hundred kilohertz and a lock-in integration time of tens of microseconds for a 300 mm/s stages velocity are attainable. Likewise, when using a chopper frequency of 40 kHz the stage velocities of tens to hundreds of millimetres per second and a lock-in integration time of 200 µs are within the reach of currently available technology. The scanning times of several seconds per 1 mm^2 with the currently available equipment provide a great possibility to be applied in industrial applications where high quality and fast measurement is required.

6.5. Conclusions

In order to investigate the possibility of reducing the cost of the system the CMIR-TI technique was developed. The cost of the detector with the power supply and the chopper was in excess of £5,000. The motorised stages cost approximately £3,000 giving a complete system cost of £11,000. Thus a cost saving of £7,000 (compared the MIR-TI technique) was possible.

The initial development involved analysing a range of factors which could limit the quality of the CMIR-TI imaging system. The resolution was measured using a USAF standard resolution measurement and found to be below 38.5 ± 5 μm (limited by the testing target bars size). These results could still be improved with a more powerful infrared source and a smaller sized pinhole.

The CMIR-TI technique provided an accurate tool for detection of micro and macro scale defects in 3Y-TZP ceramics for components up to 3.5 ± 0.1 mm thick. Table 6.15 presents all the samples tested with CMIR-TI technique and the suitability of the CMIR-TI technique for their inspection. Details of all the samples can be found in chapter 3. A more powerful infrared source could potentially increase the thickness of the 3Y-TZP ceramics which could be inspected.

The scanning times with the CMIR-TI technique were considerably increased, I comparison to the MIR-TI technique, taking hundreds of seconds for a 1 x 1 mm area for a single plane scan, However, the introduction of a faster signal modulation technique and faster sample scanning are feasible. The last part of the investigation of the CMIR-TI technique was focused on identifying the bottleneck for the limited scanning time of the system. Several parameters were varied, including lock-in integration time, $T_{lock\text{-}in}$, signal chopping frequency, $f_{chopper}$ and the number of the signal periods acquired for a single output data point, N. The optimal parameters were chosen and the scanning times for these parameters were simulated using various scenarios. The results presented in section 6.4 demonstrated promising speed capabilities for the CMIR-TI technique which could make this technique a viable industrial tool for inspecting highly scattering 3Y-TZP ceramics.

In addition, the CMIR-TI experiments revealed that other than the pinhole size, the step size had a major impact on the imaging quality. Further investigation and quantification of this phenomenon is necessary, particularly if thicker components are tested.

Table 6.15. List of the samples tested with the CMIR-TI technique. Colours indicate: green – suitable for 3Y-TZP inspection, orange – limited feedback about the detected feature, red – MIR-TI inspection of the features not possible. Macro features measure more than 1 mm in size and micro scale features measure below 1 mm in at least two dimensions.

Sample	Features inside the sample	MIR-TI inspection feasibility	
7	1. Macro scale cracks 2. Micro scale cracks	1. Possible 2. Possible	● ●
9	1. Macro scale cracks 2. Micro scale cracks	1. Possible 2. Possible	● ●
10	1. Macro scale cracks	1. Possible	●
11	1. Macro scale cracks	1. Limited – weak shadow of the drilled holes – too thick sample	●
12	1. Macro scale cracks 2. Micro scale cracks	1. Possible 2. Possible	● ●
13	1. Macro scale cracks 2. Micro scale cracks	1. Possible 2. Possible	● ●

References:

[1] M. Matysiak, J. P. Parry, F. Albri, J. G. Crowder, N. Jones, K. Jonas, N. Weston, D. P. Hand and J. D. Shephard: 'Infrared confocal imaging for inspection of flaws in yttria-stabilized tetragonal zirconia polycrystal (Y-TZP)', *Measurement Science and Technology*, 2011, **22**(12), 125502-125511.

[2] B. Matsumoto: 'Cell Biological Applications of Confocal Microscopy', 507; 1993, Academic Press.

[3] P. M. Conn: 'Techniques in Confocal Microscopy'; 2010, Academic Press.

[4] Z. Shuangmu, Z. Liqin, Z. Xiaoqin, C. Jianxin, X. Shusen and J. Xingshan: 'Determination of Tumor Stroma Scattering Coefficient Using Confocal Microscopy', Photonics and Optoelectronic (SOPO), 2010 Symposium on, 19-21 June 2010, 1-2.

[5] M. Rajadhyaksha, M. Grossman, D. Esterowitz, R. H. Webb and R. R. Anderson: 'In Vivo Confocal Scanning Laser Microscopy of Human Skin: Melanin Provides Strong Contrast', *J Investig Dermatol*, 1995, **104**(6), 946-952.

[6] www.vigo.com.pl.

[7] R. C. Jones: 'Immersed Radiation Detectors', *Appl. Opt.*, 1962, **1**(5), 607-613.

[8] R. C. Jones and L. Marton: 'Performance of Detectors for Visible and Infrared Radiation', in 'Advances in Electronics and Electron Physics', 1-96; 1953, Academic Press.

[9] J. Piotrowski and A. Rogalski: 'High-Operating-Temperature Infrared Photodetectors'; 2007, SPIE.

[10] E. Hecht: 'Optics (4th Edition)'; 2002, Addison Wesley.

[11] R. R. Alfano and N. Ockman: 'Methods for Detecting Weak Light Signals', *J. Opt. Soc. Am.*, 1968, **58**(1), 90-93.

[12] S. Durant, O. Calvo-Perez, N. Vukadinovic and J.-J. Greffet: 'Light scattering by a random distribution of particles embedded in absorbing media: full-wave Monte Carlo solutions of the extinction coefficient', *J. Opt. Soc. Am. A*, 2007, **24**(9), 2953-2962.

[13] M. Akiba, K. P. Chan and N. Tanno: 'Full-field optical coherence tomography by two-dimensional heterodyne detection with a pair of CCD cameras', *Opt. Lett.*, 2003, **28**(10), 816-818.

[14] H. Ledoux: 'Computing the 3D Voronoi Diagram Robustly: An Easy Explanation', Proceedings of the 4th International Symposium on Voronoi Diagrams in Science and Engineering, 2007, IEEE Computer Society, 117-129.

[15] J. Kohout: 'Delaunay triangulation in parallel and distributed environment', PhD thesis, University of West Bohemia, 2005.

[16] L. D. Favro, R. L. Thomas, X. Han, Z. Ouyang, G. Newaz and D. Gentile: 'Sonic infrared imaging of fatigue cracks', *International Journal of Fatigue*, 2001, **23**(Supplement 1), 471-476.

[17] D. F. Watson: 'Contouring: A Guide to the Analysis and Display of Spatial Data'; 1992, Amsterdam, Pergamon / Elsevier Science.

[18] R. Keys: 'Cubic convolution interpolation for digital image processing', *Acoustics, Speech, and Signal Processing [see also IEEE Transactions on Signal Processing], IEEE Transactions on*, 1981, **29**(6), 1153-1160.

[19] T. K. Truong, L. J. Wang, I. S. Reed and H. W. S.: 'Image data compression using cubic convolution spline interpolation.', *IEEE Transactions on Image Processing*, 2000, **9**(11), 1988-1995.

[20] S. K. Park and R. A. Schowengerdt: 'Image reconstruction by parametric cubic convolution', *Computer Vision, Graphics, and Image Processing*, 1983, **23**(3), 258-272.

[21] S. Jiazheng and S. E. Reichenbach: 'Image interpolation by two-dimensional parametric cubic convolution', *Image Processing, IEEE Transactions on*, 2006, **15**(7), 1857-1870.

[22] S. E. Reichenbach and F. Geng: 'Two-dimensional cubic convolution', *IEEE Transactions on Image Processing*, 2003, **12**(8), 857-865.

[23] J. Pawley: 'Handbook of Biological Confocal Microscopy'; 2006, Springer.

[24] R. H. Webb: 'Confocal optical microscopy', *Reports on Progress in Physics*, 1996, **59**(3), 427.

[25] V. Prasad and et al.: 'Confocal microscopy of colloids', *Journal of Physics: Condensed Matter*, 2007, **19**(11), 113102.

[26] S. Inoué: 'Foundations of Confocal Scanned Imaging in Light Microscopy', in 'Handbook Of Biological Confocal Microscopy', (ed. J. Pawley), 1-19; 2006, Springer US.

[27] X. Wang, J. D. Shephard, F. C. Dear and D. P. Hand: 'Micromachining of PSZ Ceramics Using Pulsed Nanosecond Laser', The 4th International Congress on Laser Advanced Materials Processing, Kyoto, Japan, 2006.

[28] X. Wang, J. D. Shephard, F. C. Dear and D. P. Hand: 'Optimized nanosecond pulsed laser micromachining of Y-TZP ceramics', *J. Am. Ceram. Soc.*, 2008, **91**(2), 391-397.

[29] J. P. Parry, J. D. Shephard, D. P. Hand, C. Moorhouse, N. Jones and N. Weston: 'Laser Micromachining of Zirconia (Y-TZP) Ceramics in the Picosecond Regime and the Impact on Material Strength', *International Journal of Applied Ceramic Technology*, 2011, **8**(1), 163-171.

[30] M. Matysiak, J. P. Parry, J. G. Crowder, D. P. Hand, J. D. Shephard, N. Jones, K. Jonas and N. Weston: 'Development of Optical Techniques for Noncontact Inspection of Y–TZP Parts', *International Journal of Applied Ceramic Technology*, 2009, **9999**(9999).

[31] T. Kosmac, C. Oblak, P. Jevnikar, N. Funduk and L. Marion: 'The effect of surface grinding and sandblasting on flexural strength and reliability of Y-TZP zirconia ceramic', *Dental Materials*, 1999, **15**(6), 426-433.

[32] T. Kosmac, C. Oblak and L. Marion: 'The effects of dental grinding and sandblasting on ageing and fatigue behavior of dental zirconia (Y-TZP) ceramics', *Journal of the European Ceramic Society*, 2008, **28**(5), 1085-1090.

[33] B. R. L. E. D. R. V. P. T. Yu Zhang: 'Effect of sandblasting on the long-term performance of dental ceramics', *Journal of Biomedical Materials Research Part B: Applied Biomaterials*, 2004, **71B**(2), 381-386.

[34] F. C. Dear: 'Laser Machining Of Medical Grade Zirconia Ceramic For Dental Reconstruction Applications', PhD thesis, Heriot Watt University, Edinburgh, 2008.

[35] J. Parry, R. Ahmed, F. Dear, J. Shephard, M. Schmidt, L. Li and D. Hand: 'A Fiber-Laser Process for Cutting Thick Yttria-Stabilized Zirconia: Application and Modeling', *International Journal of Applied Ceramic Technology*, 2010, no-no.

[36] F. C. Dear, J. D. Shephard, X. Wang, J. D. C. Jones and D. P. Hand: 'Pulsed laser micromachining of yttria-stabilized zirconia dental ceramic for manufacturing', *International Journal of Applied Ceramic Technology*, 2008, **5**(2), 188-197.

[37] T. Kosmac, C. Oblak, P. Jevnikar, N. Funduk and L. Marion: 'Strength and reliability of surface treated Y-TZP dental ceramics', *Journal of Biomedical Materials Research*, 2000, **53**(4), 304-313.

[38] T. W. Liao, G. Sathyanarayanan, L. J. Plebani, M. U. Thomas and K. Li: 'Characterization of grinding-induced cracks in ceramics', *International Journal of Mechanical Sciences*, 1995, **37**(9), 1035-1050.

[39] J. P. Parry, J. D. Shephard, F. C. Dear, N. Jones, N. Weston and D. P. Hand: 'Nanosecond-laser postprocessing of millisecond-laser-machined zirconia (Y-TZP) surfaces', *International Journal of Applied Ceramic Technology*, 2008, **5**(3), 249-257.

[40] B. Zhang, X. L. Zheng, H. Tokura and M. Yoshikawa: 'Grinding induced damage in ceramics', *Journal of Materials Processing Technology*, 2003, **132**(1-3), 353-364.

[41] A. H. De Aza, J. Chevalier, G. Fantozzi, M. Schehl and R. Torrecillas: 'Crack growth resistance of alumina, zirconia and zirconia toughened alumina ceramics for joint prostheses', *Biomaterials*, 2002, **23**(3), 937-945.

[42] N. Koren: 'The Imatest program: comparing cameras with different amounts of sharpening', 60690L; 2006, SPIE.

[43] www.imatest.com.

[44] A. G. Podoleanu, G. M. Dobre and D. A. Jackson: 'En-face coherence imaging using galvanometer scanner modulation', *Opt. Lett.*, 1998, **23**(3), 147-149.

[45] A. D. Aguirre, P. Hsiung, T. H. Ko, I. Hartl and J. G. Fujimoto: 'High-resolution optical coherence microscopy for high-speed, in vivo cellular imaging', *Opt. Lett.*, 2003, **28**(21), 2064-2066.

[46] E. M. C. Hillman, D. A. Boas, A. M. Dale and A. K. Dunn: 'Laminar optical tomography:demonstration of millimeter-scaledepth-resolved imaging in turbid media', *Opt. Lett.*, 2004, **29**(14), 1650-1652.

[47] C. Hitzenberger, P. Trost, P.-W. Lo and Q. Zhou: 'Three-dimensional imaging of the human retina by high-speed optical coherence tomography', *Opt. Express*, 2003, **11**(21), 2753-2761.

[48] C. Gang, P. Seong-Wook, I. C. A. Chen, C. G. Beath, R. Martini, P. D. Grant, R. Dudek and H. C. Liu: 'All-optical amplitude modulation of a middle-infrared quantum cascade laser', Terahertz and Mid Infrared Radiation: Basic Research and Practical Applications, 2009. TERA-MIR 2009. International Workshop, Nov. 3 2009-Oct. 6 2009, 2009, 15-16.

[49] I. D. Lindsay, P. Groß, C. J. Lee, B. Adhimoolam and K. J. Boller: 'Mid-infrared wavelength- and frequency-modulation spectroscopy with a pump-modulated singly-resonant optical parametric oscillator', *Opt. Express*, 2006, **14**(25), 12341-12346.

[50] P. Werle, F. Slemr, K. Maurer, R. Kormann, R. Mücke and B. Jänker: 'Near- and mid-infrared laser-optical sensors for gas analysis', *Optics and Lasers in Engineering*, 2002, **37**(2-3), 101-114.

[51] R. Ding, T. Baehr-Jones, W.-J. Kim, A. Spott, M. Fournier, J.-M. Fedeli, S. Huang, J. Luo, A. K. Y. Jen, L. Dalton and M. Hochberg: 'Sub-Volt Silicon-Organic Electro-optic Modulator With 500 MHz Bandwidth', *J. Lightwave Technol.*, 2011, **29**(8), 1112-1117.

[52] R. Cramer, F. Hillenkamp and R. F. Haglund Jr: 'Infrared matrix-assisted laser desorption and ionization by using a tunable mid-infrared free-electron laser', *Journal of the American Society for Mass Spectrometry*, 1996, **7**(12), 1187-1193.

[53] A. Zajac, M. Skorczakowski, J. Swiderski and P. Nyga: 'Electrooptically Q-switched mid-infrared Er:YAG laser for medical applications', *Opt. Express*, 2004, **12**(21), 5125-5130.

7. Reflection Mid-Infrared Imaging

7.1. Motivation

It has been discussed in this work that mid-infrared imaging provides the potential to inspect 3Y-TZP components up to thickness of 6 mm. In the visible wavelength region the material grain size (between 500 nm and 1 μm) of the 3Y-TZP ceramics was comparable to the wavelength of light, hence the light scattering significantly contributed to the reduced material optical transmittance. However, the light scattering was reduced in the mid-infrared region where the wavelength was longer than the typical grain size. In the UV region (below 400 nm [1]) and above 7 μm (see Figure 4.3.2) light absorption was the limiting factor for transmittance of 3Y-TZP [2-4]. Thus, a transmission window existed in the mid-infrared wavelength region and was therefore the most appropriate region for the inspection of flaws within the bulk of 3Y-TZP ceramics.

Apart from the 3Y-TZP components that are a few mm thick there is the need for detecting flaws in much thinner Zirconia ceramic coatings, 10 - 100 μm thick, driven by the increased use of these ceramic materials in a variety of applications such as combustion engines metal coatings, [5-8] fuel cells [9, 10] and protective coatings for mechanical tools [11, 12]. These ceramic coatings increase the mechanical stability and wear resistance, and hence increase the reliability of the coated components particularly in the harsh or extreme environments where metallic counterparts could fail more rapidly. There has been some work presented in the literature based on the infrared inspection of ceramic coatings using mid-infrared reflectance imaging [13, 14] and thermographic techniques [15-19], however limited material depth of penetration and low resolution with these techniques were their culprit (see chapter 2).

Two techniques were investigated as an alternative to currently developed inspection techniques with the aim to surpass the above mentioned limitations: the first based on the reflectance imaging technique published previously [13, 14] and the second based on a reflectance confocal pinhole scanning [20]. Both the techniques presented in this chapter used the light reflected from the ceramic surface and ceramic-metal interface to image the roughness and any structural changes or defects in the coating.

7.2. Camera Mid-Infrared Reflection Imaging (Camera-MIRI)

7.2.1. Experimental setup

The Camera Mid-Infrared Reflection Imaging (Camera-MIRI) technique used an infrared camera as a light detector. The experimental setup is presented in Figure 7.2.1. The system was based on the MIR-TI setup (see Figure 5.3.1) with the infrared source positioned at an angle as opposed to directly behind the sample. The angle of the incidence for the infrared light source was set to 20º to provide 45% of the light being reflected and 55% of the light being transmitted (see Figure 7.2.1). The angle of incidence and the optical reflection and transmission values were estimated for the wavelength of 6 µm [21]. It should be noted that the transmitted light would in turn be reflected off the substrate surface on which the ceramic was coated (usually metal) hence would also ultimately be detected in reflection.

The next step was to ensure that the angle between the camera and the sample was adjusted to maximise the light reaching the camera sensor. Due to the camera design and size 20° +/- 2º angle was used for the imaging part of the setup (see Figure 7.2.1). A further increase of the angle was not feasible due to the close proximity of one of the lenses. Although the 20º angle of reflection and 20º angle of illumination were deemed not to be critical within +/- 2º, they were nominally aligned to give the desired amount of light transmitted and reflected in the sample and to provide the maximum signal strength for the light reaching the camera sensor. The ceramic surface, particularly for the sprayed ceramic coatings has a considerable surface roughness variation, thus it was not crucial to align the system precisely to the aforementioned angles.

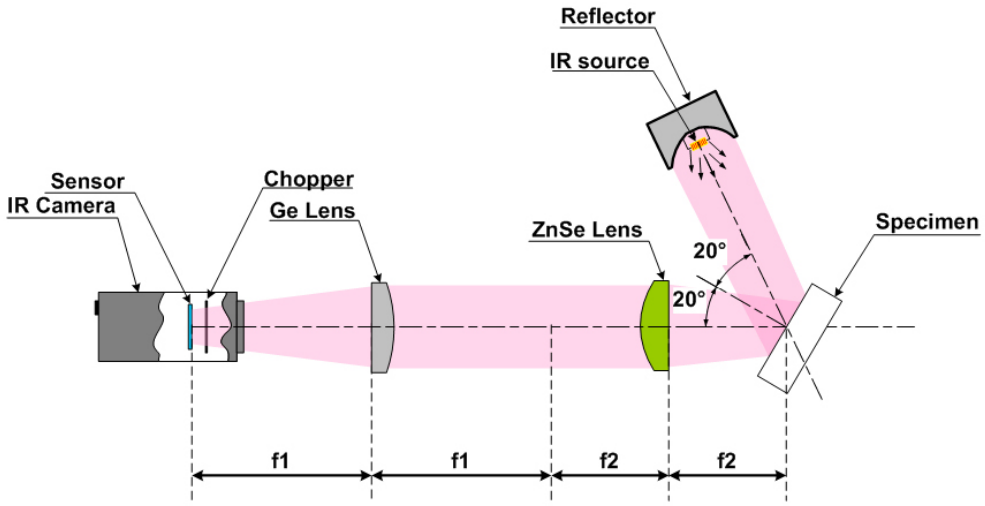

Figure 7.2.1. Camera Mid-Infrared Reflection Imaging setup. Top view.

The imaging part of the Camera-MIRI system including the infrared camera and the lenses were assembled exactly as the MIR-TI setup (see Figure 5.3.1). Due to the angled position of the sample in reference to the imaging system, only a 2 mm wide sample area was in focus in the acquired images. The height of the in-focus image remained unchanged at 7 mm (see section 5.3). Thus, to cover the entire area of the sample more images had to be taken compared to the MIR-TI technique where the in focus region covered 11 x 7 mm (see section 5.3).

The images captured by the camera were acquired using Labview program which grabbed the image frames at 10 Hz frequency. Due to the low contrast of the acquired images a Matlab "imadjust" image enhancement script was employed (see section 5.3.3) to post-process the images.

7.2.2. Camera-MIRI Imaging resolution measurements

Although the Camera-MIRI imaging part of the setup was based on the MIR-TI system (see chapter 5) the sample was placed under an angle, therefore the imaging resolution of the system had to be assessed. To quantify the Camera-MIRI setup resolution, the measurements were performed with infrared USAF target (see sections 5.3.4 and 5.3.6). The measurement procedure was described in chapter 5 and 6. For the infrared USAF target the resolution of the imaging system was estimated by determining the smallest target bars which could be resolved by the observer. Then the resolution of the system was calculated according to Equation 2.7 and Equation 2.8. The measurement error of 12% (see chapter 5) was also included in the calculated results. The acquired images of all three targets are presented in Figure 7.2.2. The resolution calculated from the Infrared USAF target was 44 µm (group 3 element 4) which with 9% bars size error resulted resolution of 48 ± 6 µm.

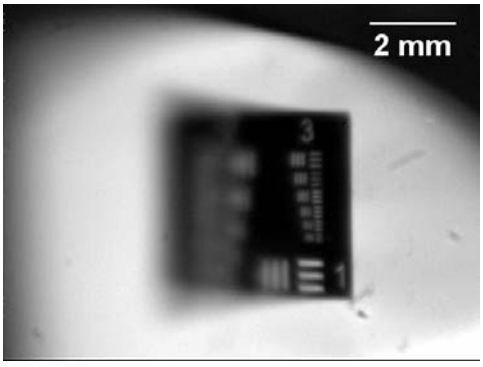

Figure 7.2.2. The images acquired during the resolution measurements using: a) Infrared USAF; b) Imatest targets.

Depth of Field (DOF) was another important parameter for the imaging system which defined the distance which is in focus and can be seen as a sharp image in the volume of the specimen tested along the optical axis of the imaging system. As the imaging part of the reflection system remained unchanged (numerical aperture and the lens system were the same) compared to the MIR-TI system (see Figure 5.3.1), the DOF was estimated to be equal to the DOF of the MIR-TI system which was 50 μm (see section 5.3.4).

7.2.3. Camera-MIRI Imaging results

The ultimate aim of the Camera-MIRI technique was an observation not only of surface changes but also detecting any changes or defects appearing on the interface between the ceramic coating and the metal substrate such as cracking or delamination. To investigate if the infrared reflection technique was capable of providing information about the subsurface flaws or defects a simple test model of a ceramic coating was developed (see Figure 3.4.1) because it was difficult to obtain samples of ceramic coated metal with known defects. To be able to quantify the suitability of the Camera-MIRI measurement technique a defect of known size was required at the ceramic-metal interface.

Samples 13 and 14 were imaged with the Camera-MIRI system and the acquired images of ceramic coatings are presented in Figure 7.2.3. The machined lines underneath the ceramic layer were observable during the measurement. The smallest line which was detected with sample 13 was the line 3 from group 3 (see Figure 3.4.2) which measured 60 ± 6 μm in width and 4 ± 0.4 μm in depth. With sample 14 the smallest measured line was 82 ± 8 μm wide and 10 ± 1 μm deep (group 2, element 1). The detection of such a small grooves was possible due to the width of the introduced defects which combined with the depth of the machined groove produced a significant simulated coating-interface defect.

The apparent blurring of the laser machined lines produced in the images was due to the fact that the light had to pass the thickness of the ceramic coating twice, so it was refracted several times and in focus position was more difficult to spot from the images. Furthermore, the presented results confirmed that the light was not only reflected from the top surface of the ceramic coating but it penetrated the material and was reflected from the metallic substrate as well (see Figure 7.2.3). This test demonstrated a potential

to inspect ceramic coatings for sub-surface flaws detection using the Camera-MIRI technique.

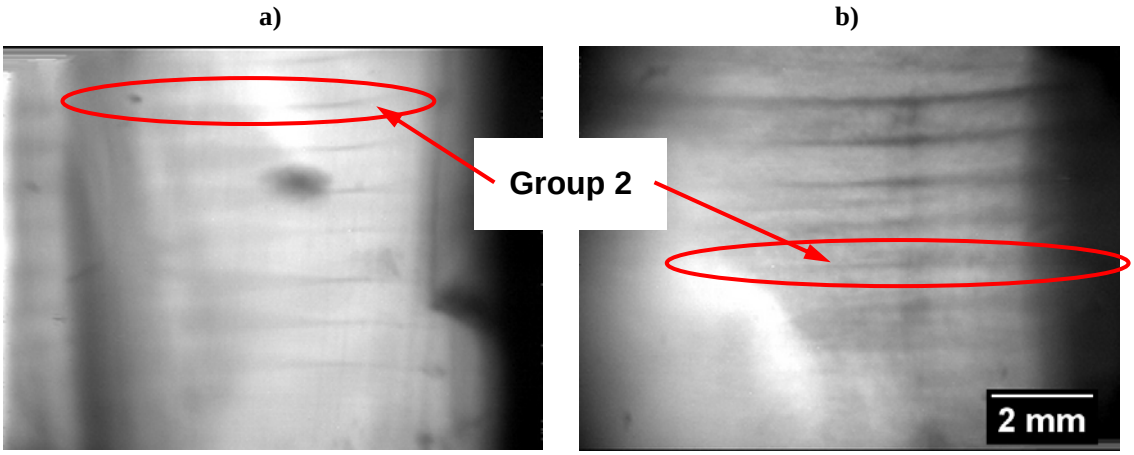

Figure 7.2.3. Sub-surface flaws detection in: a) sample 13 and b) sample 14.

Following this initial proof-of-concept, several thermal barrier coating samples were measured using the Camera-MIRI technique to assess the suitability of the technique for practical components. The Camera-MIRI images of the tested samples 15, 16 and 17 are presented in Figure 7.2.4. The image of sample 15 revealed bright spots (highlighted in red in Figure 7.2.4) near the top edge of the sample which showed the exposed TGO layer due to damage to the YSZ layer. The inspection with SEM revealed the same feature as in the infrared image (see Figure 3.4.6). However, using the visible light inspection required much higher magnification (the magnification of 5) for the imaging system in order to detect the surface flaw compared to the MIRI technique (the magnification of 1.31) Therefore using a visible light based inspection technique for these surface flaws was more time intensive and required more images to be acquired to fully inspect a given surface compared to the MIRI technique.

The bright spots in the centre of the image from Figure 7.2.4(a) indicated an exposure of the TGO layer. Apart from that the indentation defects were identified close to the edge of the samples in Figure 7.2.4(a) and (b). The change in the angle of reflection of the light bouncing off the surface caused the defects in these areas to appear darker in the image. The SEM image of one of the indentation defects is presented in Figure 3.4.5 & Figure 3.4.7. Stresses and deformation in the metallic substrate caused by the indentation led to the coating cracking and a localized spallation.

Figure 7.2.4(c) presents the Camera-MIRI image of sample 17 which was aged to investigate any structural changes of the coating during the process. No defects were

detected although some bright spots appeared in the images. Further investigation with the optical microscope and the SEM (see Figure 3.4.8) revealed that the bright spots were due to the inherent roughness of the coating. The increased angle of reflection (in reference to the sample surface) highlighted the rough or raised coating areas as bright regions (see Figure 7.2.5) due to an enhanced amount of photons reaching the detector. This created a challenge for an automated defect detection technique as exposed TGO regions and the light reflection from the raised surface produced similar effects. This phenomenon has to be further explored. In addition the high sensitivity of the Camera-MIRI due to the changing structural properties of the produced coating could potentially be used as a quality control monitor in-situ during the fabrication of the coating.

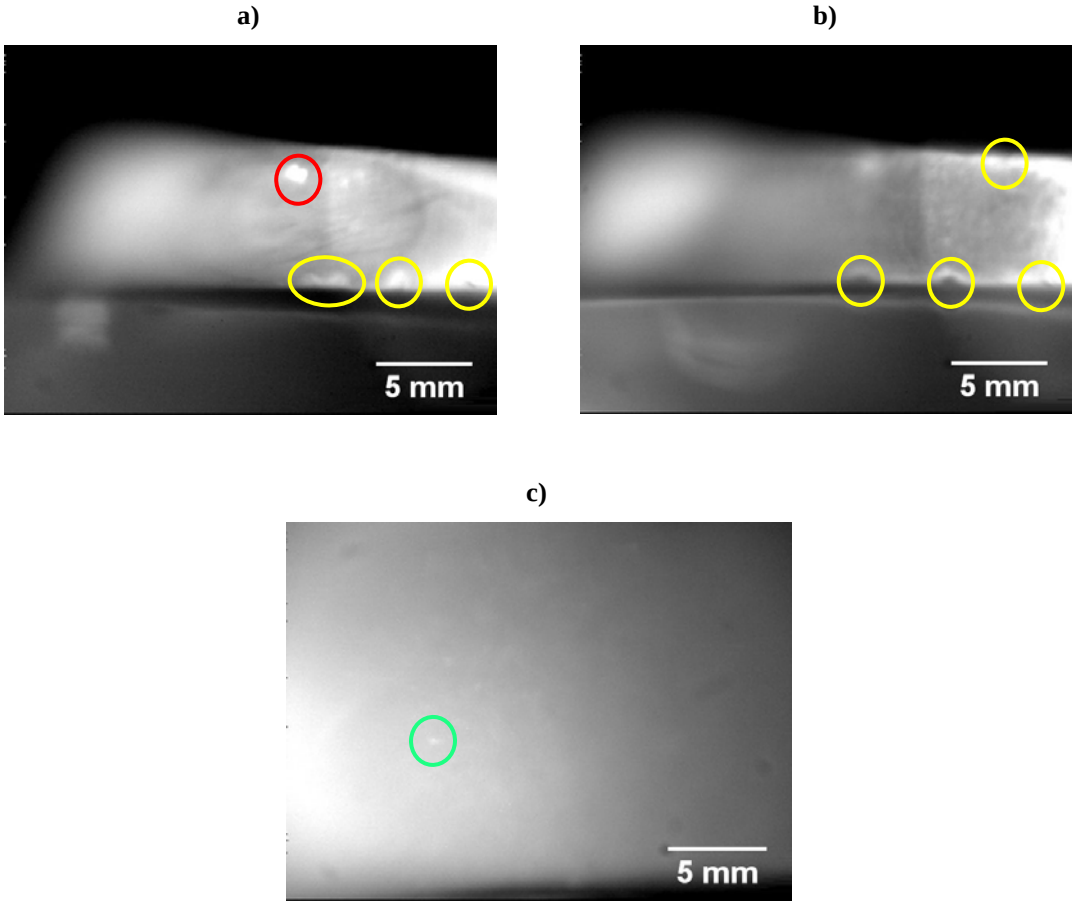

Figure 7.2.4. Camera-MIRI images of the samples: a) 15, b) 16 and c) 17 (in red the ceramic coating flaw, in yellow the surface edge indents and in green the bright spots from the rough surface are highlighted).

The above results have shown that the Camera-MIRI system was suitable for surface flaws detection. However, the subsurface analysis could not be verified due to not having a defined subsurface defect buried in YSZ coated sample. Nevertheless the

potential to detect the ceramic coating flaws via a mid-infrared reflection technique was promising.

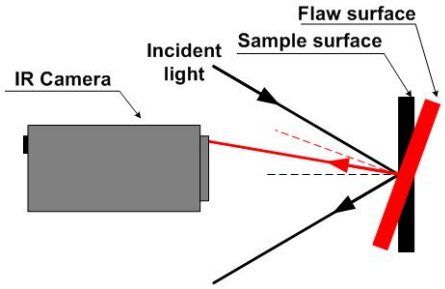

Figure 7.2.5. A simplified diagram describing how localised surface roughness change in the proximity of the surface flaw can alter the intensity of the region as imaged by the camera. The changing local angle of the surface in reference to the incident light beam change the light reflection angle leading to the variation of the light intensity.

Apart from the front of the sample the TBC is also deposited on the back surface in proximity of the cooling holes. The picture of the nozzle area of sample 17 where the coating was deposited after the holes were drilled is presented in Figure 7.2.6. There were some bright spots detected which again indicated the presence of some surface roughness in the proximity of the nozzle but no significant defect was identified. The SEM image (see Figure 3.4.9) confirmed that surface roughness was the reason for the bright spots detected in the infrared image.

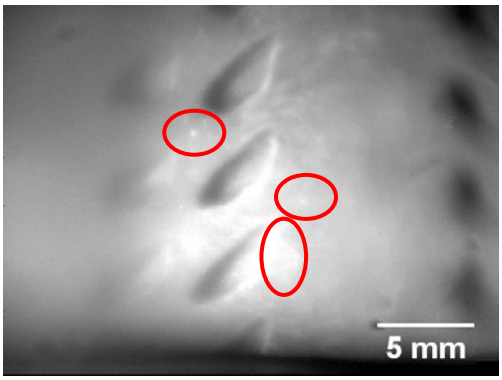

Figure 7.2.6. Camera-MIRI image of the TBC in proximity of the exhaust nozzles. The highlighted bright spots are the surface roughness variation.

The last group of samples inspected with the Camera-MIRI were samples 18, 19 and 20 from Figure 3.4.10. Due to the relatively high surface roughness produced by the spraying process (see Figure 7.2.7) detecting defects was considerably more difficult. No defects were detected during the measurement although the cracks between the deposited splats existed (see Figure 3.4.11, Figure 3.4.12 and Figure 3.4.13). The main

obstacle with micro scale crack detection on these samples was the limited camera Camera-MIRI imaging resolution and the surface roughness which caused light scattering.

All the surface structures in Figure 7.2.7 appeared to be similar because the same APS spraying process was employed for all the coatings. However, the TiO_2 coating structure had well-defined splats whereas in the Al_2O_3 and YSZ coatings the splats were separated by the cracks. These cracks were generated by thermal shock during the cooling process after the coating spray was deposited on the cooler substrate. Rapid quenching led to the thermal shock which resulted in the crack formation [22-24]. Due to the low resolution (in comparison to the crack size) and low magnification (M = 1.31) of the Camera-MIRI system and due to the rough surface of the sprayed coatings, detection of these cracks was not feasible.

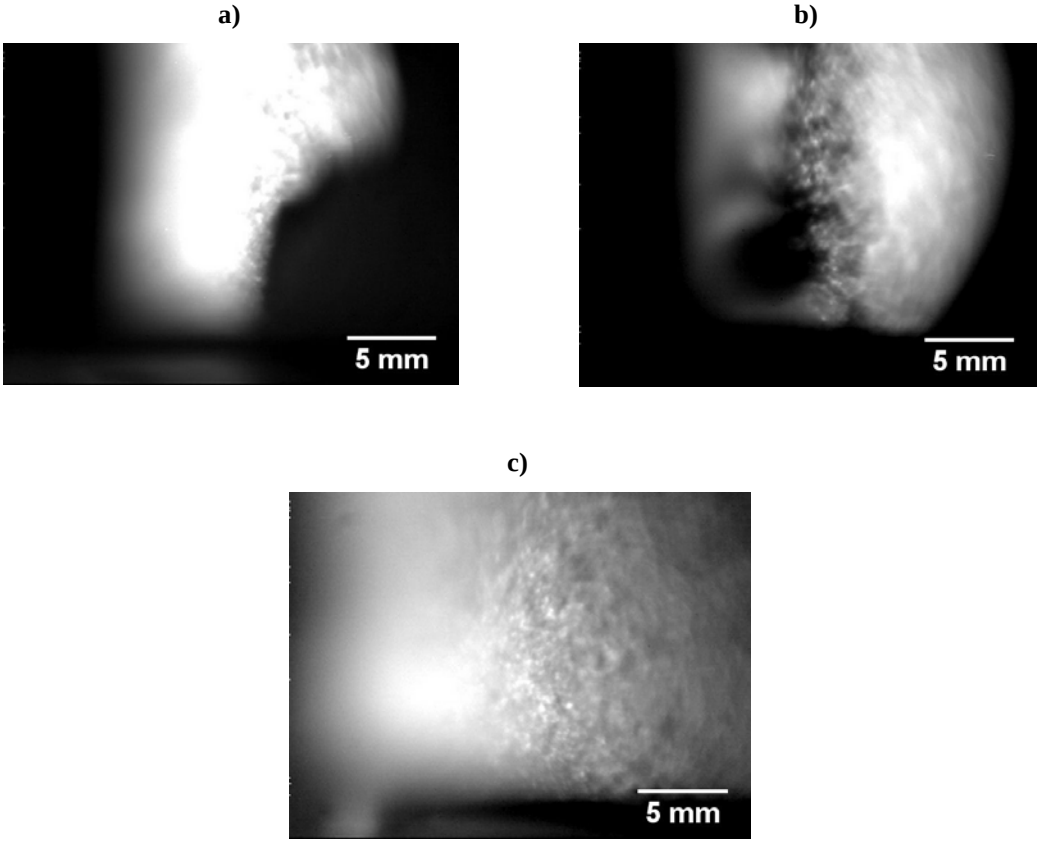

Figure 7.2.7. Camera-MIRI results of samples: a) 18, b) 19 and c) 20. The inherent roughness from the spraying process is apparent with the Camera-MIRI technique but no obvious flaws could be observed.

The images from Figure 7.2.7 acquired with the Camera-MIRI system provided mainly the information about the surface of the coatings, hence to identify if the light propagated deeper into the coating the optical transmittance spectra of a piece of 400

µm thick YSZ free-standing coating was measured with FTIR spectroscopy (see Figure 3.4.14). Although a small transmittance peak within the wavelength range similar to 3Y-TZP was observed the subsurface detection was not feasible due to surface roughness and the resulting splat-type material structure produced by the spraying process. These splats were considerably bigger in size compared to the 3Y-TZP grains presented in Figure 2.4.1 and therefore the light was scattered.

7.3. Confocal Mid-Infrared Reflection Imaging (Confocal-MIRI)

7.3.1. Experimental setup

The Confocal Mid-Infrared Reflection Imaging (Confocal-MIRI) setup was based on the CMIR-TI system (see Figure 6.2.6) where instead of the detection of the light transmitted through the sample the light reflected from the surface was acquired (Figure 7.3.1). The infrared source was mounted under the same 20º +/- 2º angle of incidence as used previously with the Camera-MIRRI to provide a similar level of the light reflected from the front surface and penetrating and reflecting from the subsurface (paragraph 7.2.1). The imaging part of the setup remained identical to the CMIR-TI setup from Figure 6.2.5. The sample was mounted on the motorised stages which x and y stages were mounted under a 20º +/- 2º angle in reference to the imaging part of the setup. The z axis stage was positioned on optical axis of the imaging part of the system to provide constant position of the sample in the acquired images when moving the sample.

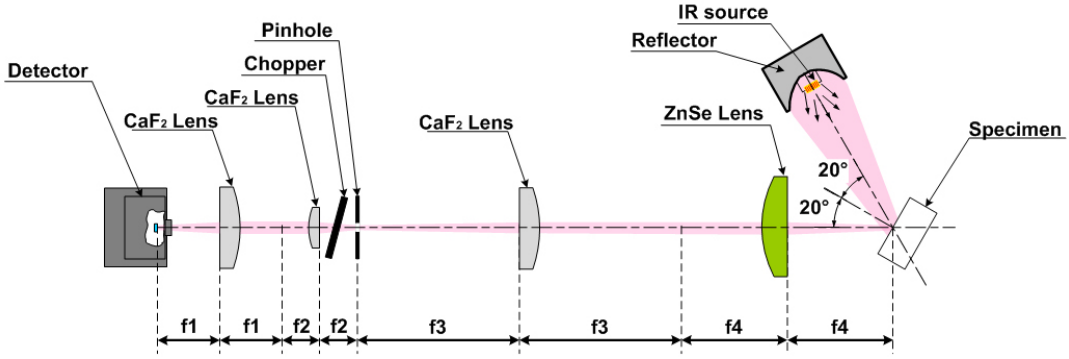

Figure 7.3.1. Confocal-MIRI setup. Top view.

The Confocal-MIRI system was controlled from Labview using the same software package as for the control of the CMIR-TI system (see section 6.2.4). As before the

images were produced using the Matlab software package (see section 6.2.5) and the plotting scale was adjusted to maximise the image contrast.

7.3.2. Confocal-MIRI Imaging resolution measurements

Once aligned an assessment of the resolution of the Confocal-MIRI system was carried out. The Infrared USAF (see Appendix B) target was employed during the measurement (Figure 7.3.2). Initially a 25 µm step scanning was employed during the resolution measurements to set the focal position. During the experiments only 25 and 10 µm step scanning were employed to achieve the most accurate results. The resolution achieved with the USAF infrared target was 61 ± 7 µm (including 9% bar size and 12% measurement errors) (group 3, element 2) for 25 µm step scanning and a minor resolution enhancement of 48 ± 6 µm (group 3, element 4) was observed for 10 µm scanning.

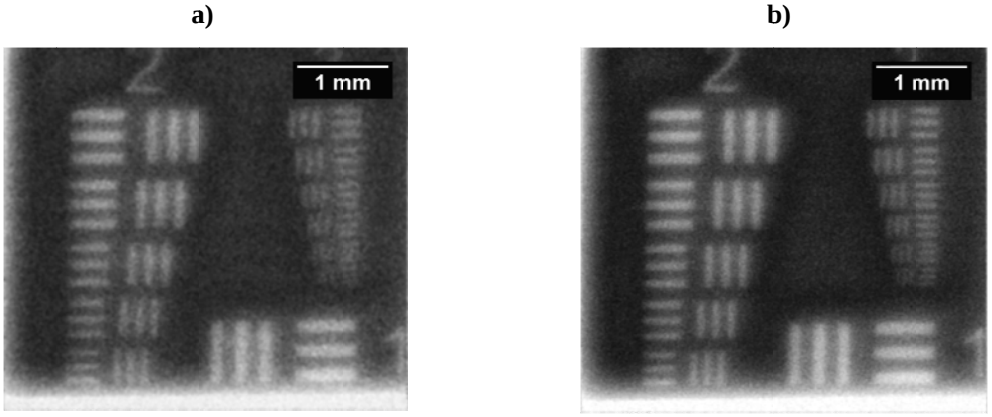

Figure 7.3.2. Confocal-MIRI resolution measurement using 50 µm pinhole with: a) Infrared USAF target, 25 µm step scanning; b) Infrared USAF target, 10 µm step scanning.

During the resolution measurements with a 50 µm pinhole the infrared source current was set to a relatively low value of I = 0.9 A (compared with I = 1.8 A used in the CMIR-TI technique) as the detected signal level strength was high. Therefore the 50 µm diameter pinhole (used for the CMIR set-up) was replaced with a 25 µm diameter pinhole, as there would be sufficient signal strength even with a reduced pinhole size. This allowed to evaluate if any further imaging resolution enhancement with reduced pinhole size was possible. The result of the Confocal-MIRI scanning with the 25 µm pinhole is presented in Figure 7.3.3.

The resolution values estimated for the 25 µm pinhole, using 25 and 10 µm step size scanning with the infrared USAF target were 54 ± 7 µm (including 9% bar size and

12% measurement errors) (group 3, element 3) and 44 ± 5 µm (group 3, element 5) respectively. However, the enhancement was not significant providing a maximum of 12% for improvement in spatial resolution. All the resolution results are presented in Table 7.1. It should be noted that measurements with a 25 µm pinhole for the CMIR-TI technique could not be carried out due to the low signal level.

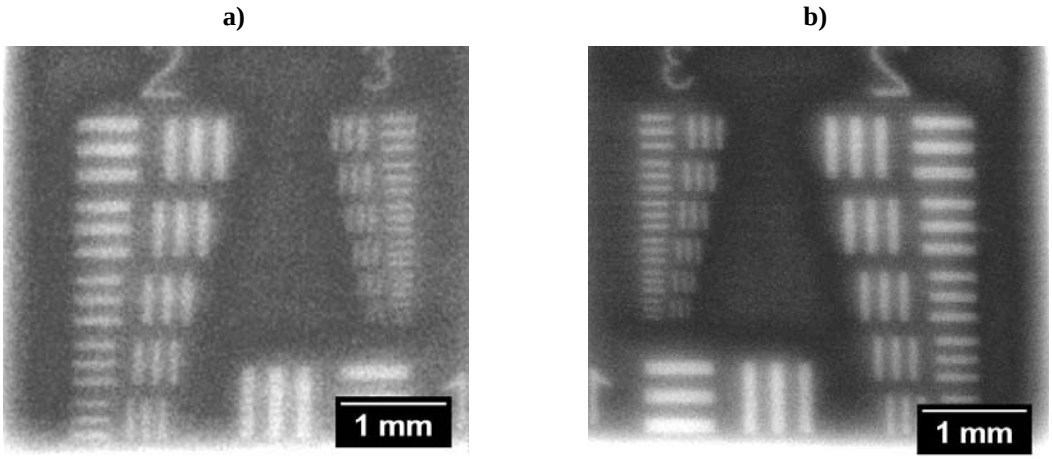

Figure 7.3.3. Infrared and Imatest targets images acquired using Confocal-MIRI system with installed 25 µm pinhole: a) 25 µm; b) 10 µm steps.

Table 7.1. Confocal-MIRI system parameters calculated using infrared USAF testing target.

Parameter / Step size/Pinhole size	Resolution R [µm]
25 µm/50 µm	61 ± 7
10 µm/50 µm	48 ± 6
25 µm/25 µm	54 ± 7
10 µm/25 µm	44 ± 5

7.3.3. Confocal-MIRI Imaging results

Following the optimisation of the Confocal-MIRI system focal position and the resolution measurement, the maximum depth through a ceramic coating that the Confocal-MIRI technique could successfully image was investigated. The test was analogous to the Camera-MIRI measurement. 50 µm pinhole, 25 and 10 µm step scanning were employed to image the same samples 13 and 14. The acquired images are presented in Figure 7.3.4.

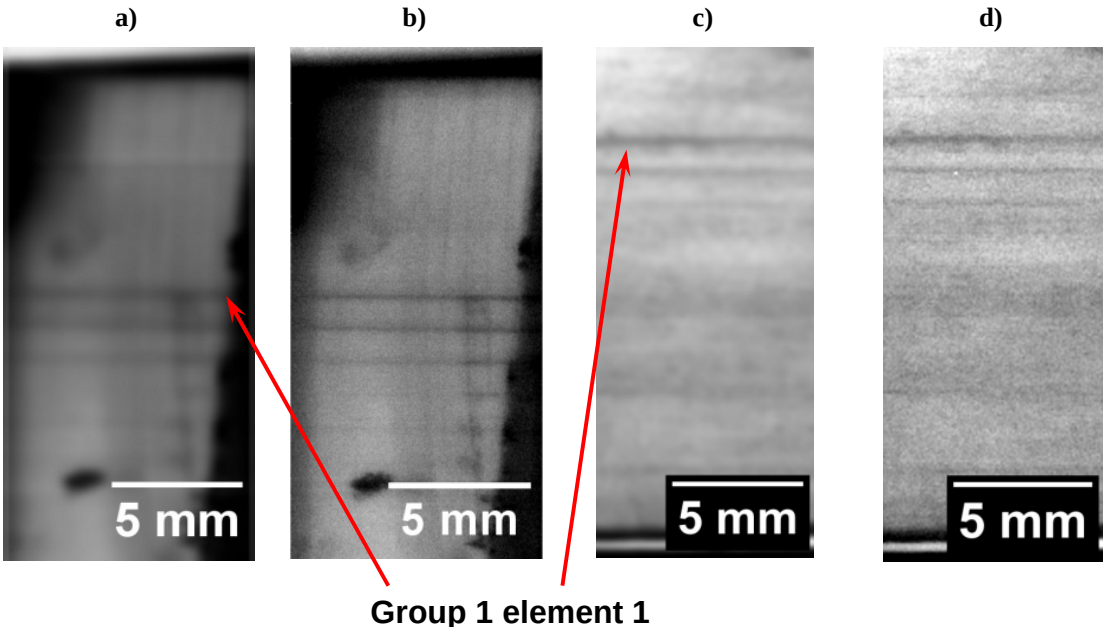

Figure 7.3.4. The estimation of the depth of penetration capabilities of the Confocal-MIRI system using: a) sample 13 - 25 µm step; b) sample 13 - 10 µm step; c) sample 14 - 25 µm step; d) sample 14 - 10 µm step scanning.

Similar to the camera system the increasing thickness of the sample reduced the imaging resolution due to the increased blurring. For sample 13 scanned with 25 µm steps the marked line measuring 82 ± 8 µm in width and 10 ± 1 µm in depth (group 2, element 1) was identified and for a 10 µm step scanning the line measuring 76 ± 8 µm in width and 7 ± 0.7 µm in depth (group 1 element 4) was detected. With sample 14 the line measuring 110 ± 10 µm in width and 35 ± 4 µm in depth (group 1, element 2) was detected with 25 µm step scanning, whereas for 10 µm scanning the line 104 ± 10 µm thick and 14 ± 1 µm deep (group 1, element 3) was identified. This showed that the detection of the marked lines with 200 and 500 µm thick coatings was comparable to the Camera-MIRI results and that it was possible to detect the sub-surface features with Confocal-MIRI technique.

As the simulated ceramic coating samples showed some promising results for sub-surface flaws detection, the jet engine blade samples 15, 16 and 17 previously tested with the Camera-MIRI (see section 7.2.3) were also tested with the Confocal-MIRI system (see Figure 7.3.5 and Figure 7.3.7). The remaining samples tested with Confocal-MIRI were measured using 50 µm pinhole and 25 µm step scanning. In Figure 7.3.5(a) the bright spot on the left was the exposed TGO area which was also detected with the Camera-MIRI technique. There were many fewer indent flaws detected with the Confocal-MIRI system due to the design of the sample holder. To repeatedly position the specimens in the Confocal-MIRI setup focal position a reference

point on the sample holder surface was required. Therefore a lip on the sample holder as a reference surface was introduced.

Figure 7.3.6 presents a picture of the sample holder, where design obscured the detection of one of the sample edges. The bright region at the bottom of the images from Figure 7.3.5(a) and (b) was a part of the sample holder and it obscured the indents at the bottom of the tested samples (see section 7.2.3). Unfortunately due to the sample geometry it was difficult to remount the samples to be able to view these indents without changing the whole setup. This was one of the drawbacks of the developed Confocal-MIRI system. The samples which were large or had the irregular shape were difficult to inspect and limited the current capabilities of this technique.

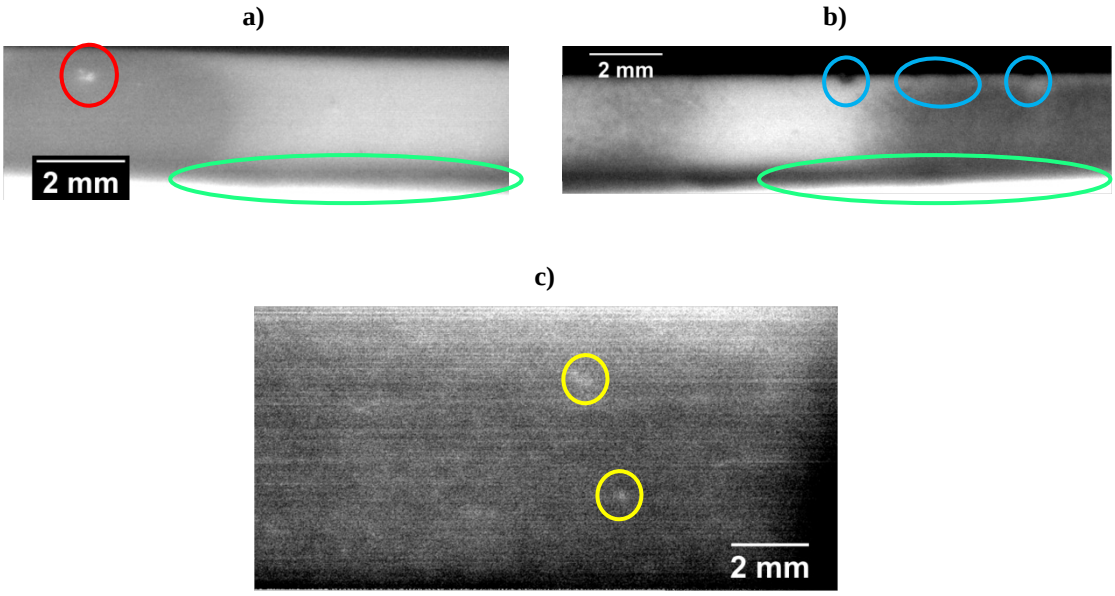

Figure 7.3.5. Confocal-MIRI results of sample: a) 15; b) 16 and c) 17. Red colour highlights the failed coating defect, green highlights the reflection from the sample holder surface, blue highlights the indents detected near the edge of the sample and yellow highlights bright spots due to surface roughness variation are shown).

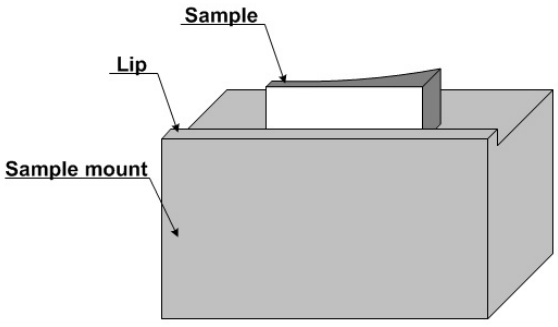

Figure 7.3.6. Confocal-MIRI sample holder. The lip on the sample mount obscures a section of the sample surface.

For sample 16 from Figure 7.3.5(b) however the indents on the top edge were detected. There were also some bright spots appearing in Figure 7.3.5(c). As with the Camera-MIRI technique the bright spots identified in the images indicated a surface roughness or texture which was also confirmed in the SEM image (see Figure 3.4.8).

The Confocal-MIRI images were sharper and clearer compared to the Camera-MIRI due to the out-of-focus photons being filtered by the confocal system. Thus, the lower quantity of photons acquired at once reduced also the quantity of photons scattered from outside of the pinhole region. Therefore more photons from the area directly covering the investigated region contributed to the light detected. A good example of this are the black dots in Figure 7.3.7(b) which indicated a rough surface. The angles of illumination and detection were insufficient for the light to enter such a deep feature and be reflected back to the detector and consequently the photons which were scattered in the neighbourhood of these features were filtered out by the pinhole. Therefore black spots in the image indicated a considerably rough surface. To actually detect how deep these craters are the angle of incidence and detection would have to be adjusted so that the light reflected and scattered from that area could reach the detector. Alternatively, in the case of the camera system the camera sensor essentially consisted of hundreds of small pinholes which acquired the light intensity signal capturing a larger area of the scattered photons. Again, as observed with the Camera-CMIRI measurements, the detection of the cracks on the surface of the coatings using the Confocal-MIRI system was not possible due to the low resolution and low magnification in comparison to the cracks size.

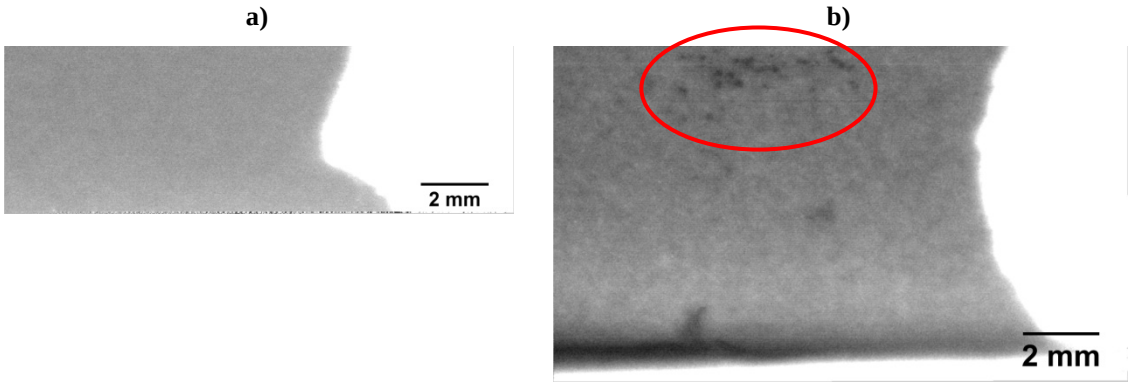

Figure 7.3.7. Confocal-MIRI results of sample: a) 18 and b) 19 respectively. In red a rough surface highlighted by the black dots is observed.

7.4. Conclusions

The need to find a rapid inspection technique for highly scattering ceramics is of significant interest particularly in jet engine applications where the engine components operate in harsh environments and reliability is extremely important. Mid-infrared reflection techniques presented in this chapter have a potential to detect some macro scale changes on the surface of the ceramic coatings used for these applications.

For the Camera-MIRI the achieved imaging resolution measured with the infrared USAF target was 48 ± 6 µm, whereas for the MIR-TI system (see chapter 5) the USAF result was 43 ± 5 µm. For the Confocal-MIRI the imaging resolution for the infrared USAF target was 48 ± 6 µm, whereas for the CMIR-TI system it was 38.5 ± 5 µm. The results for Confocal-MIRI are based on a 50 µm pinhole and 10 µm step scanning. Due to the strong signal available during the measurements a 25 µm pinhole was also used. With this reduced pinhole size the imaging resolution was improved to 44 ± 5 µm for the infrared USAF target.

The results presented for the artificially produced flaws underneath the zirconia slice (see Figure 7.2.3 and Figure 7.3.4) showed that for a 200 µm thick coating the flaws as small as 60 ± 6 µm in width and 4 ± 0.4 µm in depth could be detected and for 500 µm thick coating the flaws measuring 82 ± 8 µm in width and 10 ± 1 µm in depth could be detected by the Camera-MIRI. With Confocal-MIRI the flaws measuring 76 ± 8 µm in width and 7 ± 0.7 µm in depth for 200 µm thick coating and for 500 µm coating the flaws measuring 104 ± 10 µm in width and 14 ± 1 µm in depth were detected. These measurements revealed that subsurface defect detection, including the micro scale, was possible but further investigation is required in order to evaluate the penetration of a rough ceramic coating.

In addition to samples 13 and 14 there were other TBCs (see sample 13 and 14). Apart from these samples there were other thermal barrier coatings (see samples 15, 16 and 17) inspected with both Camera- and Confocal-MIRI techniques. The intentionally introduced indentations as well as one coating failure defect (see Figure 7.2.4 and Figure 7.3.5) were detected by both systems. Unfortunately the cracks detected with SEM (see Figure 3.4.11, Figure 3.4.12 and Figure 3.4.13) could not be detected by any of the systems presented in this chapter due to their limited imaging resolution.

Surface roughness of the coatings was also imaged during the measurements of the samples from Figure 7.2.4, Figure 7.2.6, Figure 7.3.5 and Figure 7.3.7 which could be

used for monitoring and control of the ceramic spraying process. There are inherent advantages of using infrared radiation compared to the visible light inspection due to reduced light scattering at a longer wavelength (see chapter 5 and chapter 6). In the visible wavelength region imaging the surface, particularly for surface roughness monitoring, was difficult due to the light scattering. The pictures of the tested samples from Figure 3.4.4 and Figure 3.4.10 required manual focus adjustments on the Canon DSLR camera to acquire the pictures as the autofocus did not produce sharp images. Moreover detecting some of the flaws with a visible inspection technique required higher magnification of the imaging system compared to the infrared inspection technique. Finally these MIRI techniques may offer an alternative solution for detecting the surface position which again is considerably more difficult with visible light.

Table 7.2 presents the results for all the tested samples in this chapter. For most of the samples the results using either Camera- or Confocal-MIRI inspection were comparable, the Camera-MIRI technique provides a faster measurement technique. This however increases the cost of the system in comparison to the Confocal-MIRI. The build costs for both systems were comparable to their transmission counterparts.

Table 7.2. List of the samples tested with the Camera- and Confocal-MIRI techniques. Colours indicate: green – suitable for ceramic coating inspection, orange – limited feedback about the detected feature, red – the inspection of the features not possible. Macro features measure more than 1 mm in size and micro scale features measure below 1 mm in at least two dimensions.

Sample	Features inside the sample	Camera-MIRI		Confocal-MIRI	
13	1. Micro scale flaws	1. 60 ± 6 µm wide x 4 ± 0.4 µm deep	●	1. 25 µm step - 82 ± 8 µm wide x 10 ± 1 µm deep 2. 10 µm step - 76 ± 8 µm wide x 7 ± 0.7 µm deep	● ●
14	1. Micro scale flaws	1. 82 ± 8 µm wide x 10 ± 1 µm deep	●	1. 25 µm step - 110 ± 10 µm wide x 35 ± 4 µm deep 2. 10 µm step - 104 ± 10 µm wide x 14 ± 1 µm deep	● ●
15	1. Indentations 2. TGO defect	1. Possible 2. Possible	● ●	1. Obscured by sample holder 2. Possible	● ●
16	1. Indentations	1. Possible	●	1. Possible	●
17	1. Surface roughness 2. Back surface roughness	1. Possible 2. Possible	● ●	1. Possible 2. Not measured	●
18	1. Surface roughness	1. Possible	●	1. No surface roughness detected	●
19	1. Surface roughness	1. Possible	●	1. Possible – better image contrast	●
20	1. Surface roughness	1. Possible	●	1. Not measured	

References:

[1] W. Att, M. Takeuchi, T. Suzuki, K. Kubo, M. Anpo and T. Ogawa: 'Enhanced osteoblast function on ultraviolet light-treated zirconia', *Biomaterials*, 2009, **30**(7), 1273-1280.

[2] D. L. Wood and K. Nassau: 'Refractive-Index of Cubic Zirconia Stabilized with Yttria', *Appl. Optics*, 1982, **21**(16), 2978-2981.

[3] D. L. Wood, K. Nassau and T. Y. Kometani: 'Refractive-Index of Y2o3 Stabilized Cubic Zirconia - Variation with Composition and Wavelength', *Appl. Optics*, 1990, **29**(16), 2485-2488.

[4] L. A. Dombrovsky, H. K. Tagne, D. Baillis and L. Gremillard: 'Near-infrared radiative properties of porous zirconia ceramics', *Infrared Physics & Technology*, 2007, **51**(1), 44-53.

[5] C. G. Levi: 'Emerging materials and processes for thermal barrier systems', *Current Opinion in Solid State and Materials Science*, 2004, **8**(1), 77-91.

[6] D. R. Clarke, C. G. Levi and A. G. Evans: 'Enhanced zirconia thermal barrier coating systems', *Proceedings of the Institution of Mechanical Engineers Part a-Journal of Power and Energy*, 2006, **220**(A1), 85-92.

[7] M. Duncan, M. Bashkansky and J. Reintjes: 'Subsurface defect detection in materials using optical coherence tomography', *Opt. Express*, 1998, **2**(13), 540-545.

[8] I. Birkby and R. Stevens: 'Applications of zirconia ceramics', in 'Advanced Ceramic Materials', 527-551; 1996, Clausthal Zellerfe, Trans Tech Publications.

[9] M. Atik, P. de Lima Neto, L. A. Avaca and M. A. Aegerter: 'Sol-gel thin films for corrosion protection', *Ceramics International*, 1995, **21**(6), 403-406.

[10] M. Ritala and M. Leskelä: 'Zirconium dioxide thin films deposited by ALE using zirconium tetrachloride as precursor', *Applied Surface Science*, 1994, **75**(1-4), 333-340.

[11] I. Zhitomirsky and A. Petric: 'Electrophoretic deposition of ceramic materials for fuel cell applications', *Journal of the European Ceramic Society*, 2000, **20**(12), 2055-2061.

[12] A. Syed, Z. Ilhan, J. Arnold, G. Schiller and H. Weckmann: 'Improving plasma-sprayed yttria-stabilized zirconia coatings for solid oxide fuel cell electrolytes', *Journal of Thermal Spray Technology*, 2006, **15**(4), 617-622.

[13] J. I. Eldridge, C. M. Spuckler and R. E. Martin: 'Monitoring delamination progression in thermal barrier coatings by mid-infrared reflectance imaging', *International Journal of Applied Ceramic Technology*, 2006, **3**(2), 94-104.

[14] J. I. Eldridge, C. M. Spuckler, J. A. Nesbitt and K. W. Street: 'Health Monitoring of Thermal Barrier Coatings by Mid-Infrared Reflectance', in '27th Annual Cocoa Beach Conference on Advanced Ceramics and Composites: A: Ceramic Engineering and Science Proceedings, Volume 24, Issue 3', (ed. H.-T. L. Waltraud M. Kriven), 511-516; 2008.

[15] M. K. Ferber, A. A. Wereszczak, M. Lance, J. A. Haynes and M. A. Antelo: 'Application of infrared imaging to the study of controlled failure of thermal barrier coatings', *J. Mater. Sci.*, 2000, **35**(11), 2643-2651.

[16] G. Newaz and X. Chen: 'Progressive damage assessment in thermal barrier coatings using thermal wave imaging technique', *Surface and Coatings Technology*, 2005, **190**(1), 7-14.

[17] S. Marinetti, V. Vavilov, P. G. Bison, E. Grinzato and F. Cernuschi: 'Quantitative infrared thermographic nondestructive testing of thermal barrier coatings', *Materials Evaluation*, 2003, **61**(6), 773-780.

[18] B. Franke, Y. H. Sohn, X. Chen, J. R. Price and Z. Mutasim: 'Monitoring damage evolution in thermal barrier coatings with thermal wave imaging', *Surface and Coatings Technology*, 2005, **200**(5-6), 1292-1297.

[19] B. Franke, Y. H. Sohn, X. Chen, J. R. Price and Z. Mutasim: 'Thermal Wave Imaging Application in Thermal Barrier Coatings', in 'Advances in Ceramic Coatings and Ceramic-Metal Systems: Ceramic Engineering and Science Proceedings, Volume 26, Number 3', (ed. K. P. Dongming Zhu), 112-119; 2008.

[20] N. H. H. Jones, N. J. Weston, K. B. Jonas, J. D. Shephard, D. P. Hand and M. Matysiak: 'Optical measuring method and system', Patent PCT/GB2010/000088, United Kindgdom, 20.01.2010, 2010.

[21] E. Hecht: 'Optics (4th Edition)'; 2002, Addison Wesley.

[22] K. Shinoda, Y. Kojima and T. Yoshida: 'In situ measurement system for deformation and solidification phenomena of yttria-stabilized zirconia droplets impinging on quartz glass substrate under plasma-spraying conditions', *Journal of Thermal Spray Technology*, 2005, **14**(4), 511-517.

[23] K. Shinoda, H. Murakami, S. Kuroda, S. Oki, K. Takehara and T. G. Etoh: 'High-speed thermal imaging of yttria-stabilized zirconia droplet impinging on substrate in plasma spraying', *Appl. Phys. Lett.*, 2007, **90**(19), 194103-194103.

[24] K. Shinoda, H. Murakami, S. Kuroda, K. Takehara and S. Oki: 'In Situ Visualization of Impacting Phenomena of Plasma-Sprayed Zirconia: From Single Splat to Coating Formation', *Journal of Thermal Spray Technology*, 2008, **17**(5), 623-630.

8. Conclusions and Future Work

The developed mid-infrared imaging techniques in this thesis present novel methods for measuring or detecting flaws in highly scattering ceramics. A 3mol% Yttria-Stabilised Zirconia Polycrystal (3Y-TZP) was the main material investigated in this study. 3Y-TZP as a medical material is characterised by high toughness and strength due to transformation toughening. Unfortunately, the white appearance of 3Y-TZP in the visible regime and its multicrystalline structure introduced a considerable challenge for development of a reliable but low cost method of inspection. The FTIR results presented in chapter 3 confirmed that in the visible wavelength region 3Y-TZP is highly scattering, whereas the mid-infrared region provided an opportunity for the bulk inspection due to the transmission window.

This thesis demonstrated a Mid-Infrared Transmission Imaging (MIR-TI) and a Confocal Mid-Infrared Transmission Imaging (CMIR-TI) technique for non-destructive inspection of 3Y-TZP parts. Also, a Camera Mid-Infrared Reflection Imaging (Camera-MIRI) and a Confocal Mid-Infrared Reflection Imaging (Confocal-MIRI) technique were developed for measurement and inspection of various ceramic coatings. The latter of these techniques was filed for a patent by Renishaw plc. The particular advantage of the MIR-TI and CMIR-TI techniques was their ability to measure considerably thicker components than any other method presented in the literature up to date. The techniques allowed for the detection of macro (above 1 mm in size) and micro scale (below 1 mm in size) defects in the bulk material accurately.

8.1. Visible light inspection

A benchmark for the developed mid-infrared inspection techniques was set by the limited visible light measurement capabilities of highly scattering 3Y-TZP ceramics. Although, visible light is currently applied to inspect 3Y-TZP dental parts the main disadvantages were:

a) limited detection capabilities of macro scale flaws,
b) detection of micro scale flaws was not feasible,
c) a highly skilled operator was required to carry out the measurement,
d) only thin samples (below 1 mm in thickness) could be measured.

The main advantages of visible light inspection on the other hand were:

a) low cost of the system,
b) simplicity of the setup and adjustment.

The visible light inspection of 3Y-TZP was investigated in this thesis mainly because it provides a low cost solution. The results presented in chapter 4 showed some potential in using visible light to detect macro scale flaws. Unfortunately for micro scale flaws detection was not feasible due to light scattering. The prospect of using visible light for 3Y-TZP ceramics inspection exists, however the samples cannot be thick and a skilled operator is required.

8.2. Mid-Infrared Transmission Imaging (MIR-TI)

The 3Y-TZP a mid-infrared transmission window provides an opportunity to inspect the bulk of the material non-destructively. Indeed, the MIR-TI technique provided more detailed information about the flaws in the bulk of 3Y-TZP. The main disadvantages of the MIR-TI technique were:

a) expensive infrared camera and infrared optical components,
b) limited imaging resolution due to camera pixel size (smallest features measuring 42 ± 5 μm – USAF infrared target measurement),
c) difficulty in differentiating between cracks and rough surface marks particularly for dental samples,
d) slow data acquisition due to low Labview script acquisition frequency (10 Hz),
e) the stages moved manually – positioning inaccuracy errors,
f) the developed MIR-TI system was not optimised for the wavelength range used during the measurements due to infrared camera optical characteristics.

The advantages of the MIR-TI technique were:

a) much improved imaging capabilities in comparison to visible light inspection – macro and micro scale flaws could be detected in the tested samples,
b) improved depth of inspection (up to 6 ± 0.1 mm of 3Y-TZP thickness) in comparison to visible light inspection,
c) simple and easy to use,
d) field of view of 11 x 7 mm which resulted in fast sample imaging.

The low imaging resolution of the camera and low optical power of the infrared source limited the sample thickness which could be measured and the smallest features which could be detected. Although the light scattering in the mid-infrared was considerably

minimised, it was still an issue therefore samples thicker than 6 ± 0.1 mm could not be tested successfully.

8.3. Confocal Mid-Infrared Transmission Imaging (CMIR-TI)

The main motivation for development of the CMIR-TI technique was reduction of the system cost. In the CMIR-TI setup an infrared detector in combination with a pinhole scanning approach was used, instead of an expensive infrared camera,. The pinhole scanning also provided an opportunity to enhance the imaging resolution due to a reduction in the pinhole size and the pinhole overlapping technique. The disadvantages of CMIR-TI imaging were:

a) significantly limited light reaching the detector due to pinhole filtering,
b) reduced maximum sample thickness (3.5 ± 0.1 mm) which could be inspected,
c) time consuming sample scanning – low speed motorised stages,
d) poor reliability of the motorised stages,
e) setup difficult to align,
f) setup susceptible to external noise due to lengthy scanning times,
g) time consuming image generation due to significant amount of data.

The advantages of CMIR-TI technique were:

a) improved imaging resolution – scanning steps overlapping technique (USAF target resolution measurement resulted in imaging resolution below 38.5 ± 5 µm),
b) flexibility in setting the CMIR-TI technique resolution by changing the pinhole size and the scanning step size,
c) automated sample scanning,
d) confocal sample imaging – slicing the samples during imaging which improved the images contrast and sharpness of the flaws detected,
e) reduced cost of the system due to reduced cost of the infrared detector,
f) optical characteristics more suitable to the transmission window of 3Y-TZP,
g) compact setup.

Due to the low speed motorised stages the CMIR-TI technique scanning times were high. The scanning speed was mainly dependent on the velocity of the motorised stages but also on the chopping frequency and the developed software. The feasibility analysis of a potential scanning speed improvement was investigated in section 6.4 where various scenarios were presented. The modifications of the CMIR-TI setup presented

considerable improvements in scanning speed where a single plane of the sample volume could be imaged in tens of seconds. Nevertheless, the CMIR-TI system was slow, but it produced the sharpest images for samples up to 3.5 ± 0.1 mm thick.

8.4. Comparison of MIR-TI and CMIR-TI techniques

The MIR-TI and CMIR-TI techniques were developed for 3Y-TZP parts inspection to provide non-destructive detection of flaws. This section compares both inspection techniques in terms of the imaging capabilities. Table 8.1 presents the comparison of the imaging resolution results between the MIR-TI and the CMIR-TI techniques measured with a USAF standard testing targets. Table 8.2 presents the suitability of the MIR-TI and the CMIR-TI techniques for the samples tested with both systems. Green colour indicates that the technique provided greater detail about the flaws buried inside the sample, whereas orange circle shows technique which also detected the flaws, however the data/images quality was lower.

Table 8.1. The comparison of all the resolution results for the MIR-TI and the CMIR-TI techniques.

Target used	MIR-TI	CMIR-TI
USAF target	**44 ± 5 µm**	**31.3 ± 4 µm**
USAF infrared target	**43 ± 5 µm**	**< 38.5 ± 5 µm**
USAF infrared target with the infrared band-pass filter	**42 ± 5 µm**	**< 38.5 ± 5 µm**

Table 8.2. The comparison of all the resolution results for the MIR-TI and the CMIR-TI techniques.

Sample	Features inside the sample	MIR-TI inspection		CMIR-TI inspection	
7	**1. Macro scale cracks** **2. Micro scale cracks**	🟠 🟠		🟢 🟢	**Sharper images and** **Better images contrast**
9	**1. Macro scale cracks** **2. Micro scale cracks**	🟢 🟠	**Better image contrast**	🟠 🟢	 **Better image contrast**
10	**1. Macro scale cracks**	🟢		🟢	**Results comparable**
12	**1. Macro scale cracks** **2. Micro scale cracks**	🟠 🟠		🟢 🟢	**Sharper images and** **Better image contrast**

From the above tables it was concluded that the CMIR-TI technique provided sharper images, particularly for micro scale flaws in thinner than 3.5 ± 0.1 mm samples. This was due to the step overlapping technique during scanning which compensated for image quality losses due to optical aberrations. Unfortunately, as discussed previously slow sample scanning was the main disadvantage of the CMIR-TI technique. MIR-TI imaging on the other hand was much faster but did not provide the image quality as good as CMIR-TI technique. However, much thicker samples (up to 6 ± 0.1 mm) could be tested with the MIR-TI technique.

8.5. Reflection Mid-Infrared Imaging

Based on the mid-infrared transmission imaging techniques discussed above Camera Mid-Infrared Reflection Imaging (Camera-MIRI) and Confocal Mid-Infrared Reflection Imaging (Confocal-MIRI) techniques were investigated. These techniques used the light reflected from the surface and bulk features in the material to detect the flaws. This approach could be applied when inspecting ceramic-based TBCs which protect the substrate below the coating from a harsh environment.

The presented methods detected the flaws below the artificial TBC samples and the surface defects in real TBC samples. Sample 15 (see Figure 3.4.4(a)) had an exposed oxidised (thermally grown oxide - TGO) layer which was detected by the Camera- and Confocal-MIRI techniques. The exposed area should be further examined experimentally to confirm that this was in fact the TGO layer. The above samples had a relatively smooth surface. Rough TBC samples 18, 19 and 20 were also inspected, however due to the material structure, the optical transmittance of the specimens was considerably lower compared to 3Y-TZP samples. Additionally, the rough surface of the specimens caused significant scattering and reflection from the surface thus complete in-depth sample inspection of these rough TBCs was not feasible.

Both the Camera- and Confocal-MIRI techniques were based on their transmission counterparts, thus the setups were not optimised for the reflection measurements. This was confirmed by the imaging resolution results which were considerably lower compared to the MIR-TI and the CMIR-TI techniques. For the Camera-MIRI the resolution was 62.5, 48 μm for a standard and an USAF infrared target measurements respectively. The Confocal-MIRI system imaging resolution was 48 μm for 10 μm step scanning for the infrared USAF target measurement. To this end, together with our

industrial partners Renishaw Plc, we have filed a patent protecting this invention and any further commercially viable techniques that may be developed.

8.6. Future work

All the presented inspection methods proved to be a useful tool in inspecting highly scattering ceramics. However, implementing further improvements for all the described methods is possible. The factors presented below set the challenges to further enhance the imaging capabilities and to automate the inspection of 3Y-TZP and other scattering ceramics.

The MIR-TI and CMIR-TI systems had their imaging capabilities limited by various components including optics, infrared source, detectors and the means of sample scanning. The overall optimisation of the setups and their components is feasible and should be carried out to further enhance imaging capabilities.

The image plotting and enhancement methods used in this study relied on simple Matlab scripts which often required manual adjustments to maximise the images contrast. To automate the crack detection different models are required where software, in addition to generating high quality and high contrast images, is able to detect flaws in micro and macro scale and control the whole system so that human intervention is not required.

During crack detection the challenge arises due to the fact that each crack is different, therefore a model based approach where attempting to locate features having certain characteristics is not feasible. The solution can be an anomaly detection algorithm, where the software detects the changes and compares them with a model of the machined part. Another approach could be rarity detection where the software detects features that are different to anything else in the component. Both of these approaches suffer from one drawback, they require a considerable effort to calibrate the device. There is a software learning procedure required, where there are many samples with defined flaws which have to be tested and quantified by the system. In addition, defining the threshold at which a crack is not a crack any more is also challenging. The problem is particularly difficult in the medical field where each part is different and the shapes of the components are unique. All these factors have to be considered when designing the software platform.

Further investigation should be carried out for the step overlapping technique used during CMIR-TI scanning. This approach enhanced the resolution of the images, however determination as to whether the resolution improvement was caused by the higher number of data points or a combination of factors including the plotting method and the algorithm used to plot the data, needs to be carried out.

Using Camera- and Confocal-MIRI techniques for TBCs confirmed that the inspection was feasible, however the quantification of both reflection techniques was not possible due to the lack of samples and the defined flaws which could be tested. For that reason further study is required. There is also a considerable scope for improving the imaging resolution for both reflection techniques as both Camera- and Confocal-MIRI systems were based on their transmission counterparts, therefore setups specifically optimised for reflection measurements should be developed.

Appendix A. Material properties

Table A.1. Material Properties of 3%mol Yttria-Stabilised Zirconia Polycrystal

Properties	Units	Value
Density	gm/cc	**6.02**
Crystal Size	microns	**1**
Water Absorption	%	**0**
Gas Permeability	-	**0**
Color	-	**Ivory**
Flexural Strength (MOR)	MPa (psi·10^3)	**900 (130)**
Elastic Modulus	GPa (psi·10^6)	**210 (30)**
Poisson's Ratio	-	**0.23**
Compressive Strength	MPa (psi·10^3)	**2500 (363)**
Hardness	GPa (kg/mm^2)	**12.7 (1300)**
Tensile Strength	MPa (psi·10^3)	**-**
Fracture toughness	MPa·$m^{1/2}$	**13**
Thermal Conductivity (20 º C)	W·m·K	**2.2**
Coefficient of Thermal Expansion	1·10^{-6}/degrees C	**10.3**
Specific Heat, 100 º C	J/kg*K	**400**
Thermal Shock Resistance	degrees C	**350**
Maximum Use Temperature	degrees C	**1500**
Dielectric Strength	ac-kV/mm (acV/mil)	**9.0 (228)**
Dielectric Constant, 1MHz	25 º C	**29.0**
Dielectric Loss (tan delta) 1MHz	25 º C	**0.0010**
Volume Resistivity 25 º C	Ohm-cm	**> 10^{13}**
500 º C	Ohm-cm	**2 x 10^4**
1000 º C	Ohm-cm	**>10^3**

Appendix B. 1951 USAF infrared testing target

USAF infrared testing target was developed to carry out the imaging resolution measurement in mid-infrared. A 1 mm thick Calcium Fluoride (CaF_2) glass was chosen as a substrate because of the high optical transmittance in the mid-infrared wavelength region. A 170 nm thick aluminium coating was deposited on top of the glass using a thermal evaporation technique.

The target bars were machined using a Trumph TruMicro 5050 picosecond laser system operating at a wavelength of 354 nm. The testing target was machined with two laser passes perpendicular to each other. It was only possible to laser machine group two and group three bars from the USAF target due to the fact that machining of group four bars was highly inaccurate. During the machining process the average power of the laser was 83 mW at 33 kHz repetition rate which provided 2.5 µJ pulse energy (equation (B.1)).

$$E = \frac{P_{avg}}{f_{rep}} \qquad \text{(B.1)}$$

where P_{avg} is the laser average power and f_{rep} is the laser repetition rate. The spot size of the laser beam was measured to be 8 µm in diameter. With the repetition rate of 33 kHz and the 100 mm/s galvanometer speed consecutive pulses were centred on a 3 µm pitch, resulting in an overlap. The picture of the machined USAF infrared target is presented in Figure B.1.

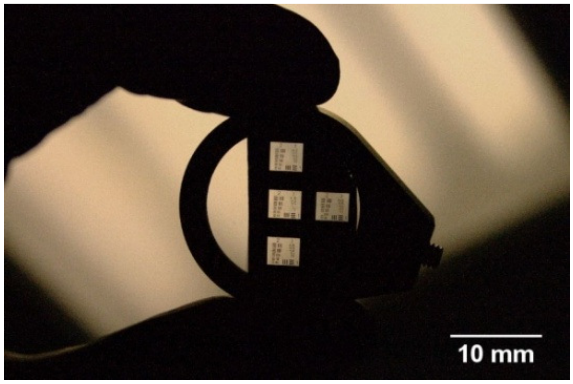

Figure B.1. Machine USAF infrared target.

The comparison of the optical transmittance of the USAF target and USAF infrared target is presented in Figure B.2. The contrast between the CaF_2 optical transmission

and the aluminium coating deposited on the glass revealed an 8:1 contrast which provided a high contrast target throughout the measured wavelength range.

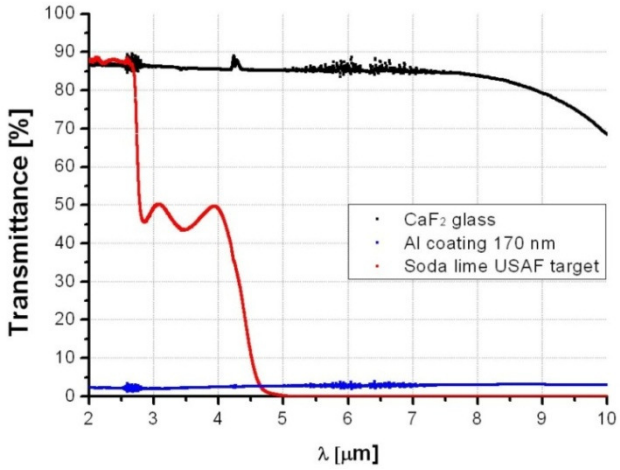

Figure B.2. Optical transmittance of: a standard soda lime glass USAF target, CaF_2 glass infrared target and aluminium coating deposited on the CaF_2 glass.

The microscope images of the standard USAF target and the machined target bars are shown in Figure B.3. The machined target bars were 9% smaller due to issues with the laser stability which was later diagnosed as a cracked laser crystal, hence this error had to be considered when analysing the resolution results based on the infrared target measurement.

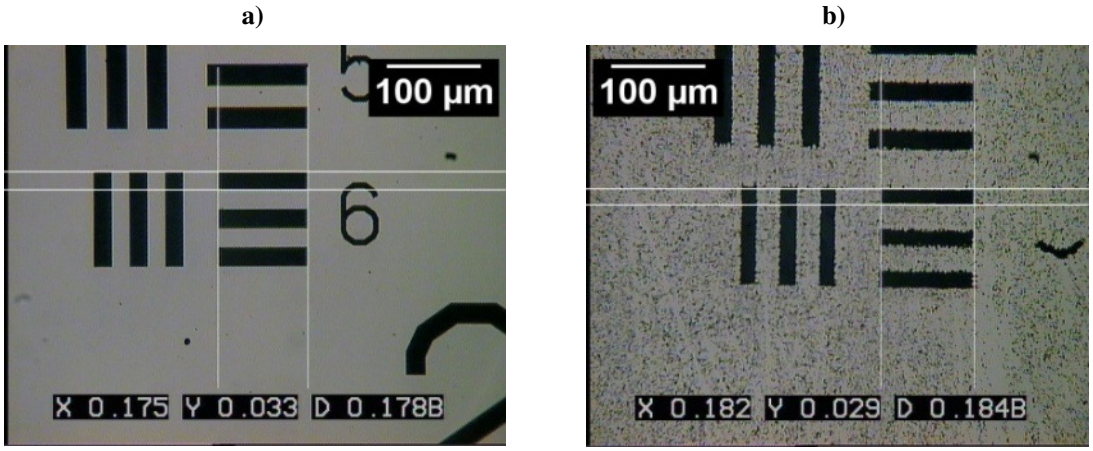

Figure B.3. Microscope images of the testing target bars: a) soda lime USAF target; b) CaF_2 infrared target. The images present the sixth element from the third group.

Appendix C. Selected images of sample 7 acquired during MIR-TI scanning

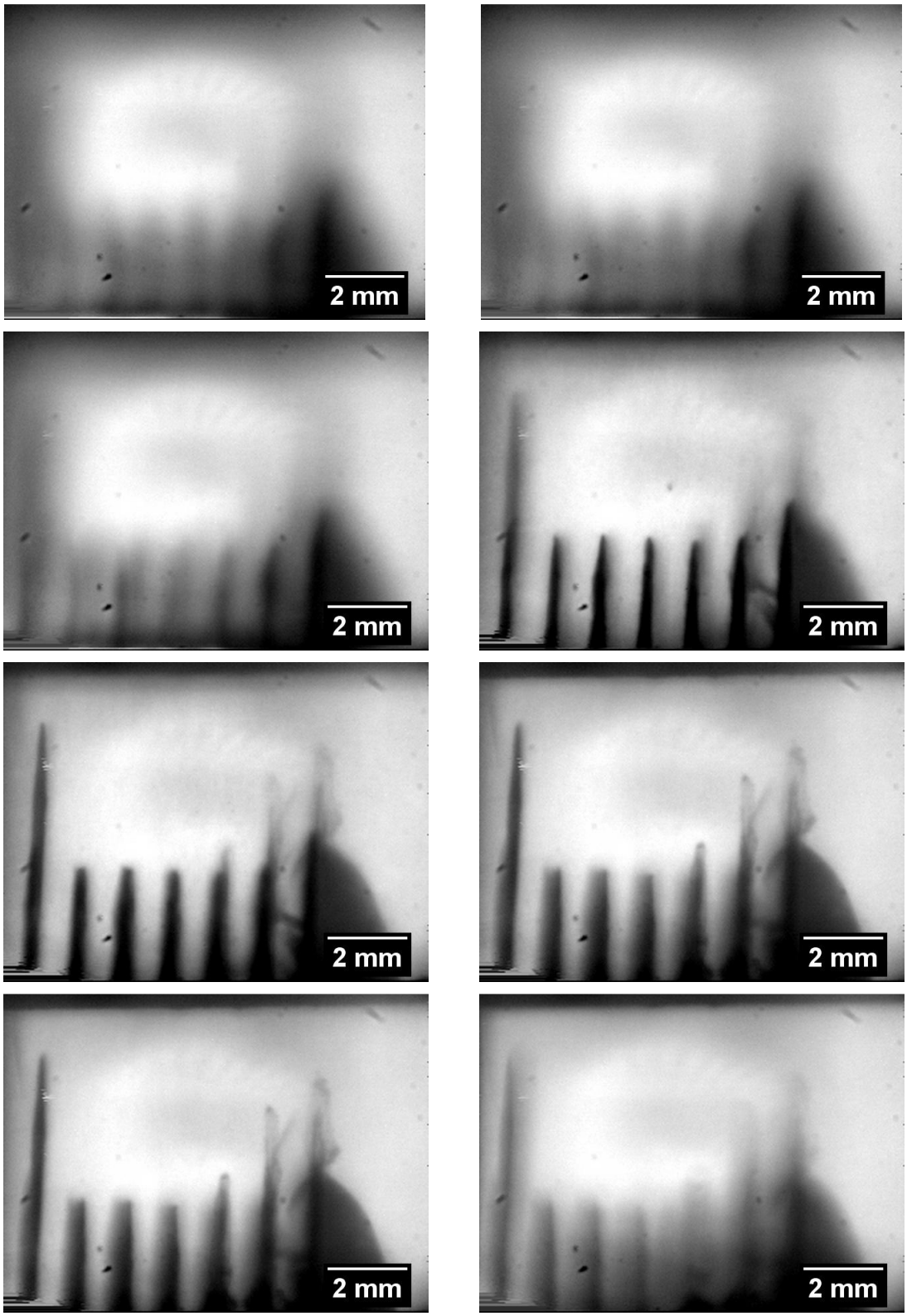

Figure E.1. MIR-TI scanning of Sample 7.

Appendix D. CMIR-TI images sequence from sample 7 scanning

A sequence of CMIR-TI images pitched by 250 µm.

Imaging parameters: 50 µm pinhole, 10 µm step scanning, $f_{chopper}$ = 1.6 kHz, the stages velocity was 160 µm/s, $T_{lock\text{-}in}$ = 30 ms and S = 300 µV.

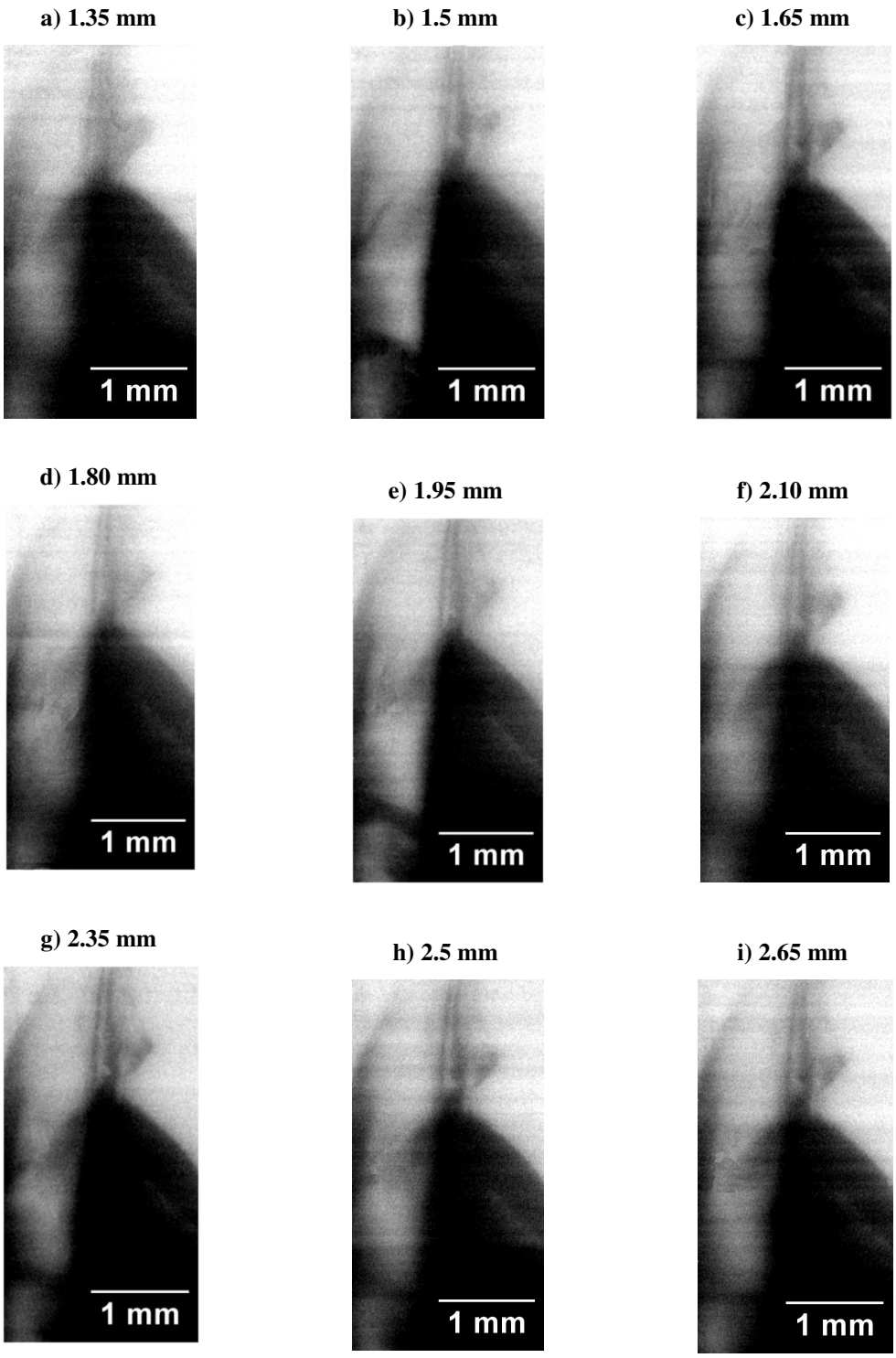

Figure D.1. CMIR-TI images sequence from sample 7 scanning.

Appendix E. CMIR-TI images contrast estimation

To quantify the contrast of the detected cracks in reference to the background illumination, the area between the holes where the cracks were detected and the crack regions were cut out from the images as highlighted in Figure E.1. The image histograms of the areas are presented in Figure E.2.

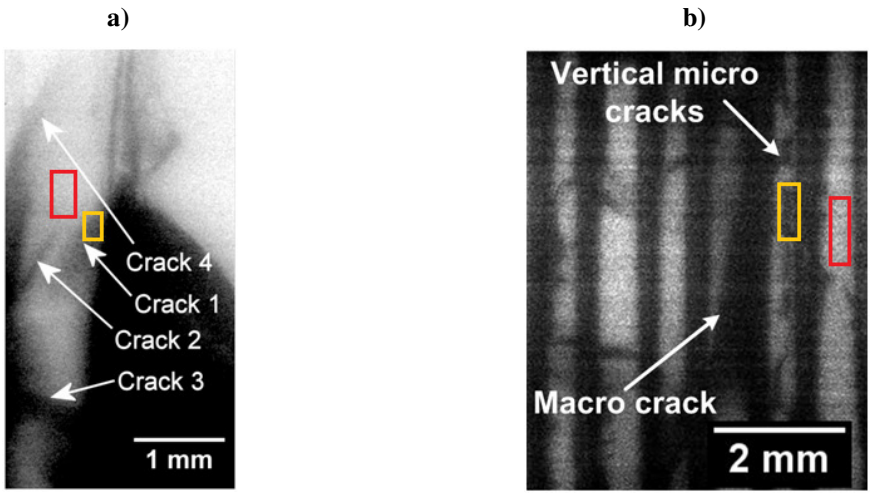

Figure E.1. The images of: a) sample 7 and b) sample 12. In red are the background regions and in orange the crack areas used to plot the histograms.

The histograms were used to calculate the images intensity difference between the background signal and the crack region. A Gaussian curve was fitted to the shape of the histograms. The centre of the Gaussian curve was used as a reference for the average pixel intensity for the background and the crack area. Parameter Pix_{avg} determined the relation between the light intensity of the background and the crack region was used as a contrast estimator and it was calculated from equation (E.1).

$$Pix_{avg} = (1 - \frac{Pix_{crack}}{Pix_{background}}) \cdot 100\% \qquad (E.1)$$

where $Pix_{background}$ and Pix_{crack} are the average pixel intensities (for full pixel intensity range between 0 and 255) for the area between the holes, around the crack and the crack itself respectively.

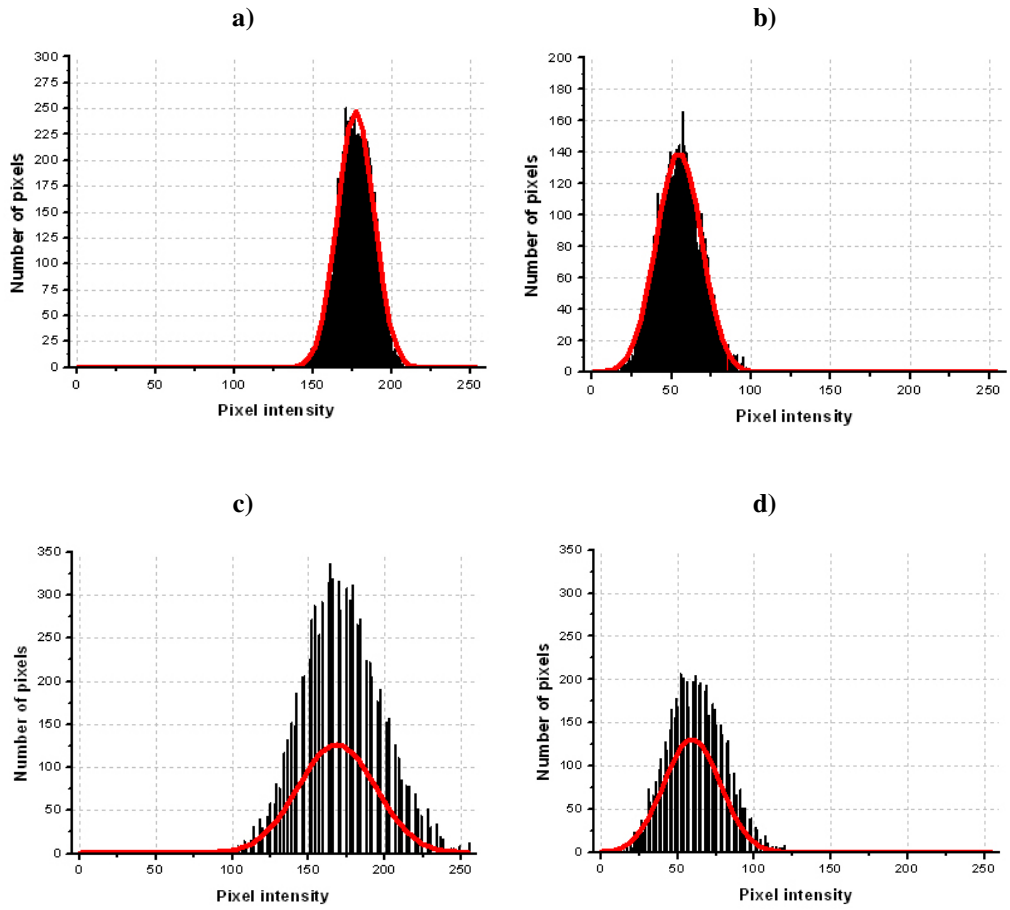

Figure E.2. The histograms of the images from Figure E.1 for: a) sample 7 – background region; b) sample 7 – crack region; c) sample 12 – background region; d) sample 12 – crack region. In red the Gaussian fit is shown. The histograms indicate the average pixels intensity (centre of the Gaussian fit) for the measured regions.

The results for sample 7 and 12 from Figure E.2 are presented in Table E.1. For sample 7 and 12 the pixel intensities from the photons travelling through the non-cracked area and the photons travelling through the cracked region varied more than 60% difference, whereas for thicker samples the contrast dropped steadily. From all the samples tested it was determined that below Pix_{avg} = 23% the detection of the cracks was difficult and cracks could be easily undetected.

Table E.1. The comparison of all the resolution/image sharpness results for MIR-TI technique.

	$Pix_{background}$	Pix_{crack}	Pix_{avg} [%]c
Sample 7	**177.1**	**54.4**	**69.3**
Sample 12	**168.5**	**59.3**	**64.8**